การเพิ่มประสิทธิภาพของไททาเนียมไดออกไซด์โดยการปรับปรุงในรูปของวัสดุนาโนคอมโพสิตกับคอปเปอร์พทาโลไซยานีนและนิกเกิลออกไซด์ โดยใช้กระบวนการบดด้วยลูกบดช่วย

PERFORMANCE EFFICIENCY ENHANCEMENT OF TiO_2 MODIFIED IN FORM OF NANOCOMPOSITE WITH CuPc AND NiO BY BALL-MILLING-ASSISTED PROCESS

วณิชยา เมฆประสาท

WANICHAYA MEKPRASART

วิทยานิพนธ์นี้สำหรับการศึกษาตามหลักสูตรปริญญาปรัชญาดุษฎีบัณฑิต
สาขาวิชานาโนวิทยาและนาโนเทคโนโลยี
วิทยาลัยนาโนเทคโนโลยีพระจอมเกล้าลาดกระบัง
สถาบันเทคโนโลยีพระจอมเกล้าเจ้าคุณทหารลาดกระบัง
พ.ศ. 2555

KMITL-2012-NT-D-001-002

PERFORMANCE EFFICIENCY ENHANCEMENT OF TiO_2 MODIFIED IN FORM OF NANOCOMPOSITE WITH CuPc AND NiO BY BALL-MILLING-ASSISTED PROCESS

WANICHAYA MEKPRASART

A THESIS SUBMITTED IN PARTIAL FULFILLMENT

OF THE REQUIREMENT FOR THE DEGREE OF

DOCTOR OF PHILOSOPHY IN NANOSCIENCE AND NANOTECHNOLOGY

COLLEGE OF NANOTECHNOLOGY

KING MONGKUT'S INSTITUTE OF TECHNOLOGY LADKRABANG

2012

KMITL-2012-NT-D-001-002

หัวข้อวิทยานิพนธ์	การเพิ่มประสิทธิภาพของไททาเนียมไดออกไซด์โดยการปรับปรุงในรูปของวัสดุคอมโพสิตกับคอปเปอร์พทาโลไซยานีนและนิกเกิลออกไซด์ด้วยกระบวนการบดเคลือบด้วยลูกบดช่วย
นักศึกษา	นางสาววณิชยา เมฆประสาท
รหัสประจำตัว	51614252
ปริญญา	**ปรัชญาดุษฎีบัณฑิต**
สาขาวิชา	นาโนวิทยาและนาโนเทคโนโลยี
พ.ศ.	2555
อาจารย์ที่ปรึกษาวิทยานิพนธ์	รศ.ดร.วิษณุ เพชรภา

บทคัดย่อ

ในงานวิจัยนี้ได้ทำการสังเคราะห์ไททาเนียมไดออกไซด์อนุภาคระดับนาโนในรูปของวัสดุคอมโพสิตในรูปของสารอินทรีย์-สารอนินทรีย์หรือไฮบริด และสารอนินทรีย์-สารอนินทรีย์ รวมถึงการนำไปประยุกต์ใช้งาน กระบวนการที่ใช้ในการปรับปรุงวัสดุคอมโพสิตจะใช้กระบวนการบดผสมด้วยลูกบดร่วมกับกระบวนการอื่น เช่น กระบวนการกวนสารโดยใช้แท่งแม่เหล็ก กระบวนการปั่นด้วยความเร็วรอบสูง และกระบวนการโซลเจล การวิเคราะห์ทางโครงสร้างของวัสดุคอมโพสิตจะทำการวิเคราะห์ด้วยเครื่องวิเคราะห์การเลี้ยวเบนลำรังสีเอ็กซ์ กล้องจุลทรรศน์อิเล็กตรอนแบบเลื่อนกราด กล้องจุลทรรศน์อิเล็กตรอนแบบส่องผ่าน สเปกโตรสโคปีการดูดกลืนรังสีเอกซ์ และ สเปคโตรสโคปีของอนุภาคอิเล็กตรอนที่ถูกปลดปล่อยด้วยรังสีเอกซ์ ส่วนสมมบัติทางเคมีจะทำการวิเคราะห์ด้วยเครื่องรามานสเปกโตรสโคปี และเครื่องวิเคราะห์การเปลี่ยนแปลงน้ำหนักและพลังงานความร้อนของวัสดุ ในขณะที่สมบัติการดูดกลืนทางแสงจะทำการวิเคราะห์ด้วยเครื่องวัดการดูดกลืนรังสียูวี และพื้นที่ผิวจำเพาะของวัสดุคอมโพสิตจะทำการวิเคราะห์ด้วยวิธี Brunauer–Emmett–Teller วัสดุไฮบริดคอมโพสิตเตรียมจากการผสมระหว่างไททาเนียมไดออกไซด์กับคอปเปอร์พทาโลไซยาไนด์ผ่านกระบวนการบดผสมด้วยลูกบดร่วมกับการปั่นด้วยความเร็วรอบสูงพบว่าการดูดกลืนแสงของวัสดุคอมโพสิตเพิ่มมากขึ้นในย่านรังสีอัตราไวโอเลตและแสงในย่านที่ตามองเห็น อีกทั้งยังเป็นการลดการรวมตัวของคู่อิเล็กตรอนและความต้านทานที่รอยต่อของไททาเนียมไดออกไซด์ เมื่ออยู่ในรูปวัสดุคอมโพสิตที่มีคอปเปอร์พทาโลไซยานีน วัสดุคอมโพสิตในรูปของสารอนินทรีย์-สารอนินทรีย์ซึ่งอาจจะอยู่ในรูปของรอยต่อพีเอ็นเตรียมจากการผสมระหว่างไททาเนียมไดออกไซด์กับนิกเกิลออกไซด์ด้วยกระบวนการบดผสมด้วยลูกบดและโซลเจล ซึ่งผลของการมีชั้นของนิกเกิลออกไซด์จะเป็นการยับยั้งการรวมตัวของคู่อิเล็กตรอน-โฮล อีกทั้งยังเป็นการเพิ่มจำนวนการทะลุผ่านของอิเล็กตรอนผ่านชั้นนิกเกิลออกไซด์ที่

บริเวณรอยต่อ โดยวัสดุคอมโพสิตที่ได้ทำการสังเคราะห์นั้นจะนำไปใช้ในงานด้านส่วนประกอบของขั้วทำงานในเซลล์แสงอาทิตย์ชนิดสีย้อมไวแสงและเป็นตัวเร่งปฏิกิริยาทางแสงในปฏิกิริยาการย่อยสลายสารอินทรีย์ในสีย้อม ซึ่งผลที่จะได้จะแสดงให้เห็นว่า การพัฒนาในรูปแบบของวัสดุคอมโพสิตจะสามารถเพิ่มประสิทธิภาพการทำงานของไททาเนียมไดออกไซด์เมื่อเปรียบเทียบกับไททาเนียมไดออกไซด์ทั่วไป

คำสำคัญ : วัสดุคอมโพสิต, ไททาเนียมไดออกไซด์, คอปเปอร์พทาโลไซยาไนด์, นิกเกิลออกไซด์, กระบวนการบดด้วยลูกบด

Thesis Title	Performance Efficiency Enhancement of TiO_2 Modified in form of Nanocomposites with CuPc and NiO by Ball-milling-assisted Process
Student	Ms. Wanichaya Mekprasart
Student ID	51614252
Degree	Doctor of Philosophy
Program	Nanoscience and Nanotechnology
Year	2012
Thesis Advisor	Assoc. Prof. Dr. Wisanu Pecharapa

ABSTRACT

The main objective of this work focuses on the synthesis of functional composite of TiO_2 nanoparticles in form of hybrid composite and p-n junction composite and their applications. The composites were synthesized via ball-milling-assisted process in combination with facile methods including mechanically stirring method, homogenization and sol-gel process. Structural properties of as-prepared composites were characterized by X-ray diffraction, field emission scanning electron microscopy, transmission electron microscopy, X-ray absorption near edge structure and X-ray photoelectron spectroscopy. Chemical properties of the nanocomposites were investigated by Raman spectroscopy and thermal differential analyses, meanwhile their relevant optical properties were thoroughly investigated by UV-Vis spectroscopy. Specific surface area of the nanocomposites was determined by Brunauer–Emmett–Teller method. The hybrid nanocomposite was prepared by mixing TiO_2 with copper phthalocyanine (CuPc) via ball milling process and homogenization. Absorptivity in UV region of the composite is heightened and shifted to visible light due to strong absorbance in blue-green spectrum of CuPc. The existence of CuPc in the hybrid composite may result to the decrease of recombination of photo-injected electrons and reduction of charge transfer resistances at the interface of TiO_2. The p-n junction nanocomposites of TiO_2 were synthesized by mixing TiO_2 with nickel oxide (NiO) via sol-gel ball milling process. The presence of NiO on TiO_2 surface may retard the recombination of electron-hole pair and enhance the number of electrons tunneling through the NiO layer at the interface. These two composites were utilized as modified working electrode materials in dye-sensitized solar cell and photocatalyst for organic pollutant degradation. The

corresponding results exhibited significant enhancement in their performance comparing to bare TiO_2.

Keywords: Nanocomposite, Titanium dioxide, Copper Phthalocyanine, Nickel oxide, Ball milling process

ACKNOWLEDGEMENT

The success of this thesis can be attributed to the assistance and support of my best advisor and teacher, Assoc. Prof. Dr. Wisanu Pecharapa. I would like to express my sincere gratitude to him due to his great support, guidance and countless suggestions in my life and research. My life in master student was started with failure in work and love that made me in negative mode. Because of his positive advice, good encouragement and believe in my potential made me stronger and encounter with difficult obstacles. Great time and excellent experience were obtained in four year of my studying. I will keep in mind and try to guide the best instructions to another person.

This thesis would not have been possible without support, instruction and guideline of Dr. Wirat Jarernboon for DSSC fabrication and Dr. Darinee Phromyothin for the processing simulation of quantum chemistry that excessively difficult to me.

I would like to thank my single girl gang, who is always stand by me when I met strong problems and resolve it.

I wish to acknowledge Thailand Center of Excellence in Physic (ThEP) and National Nanotechnology Center (NANOTEC) for scholarship and financial research support and College of Nanotechnology, King Mongkut's Institute of Technology Ladkrabang for public utility.

This thesis has been supported by the thesis scholarship of King Mongkut's Institute of Technology Ladkrabang.

Finally, I would like to thank my parents and my sister for their support throughout, as always, for which my mere expression of thanks likewise does not suffice. I have good chance in high education hence I would like to dedicate this thesis to my family who is my love.

Wanichaya Mekprasart

CONTENTS

CONTENTS (CONT.)

CONTENTS (CONT.)

CONTENTS (CONT.)

CONTENTS (CONT.)

LIST OF TABLES

LIST OF FIGURES

LIST OF FIGURES (CONT.)

LIST OF FIGURES (CONT.)

LIST OF FIGURES (CONT.)

LIST OF FIGURES (CONT.)

CHAPTER 1
INTRODUCTION

1.1 Motivation

Among functional metal oxide semiconductors, Titanium dioxide (TiO_2) is currently one of the most widely used materials due to its distinguished properties including wide optical band gap (~3.2 eV), strong ultraviolet absorptivity, and non-toxicity. Owing to its excellent properties, TiO_2 is utilized in various applications ranging from photocatalyst for organic pollutants degradation, the filler in polymer matrix as photo-carrier collector in optical devices, and electron transport layer in optoelectronic device applications. However, the rather high recombination of photogenerated electron-hole pairs and the weak absorption in visible region are its major drawbacks. Therefore, various techniques have been proposed in order to modify TiO_2 powder to overcome these inferiorities. A number of research works have employed the advantage of comparably large surface area of TiO_2 nanostructures such as thin film structure, nanoparticle, nanorod, nanosheet and nanotube to improve its performance [1-5]. Recently, it was also reported that TiO_2 incorporated with appropriate semiconductors in form of composite material is one of alternating method for solving its disadvantages. The decreasing of the charge recombination and the enhancement of the absorption in visible region of TiO_2 can be accomplished when it is incorporated with compatible materials in form of composites [6-8].

Many group researches have dedicated on the preparation of TiO_2 composite material by various potential processes such as dye coating process, sol-gel process, mechanically stirring process and ball-milling process ,etc. However, for practical usage, the necessity of suitable method that can make the homogeneous dispersion between two materials is required. Among these processes, ball milling has been chosen as a potential process for simple blending solid-state powder technique which could produce homogenized powder. The idea in this research stresses on the processes that can effectively modify functionality of TiO_2 and improve its performance in form of organic-inorganic hybrid composite and p-n junction composite via ball-milling process assisted homogenization and sol-gel process. It is believed that TiO_2 in the composite form can retard the recombination of photo-

generated electron - hole pair of TiO_2 and can increase the absorption capability in the visible region of the composite. These functional composites were applied as modifying working electrode materials in dye sensitized solar cell and the photocatalyst in dye photodegradation.

1.2 Objective

This research is conducted in order to

1.2.1 Study the properties of precursor materials; titanium dioxide, copper phthalocyanine and nickel oxide.

1.2.2 Study the meaning, classification, notable properties and applications of composite, nanocomposite, hybrid nanocomposite and p-n junction nanocomposite.

1.2.3 Study theories, principles and methods of synthesis; ball-milling process, homogenization and sol-gel.

1.2.4 Study the principle of dye sensitized solar cell and the photocatalyst in dye photocatalytic degradation.

1.2.5 Study the improvement of TiO_2 commercial powder properties and mechanism of pure TiO_2 and TiO_2 in the nanocomposite form of hybrid and p-n junction materials.

1.2.6 Study the appropriate preparation of TiO_2 in form of nancomposite with guest materials and the applications of TiO_2 nanocomposite.

1.3 Scope of Study

The scope of this study is as follows,

1.3.1 Synthesis TiO_2 in form of hybrid and p-n nanocomposite with copper phthalocyanine and nickel oxide.

1.3.2 Investigate the crucial preparation parameters of composite materials via ball-milling process on functionality of TiO_2.

1.3.3 Analyze the structural properties, morphology and optical properties of synthesized materials in form of TiO_2 nanocompsite.

1.3.4 Prove the enhancement in performances of these utilizations in form of TiO_2 nanocomposite comparing to pure TiO_2.

1.3.5 Utilize TiO_2 nanocomposite for dye sensitized solar cell and photocatalytic degradation application.

1.4 Expected Results

1.4.1 Properties and their applications of precursor materials will be acknowledged.

1.4.2 The meaning, classification, notable properties and applications of composite, nanocomposite, hybrid nanocomposite and p-n junction nanocomposite will be clearly understood.

1.4.3 Theories and principles of ball-milling process, homogenization and sol-gel and the appropriate methods for synthesis in form of composite can be clarified.

1.4.4 The relevant parameters such as ball-milled time, guest doping content, post treatment temperature, affecting TiO_2 properties and functionality will be notified.

1.4.5 The enhancement of efficiency in the applications with TiO_2 nanocomposites will be proven.

CHAPTER 2
THEORETICAL BACKGROUNDS

The main objective of this study is to understand relevant properties of starting materials for composite synthesis, the meaning of composite, composite synthesis processes and the application of hetero-semiconductor nanocomposite in DSSC and dye photodegradation. In this chapter, the corresponding theories are also presented.

2.1 Titanium Dioxide

2.1.1 History of Titanium Dioxide

Titanium element was discovered in 1791 by William Gregor, in England. A sample of a black sandy substance in his neighborhood was studied, which led him to his discovery and called it "menachanite". Four years later, Martin H. Klaproth encountered a new chemical element in this mineral and named it "Titanium or Titans". This discovery was humongous monsters that ruled the world in Greek mythology. The pure element of titanium was not able to use, however, the suitable structure and useful material is in the form of titanium oxide [9].

2.1.2 Structural and Properties of Titanium Dioxide

Titanium dioxide with chemical formula TiO_2, is also known as titanium (IV) oxide or titania. The physical feature of TiO_2 is fine white powder and its structure is classified to 3 phases; anatase, rutile and brookite as shown in Figure 2.1(a) and (b), respectively. The crystalline structures of anatase and rutile phase are tetragonal but brookite phase is orthorhombic structure. A rutile unit cell contains six atoms, with lattice constants of a_0 = 4.593 Å and c_0 = 2.958 Å. An anatase unit cell contains twelve atoms per unit cell with lattice parameters a_0 = 3.785 Å and c_0 = 9.511 Å. Last phase, brookite unit cell parameters are a_0 = 5.4558 Å and c_0 = 5.1429 Å with eight atom per unit cell. Anatase form is generally produced as white powder, whereas rutile grade is often off-white depending on light reflectance in the physical form. The appearance of brookite is usually in brown (sometimes yellowish or reddish brown or even black) with a submetallic luster.

As a bulk material, TiO_2 in rutile phase is stable phase at high temperature meanwhile anatase and brookite phase are obtained by solution-phase methods and

thermal process. Anatase phase nanoparticles with diameters ranging from 6–30 nm are generally prepared from titanium (IV) isopropoxide and acetic acid. When stronger acids are used, a fraction of the product usually consists of brookite nanoparticles. Larger anatase particles are difficult to synthesize due to transformation to rutile upon increasing treatment times and/or temperature. Brookite-phase nanoparticles in range of 5-10 nm have been synthesized by thermolysis of $TiCl_4$ in aqueous HCl solution. High reaction product of brookite phase (up to 80%) was strongly dependent on the concentration ratio of Ti:Cl. Rutile-phase-nanoparticles have been prepared from $TiCl_4$ or $TiCl_3$ in HCl solution or from titanium (IV) isopropoxide in nitric acid at pH = 0.5 [10].

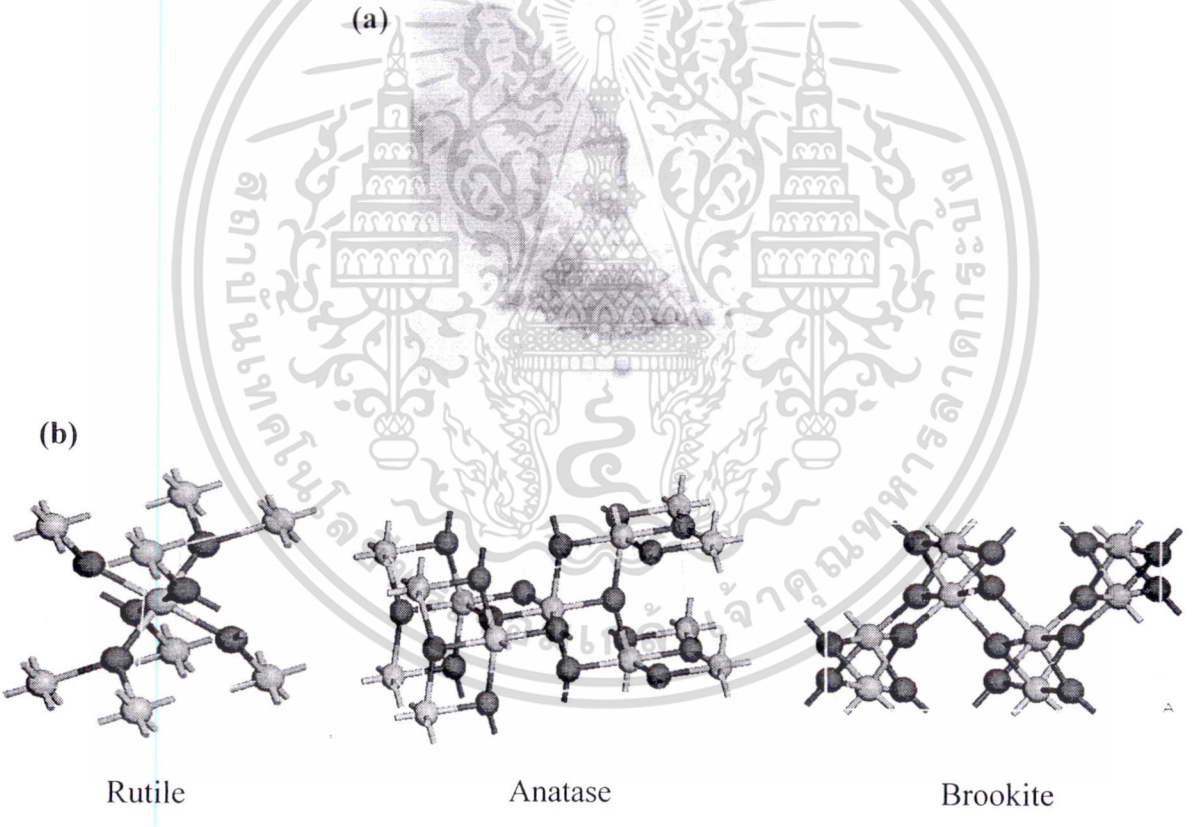

Figure 2.1 (a) TiO_2 powder and (b) crystalline structure of TiO_2 rutile, anatase and brookite phase.

Table 2.1 Physical properties of TiO_2.

Physical properties of TiO_2	
Molecular weight	79.87 g/mol
Density	4.23 g/cm^3
Melting point	1870 °C
Boiling point	2972 °C
Porosity	0%
Dielectric constant (1MHz)	85
Thermal conductivity (25°C)	11.7 WmK^{-1}
Electrical resistivity (25°C)	10^{12} ohm.cm
Electrical resistivity (700°C)	2.5×10^{4} ohm.cm
Young's modulus	230 GPa

Source: Pollution Control Department [11].

The physical properties of TiO_2 are shown in Table 2.1. The typical properties of TiO_2 include wide optical band gap (~3.2 eV), strong ultraviolet absorptivity, non-toxicity, long-term chemical stability, excellent photocatalysis and high energy conversion efficiency. Due to these distinguished properties, TiO_2 is utilized in various applications ranging from photocatalyst for organic pollutants degradation in water treatment process, the filler in polymer matrix for improving their optical function as photo-carrier collector, and electron transport layer in optoelectronic device applications such as the working electrode material in dye-sensitized solar cell.

Commercial TiO_2 nanoparticle in this research is Degussa (Evonik) P25, Aeroxide TiO_2 P-25. The physical-chemical properties of TiO_2 P-25 are shown in Table 2.2. Because of its relatively high levels of activity, titanium dioxide photocatalyst has been widely used in many photocatalytic reaction systems. TiO_2 P25 is typically composed of anatase and rutile crystallites with ratio 70:30 or 80:20.. The co-presence of anatase and rutile crystallites can induce charge transfer of photoexcited electrons and positive holes between interconnecting anatase and rutile particles enhancing charge separation and improving the efficiency of utilization of electron-hole pairs.

Table 2.2 Physical and chemical properties of TiO_2 P-25.

Properties	Value
BET surface area	50±15 m^2/g
Average particle size	30 nm
Moisture	< 1.5%
Ignition loss	< 1.5%
pH in 4% aqueous suspension	3 - 4
Structure ratio (Anatase:Rutile)	80:20
Density	3.98 g/cm^3
Titanium dioxide	>99.5 %
Aluminum oxide	< 0.3%
Silica	< 0.01%
Iron oxide	< 0.01%
HCl	< 0.3%

Source: Degussa [12]

2.2 Copper Phthalocyanine

2.2.1 Structural and Properties of Copper Phthalocyanine

Copper phthalocyanine (CuPc) with chemical formula $C_{32}H_{16}CuN_8$ is typically bright blue with purple lustre powder and also known as *monastral blue*, *phthalo blue*, *helio blue*, *thalo blue etc.* CuPc is a kind of phthalocyanine that is composed of four macrocyclic compounds with a stable conjugated π system as shown in Figure 2.2. It is well-known for excellent resistance of chemical degradation, strong absorption in blue-green region and good thermal stability [13]. The important physical properties of CuPc are shown in table 2.3.

The crystalline phases of CuPc are two different phases, the α- and β-forms, that are both monoclinic crystalline structure. The α-phase structure has 4 molecules per 1 unit cell with a = 25.9 Å, b = 3.8 Å and c = 23.9 Å at α=92° meanwhile the β- forms has 2 molecules per 1 unit cell with a = 19.4, b = 4.8 Å and c = 14.6 Å at β=120°. The β - form is more stable phase in chemical oxidization and may be thermally derived over 200 °C from the α - phase [14]

(a)

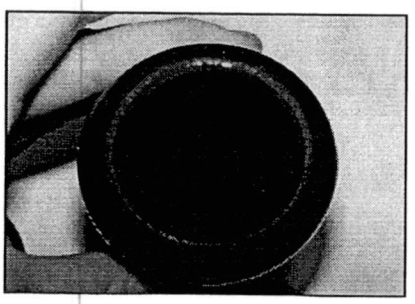

(b)

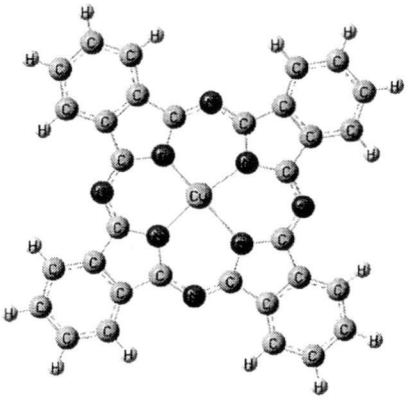

Figure 2.2 (a) CuPc powder and (b) molecular structure.

Table 2.3 Physical and chemical properties of CuPc [15].

Physical properties of CuPc	
Molecular weight	576.08 g/mol
Density	1.61-1.62 g/cm^3
Melting point	350 °C
Vapor Pressure	375×10^{-7} kPa at 384 °C
Water Solubility	Not soluble

2.2.2 Optical Properties of Copper Phthalocyanine

The absorption of CuPc possesses two distinct broad bands. The first region called Q-band covers the wavelength range of 600-900 nm. This absorption spectrum in the visible region has generally been interpreted in terms of π-π^* excitation between bonding and antibonding molecular orbital of phthalocyanine molecules. The second region in UV range (300-500 nm) is called B-band or Soret band that is attributed to the transition of π-d excitation in center atom of Pc occurs in this absorption region [16]. This absorption is illlustrated in Figure 2.3.

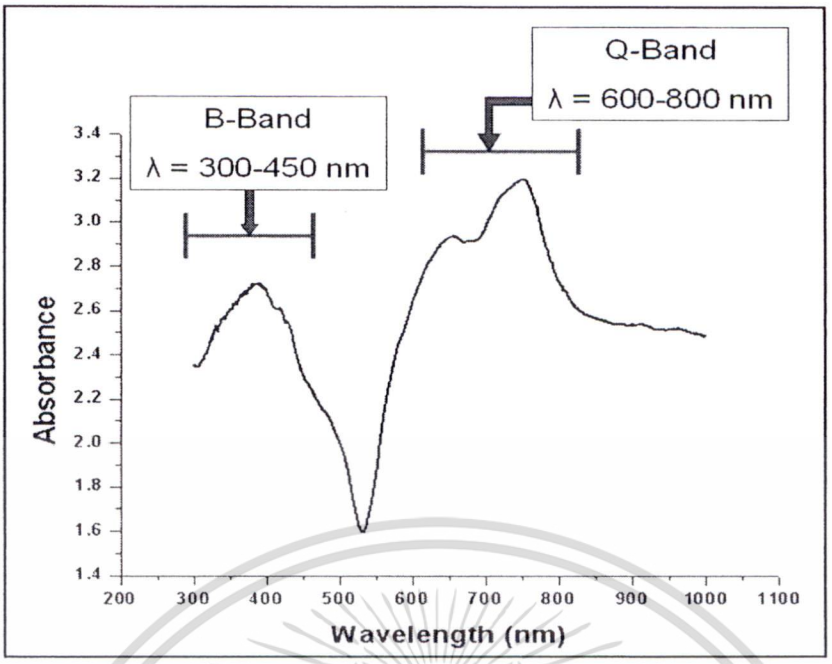

Figure 2.3 The optical absorbance of CuPc [16].

2.3 Nickel Oxide

2.3.1 Historical of Nickel

In the 17th century, a red colored ore was discovered by German miners and believed that it was composed of copper element. From the characterization, copper composition was though not detected. They thought that this element was useless and labeled to "Kupfernickel" or Old Nick's Copper, which meant false or bad copper. Baron Axel Frederich Cronstedt, Swedish scientist, finally isolated nickel from an ore closely resembling kupfernickel in 1751. Hence, he named this new element after the traditional mineral. The oxidation state of Nickel is between -1 to +4 but the most important oxidation state known primarily for its divalent compounds is +2. Blue and green are the characteristic colours of nickel compounds illustrated in Figure 2.4(a) [17].

2.3.2 Structural and Properties of Nickel Oxide

Nickel (II) oxide is the most well-known chemical compound of nickel with the formula NiO as shown in Figure 2.4(b). It is classified as a basic metal oxide. Several million kilograms are produced in varying quality annually, mainly as an intermediate in the production of nickel alloys. NiO structure is face-centred cubic

(fcc) with Ni (II) and O^{2-} site that is similar to NaCl which processes rock salt structure. A rhombohedral unit cell of NiO with a_0 = 2.9518 Å, α = 60°4.2′, Z = 1 and space group $R\bar{3}m$ at 291 K. When the temperature is cooled at 77 K, the distortion increases and parameters become a_0 = 2.9469 Å and α = 60°12′. At 523 K, NiO transforms to fcc structure with a_0 = 4.1684 Å, Z = 4 and space group $Fm3m$ and a paramagnetic state simultaneously [18]. Similar to many other binary metal oxides, NiO is often non-stoichiometric accompanied by a color change, meaning that the Ni:O ratio deviates from 1:1. In nickel oxide, the stoichiometrically correct NiO is being green and the non-stoichiometric NiO is being black [19].

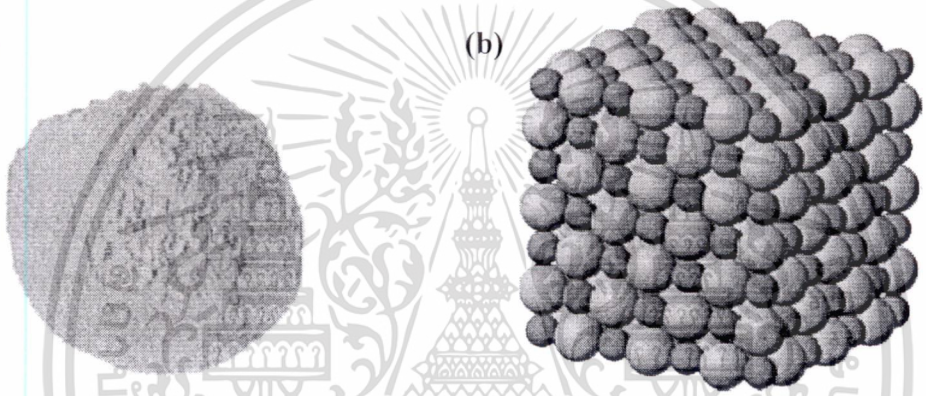

Figure 2.4 NiO (a) powder and (b) chemical structure.

Table 2.4 Physical properties of NiO [19].

Physical properties of NiO	
Molecular weight	74.69 g/mol
Density	6.67 g/cm^3
Melting point	1955 °C
Water Solubility	Not soluble
Refractive index	2.1818

NiO is a natural *p*-type semiconductor material with a relatively wide bandgap (3.6–4.0 eV) and excellent durability, large span optical density, chemical and electrical stability. Therefore NiO is a very prosperous material and attracting features extensively used in catalysis, battery cathodes, gas sensors, electrochromic films, super capacitor and magnetic materials [20-24].

2.4 Composite and Nanocomposite

2.4.1 Composite

Composite is the combination of two or more materials in microstructure that are non-soluble in each other. The main material is called "matrix" and the adding material for enhancing matrix properties that is the most of reinforcing material is called "guest phase". The matrix material is generally a continuous and homogenous structure meanwhile the guest phase material may be in form of fiber, flake and particle. The materials in composite form are more effective in their performances than traditional form, for example, the enhancement of the strong property of concrete by the reinforcement with steel and the increase of efficiency in epoxy by the reinforcement with graphite fibers. Composite forms are classified in 3 types by the reinforcement material; particle, flake or layered and fibrous materials [25]. The structures of these composites are shown in Figure 2.5.

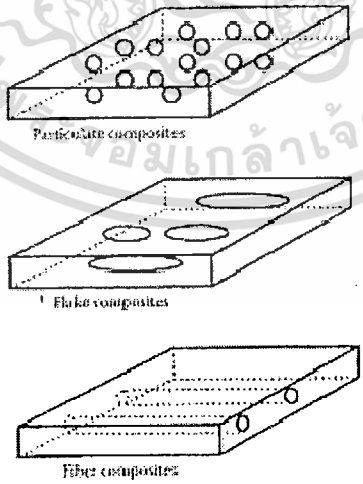

Figure 2.5 Types of composites based on reinforcement shape [25].

• Particulate composites

Particulate composites are the guest particles that are randomly immersed in matrix phase such as alloys and ceramic. The advantages of particulate composites cover improved strength, increased operating temperature and oxidation resistance. The examples of this composite type include aluminum particles in rubber, silicon carbide particles in aluminum, and the component of concrete with gravel, sand and cement.

• Flake composites

Flake composites are the flat reinforcements in matrix phase. The advantages of flake composites are high out-of-plane flexural modulus, high strength, and low cost. However, the efficiency of flake composites is limited by the difficult orientation in the matrix and a few materials for the guest materials.

• Fibrous composites

Fibrous composites are the reinforcement in form of short or long fiber mixed in matrix phase. The examples of fibrous reinforcement are carbon and aramides. The types of matrices include polymer (epoxy), metal (aluminum), ceramic (calcium-alumino silicate) and carbon.

2.4.2 Nanocomposites

Nanocomposites consist of materials at least one of the phases in the range of nanometers (10^{-9} m) that scale agreement in nanometer range is less than 100 nm. Nanocomposite materials have emerged as suitable alternatives to overcome limitations of microcomposites and monolithics, while posing preparation challenges related to the control of elemental composition and stoichiometry in the nanocluster phase. These materials were reported on 21st century in the view of possessing design uniqueness and property combinations that are not discovered in conventional composites [26].

The properties of materials in nanoscale show excellent performance that is different from bulk materials, for example, the improvement of elastic modulus, transmission rate for water vapor and the decrease of toughness and impact strength.

Nanocomposites are categorized by their matrix materials, in three different categories [26];

- Ceramic Matrix Nanocomposites

The potential of ceramic matrix nanocomposites was revealed by the pioneering work of Al_2O_3/SiC system. Most studies reported that the noticeable strengthening of Al_2O_3 matrix was increased after adding low volume fraction of suitable SiC particle size in the mixture. Some studies have explained this toughening mechanism based on the crack-bridging role of the nanosized reinforcements. Consequently, the incorporation of high strength nanofibers into ceramic matrices has allowed the preparation of advanced nanocomposites with high toughness and superior failure characteristics compared to the sudden failures of ceramic materials.

- Metal Matrix Nanocomposites

Metal matrix nanocomposites refer to materials consisting of a ductile metal or alloy matrix in which some nanosized reinforcement material is implanted. These materials combine metal and ceramic features, i.e., ductility and toughness with high strength and modulus. Thus, metal matrix nanocomposites are suitable for production of materials with high strength in shear/compression processes and high service temperature capabilities. They show an extraordinary potential for application in many areas, such as aerospace and automotive industries and development of structural materials.

- Polymer Matrix Nanocomposites

Polymer materials are widely used in industry due to their ease of production, lightweight and often ductile nature. However, some disadvantages were occurred such as low modulus and strength comparing to metals and ceramics. One of effective approach for improving mechanical properties is the addition of fibres, whiskers, platelets or particles as reinforcements to the polymer matrix.

2.5 Ball Milling Process

2.5.1. Background and Perspective of Ball Milling Process

The milling process has originated from ceramic and powder industrial applications for many years. The general objectives of milling process include particle size reduction, amorphization, shape changing, agglomeration, solid-state blending, modified properties of a material and mixing or blending of two or more materials phases.

The mechanical milling process in the first time was called ''Mechanical Alloying (MA)'' that was used as the production of homogenous materials from blending powder mixtures and the decrease of particle size. This process was developed by John Benjamin and his group at the International Nickel Company (INCO Co.) in 1966 and published the first paper in 1970. Nickel-chromium-aluminum-titanium alloy was the primary alloy form synthesized via high energy mechanical grinding by this research group. Later, the materials were produced in a one-gallon stirred ball mill that was the starting process for the synthesis of oxide dispersion-strengthened alloys in the industries. After that, this method was extensively used as an effective synthesis technique for a large variety of materials such as alloys with Cu, Al, Mg, superconductors and ceramics [27].

The advantages of ball milling process have been proposed as follows [28];

- Deformation cold welding and reduction of processing times.
- Production of a mixture with various elements.
- Surface-active agents which would produce fine pyrophoric powder as well as contaminate the powder are unnecessary.
- Relying on a constant interaction between welding and fracturing to powder product with a refined internal structure, fine powders, reduced particle size and stable phase.

2.5.2. Principles of Ball Milling Process

The ball-milling is generally used as a mechanical co-grinding of powders for the reduction of particle size, the synthesis of new materials and the increase of homogeneous powder. The fundamental principle in mechanical milling devices is the energy transfer between the milling media and powder during the impaction. The mechanism of ball milling is illustrated in Figure 2.6. Cylindrical container called

vials containing balls with the rotation on roller is operated in this method. The simulation of the movement of balls and powder in vial is shown in Figure 2.6(a). Trapping of particles is induced by ball collision that producing a space occupied from a dense cloud, dispersion, or mass of powder particles.

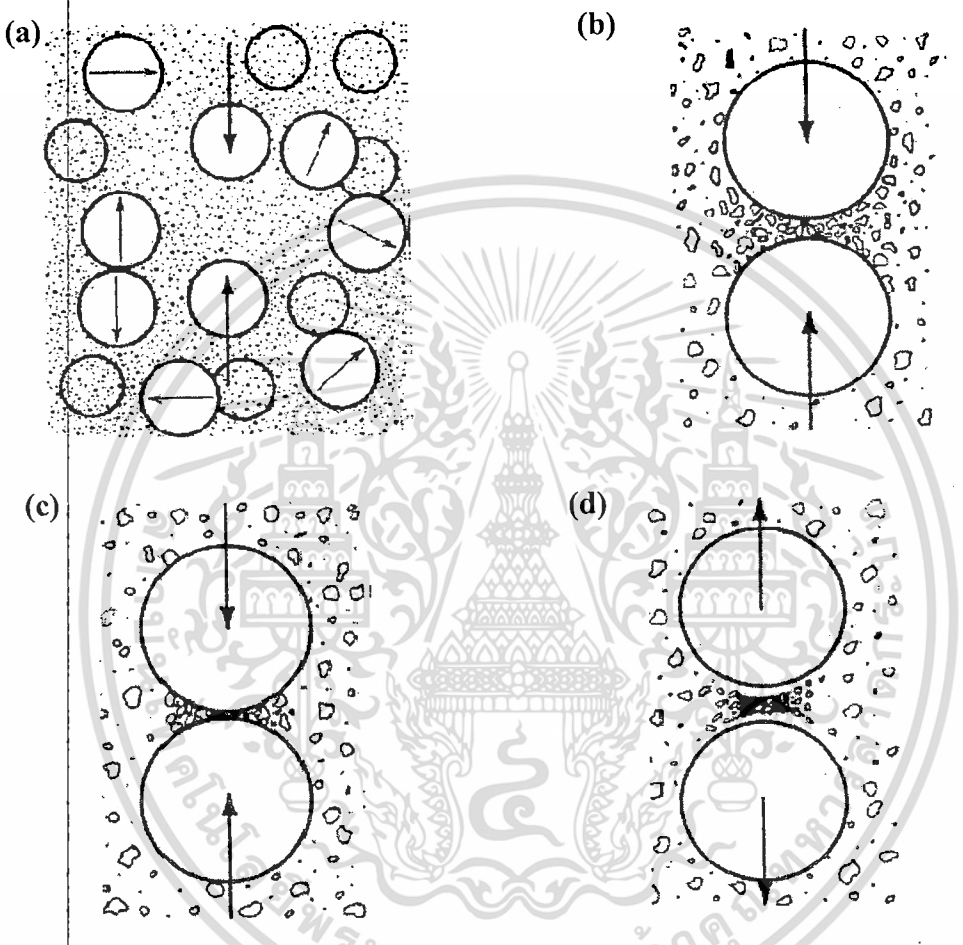

Figure 2.6 Ball milling operation (a) a randomly agitated movement of balls and powder, (b) trapping and compaction of particles, (c) Agglomeration and (d) release of agglomerated powder [27].

The mechanism of the compaction in ball milling process typically has 3 stages to produce small particle and homogenous powder. The first stage, shown in Figure 2.6(b), introduces the compaction of two balls and material for rearrangement and restacking of particles. Deformation and fracture of particles and some fine powder are initially raised at this stage by the energy transfer from the compaction. In the second stage, the elastic and plastic deformation of particles and cold welding are performed resulting to the agglomeration of particles as illustrated in Figure 2.6(c). The involving particle fracture is released in further deformation and/or fragmentation of the particles leading to a homogenous powder (Figure 2.6(d)).

2.5.3. Classification of Ball Milling System

The most common milling systems are planetary, vibrant, attritor and cannon-ball types. The planetary and vibrant mills are mostly used in laboratories because of their capacity in several grams. Whereas attritor or cannon-ball mills are chosen as the industrial application which the capacity can be synthesized in several tons of powders [29].

2.5.3.1 Vibrant Mill

Vibrant mill or Shaker mill basically works with small vials containing sample and grinding media at maximum volume of several 10 cm^3. The operation is oscillated linearly by one, two or three-axial translations with several thousand times per minute as shown in Figure 2.7. During the back and forth shaking motion in the vial, powder and hard milling balls can cause the impact against each other and the end of the vial resulting to both milling and mixing simultaneously.

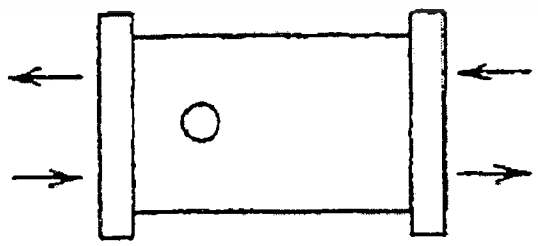

Figure 2.7 Vibrant milling operation [29].

2.5.3.2 Planetary Mill

Planetary mill is most commonly used for MA experiment in laboratory due to the capacity of powder milling in a few hundred grams. The name of planetary ball mill refers to the planet because of the rotation of vials around their own axes. The vials are arranged on a rotating tray and moved in the opposite direction. The grinding balls and powder are flown in the vial by the centrifugal forces causing the friction effect. After that, the balls lift off and move freely through the inside of vial and collide against the opposing inside wall by the gravity force resulting to the impact effect. The reaction in the planetary mill is illustrated in Figure 2.8.

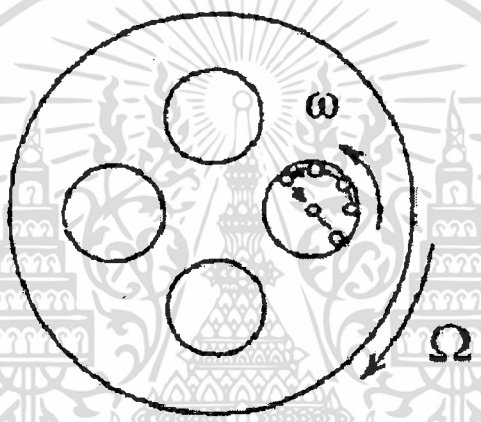

Figure 2.8 Planetary milling operation [29].

2.5.3.3 Attrition Mill

An attritor is one of ball milling which consists of a vertical drum with a series of impellers inside it as shown in Figure 2.9. Large quantities of powder (about 0.5 to 40 kg) can be milled in a stationary tank with the grinding media. When the impeller rotates in the chamber with high speed of 250 rpm, the reduction of particle size and homogenous mixture are obtained by the impact between balls; balls and the container wall and the balls with the agitator shaft and the impellers. The laboratory attritor works up to 10 times faster than conventional ball mills.

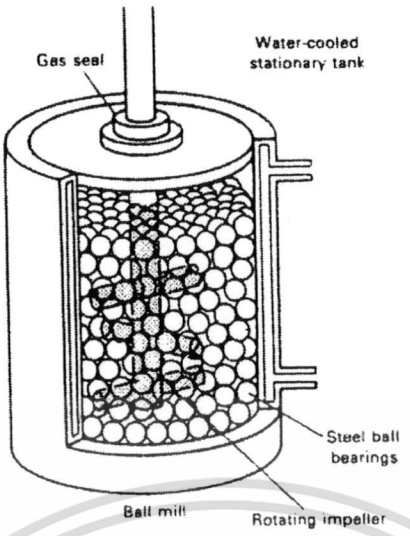

Figure 2.9 Attrition milling operation [27].

2.5.3.4 Cannon Ball Milling

The principle of cannon ball milling is operated by the horizontal rotation of the vial around its revolution axis as illustrated in Figure 2.10. Some of powder and balls are dragged by the inside wall and fall down by the gravity that inducing the collision between material and balls. The friction and reduction of particle are induced by these mechanisms which depend mainly on the rotation speed and diameter of the vial [22]. In industrial application, this mill is widely chosen as milling instrument due to high capacity at once of several tons of powders in the vial. However, the milling period is longer than several hundred hours comparing to other methods.

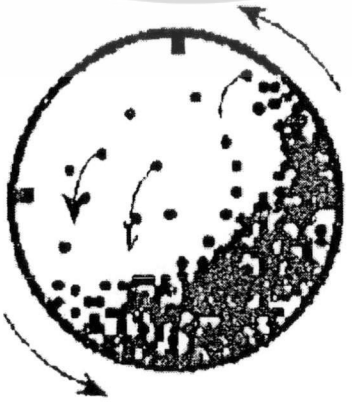

Figure 2.10 Cannon ball milling operation [29].

Energy in ball milling system may be classified as two types; one is high energy ball milling and the other is low energy ball milling. For high energy ball milling, the term "ball mills" is often replaced by the terms of "stirred ball mills" or "attritions" because milling process is operated by high centripetal force with vertical direction of its rotation. The advantages of attrition are able to take samples at any time and making formulation adjustments during high energy ball milling. Attritors stir the media in a stationary tank with a shaft attached arms or discs resulting in a more efficient use of energy for the milling process. Further, attritor tanks are all jacketed which allows for more precise temperature control during high energy ball milling. Small particle size was obtained by this process comparing to conventional ball milling. Nevertheless, fracture is a problem of energetic, the propagation of the initially-formed cracks, requires that the energy of elastic deformation should be at least as high as the interfacial energy of the system [30]. Low energy ball milling is consisted of a cylindrical chamber rotating about a horizontal axis with either rods or balls as the milling media related to the conventional process. This process may require increased milling times to produce homogenous and uniform products. Good point of this milling is relatively inexpensive and applies to in-house for an economical price [31]. The potential for releasing in case of an emergency or power failure is reduced by low energy ball milling.

2.6 Sol-Gel Process [32-33]

Sol-gel technique classified as one of bottom-up approach is described as the formation of inorganic networks via condensation reactions of a molecular precursor in a liquid. "Sol" is a stable dispersion of colloidal particles or polymers in a solvent. "Gel" is a three dimensional continuous network of liquid phase to form a network from sol gelation. The reaction of sol-gel process is based on hydrolysis and condensation of alkoxide-precursor materials that dispersed in water or dilute acid for the sol-gel formation. Calcination is used for removal of liquid in the process resulting to the production in oxide form. Sol-gel synthesis may be prepared materials in various shapes, for example porous structures, thin fibers, dense powders and thin films as shown in Figure 2.11.

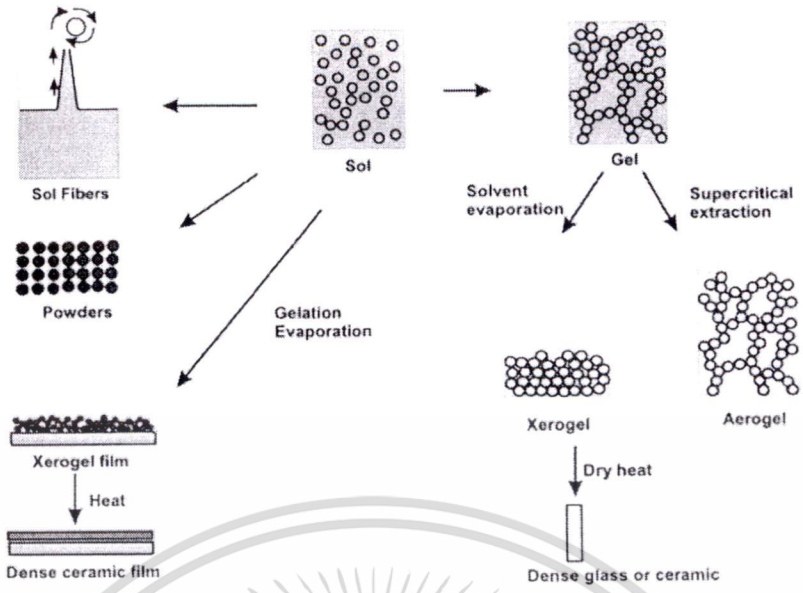

Figure 2.11 Schematic of sol-gel process.

The sol-gel method was developed in the 1960s and discovered for new synthesis in the nuclear industry. The idea of sol-gel synthesis is to "dissolve" the compound in a liquid in order to bring it back as a solid in a controlled manner. Structure control, small particle size, homogeneous material and reducing agglomeration can be produced by this process. Multi component compounds are obtained by preparing a controlled stoichiometry of mixing sols. Sol-gel technique is not only reported to low cost method but also synthesizes the productions in nanometer size. However, this method is needed the place without dust lower sintering temperature.

2.7 Dye Sensitized Solar Cell

Dye sensitized solar cells (DSSC) are considered as one of the promising photovoltaic solar cells that are effectively able to convert solar light into direct current (DC). DSSC is categorized into photoelectrochemical type because of redox electrolyte mechanism in its cell. DSSC has been extensively attracted to several researches due to low production cost, simply fabrication and relatively high optical conversion efficiency. By varied colors from different dyes in devices and the fabrication on flexible substrates, DSSC has been used as Building Integrated Photovoltaics (BIPV) such as flat roof, skylight. The conversion efficiency varies between 6 -10 % depending on the module size and the technology is currently on the pilot plant scale.

2.7.1 History of DSSC

DSSC was originated from the sensitized chlorophyll on a zinc oxide (ZnO) electrode in 1972. For the first time, photons were converted into an electric current by charge injection of excited dye molecules into a wide bandgap semiconductor. The primary fundamental research was carried on ZnO-single crystals but the efficiency of the device was somewhat poor. The main problem was small absorption of the incident light on dye molecule layer. Therefore, nanoporous TiO_2 has been chosen as working electrode material instead of ZnO because of roughness factor of ca. 1000. The first development of DSSC efficiency up to 7 % was discovered by O'Regan and Grätzel in 1991. In following the years, the improvement of DSSC performance has received increasing attention and its drawbacks have been proposed how to overwhelm this problem.

2.7.2 Structural and Material in DSSC

The schematic structure of DSSC is shown in Figure 2.12. DSSC is composed of 3 main parts; counter electrode, working electrode and electrolyte. Materials and functionalities of each part are described in this section.

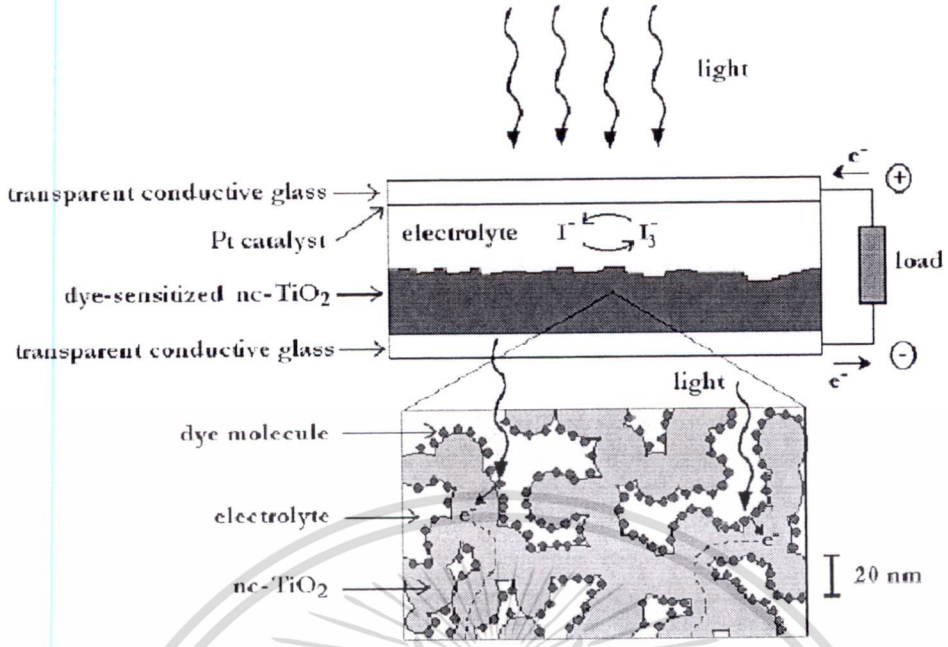

Figure 2.12 Assembly of DSSC Structure.

2.7.2.1 Counter Electrode

The main function of counter electrode is the transition of electron from outside circuit into electrolyte solution. The major functions of counter electrode should be good conductivity, high porosity and suitable excited catalyst. Platinum is usually chosen as the counter electrode material because of its high electrocatalytic activity. However, Pt cost is rather expensive comparing to other materials therefore carbon or conducting polymer are potential substitutions for counter electrode material.

2.7.2.2 Working Electrode

1) Transparent Conducting Oxide-coated Glass Substrate

Transparent conducting oxide-coated glass is typically chosen as the substrate for metal oxide photoelectrode. Low sheet resistance and high transparency in visible light are required for high performance of DSSC. Indium-tin oxide (ITO) is one of the most famous transparent substrate in solar cell application due to its low resistance at room temperature. Nevertheless, non-stable property in ITO arises at high temperature due to the increase of its resistance in air. Therefore fluorine-doped tin oxide (FTO) can be alternatively used as the transparent conducting glass substrate owing to

comparably low sheet resistance, good conductivity and more stable at high temperature. Moreover, an interesting alternative material for transparent conducting substrate is flexible conducting plastic which has been introduced and studied especially the commercialization of DSSC.

2) Oxide Semiconductor Layer

The photoelectrode materials in common solar cell device, for example Si, GaAs, InP and CdS, are mismatched for DSSC fabrication because of the corrosion of the electrolyte in the device under irradiation. Therefore, oxide semiconductors are the preferential materials in photoelectrochemistry because of their exceptional stability against photo-corrosion on optical excitation in the band gap [30]. Furthermore, the large band gap (>3 eV) of the oxide semiconductors is needed in DSSCs for the transparency of the semiconductor electrode for the large part of the solar spectrum [35]. Oxide semiconductors are used for a photoelectrode in DSSC included ZnO, CdSe, CdS, WO_3, Fe_2O_3, SnO_2, Nb_2O_5, Ta_2O_5 and TiO_2. For high DSSC performance, TiO_2 is chosen as the photoelectrode material due to good chemical stability in solution, high porosity, nontoxic and cost-effectiveness.

The interesting properties of nanostructured TiO_2 electrodes have been studied for the development of DSSC efficiency. Controlling the morphology and interfacial properties of the nanostructured-TiO_2 electrode are related to high dye adsorption, increased porous structure and convenient electron transfer on its surface, resulting to the increase of DSSC performance.

3) Dye Sensitizer

Sensitized-dye molecules, deposited on metal oxide surface of working electrode are function of light absorption and electron generation in the device. Good properties of dye sensitizer are long-term chemical stability, high absorption in visible light and non-toxic. Ruthenium (Ru) complexes developed by Gräzel's group are delegated for the most suitable dye photosensitizers. When anchoring Ru complexes are adsorbed on TiO_2 surface by carboxyl groups, large effective electrons are occurred by the interaction between ligand and the conduction band of TiO_2 [35]. Nowadays, natural dyes extracted from plants such as chlorophyll, anthocyanin and carotenoid have been extensively attracted as natural dye sensitizer for DSSC because of reducing environment pollutions and low-cost production comparing to Ru

complex dye. Therefore the synthesis of natural dye is also one of methods for the improvement in DSSC technology.

2.7.2.3 Redox Electrolyte

The ideal characteristics of the redox electrolyte in DSSC device have been described by Wolfbauer et al. (2001) as follows [34];

- Redox potential thermodynamically (energetically) favorable with respect to the redox potential of the dye to maximize cell voltage;
- High solubility to the solvent to ensure high concentration of charge carriers in the electrolyte;
- High diffusion coefficients in the used solvent to enable efficient mass transport;
- Absence of significant spectral characteristics in the visible region to prevent absorption of incident light in the electrolyte;
- High stability of both the reduced and oxidized forms of the couple to enable long operating life;
- Highly reversible couple to facilitate fast electron transfer kinetics;
- Chemically inert toward all other components in the DSSC.

The electrolyte used in the DSSCs commonly consists of iodine (I^-) and triiodide (I_3^-) as a redox couple ion that can compensate electrons between the working electrode and the counter electrode. The compounds of iodides are in form of salt such as LiI, NaI, KI and tetraalkylammonium iodide (R_4NI) that can be dissolved in nonprotonic solvent with other substances for improving the properties of the electrolyte and the performance of the operation of DSSC.

2.7.3 Operation Principle of DSSC

DSSC is typically composed of dyed-metal oxide layer used as working electrode, redox electrolyte and counter electrode. The mechanism of DSSC is generally similar to plant photosynthesis, working on the mechanism of the excited chlorophyll by sunlight. The beginning phenomenon of DSSC starts from excitation of dye molecules with illumination. Dye consequently generates electrons to TiO_2 layer that are transferred to Pt counter electrode through an external load. The redox electrolyte containing a reduction-oxidation couple of I^-/I_3^- ion is used for oxidized dye

compensation. This mechanism is illustrated in Figure 2.13. The voltage generated under illumination corresponds to the difference between the Fermi level of the electron in the solid and the redox potential of the electrolyte. Overall, the device generates electric power from light without suffering any permanent chemical transformation [36].

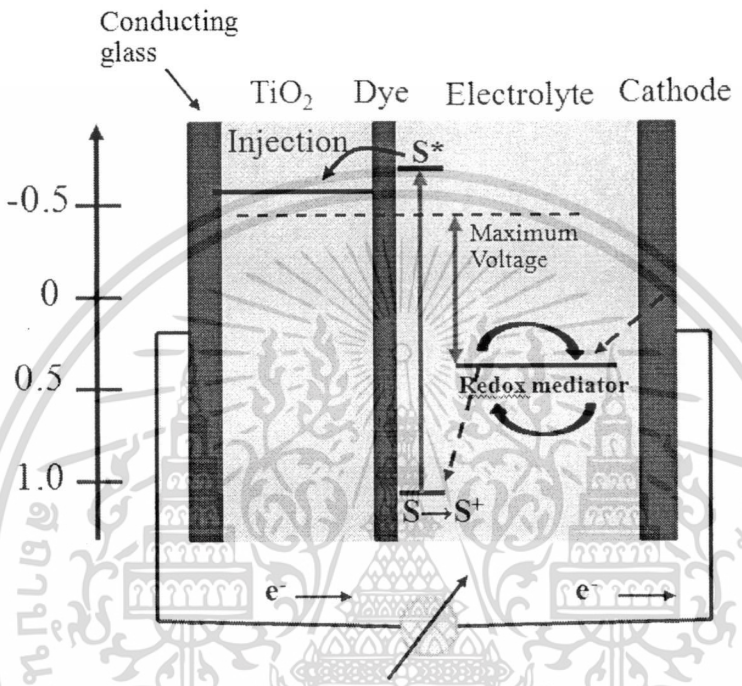

Figure 2.13 Principle of operation and energy level scheme of the dye-sensitized solar cell.

2.8 Photocatalytic Reaction

Photocatalytic Reaction is one of advanced oxidation processes (AOPs) defined as the acceleration of photoreaction in the presence of catalyst. Excited energy in the reaction is reduced by the catalyst resulting to increasing reaction rate but the product still equal the reaction without catalyst. The catalyst is responded to light source and unchanged itself in the chemical reaction. The photocatalytic reaction system is composed of photocatalyst, light source, water and oxygen or oxidant. Semiconductors, such as TiO_2, are chosen as the photocatalyst because of good working functionality in near- UV and visible light source, high chemical resistance and reusable material.

When TiO_2 photocatalyst absorbs UV irradiation from sunlight or illuminated light source (fluorescent lamps), excited electrons of the valence band (VB) are promoted to the conduction band (CB) therefore the production of the negative-electron (e_{CB}^-) and positive-hole (h_{VB}^+) pairs is obtained in equation 2.1;

$$TiO_2 + h\nu \rightarrow e_{CB}^- + h_{VB}^+ . \quad (2.1)$$

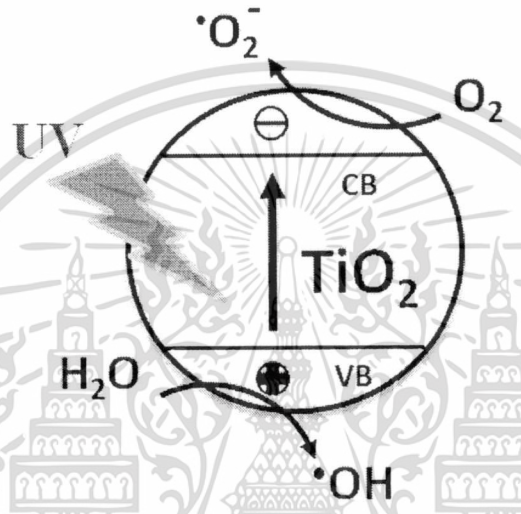

Figure 2.14 Mechanism of TiO_2 photocatalyst.

These electron-hole pairs can react in a redox reaction with other species on the surface. The production of hydroxyl radical ($OH^{\cdot}$) was easily occurred by the reaction of h_{VB}^+ with water molecule (H_2O) followed as equation 2.2. Whereas, the reaction of e_{CB}^- with oxygen (O_2) leads to super oxide radical anions ($O_2^{\cdot -}$) shown in equation 2.3 [37].

$$H_2O + h_{VB}^+ \rightarrow OH^{\cdot} + H^+ , \quad (2.2)$$

$$O_2 + e_{CB}^- \rightarrow O_2^{\cdot -} . \quad (2.3)$$

It has been suggested that the hydroxyl radicals and superoxide radical anions are the primary oxidizing species in the photocatalytic processes as shown in Figure 2.14. The reaction of super oxide radical with H_2O may increase hydroxyl radical in the system due to decomposition of H_2O_2 product as followed equation 2.4 and 2.5;

$$O_2^{\bullet-} + H_2O \rightarrow H_2O_2, \quad (2.4)$$

$$H_2O_2 \rightarrow 2OH^{\bullet}. \quad (2.5)$$

The hydroxyl is extremely powerful oxidation agent because of its potential. This radical is very reactive and attack pollutant molecules to degrade into other species including carbon dioxide and water [38]. This mechanism is related to decolorization of dye or complete mineralization as followed equation 2.6 and 2.7;

$$OH^{\bullet} + \text{dye} \rightarrow \text{dye}_{ox}^{*}, \quad (2.6)$$

$$\text{dye}_{ox}^{*} + O_2^{\bullet-} \text{ or } OH^{\bullet} \rightarrow\rightarrow \text{degradedomineralizaedproducts} \quad (2.7)$$

The majority of researchers assume that the photocatalytic degradation of most organic compounds is described by pseudo first-order model [39];

$$r_i = -\frac{dC_i}{dt} = k_{obs} C_i, \quad (2.8)$$

where r_i is the reaction rate,

t is the irradiation time,

C_i is the molar concentration of substance and

k_{obs} is the observed pseudo first-order reaction constant.

The integration of equation 2.8 results to the expression;

$$\ln \frac{C}{C_0} = -k_{obs} t, \quad (2.9)$$

where C_0 is the initial concentration of substance. From equation 2.9, the relationship of $\ln(C/C_0)$ and irradiation time is a straight line and k_{obs} is calculated from a slope from this line.

2.9 Characterization

2.9.1 X-ray Diffraction

X-ray Diffraction (XRD) is one of non-destructive analytical techniques which are able to reveal information about the crystal structure, chemical composition, and physical properties of materials and thin films. These techniques are based on observing the scattered intensity of an X-ray beam hitting a sample as a function of incident and scattered angle, polarization, and wavelength or energy [40].

XRD is based on constructive interference of monochromatic X-rays and a crystalline sample. X-ray beams are generated by a cathode ray tube, filtered to produce monochromatic radiation, collimated to concentrate, and directed toward the sample. When the incident beam passes through matter and interacts with the electrons in the atoms resulting to the scattering beam that illustrated in Figure 2.15. If the atoms are organized in planes (i.e., the matter is crystalline) and the distances between the atoms are of the same magnitude as the wavelength of the X-rays, constructive and destructive interference will occur. These results in diffraction where X-rays are emitted at characteristic angles based on the spaces between the atoms organized in crystalline structures called planes. The interaction of the incident rays with the sample produces constructive interference (and a diffracted ray) when conditions satisfy Bragg's Law [41];

$$n\lambda = 2d\sin\theta, \tag{2.10}$$

where n is an integer,

λ is the wavelength of incident wave,

d is the spacing between the planes in the atomic lattice and

θ is the angle between the incident ray and the scattering planes.

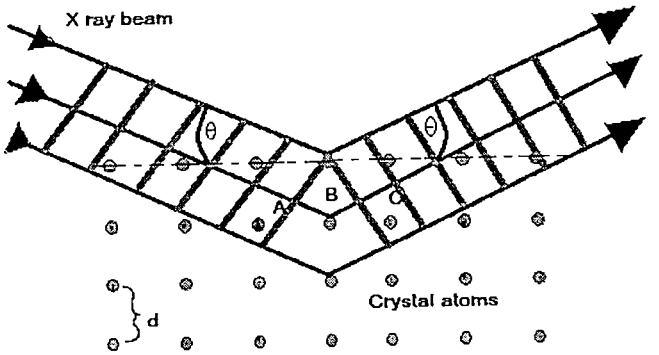

Figure 2.15 Diffraction of X-ray in material.

The crystalline size of the solid material can be calculated from XRD peak in a diffraction pattern from Scherrer's equation as follows [42];

$$\tau = \frac{K\lambda}{\beta \cos\theta}, \tag{2.11}$$

where τ is crystallite size,

K is constant dependent on crystallite shape (0.9),

λ is X-ray wavelength (1.5405 Å),

β is full width at half maximum (FWHM) and,

θ is the angle of diffraction.

2.9.2 Scanning Electron Microscopy

Scanning Electron Microscope (SEM) is a microscope that uses electron source instead of light for inspecting topographies of specimens at high magnification. The signals derived from electron-sample interactions reveal the information of the sample including external morphology (texture), chemical composition, and crystalline structure and orientation of materials. SEM has allowed researchers to examine a much bigger variety of specimens for example, electronic device or the materials in the medical and physical science communities. The advantages of SEM are more over than traditional microscopes. Large depth of field in SEM, a large amount of a specimen can be in focus at one time and produces three-dimension image of specimen. Closely spaced specimens can be magnified at much higher levels

that are controlled by electromagnets. All of these advantages, as well as the actual strikingly clear images, make the scanning electron microscope one of the most useful instruments in today research.

The starting SEM operation, incident accelerated electrons are produced in electron beam at the top of the microscope by an electron gun. The electron beam follows a vertical path through the microscope in a vacuum system. The beam travels through electromagnetic fields and lenses, which focus the beam down toward the sample. When the bombarding electrons (primary electrons) collide with the sample, electrons and X-rays are ejected from the sample. X-rays, backscattered electrons, and secondary electrons are collected by detectors and converted into a signal that sent to a screen similar to a television screen for the production of final image [43]. These phenomena are illustrated in Figure 2.16.

The variety of signals are produced by primary electrons-sample interactions including secondary electrons (SE), backscattered electrons (BSE), diffracted backscattered electrons (EBSD), photons (characteristic X-rays), visible light (cathodoluminescence; CL), and heat as shown in Figure 2.17. The production of SEM images is occurred by SE and BES phenomena; morphology and topography on samples performed by secondary electrons and backscattered electrons are most valuable for illustrating contrasts in composition in multiphase samples. SEM analysis is considered to be "non-destructive"; that is, x-rays generated by electron interactions do not lead to volume loss of the sample that let the repetition of SEM measurement possible.

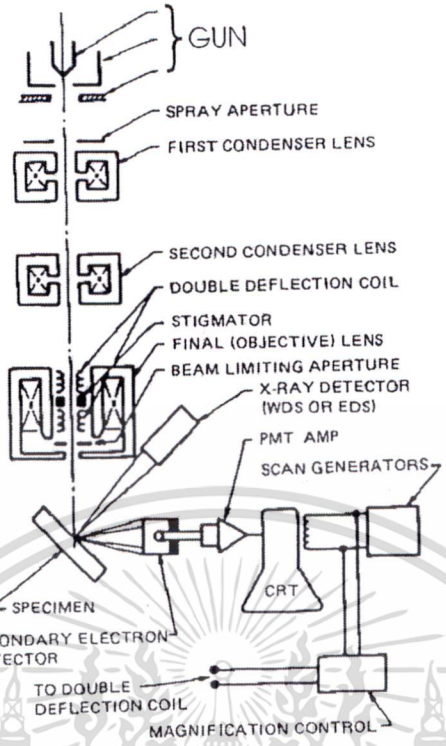

Figure 2.16 Schematic of the operation in SEM.

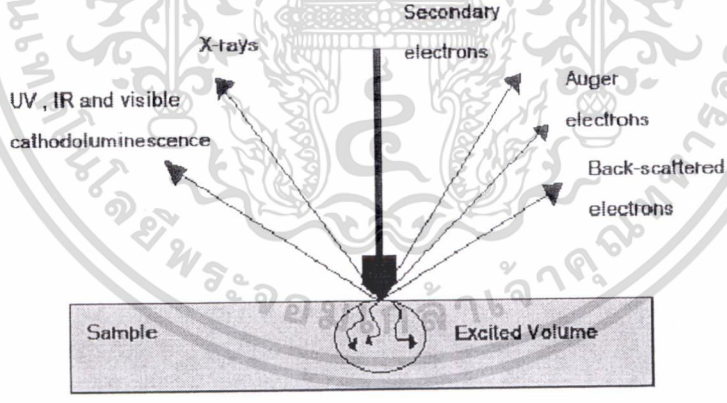

Figure 2.17 Interaction of the electron beam and sample in SEM.

2.9.3 Transmission Electron Microscopy

Transmission Electron Microscopy (TEM) is one of techniques using electron beam for the sample imaging. Outstanding image resolution in bright and dark field modes, the element mapping and the characterization of crystallographic phases and their orientation can be obtained by TEM analysis [44].

The electron beam is generated at the top of the microscope by electron gun and travels in the vacuum system in column. Electromagnetic lenses are employed for controlling size of electron beam. The electron beam is focused on the sample. Depending on the density of materials, some of transmitted electrons are detected at the bottom of microscope and hit to the fluorescent. The shadow image of the sample is occurred in varied darkness according to their intensity. The image can be studied directly by the operator or photographed with the camera. The components and operation of TEM are illustrated in Figure 2.18.

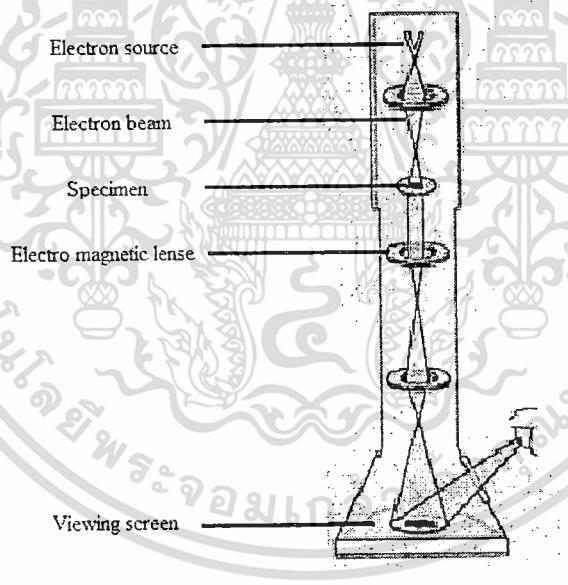

Figure 2.18 TEM instrument and schematic of the operation.

2.9.4 X-ray Absorption Near Edge Structure

X-ray Absorption Near Edge Structure (XANES), also known as Near edge X-ray Absorption Fine Structure (NEXAFS), is defined as the analysis of the spectra obtained in X-ray absorption spectroscopy experiments. The partial density of the empty states of a molecule is determined by specific element and local bonding-sensitive spectroscopic analysis [45].

When a sample is attacked by X-rays, the oscillating electric field of the electromagnetic radiation interacts with the electrons bound in an atom. Either the radiation will be scattered by these electrons or absorbed and excite the electrons as shown in Figure 2.19. A narrow parallel monochromatic x-ray beam of intensity (I_0) passing through a sample of thickness (x) will get a reduced intensity (I) according to the expression [46]:

$$\ln(I_0 / I) = \mu x \ , \tag{2.12}$$

where μ is the linear absorption coefficient, which depends on the types of atoms and the density ρ of the material. When the photon energy is large enough, the photoeffect in one of the core shells can occur. This result in the step-like shape of the absorption spectrum: the increased photoabsorption cross-section due to the knocking-out of an electron is called absorption edge (Figure 2.20). The energies of the absorbed radiation at these edges correspond to the binding energies of electrons in the K, L, M, etc, shells of the absorbing elements corresponding to the transition of an excited electron [47].

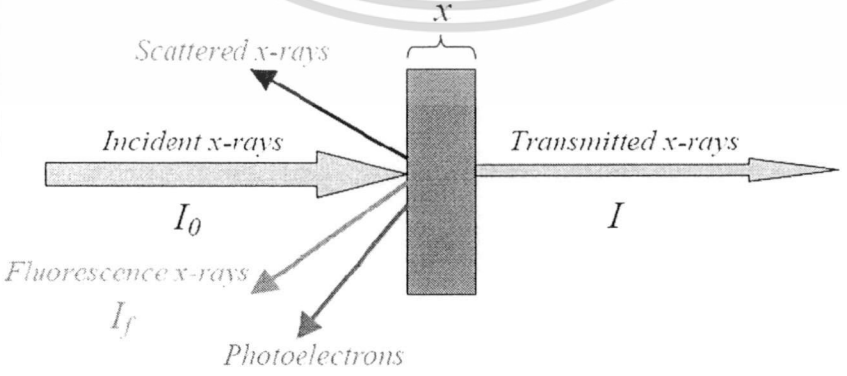

Figure 2.19 X-ray mechanism in the material.

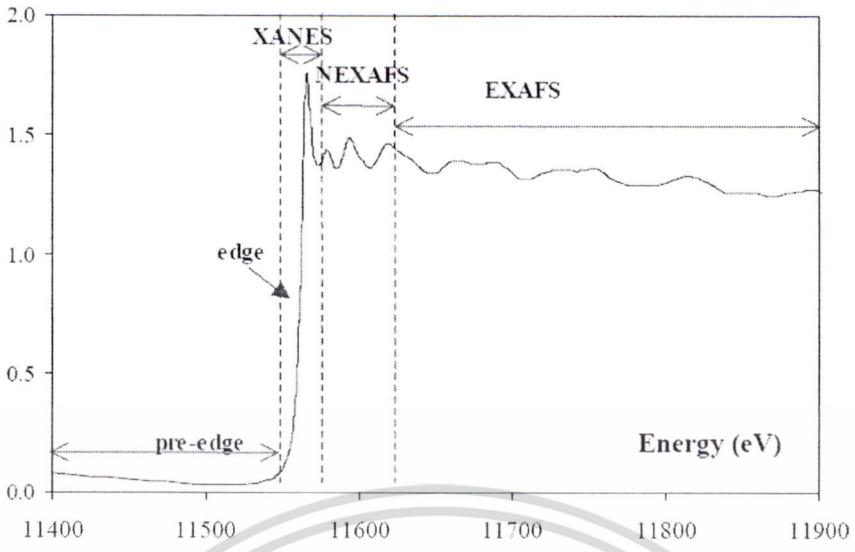

Figure 2.20 Schmatic illustration of an X-ray absorption edge [46].

X-ray absorption spectrum is generally divided into 4 sections;

1) Pre-edge ($E < E_0$).
2) X-ray absorption near edge structure (XANES), where the energy of the incident x-ray beam is $E = E_0 \pm 10$ eV.
3) Near edge x-ray absorption fine structure (NEXAFS), in the region between 10 eV up to 50 eV above the edge.
4) Extended x-ray absorption fine structure (EXAFS), which starts approximately from 50 eV and continues up to 1000 eV above the edge.

In the XANES region, transitions of core electrons to non-bound levels with close energy occur. Because of the high probability of such transition, a sudden raise of absorption is observed. In NEXAFS, the ejected photoelectrons have low kinetic energy ($E-E_0$ is small) and experience strong multiple scattering by the first and even higher coordinating shells.

2.9.5 X-ray Photoelectron Spectroscopy

X-ray photoelectron spectroscopy (XPS) is one of quantitative spectroscopic technique and nondestructive method for studying elemental composition, empirical formula, chemical state and electronic state within a material. XPS spectra are obtained by irradiating a material with soft X-rays beam and measuring the kinetic energy and number of electrons that escape from depths greater than 10 nm in the material [48]. A diagram of a typical XPS instrument is illustrated in figure 2.21.

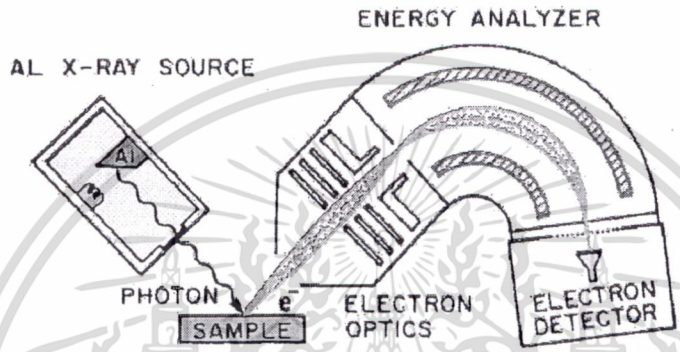

Figure 2.21 Basic components of XPS system.

Photoelectron spectroscopy is based upon photoelectric effect given by the Einstein relation;

$$E = h\nu , \tag{2.13}$$

where h is Planck's constant (6.62×10^{-34} J·s)

ν is frequency of the radiation (Hz).

In XPS, the photon is absorbed by an atom in a molecule or solid, leading to ionization and the emission of a core (inner shell) electron. First, the energy of an incident photon ($h\nu$) is transferred to a bound electron. If the energy is greater than the binding energy of the electron and overcomes the work function (ϕ) of the solid, the photoelectron will occur followed as Figure 2.22 and equation 2.14 [49];

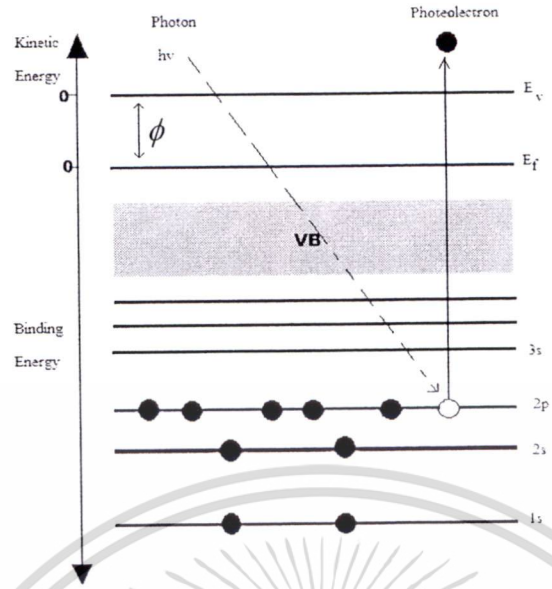

Figure 2.22 Schematic representation of the photoemission.

$$A + h\nu \rightarrow A^{*} + e^{-} + \phi \quad . \tag{2.14}$$

Due to the emission of the electron, the inner shell of the atom (A) is ionized. The energy conservation requires as shown in equation 2.15;

$$E(A) + h\nu = E(A^{*}) + E(e^{-}) + \phi \, . \tag{2.15}$$

Since the electron's energy is presented as kinetic energy (KE). Equation 2.15 can be rearranged to give the following expression (equation 2.16) for the KE of the photoelectron;

$$KE = h\nu - [E(A^{*}) - E(A)] - \phi \, . \tag{2.16}$$

The final term in brackets, representing the difference in energy between the ionized and neutral atoms, is generally called the *binding energy* (BE) of the electron leads to the following commonly quoted equation 2.17;

$$KE = h\nu - BE - \phi \, . \tag{2.17}$$

2.9.6 Raman Spectroscopy

Raman spectroscopy is a spectroscopic technique based on inelastic scattering or Raman scattering of monochromatic light, usually from a laser source. Photons of the laser light are absorbed by molecules in sample resulting to emission of phonons or other excitations in the system. Frequency of the reemitted photons is shifted up or down in comparison with original monochromatic frequency called Raman effect. This shift provides information about vibrational, rotational and other low frequency transitions in molecules. Raman spectroscopy can be used to study solid, liquid and gaseous samples.

The Raman effect is based on molecular deformations in electric field ($\vec{E}$) determined by molecular polarizability (α). The electric dipole moment ($\vec{P}$); $\vec{P} = \alpha \vec{E}$ is induced by the interaction in sample resulting to deformed molecules. Because of periodical deformation, molecules start vibrating with characteristic frequency (ν_m) [50]. Amplitude of vibration is called a nuclear displacement. In other words, monochromatic laser light with frequency ν_0 excites molecules and transforms them into oscillating dipoles. Such oscillating dipoles emit light of three different frequencies (Figure 2.23) as follow;

1. A molecule with no Raman-active modes absorbs a photon with the frequency υ_0. The excited molecule returns to the initial vibrational state and emits irradiation with frequency ν_0 as an excitation source. This type of interaction is an elastic collision and called "Rayleigh scattering".

2. A photon with frequency υ_0 is absorbed by Raman-active molecule which at the time of interaction is in the basic vibrational state. Part of the photon's energy is transferred to the Raman-active mode with frequency υ_m and the resulting frequency of scattered light is reduced to $\nu_0 - \nu_m$. This Raman frequency is called "Stokes frequency" or "Stokes scattering".

3. A photon with frequency ν_0 is absorbed by Raman-active molecule, which, at the time of interaction, is already in the excited vibrational state. Excessive energy of excited Ramanactive mode is released, molecule returns to the basic vibrational state and the resulting frequency of scattered light goes up to $\nu_0 + \nu_m$. This Raman frequency is called "Anti-Stokes frequency" or "Anti-Stokes scattering".

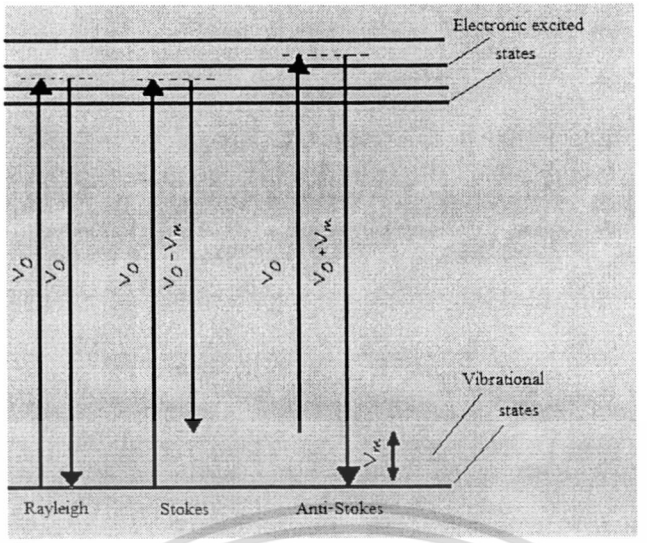

Figure 2.23 Raman transitional schemes.

2.9.7 Thermogravimetric Analysis [51]

Thermogravimetric analysis or thermal gravimetric analysis (TGA) is a type of testing materials that determines the change of weight as function of temperature or time in a controlled atmosphere. TGA technique relies on a high degree of precision in three measurements: weight, temperature, and temperature change due to decomposition, oxidation, or dehydration of weight loss. TGA schematic operation is illustrated in Figure 2.24. A sample pan supported by a precision balance is placed in a furnace and heated or cooled during the experiment. The mass of the sample is monitored during the experiment under inert or a reactive gas in order to prevent oxidation or other undesired reactions.

TGA is a process that utilizes heat and stoichiometry ratios to determine the percent by mass of a solute. Analysis is carried out by raising the temperature of the sample gradually and plotting weight (percentage) against temperature. The temperature in many testing methods routinely reaches 1000°C or greater. After the data are obtained, curve smoothing and other operations may be done to find the exact points of inflection.

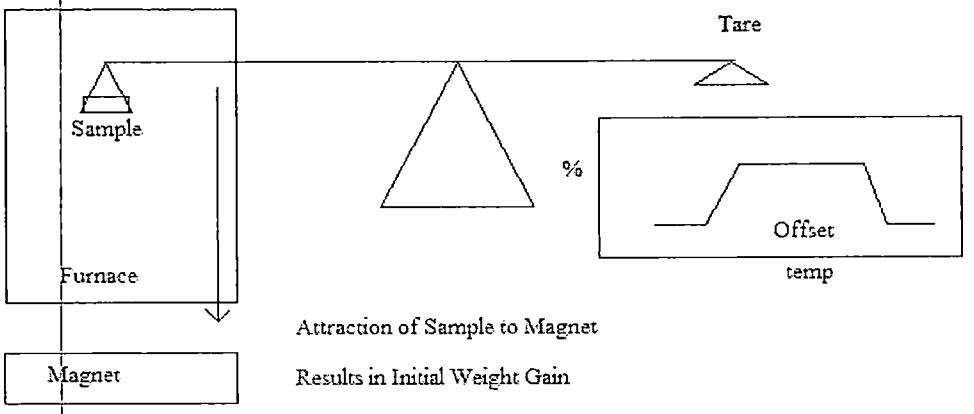

Figure 2.24 Basic components of TGA system.

2.8.8 Ultraviolet-Vis Spectroscopy [52]

Ultraviolet–visible spectroscopy or ultraviolet-visible spectrophotometry (UV-Vis) refers to absorption spectroscopy or reflectance spectroscopy in the ultraviolet-visible spectral region. A diagram of the components of a typical spectrometer is shown in Figure 2.25. A beam of light from UV and visible light source is separated into its component wavelengths by a prism or diffraction grating. Each monochromatic beam in turn is split into two equal intensity beams by a half-mirrored device. One beam, the sample beam, passes through a small transparent container (cuvette) containing a solution of the compound being studied in a transparent solvent. The other beam, the reference, passes through an identical cuvette containing only the solvent. The intensities of these light beams are measured and compared by electronic detectors. The intensity of the reference beam, which should have suffered little or no light absorption, is defined as I_0. The intensity of the sample beam is defined as I. Over a short period of time, the spectrometer automatically scans all the component wavelengths in the manner described.

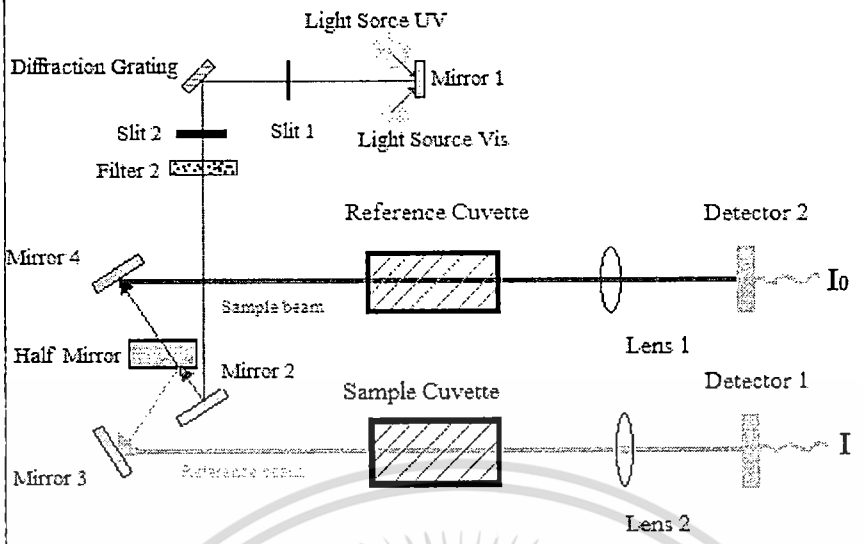

Figure 2.25 Basic components of UV-Vis spectrometer.

2.9.9 DSSC Measurement

DSSC is the type of photovoltaic device, which converts incident light to electrical energy. Generation of electrical power under illumination is achieved by the capability of the photovoltaic device to produce voltage over an external load and current through the load synchronously [53]. DSSC efficiency is typically characterized by the current-voltage (*IV*) curve of the cell at certain illumination and temperature as illustrated in Figure 2.26.

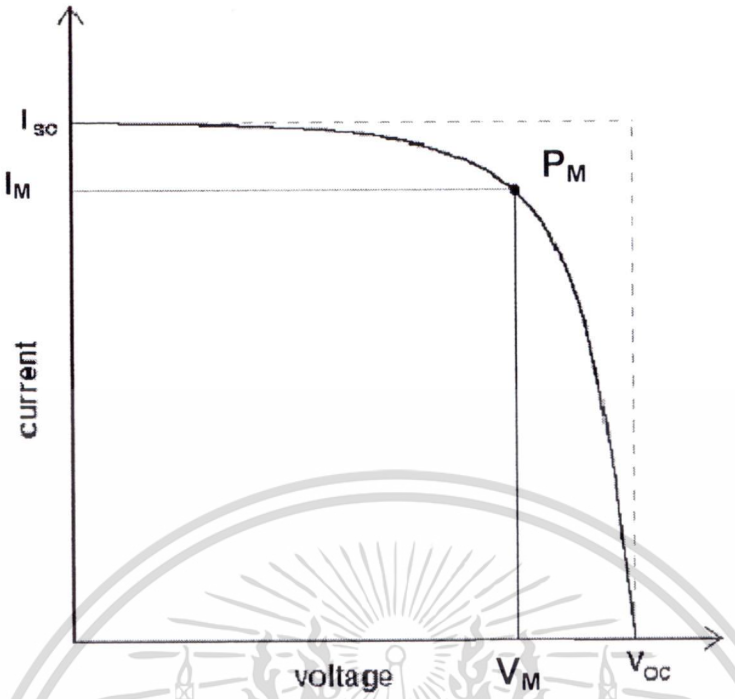

Figure 2.26 Current-voltage (*I-V*) curve of a photovoltaic cell.

Maximum current or short circuit current (I_{SC}), is generated by the short circuit condition under illumination. At an open-circuit condition, the absent current provides the maximum voltage that called the open-circuit voltage (V_{OC}). The point in the IV-curve yielding maximum product of current and voltage, i.e. power, is called the maximum power point (P_M). The voltage and current at P_M are signified as V_M and I_M, respectively. Another important characteristic of the solar cell performance is the fill factor (FF), which is defined as,

$$FF = \frac{V_M \bullet I_M}{V_{OC} \bullet I_{SC}} , \tag{2.18}$$

and solar energy conversion efficiency (η) can be calculated by the relation expressed in Eq. (2.19) [54];

$$\eta(\%) = \frac{P_{out}}{P_{in}} \times 100 = \frac{V_M \times I_M}{P_{in}} \times 100 = V_{OC} \times I_{SC} \times FF , \tag{2.19}$$

The efficiency of the solar cell highly depends on the temperature of the cell, and which is even more important, on the quality of the illumination, i.e. the total light intensity and the spectral distribution of the intensity. In the standard condition used for testing of terrestrial solar cells the light intensity is 1000 W/m^2, the spectral distribution of the light source is that of AM1.5 global standard solar spectrum, and temperature of the cell is 25°C.

I-V characteristic is evaluated by solar cell I-V measurement system that includes the light source, the measurement electronics, computer, and software. Its solar simulator illuminates the test device while the electronic load sweeps the cell voltage from a reverse-bias condition, through the power quadrant, and beyond V_{oc}. The system's computer gathers data, calculates solar cell parameters, generates printable test reports, and saves test data in text files.

2.10 Literature Reviews

Semiconductor materials with superior physicochemical and optical properties are being employed in diverse applications. One of the most potential semiconductors in form of metal oxides is TiO_2 because of its unique electronic band structure since the early twentieth century. In 1972, the photocatalytic splitting of water on TiO_2 electrode under UV illumination for producing hydrogen and oxygen gas was discovered by Fujishima and Honda. This discovery of TiO_2 photocatalyst is sparked and widely propagated for the researches of TiO_2 material as a possible approach. Many promising applications of TiO_2 can be roughly divided into energy and environmental categories. TiO_2 is utilized in ranging from photocatalyst for organic pollutants degradation in water treatment process [55-56], the filler in polymer matrix for improving their optical function as photo-carrier collector [57], and electron transport layer in optoelectronic device applications such as the working electrode material in dye-sensitized solar cell [58-60]. However, the rather high recombination of photogenerated electron–hole pairs and the weak absorption in visible region are its main drawbacks [61-62]. Therefore, various techniques have been proposed in order to modify TiO_2 to overcome these inferiorities. With the rapid development of nanotechnology, appropriated TiO_2 nanostructures in various forms are designed for increasing performance in several applications because of their specifically size-related properties. The discrete energy band structure has been occurred in nanometer-

scale TiO_2. The photophysical, photochemical, and surface properties are quite different from the bulk ones due to the quantum size effect. Therefore, many works have focused on the synthesis of nanocrystalline TiO_2 with a large specific surface area [63]. Higher porosity and small grains of TiO_2 can be obtained by modifying in thin film structure that corresponds to high surface roughness and low contact angle. This research was improved by L. Andronic and coworker [64]. Increasing surface area of TiO_2 photocatalyst for the development of hydrogen gas production with good photocatalytic activity was received by TiO_2 nanocrystalline mesoporous that was researched by J. Jitputti and group [65]. TiO_2 structures of nanorod, nanowire and nanotube were designed for the increase of surface area and electron-hole transfer that applied to light waveguide and the template materials in optical device [66].

Due to high cost of synthesized system for the production of TiO_2 nanostructures, the incorporation with appropriate semiconductors in form of TiO_2 composite material is one of the alternating methods for solving its disadvantages. Metal, metal oxide and non-metal are chosen as the guest materials in TiO_2-based composites in order to enhance itsperformance for various applications. K.H. Ko *et al.* reported that the increasing of open circuit voltage and short circuit current in DSSC was attained by doping aluminum and tungsten into TiO_2 [67]. Yuning Huo and co-workers reported that the efficiency of photocatalytic activity of TiO_2 could be improved by doping Lanthanum (La) into TiO_2, which might hinder the photoelectron-hole recombination and also facilitate the adsorption for reactant molecules and photons [68]. L.R. Hou *et al.* gave the report on decreasing the recombination of electron–hole pairs in photoreactivity using SnO_2/TiO_2 nanotube composite [69]. Yue-hua Xu *et al.* synthesized Cu_2O-TiO_2 photocatalyst with efficient photocatalytic degradation due to the existence of Cu_2O on the surface of TiO_2 that can effectively trap electrons of TiO_2, thereby avoiding electron-hole recombination [70]. Y. Xiaodan *et al.* successfully enhanced visible light absorption of TiO_2 using ZnS/TiO_2 nanocomposite [71]. J. Li *et al.* proved that the significant visible light response and strong increase of photocurrent under UV and visible range were obtained by N-doped TiO_2 [72]. Teruhisa Ohno and colleague reported that strong absorption in visible light and high activities in photocatalytic degradation could be obtained by doping sulphur in TiO_2 matrix [73]

Recently, it has been also reported that the idea for improving the performance of TiO_2 in form of organic–inorganic hybrid nanocomposite, which is one of the effective techniques. M. Wang and workgroup reported that the photoelectric conversion in solar cell could be increased by PPV/TiO_2 hybrid nanocomposite [74]. Yunfeng Zhu *et al.* were able to synthesize P3HT on TiO_2 surface to ameliorate its photoresponse in visible range, leading to an effective photocatalytic reaction [75]. Xifeng Lu and co-workers reported that significant increase in optical absorptivity in visible region and improvement of TiO_2 photocatalytic activity were achieved by g-C_3N_4/TiO_2 hybrid composite because of the existence of N-Ti-O and N-Ti-N bonding in the composite [76]. A. Nakajima and colleague reported on high transparent and the reduction of excitation in the visible wavelength range by using Keggin ions in TiO_2 hybrid film composite ($[PW_xMo_{12-x}O_{40}]^{3-}$/$TiO_2$) [77]. Won-Chun Oh and co-workers reported that improving quantum efficiency and charge transfer of photocatalyst in organic degradation were obtained by synergistic effect between TiO_2 matrix and fullerene [78]. L. Tian and co-workers reported that the photoabsorbance of MWCNT/TiO_2 hybrid nanocomposite materials in the visible light region and the efficiency of visible-light degradation could be enhanced by the formation of the carbonaceous Ti–C bonds on the interface between TiO_2 and MWCNTs [79]. W.C. Lin and group reported that the TiO_2/Ag hybrid particles showed antibacterial activity against gram-negative *E. coli* both in the presence and absence of UV irradiation [80]. Typically, the potential organic material for loading in the composite is metal phthalocyanine (MPc) because of excellent resistance of chemical degradation, strong absorption in blue-green region and good thermal stability. MPc has been utilized as functional material in many applications such as diode, transistor, gas sensor and photovoltaic device. Meanwhile the research of pollutant photodegradation disclosed that MPc photocatalyst exhibited good performance in this process. P. Borker and co-workers reported that MPc is typically good photocatalyst under solar light in photocatalytic activity for complete degradation of Naphthol Blue Black [81]. The hybrid composite of MPc and TiO_2 nanostructure has been intensively investigated, in particular, the improvement of UV and visible light absorption, the modification of charge transfer and the decrease of charge recombination in TiO_2. Antonio E. H.Machado *et al.* reported that the enhancement of absorption spectra in UV-visible range and a good photocatalytic reaction of wastewater were well accomplished by

TiO_2/ZnPc composite [82]. V. Iliev and co-workers gave the report on the improvement of sulfide and thiosulfate ion photoxidation under visible light using phthalocyanine modified TiO_2 or WO_3-catalysts [83].

In semiconductor material, charge separation is occurred by the presence of schottky barrier. However the ideal Schottky barrier is absent in nanocrystalline semiconductor materials resulting to the deficiency of driving force for charge separation. A potential gradient arising from varying degree of electron accumulation with in the semiconductor particles acts as a driving force for transport of injected electrons [84]. Meanwhile, the presence of p–n junction would be one of the methods to introduce the potential gradient that is interesting for new functional form of composite. J. Bandara and research group studied on the increase of sensitized photocurrent, photovoltage and electron transfer by coating nanocrystalline SnO_2 thin film with a thin layer of p-type NiO [85]. C. Shifu and coworker discovered that the separation of photo-excited carriers and the photocatalytic activity were enhanced by the formation of relative p-n junction of Fe-TiO_2/TiO_2 photocatalysts [86]. L. Xiong and research group reported that the effective stability of oxidative energy in energy storage was obtained by p-n junction TiO_2/$Ni(OH)_2$ composite. The electrical neutrality will be retained by the intercalation of the anions or the deintercalation of the cations providing ion consistency in the system [87]. X. Li *et al.* gave a report on increasing the separation of photogenerated electrons and hole by the internal electric field from p–n junction between p-type Bi_2O_3 and n-type Bi_2WO_6 interface [88].

A number of techniques of the synthesis of TiO_2 composite were recently reported, including dry mixing, the sol–gel process, chemical deposition mechanical magnetic stirring method and hydrolysis [89-93]. However, for practical usage, the necessity of suitable method that can make the homogeneous dispersion between two materials is required. Among these processes, ball milling has been chosen as a potential process for simple blending solid-state powder technique which could produce nanocrystalline powder [94]. High energy ball milling process can reduce particle size because of their high smashing between the materials–materials and material–internal wall of the vial. High temperature and the accumulation of defects in powder were produced by this method therefore low-energy ball milling process is a kind of method for composite synthesis. The advantages of low-energy ball milling process are reported that it is simple and cost-effective process. Nanocrystalline powder is not only produced in this process, but also the attrition in equipment is

reduced because of its negligible heating by impact [95]. R. Angers and colleague were able to synthesize uniform composite of b-SiC particles in the 2024 aluminum matrix resulting to the enhancement of mechanical properties especially yield strength and Young's modulus [96]. K.Y. Zhao and co-worker successful produced bulk nanocrystalline aluminum from aluminum elemental powders using low-energy ball milling at room temperature [97]. The electrical conductivity, density and compaction of Cu–Al_2O_3 composite were improved by low-energy ball milling process. This research was carried out by Z. Hussain and group [98].

In this work, we report on the synthesis of TiO_2 nanocomposite based on ball milling process at low temperature. We believed that the assisted process with ball milling could improve the dispersion of guest material in TiO_2 matrix and the homogeneity in the composite form.

CHAPTER 3
EXPERIMENTS

The synthesis TiO_2 nanocomposite with CuPc and NiO are described in this chapter. The utilizations of these composites for DSSC and photocatalytic degradation are also explained.

3.1 Materials and equipments

3.1.1 Materials and Equipments for TiO_2 Nanocomposite Synthesis

Precursor materials

1) TiO_2 nanoparticles P-25, Deguessa
2) CuPc ($C_{32}H_{16}CuN_8$) with dye content of 97% ,Aldrich
3) Nickel (II)-acetate tetrahydrate ,Aldrich
4) Ethanol solution (Absolute and 95%)
5) Diethanolamine; DEA

Figure 3.1 Photograph of precursor materials for modified-TiO_2 nanocomposite (a) TiO_2 P25, (b) CuPc and (c) nickel (II)-acetate tetrahydrate.

Equipments

1) Zirconia balls with diameter 1.45 and 5.36 mm.
2) Cylindrical plastic vial of height 7.7 cm. and inner diameter 4.5 cm.
3) Rotation bar with speed adjustment
4) Magnetic stirrer with heater
5) Homogenizer with speed adjustment
6) Oven
7) Mortar
8) Crucible

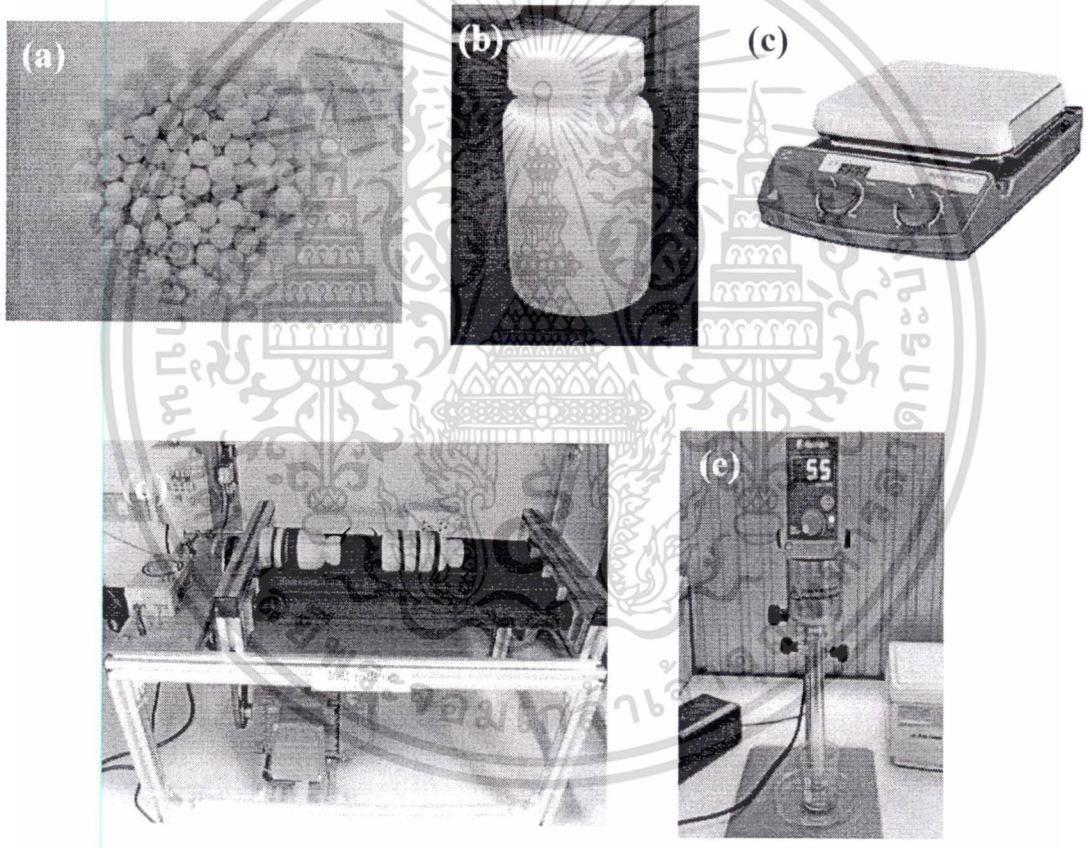

Figure 3.2 The equipments in the experiment (a) zirconia balls, (b) cylindrical plastic, (c) magnetic stirrer, (d) rotation bar and (e) homogenizer.

3.1.2 Materials and Equipments of DSSC and Electrolyte for the Utilizations of TiO_2 Nanocomposite

1) As-prepared TiO_2 nanocomposite
2) Deionized water (DI)
3) Fluorosilicic acid binder
4) Fluorine-doped tin oxide substrate (FTO, 15 Ω/□)
5) N719 dye solution [cis-bis(isothiocyanato)bis(2,2′-bipyridyl-4,4′-dicarboxylato)-ruthenium (II)bis-tetrabutylammonium]
6) Iodine (I_2)
7) Litium iodine (LiI)
8) Ethylene carbonate
9) Propylene carbonate

3.2 Experimental

3.2.1 Synthesis of TiO_2 Nanocomposite

3.2.1.1 Preparation of TiO_2/CuPc Hybrid Nanocomposite

1) The speed of ball-milling process for the synthesis of TiO_2/CuPc hybrid nanocomposite with a ball-to-powder weight ratio 30:1 is fixed at 100 rpm because D-direction in the vial for the attack between balls and substance is obtained by this speed.
2) CuPc was loaded in ethanol solution with a ball-to-powder weight ratio of 10:1 via ball-milling process for 18 h at room temperature. After that, CuPc solution was stirred at 120 °C until ethanol completely evaporated and kept at 100 °C for 24 h. CuPc obtained by this process was recognized as ball-milled CuPc.
3) CuPc and TiO_2 were loaded with ethanol solution via ball-milling process for 5, 12, 18 and 24 h. This condition is determined to the suitable time for homogenize powder between TiO_2 and CuPc.
4) The synthesis of TiO_2/CuPc hybrid composites was carried out via homogenization and ball-milling process by four different methods as follows:

Method 1 (CM1): CuPc was mixed with TiO_2 in 100 ml ethanol solution using homogenizer at room temperature with speed of 7000 rpm for 30 min and stirred at 120 °C until ethanol completely evaporated. As-prepared solid precipitate of TiO_2/CuPc nanocomposite was dried at 100 °C for 24 h. The composite in method 1 was recognized as CM1.

Method 2 (CM2): Ball-milled CuPc was obtained and introduced into TiO_2 dispersed in 100 ml ethanol solution. The suspension was homogenized at 7000 rpm for 30 min and stirred at 120 °C until ethanol completely evaporated. As-prepared solid precipitate of TiO_2/CuPc nanocomposite was dried at 100 °C for 24 h. The composite in method 2 was recognized as CM2.

Method 3 (CM3): Ball-milled CuPc was then supplied to TiO_2 dispersed in ethanol solution for ball milling process conducted at room temperature. After that, the suspension was stirred at 120 °C until ethanol completely evaporated. As-prepared solid precipitate of TiO_2/CuPc was dried at 100 °C for 24 h. The composite in method 3 was recognized as CM3.

Method 4 (CM4): Ball-milled CuPc was mixed with TiO_2 dispersed in 100 ml ethanol solution by homogenizer at room temperature with speed of 7000 rpm for 30 min. The suspension was stirred at 120 ◦C until solid precipitate was obtained. After that, the solid precipitate was milled at room temperature. After that the suspension was stirred at 120 ◦C until ethanol completely evaporated. Finally, as-prepared solid precipitate of TiO_2/CuPc was dried at 100 ◦C for 24 h. The composite in method 4 was recognized as CM4.

The ratio of loading CuPc in 5 g of TiO_2 nanoparticle for all methods was fixed at 0.05, 0.1, 1 and 2 wt.%. For comparison to four methods, TiO_2 nanopowder was used as the reference powder in the applications.

3.2.1.2 Preparation of TiO_2/NiO p-n Nanocomposite

1) The speed of ball-milling process for the synthesis of TiO_2/NiO nanocomposite with a ball-to-powder weight ratio 30:1 is fixed at 80 rpm because D-direction in the vial for the attack between balls and substance is obtained by this speed.
2) The period for TiO_2/NiO nanocomposite in ball-milling process were varied as 5, 12, 18 and 24 h. This condition is determined to the suitable time for homogenize powder between TiO_2 and NiO.
3) Nickel acetate tetrahydrate was dissolved in 10 ml absolute ethanol and 1 ml DEA and was stirred at 80 °C for 2 h. Afterwards, the gel solution was supplied to TiO_2 dispersed in ethanol solution via ball milling for 18 h. The suspension was stirred at 100 °C until the ethanol was completely evaporated. The as -prepared solid precipitate of TiO_2/NiO was dried at 100 °C for 24 h. The ratio of NiO loading onto 3 g TiO_2 were fixed at 0.1, 1, and 2 wt%. Finally, the composites with varied amounts of NiO in TiO_2 were heated in air at 350, 450, and 550 °C for 2 h, respectively.

3.2.2 Fabrication of DSSC with TiO_2-Nanocomposite Based Working Wlectrode

3.2.2.1 Fabrication of DSSC with TiO_2/CuPc Working Electrode

1) 1 g of each hybrid composite was blended with 2 ml deionized water and fluorosilicic acid binder. After that the mixture was ground in a white mortar for 5 min.
2) The blue TiO_2/CuPc colloid was deposited on FTO substrate by doctor blade technique. These working electrodes were dried at 150 ◦C for 1 h in ambient air, followed by immersing in concentration 3×10^{-4} mol of N719 dye solution at room temperature for 24 h in dark environment. Finally, TiO_2/CuPc working electrodes in each method were obtained.
3) DSSC was designed in the sandwich structure with TiO_2/CuPc working electrode and platinum film coated on FTO counter electrode. Para polymer film was inserted between both

electrodes to prevent short circuit of the device. The structure of DSSC is shown in Figure 3.3.

4) Liquid electrolyte consisting of 0.1M I_2, 0.5M LiI, and 0.5M ethylene carbonate in 10 ml propylene carbonate was finally filled in the device.

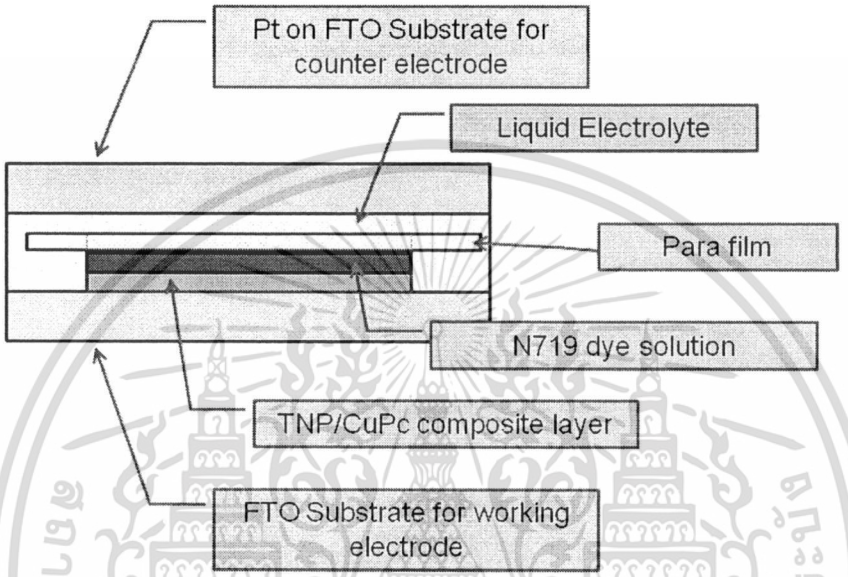

Figure 3.3 The sandwich structure of DSSC with TiO_2/CuPc modified working electrode.

3.2.2.2 Fabrication of DSSC with TiO_2/NiO working electrode

1) 0.2 g of each loading amount of NiO was blended in TiO_2 with a few drop of acetic acid, 2 ml of deionized water and Triton-X binder. After that the mixture was ground in a white mortar for 5 min.

2) TiO_2/NiO colloid was deposited on the top part of the dense layer on FTO substrate by doctor blade technique. These working electrodes were dried at 100 °C for 1 h in ambient air, followed by annealing at 450 °C for 1 h.

3) The working electrodes were immersed in a concentration 3×10^{-4} mol of N719 dye solution at room temperature for 24 h in the dark. Finally, TiO_2/NiO working electrodes in each method were obtained.
4) DSSC was designed in the sandwich structure with TiO_2/NiO working electrode and platinum film coated on FTO counter electrode. The para polymer film was inserted between both electrodes to prevent short circuit of the device. The structure of DSSC is shown in Figure 3.4.
5) The composite gel electrolyte consisting of 3 ml of 6 g polyethylene glycol (PEG-6000) dispersed in 10 ml acetonitrile with 0.05 M I_2, 0.5 M KI, 0.2 M *t*-butyl pyridine, and 0.2 g TiO_2 P-25 was finally made to fill into the device. The efficiency of composite gel in DSSC was compared with liquid electrolyte that used as in the part 3.2.2.1

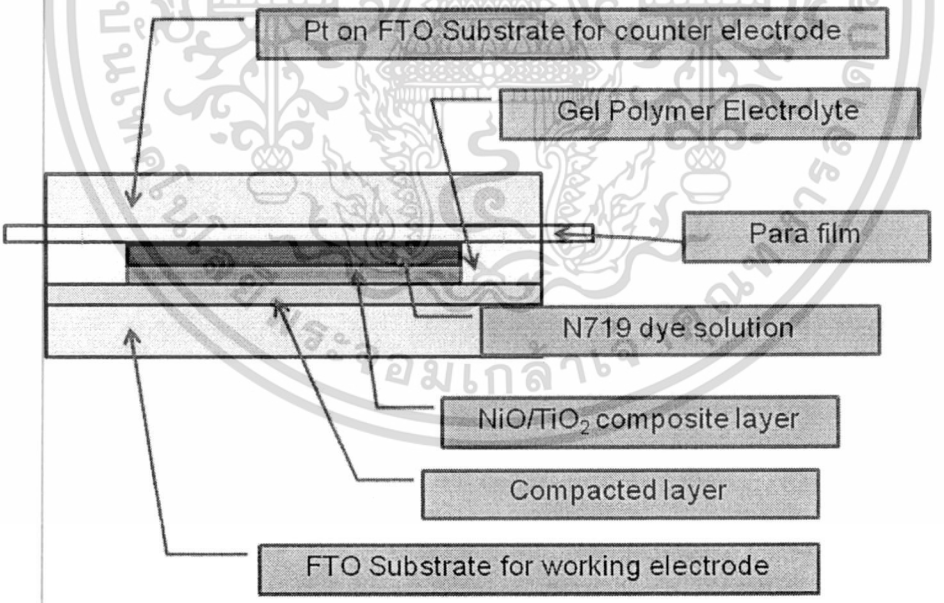

Figure 3.4 The sandwich structure of DSSC with TiO_2/NiO modified working electrode.

3.2.3 Photocatalytic degradation with TiO_2-nanocomposite photocatalyst

Rhodamine B (RhB) is a chemical compound and a kind of dye. RhB structure is shown in Figure 3.5. Rhodamine dyes are extensively utilized in biological treatment and industry, for example, tracer within water, fluorescence microscopy, staining fluorescent dye and dye laser. Due to high dye requirement, coloured organics and dye pollutants are emanated as a waste from dyeing process. Therefore RhB is used as model organic dye for studying its photodegradation under UV illumination.

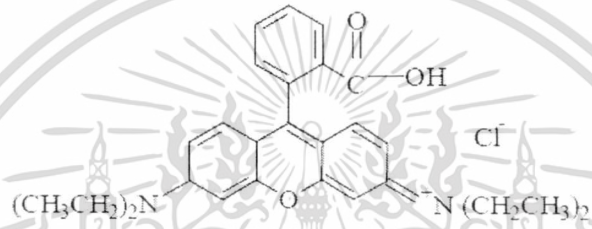

Figure 3.5 RhB chemical structure.

For dye degradation process, the experiment was proposed as following;

1) 50 mg of TiO_2/CuPc nanocomposites and TiO_2 P25 were dispersed in 1×10^{-6} mol/ℓ of RhB solution as illustraed in Figure 3.6.

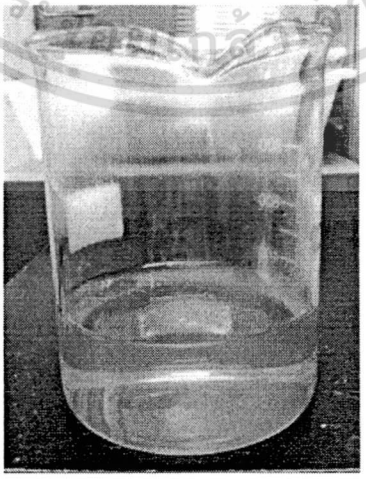

Figure 3.6 RhB solution.

2) Stirred for 20 min in the dark to obtain absorption/desorption equilibrium between RhB and the catalyst surfaces.
3) This solution was irradiated in UV exposed system at room temperature as shown in Figure 3.7. The system is composed of 2 UVA lamps (10 W, 0.1 mW/cm^2) and 1 UVB lamp (15 W, 0.2 mW/cm^2). The distance between UV lamp and sample is approximately 10 cm. The irradiation is continuously until the decolorization is complete reaction.
4) In addition, RhB solution were carried out with the absence of photocatalyst and ball milled TiO_2 at various time as controlling condition in this section for comparing to the reaction under UV irradiation.
5) RhB degradations were investigated each 5 min until completely in 30 min. Dye degradation was investigated by its absorbance at maximum wavelength of RhB at 554 nm via UV-Vis spectrophotometer.

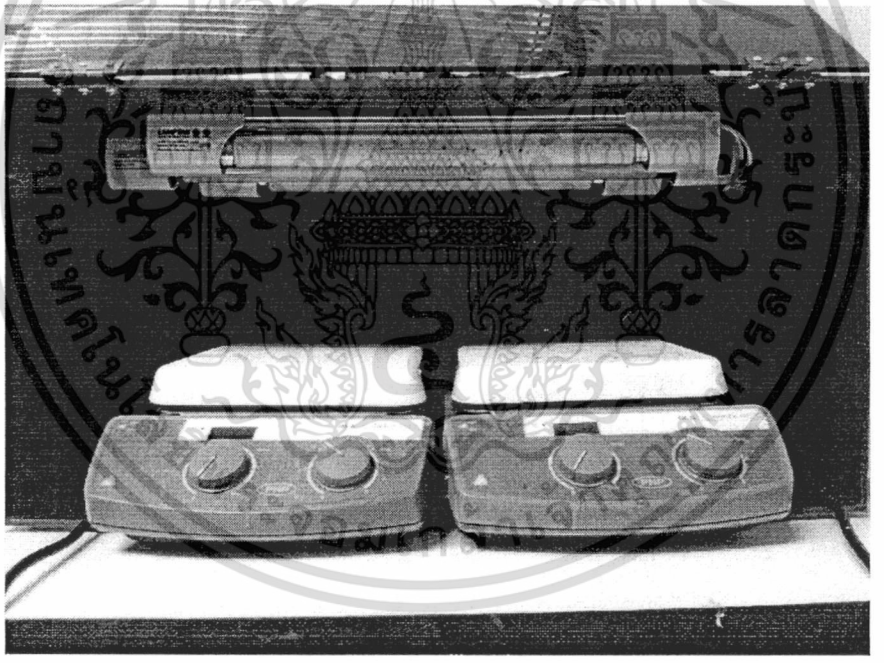

Figure 3.7 UV illumination system.

3.3 Characterizations

3.3.1 Scanning Electron Microscope

The morphology of pure TiO_2, as-prepared TiO_2 nanocomposites and modified working electrode of TiO_2 nanocomposite were monitored by field emission-scanning electron microscope (Hitachi S-4700) and scanning microscope (JEOL JSM-6340F). Sample surface was coated by gold particle for enhancing conductivity.

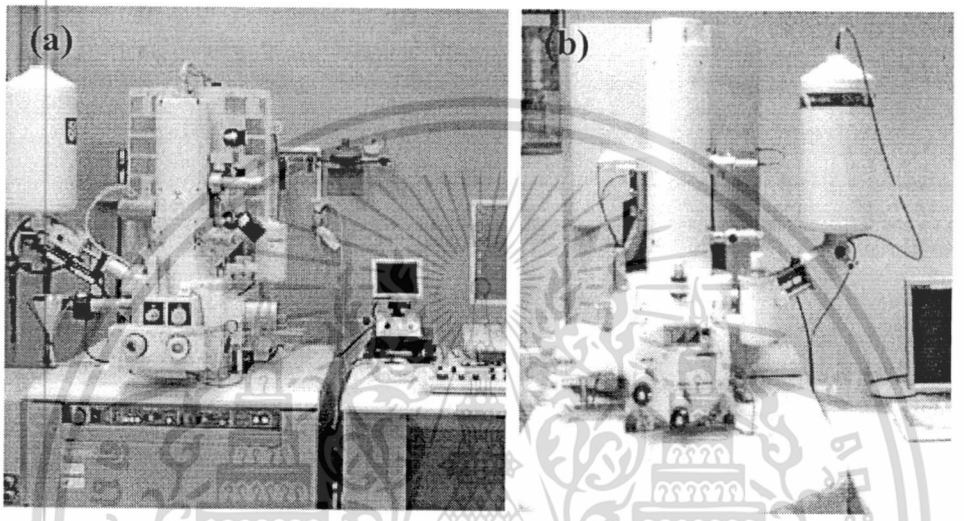

Figure 3.8 (a) Field emission-scanning electron microscope (Hitachi S-4700) and (b) Scanning microscope (JEOL JSM-6340F).

3.3.2 Transmission Electron Microscope

The structural properties of pure TiO_2, as-prepared TiO_2 nanocomposites were monitored by transmission electron microscope (FEI TECNAI G2 20). Bright filed images and selected area electron diffraction pattern were obtained.

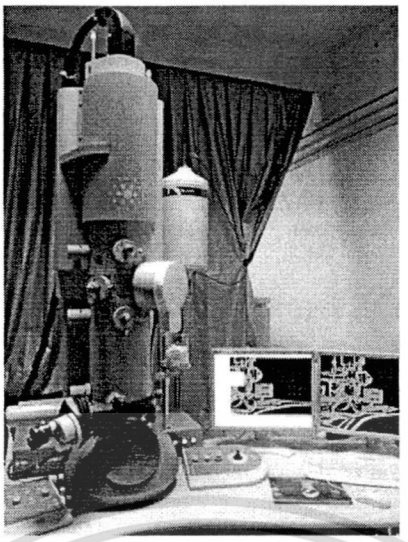

Figure 3.9 Transmission electron microscope (FEI TECNAI G2 20).

3.3.3 X-ray Diffractrometer

The structure of pure TiO_2 and as-prepared TiO_2 nanocomposites was characterized by X-ray diffractrometer (BRUKER D8 Discover). Cu KPhase structure and crystalline size in materials were obtained by this technique.

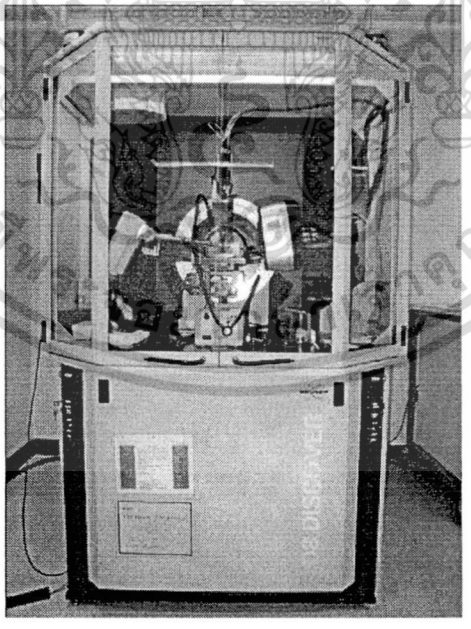

Figure 3.10 X-ray diffractrometer (BRUKER D8 Discover).

3.3.4 Raman Spectroscopy

Chemical bonding and functional group were investigated by Raman spectroscopy (Thermo SCIENTIFIC Nicolet 6700). Light scattering by stimulated infrared source was interpreted in this characterization.

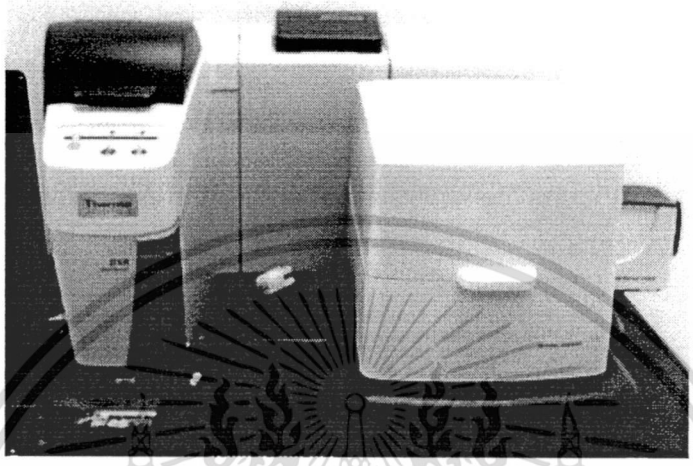

Figure 3.11 Raman Spectroscopy (Thermo SCIENTIFIC Nicolet 6700).

3.3.5 X-ray Absorption Near Edge Structure

X-ray absorption near edge structure has been carried out employing synchrotron radiation at the Siam Light Research Institute (SLRI), Thailand. Cu K edge (8979 eV) measurement was carried out using a Ge (220) crystal monochromator with a table step of 1 eV.

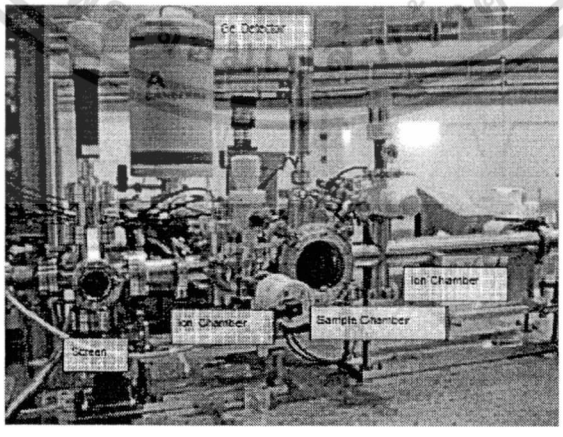

Figure 3.12 X-ray absorption near edge structure at experiment station, beamline 8.

3.3.6 X-ray Photoelectron Spectroscopy

The composition on material surface and oxidation state of atom were investigated by X-ray Photoelectron Spectroscopy (Kratos Analytical AXIS Ultra DLD)

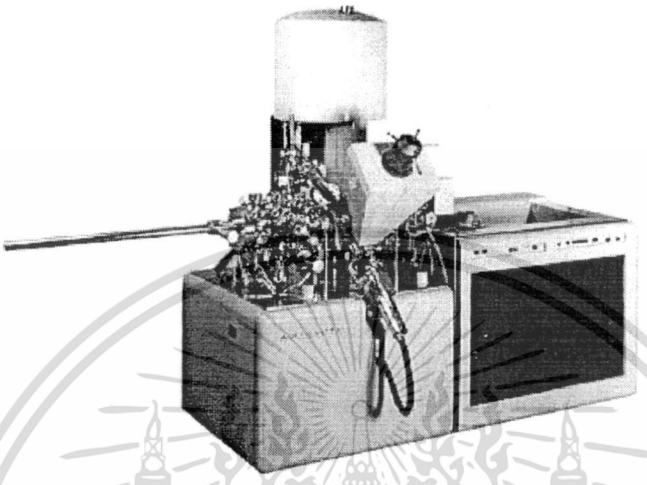

Figure 3.13 X-ray Photoelectron Spectroscopy (Kratos Analytical AXIS Ultra DLD).

3.3.7 Ultraviolet–visible spectroscopy

Absorbance of pure TiO_2 and as-prepared TiO_2 nanocomposites was analyzed by Ultraviolet–visible spectrophotometer (PG Instrument T90). Dye degradation by TiO_2 nanocomposites was proved by this technique in range of 450-650 nm.

Figure 3.14 Ultraviolet Visible Spectrophotometer.

CHAPTER 4
TiO_2/CuPc INORGANIC/ORGANIC HYBRID NANOCOMPOSITE

4.1 Characterizations of TiO_2/CuPc Hybrid Nanocomposite

4.1.1 Effect of Ball-milling on CuPc, TiO_2 Nanoparticle and TiO_2/CuPc Nanocomposite

4.1.1.1 Ball-Milled CuPc Powders

The physical structure of CuPc precursor is naturally acicular shape with approximately 15 μm as shown in Figure 4.1(a). Therefore ball milling process is essential to minimize its size before using in nanocomposite form. After ball milling, the minimized structures and magnificent dispersion of CuPc in form of flake powder can be obtained as illustrated in Figure 4.1(b). Therefore ball milled CuPc and TiO_2 matrix is well corporate in nanocomposite form via ball milling assisted process.

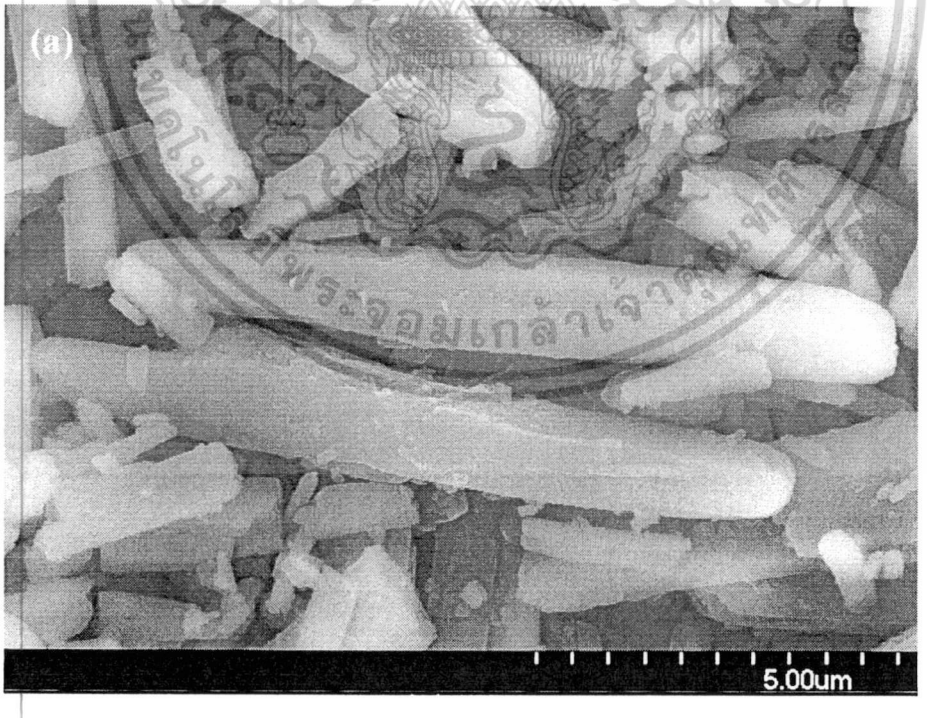

Figure 4.1 CuPc powder (a) before and (b) after ball milling process.

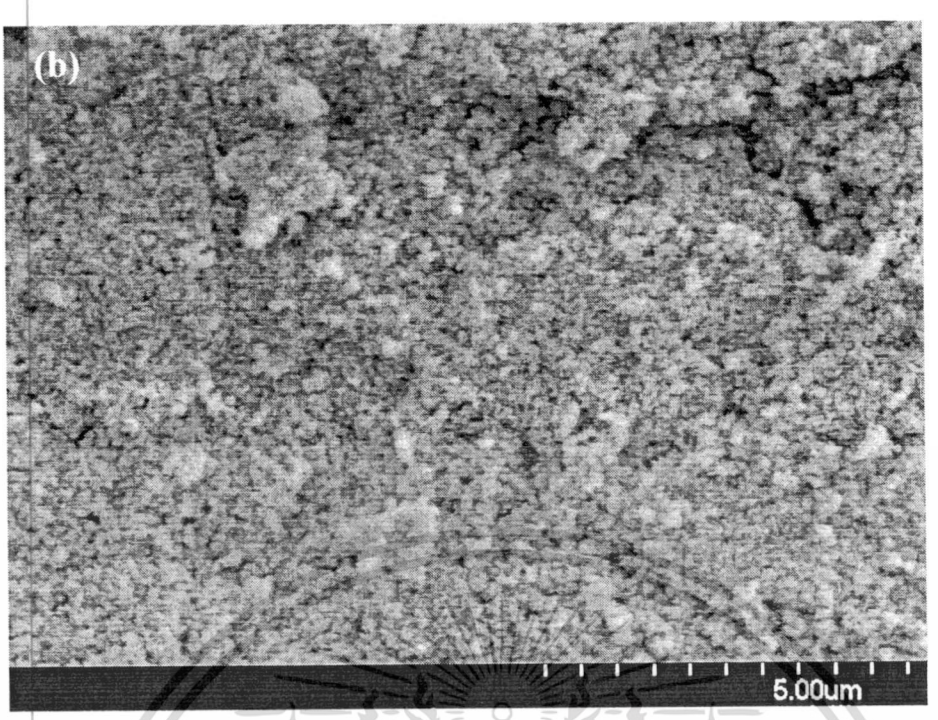

Figure 4.1 (cont.) CuPc powder (a) before and (b) after ball milling process at 18 h.

4.1.1.2 Effect of Ball Milling Time of TiO_2 P25

The effect of ball-milling time of TiO_2 P25 was investigated via surface area analysis with BET method. Nitrogen adsorption was chosen as the determination of specific surface area value and pore size diameter of TiO_2 as illustrated in Figure 4.2. Specific surface area measurements of TiO_2 at various milling time of 5, 12, 18 and 24 h are found to be 48, 52, 50 and 53 m^2/g, respectively. Comparing to as-prepared TiO_2, its surface area was slightly increased by increasing milling time. The breaking of crystals may be insignificantly occurred because of insufficient high energy in the system. Meanwhile, pore size diameter of as-prepared TiO_2 was decreased via ball-milling process. These results suggest that the influence of ball-milling process in this experiment is more effective on pore geometry than its surface area.

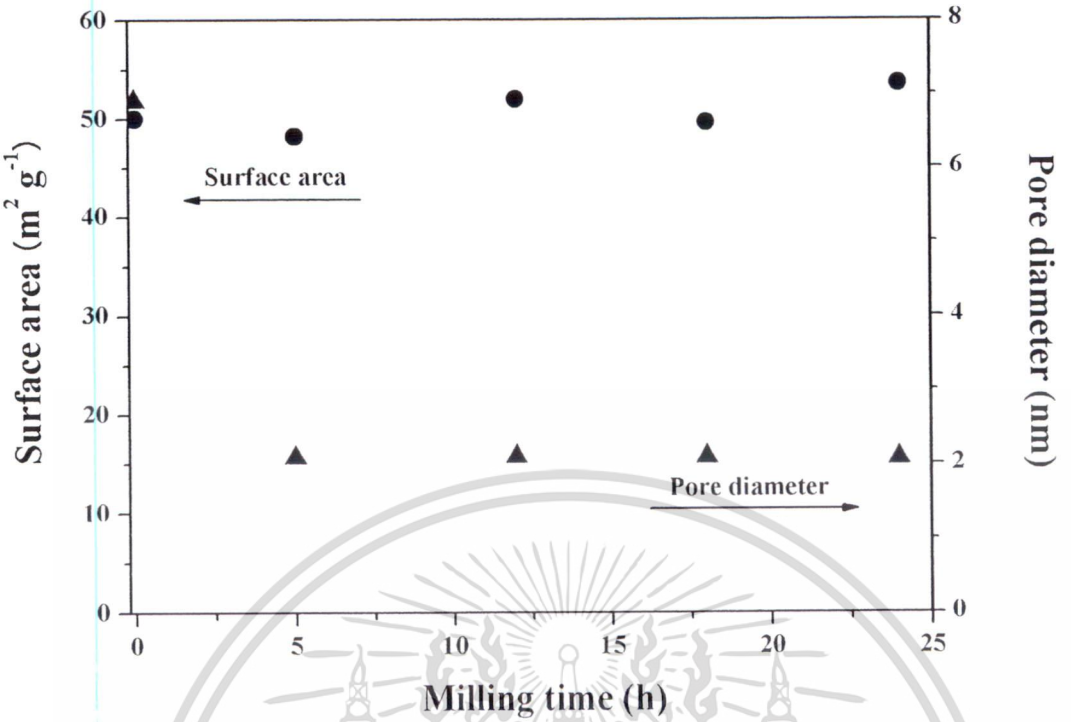

Figure 4.2 BET specific surface area and pore diameters of ball milled TiO_2 with varied milling time.

4.1.1.3 Effect of Ball Milling Time in TiO_2/CuPc Hybrid Nanocomposite

Low-energy ball milling in this experiment was operated by the conventional horizontal ball milling process which can reduce the particle size to sub-micron or nano range. The main factors for the particle size in this method depend on ball size, the ratio of ball and powder, rotation speed, the medium of ball milling and milling period. However, milling time was chosen as a major parameter affecting its size reduction. The other parameters were kept constantly because the optimized d-rotation in ball-milling process was obtained by these conditions as mentioned in chapter 3. The rotation speed is kept at 100 rpm with ball-to-powder weight ratio of 30:1 in ethanol solution which is an optimized condition for CuPc and TiO_2 blending. The milling times of the nanocomposite were varied at 5, 12, 18 and 24 h as illustrated in Figure 4.3. CuPc size was investigated to optimizing the suitable time for ball milling process. After milling time for 5 h, the structure of CuPc was in rod shape with size of approximately 12 μm and obviously secluded from TiO_2 matrix. CuPc size in the composite was decreased to 5 and 1.5 μm by increasing milling time

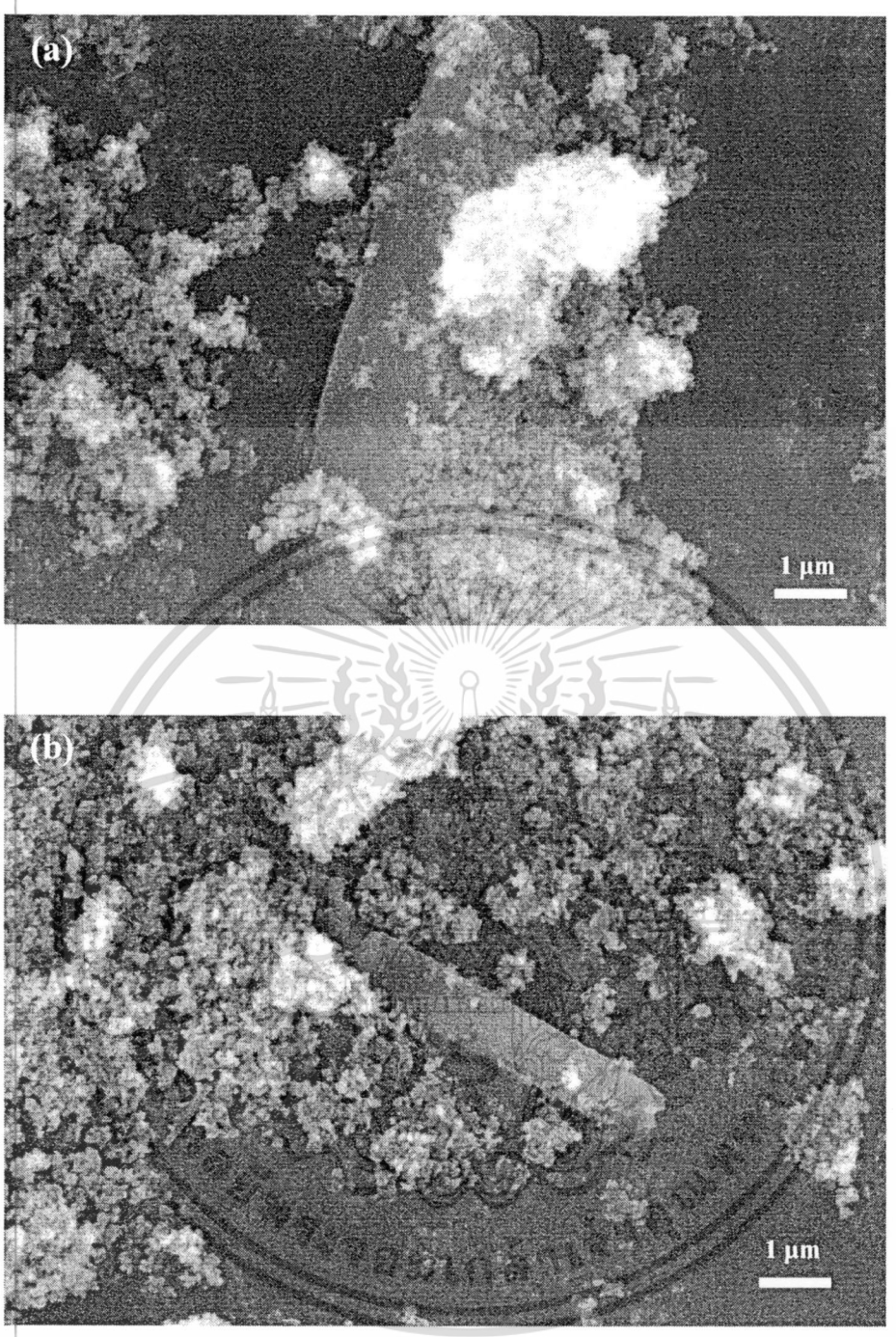

Figure 4.3 TiO_2/CuPc nanocomposite prepared at variousball-milling times, (a) 5h, (b) 12h, (c) 18h and (d) 24h.

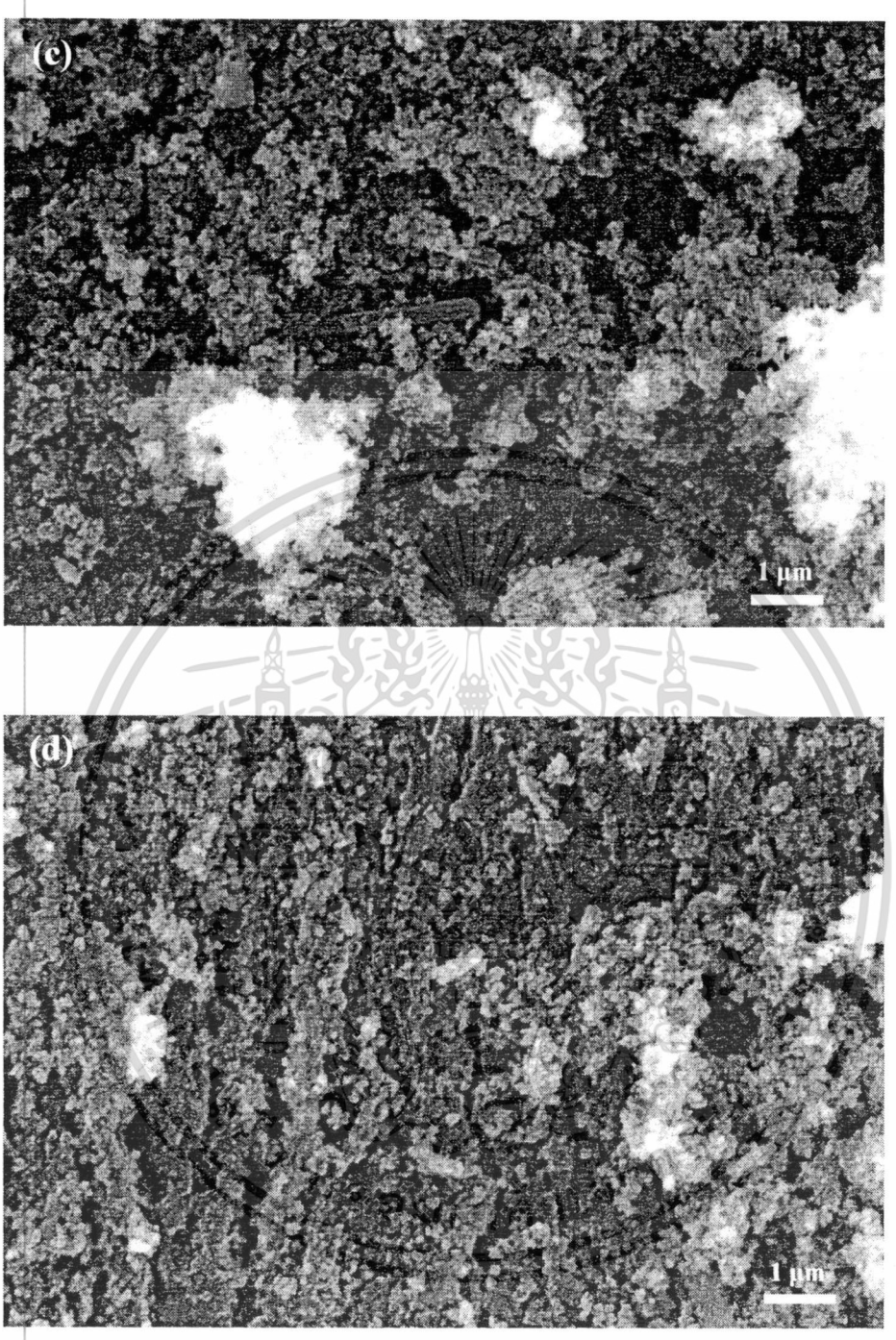

Figure 4.3 (cont.) TiO_2/CuPc nanocomposite prepared at various ball-milling times, (a) 5h, (b) 12h, (c) 18h and (d) 24h.

to 12 and 18 h, respectively. After being milled for 24 h, CuPc size was drastically decreased to smaller size comparing to the others. However, the closed packing of TiO_2 and the agglomeration was occured due to high energetic collision in the system. These results indicated that the length of CuPc is in the same size as precursor for short milling period. Meanwhile size reduction of CuPc is obtained by increasing time in ball milling process. The agglomeration of particle, however, is occurred by long period in ball milling time. The optimized time for the combination of TiO_2/CuPc nanocomposite via ball milling process is found to be 18 h. The excellent dispersion of CuPc on TiO_2 surface at 18 h was confirmed by SEM image in back scattering mode. Two-different phases showed in different color in the image reveals that TiO_2 surface in bright region was covered by CuPc (grey region) as illustrated in Figure 4.4. This result indicates that decreasing CuPc size and good spreading of CuPc on TiO_2 matrix without the agglomeration can be obtained by suitable milling time.

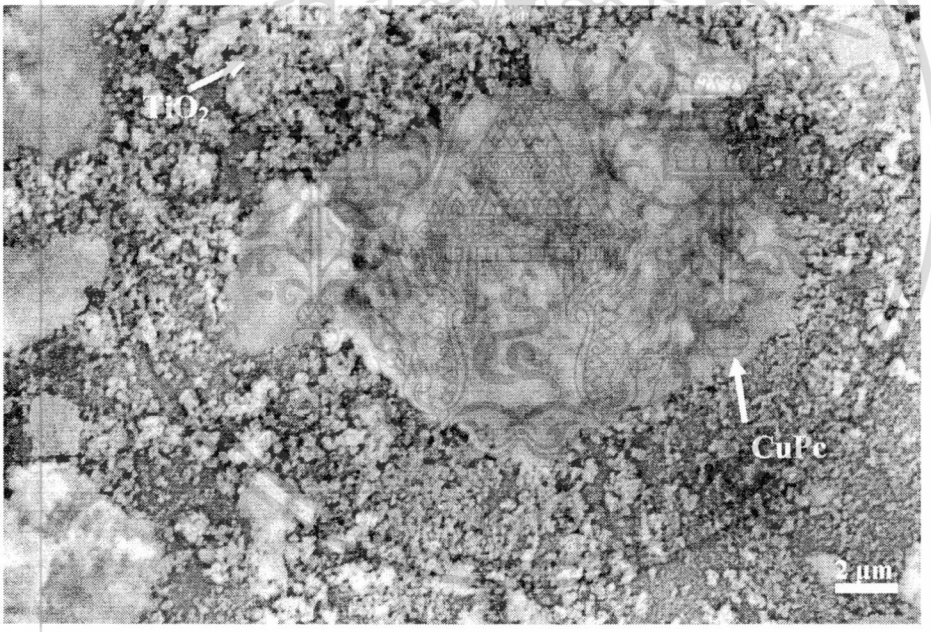

Figure 4.4 SEM image of TiO_2/CuPc nanocomposite at milling time 18 h.

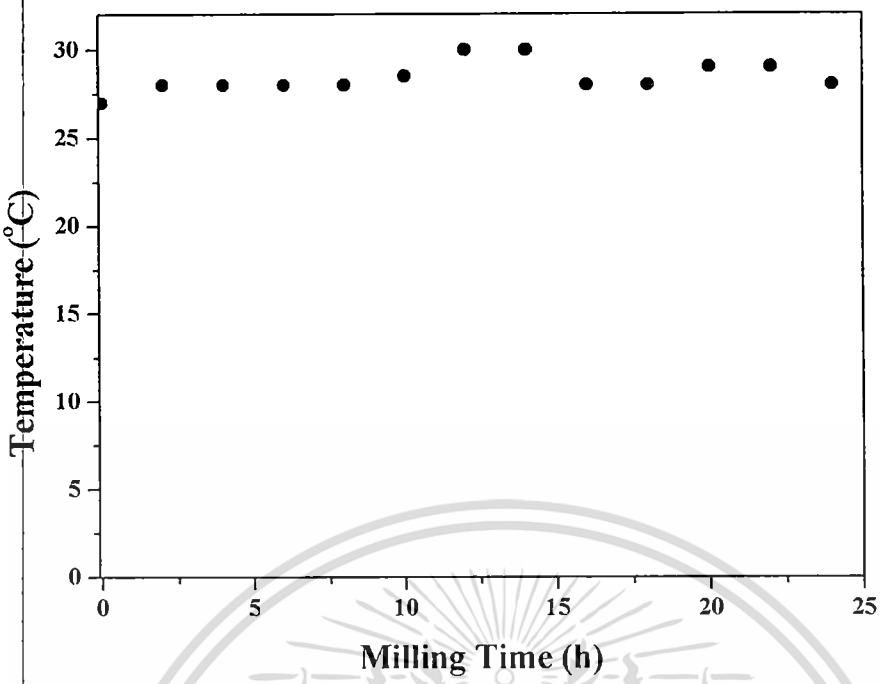

Figure 4.5 Temperature of TiO_2/CuPc nanocomposite in ball-milling process at certain milling time.

Temperature versus milling time in ball-milling process for the synthesis of TiO_2/CuPc nanocomposite was carried out every 2 hours as illustrated in Figure 4.5. The temperature in the system was in range of 27-30 °C relating to room temperature at that moment. This result suggests that ball milling process in this experiment is classified as low-energy process. The effect of heat treatment with high energy can be voided due to the insufficient energy for phase transformation and heat accumulation in the system.

4.1.2 TiO_2/CuPc Hybrid Nanocomposite Prepared by Various Methods

4.1.2.1 Morphology Characterization by SEM and TEM

The morphologies of TiO_2 nanoparticles, ball-milled CuPc and TiO_2/CuPc nanocomposites monitored from SEM and TEM images are illustrated in this section. It is obviously noticed from Figure 4.6(a) and (b) that TiO_2 nanoparticles is in well-defined crystalline and good dispersion with average particle size of 20-30 nm as seen in SEM and TEM images. The selected area electron diffraction (SAED) patterns in Figure 4.6(c) indicate the polycrystalline nature of anatase and rutile phases of as-received TiO_2 P25 powders.

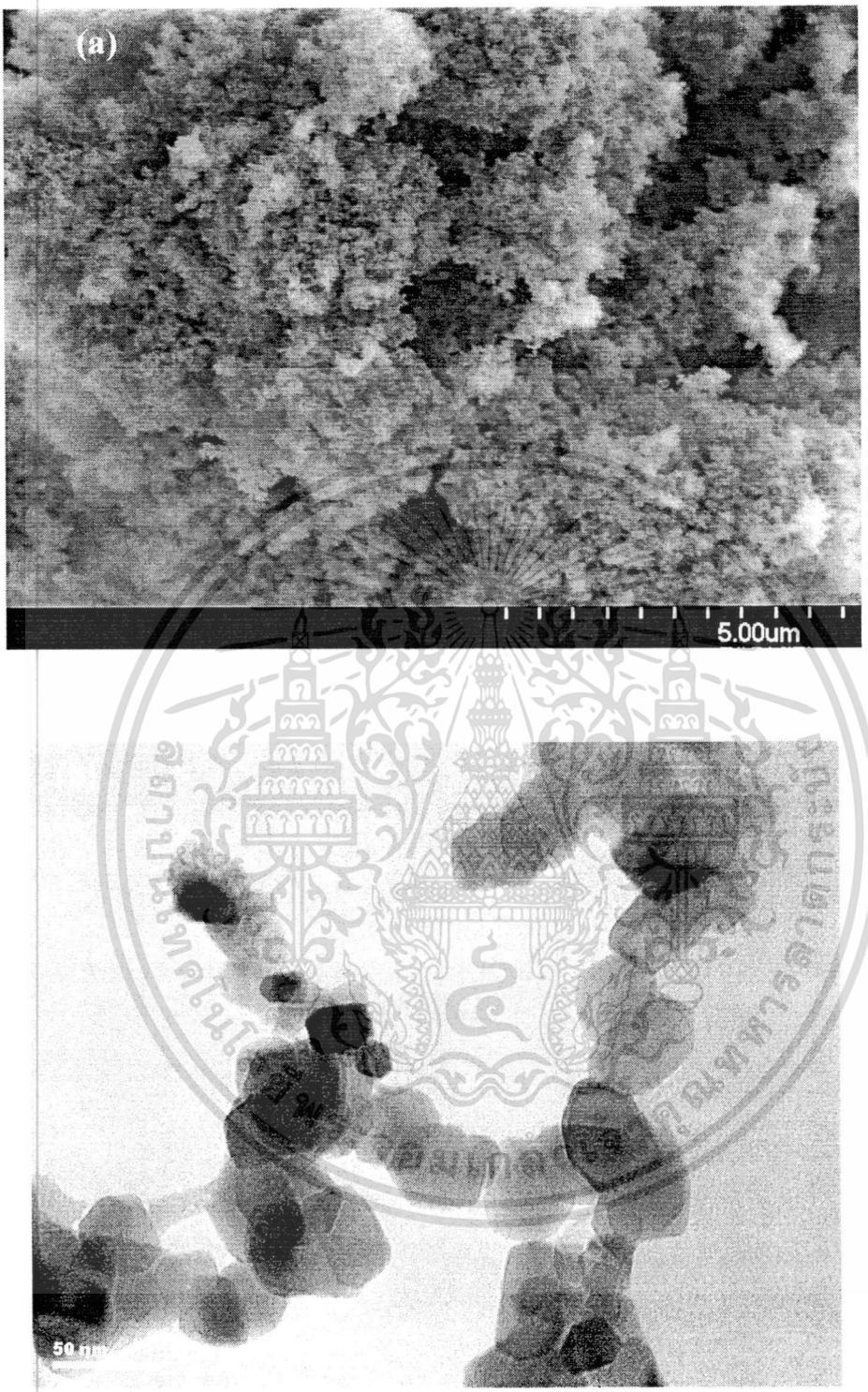

Figure 4.6 (a) SEM, (b) TEM images and (c) selected area pattern of commercial TiO_2 nanoparticles (P-25).

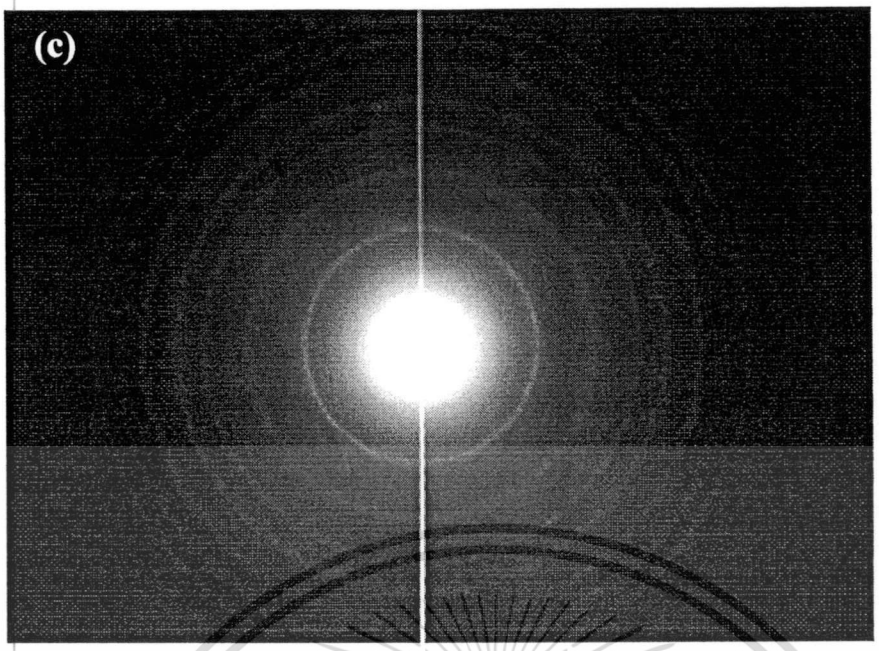

Figure 4.6 (cont.) (a) SEM, (b) TEM images and (c) selected area pattern of commercial TiO_2 nanoparticles (P-25).

SEM images of TiO_2/CuPc nanocomposites prepared by four different methods with 1 wt.% loading of CuPc are shown in Figure 4.7(a)-(d). This image indicates that the homogeneous dispersion and the spreading deposition of CuPc guest onto TiO_2 host matrix was attained after ball-milling process and the small particles of TiO_2 were covered with the expanding sheet of CuPc. These results imply that, during ball milling process, CuPc powder and TiO_2 may obtain sufficient thermo-mechanical energy for attaching them together to form a well-defined composite [99].

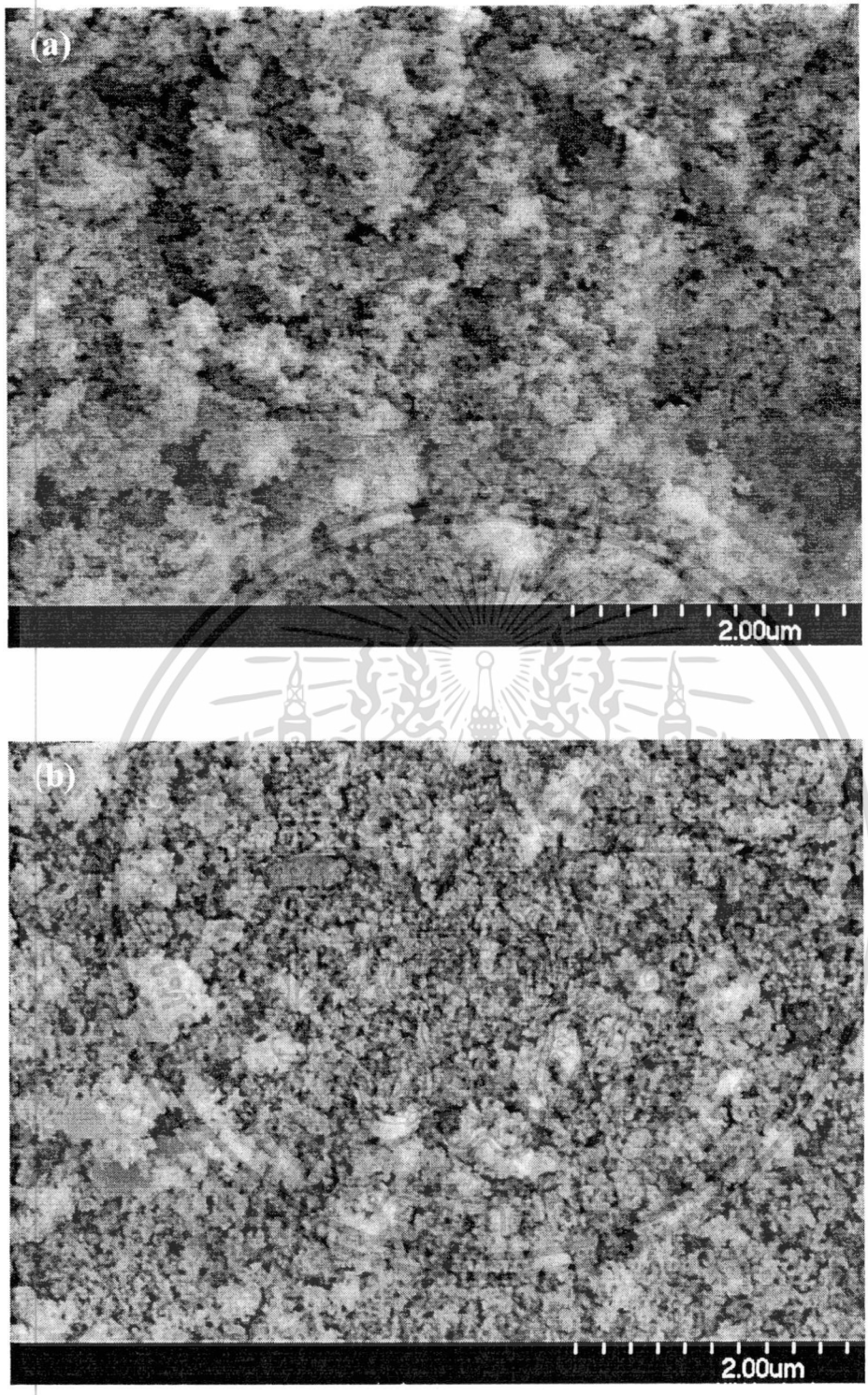

Figure 4.7 FE-SEM images of TiO_2/CuPc hybrid nanocomposites prepared by (a) CM1, (b) CM2, (c) CM3 and (d) CM4.

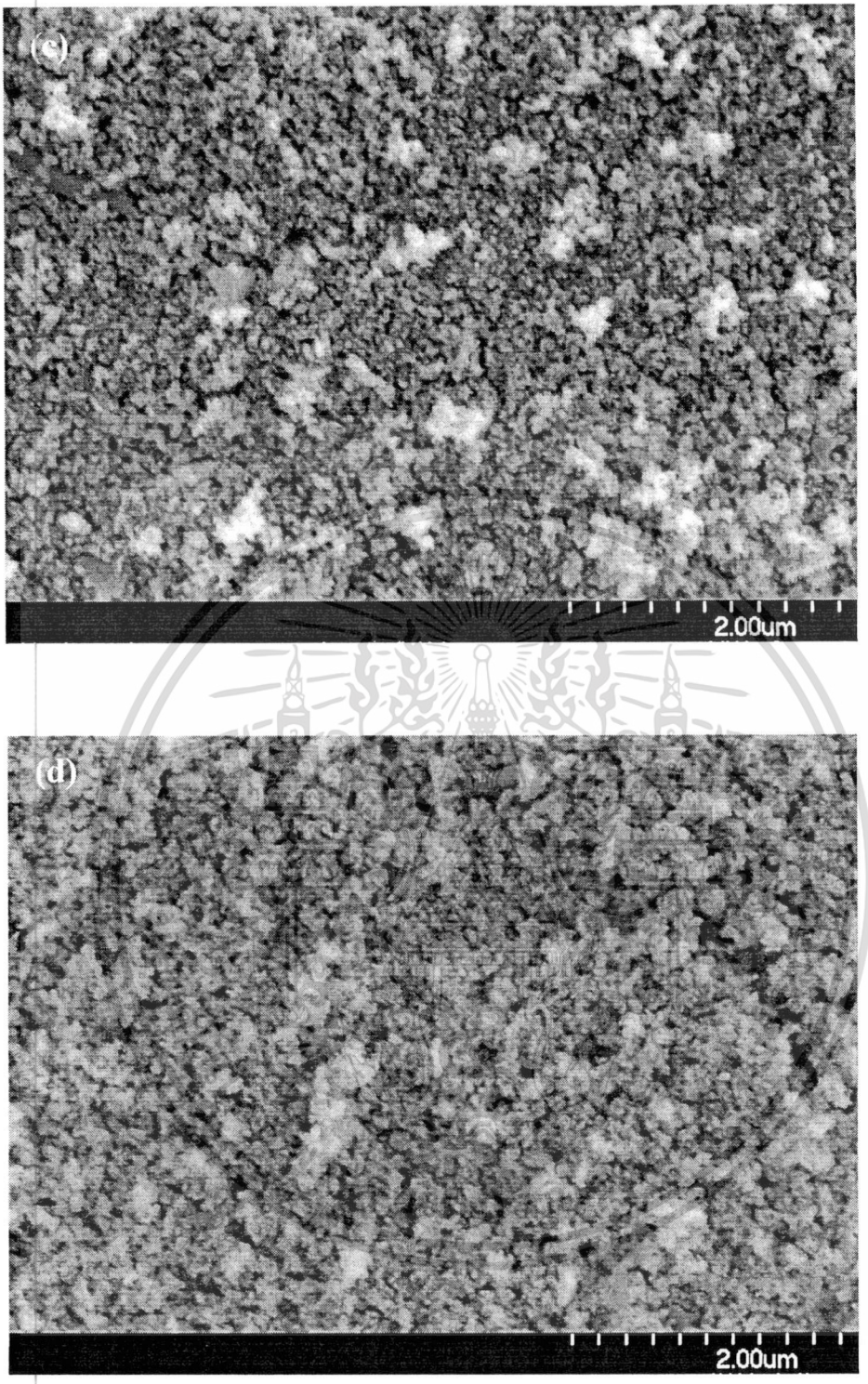

Figure 4.7 (cont.) FE-SEM images of TiO_2/CuPc hybrid nanocomposites prepared by (a) CM1, (b) CM2, (c) CM3 and (d) CM4.

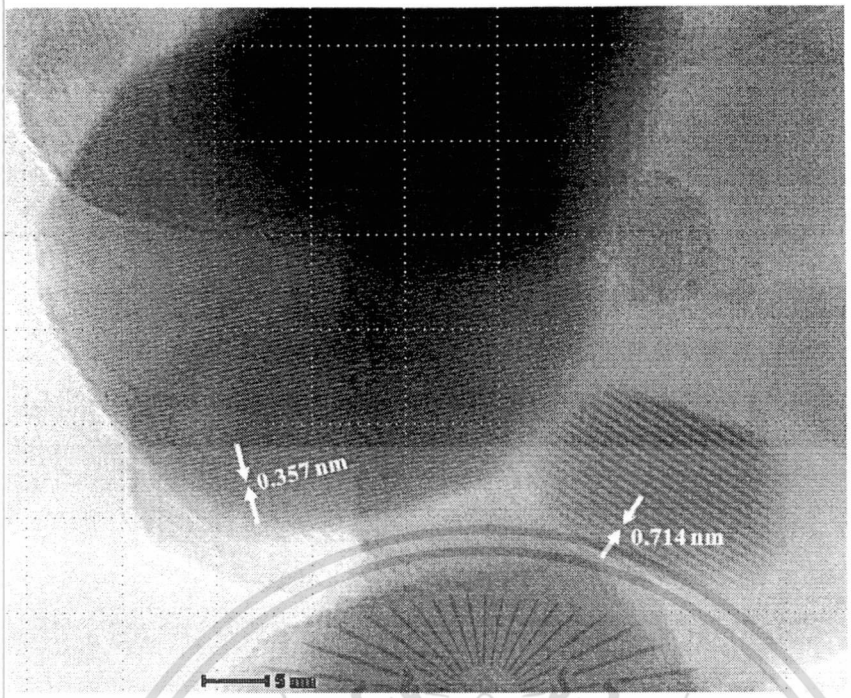

Figure 4.8 TEM images of TiO_2/CuPc hybrid nanocomposites.

The selected area electron diffraction (SAED) pattern of TiO_2/CuPc nanocomposite is illustrated in Figure 4.8. TEM image clearly exhibits TiO_2 fringe with d-spacing of 0.35 nm relating to anatase phase at (101) plane and CuPc fringe with the interplanar spacing of 0.71 nm assigning to $(\bar{2}02)$ plane of β-phase. This result confirms that CuPc structure is existed and throughly dispersed in TiO_2 matrix via an assistance of ball-milling process.

4.1.2.2 XRD Characterization

The XRD patterns of CuPc, TiO_2 nanoparticle and TiO_2/CuPc hybrid nanocomposites prepared by four different methods are illustrated in Figure 4.9. For TiO_2 nanoparticle, the XRD peaks situated at 2θ = 25.4°, 38.1°, 48.1°, 55.1° and 62.5° , correspond to (101), (004), (200), (211) and (204) planes of anatase phase (ICDD 21-1272), consecutively. Whereas rutile phase in (110), (101), (111), (211) and (220) plane is related to the peak at 2θ = 27.5°, 36.2°, 41.2°, 54.3° and 56.6°, respectively (ICDD 21-1276). This basic crystalline of anatase phase indicates tetragonal point group $I4_1/amd$ with lattice parameter a = 4.71 Å and c = 9.41 Å meanwhile the structure of rutile phase identifies primitive tetragonal point group $P4_2/mnm$ amd with lattice parameter a and c = 4.97 Å. The crystalline size of TiO_2 is

approximately 20.64 nm calculated by Scherrer equation from the major peak of anatase phase (101). The XRD patterns of CuPc in the range of 7° to 30° are assigned to beta phase of CuPc (β-CuPc) (ICDD 11-0893). Meanwhile, XRD characteristics of all TiO_2/CuPc hybrid nanocomposites are identical to TiO_2 XRD patterns without noticeable peaks of CuPc. However, the intensity of TiO_2 major peak exhibits a significant decrease when using different method, implying the decrease of TiO_2 crystalline by CuPc dispersion on TiO_2 surface. The inferior intensity of CuPc in composite XRD patterns oppressed by TiO_2 may be due to small loading of CuPc in TiO_2 matrix. These results also indicate that CuPc additive insignificantly affects the basic crystal structure of TiO_2. This similar feature was supported by previous published work reported by Chuen-Shii Chou and co-workers [100].

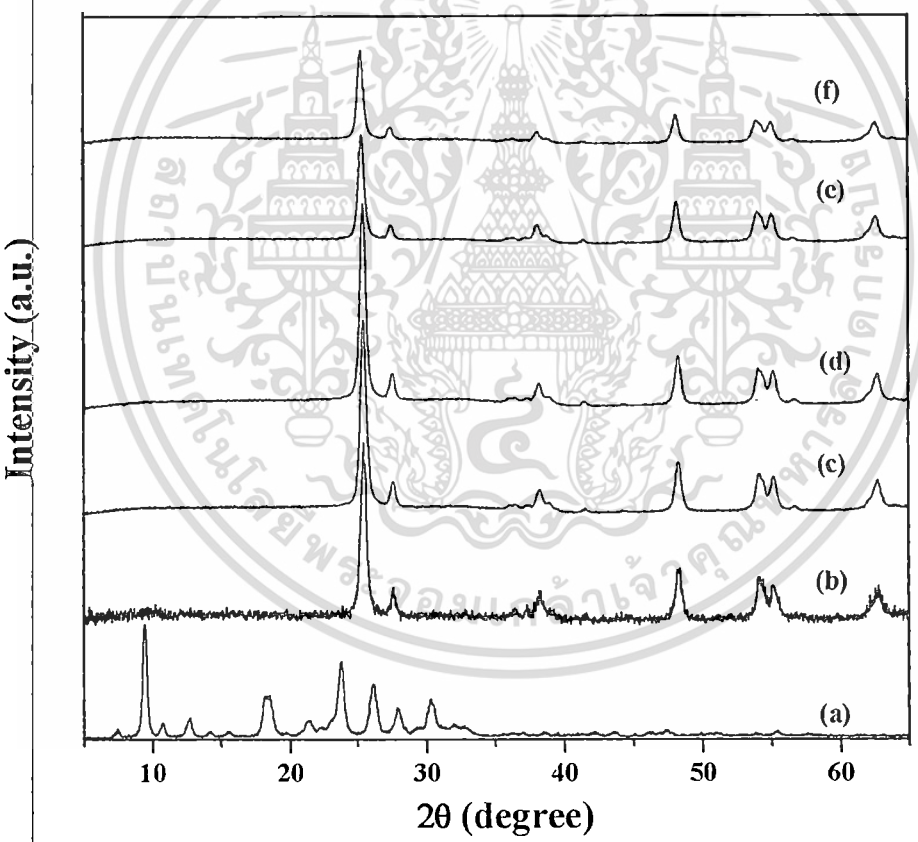

Figure 4.9 XRD patterns of (a) CuPc, (b) TiO_2 nanoparticles, and TiO_2/CuPc hybrid nanocomposites prepared by (c) CM1, (d) CM2, (e) CM3 and (f) CM4.

4.1.2.3 Raman Characterization

The Raman spectra of TiO_2 and TiO_2/CuPc hybrid composites in range of 150-2000 cm^{-1} are illustrated in Figure 4.10. For TiO_2 P25, Raman bands at 144, 197, 395, 515 and 683 $cm^{-1}$are attributable to anatase phase which related to Raman-active mode with the symmetries of E_g, E_g, A_{1g}, B_{1g} and E_g, respectively. Whereas rutile phase in Raman band appeared at 235 cm^{-1} attributes to two-phonon scattering mode. For TiO_2/CuPc nanocomposites, peak positions are identical to those of TiO_2 P25 accompanying CuPc peaks which are obviously observed in wavenumber range of 1000-1600 cm^{-1} as signified in Figure 4.11. The wave numbers of Raman mode of CuPc correspond to the symmetries of vibration. The symmetry of $A1_g$ and $B2_g$ mode are noted as in-plane vibrations. The strongest peak of CuPc at 1530 cm^{-1} corresponds to C–N_m–C bonds as well as pyrrole rings expanding coupled with C–H bond in-plane bending vibrations [96]. Comparing to CuPc spectra, the Raman peak of TiO_2/CuPc composites is slightly moved to high frequency. This noticeable shift may be initiated from anharmonic scattering effect from TiO_2 closely adhered to CuPc particle [101-102].

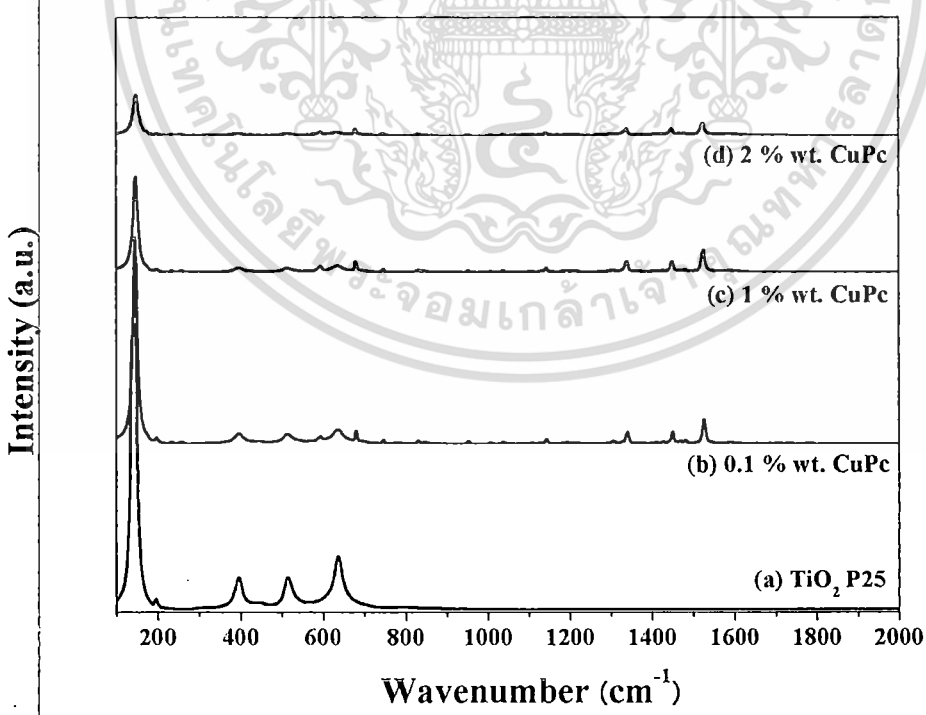

Figure 4.10 Raman spectra of (a) TiO_2 P25 and TiO_2/CuPc nanocompsite at loading CuPc (b) 0.5, (c) 1 and (d) 2 wt.%

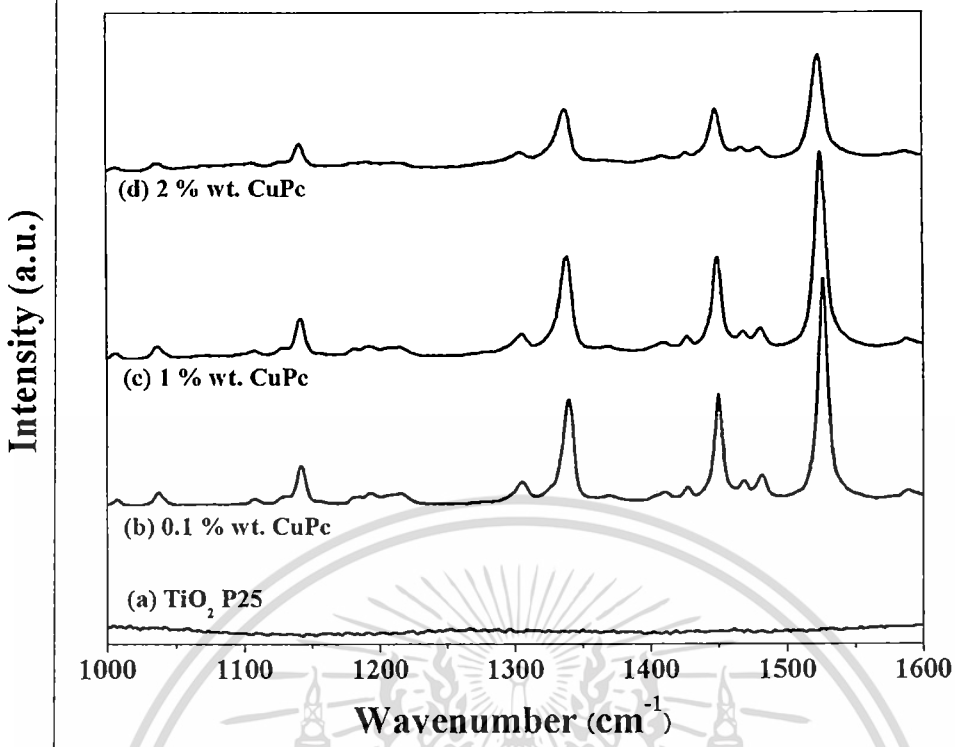

Figure 4.11 Raman spectra in rage 1000-1600 cm^{-1} of (a) TiO_2 P25 and TiO_2/CuPc nanocompsite at loading CuPc (b) 0.5, (c) 1 and (d) 2 wt.%.

4.1.2.4 XANES Analysis

The Cu K edge X-ray absorption spectra of CuPc, TiO_2/CuPc nanocomposites are shown in Figure 4.12. A prominent absorption peak can be observed on the absorption edge at 8979 eV. When CuPc was loaded into TiO_2, XANES spectrum of the composite was similar to that of CuPc. This result suggests that local structure of CuPc loaded in TiO_2 matrix scarcely changes. This implication is in good accordance with the results revealed by XRD. Moreover, TiO_2/CuPc nanocomposite may compatibly form in physical sorption without new bonding between two materials. However, the ripple of extended absorption regime in TiO_2/CuPc nanocomposite can be observed, which may be attributed to the vibration between the molecules of Cu and neighbor atom by the disturbance of TiO_2.

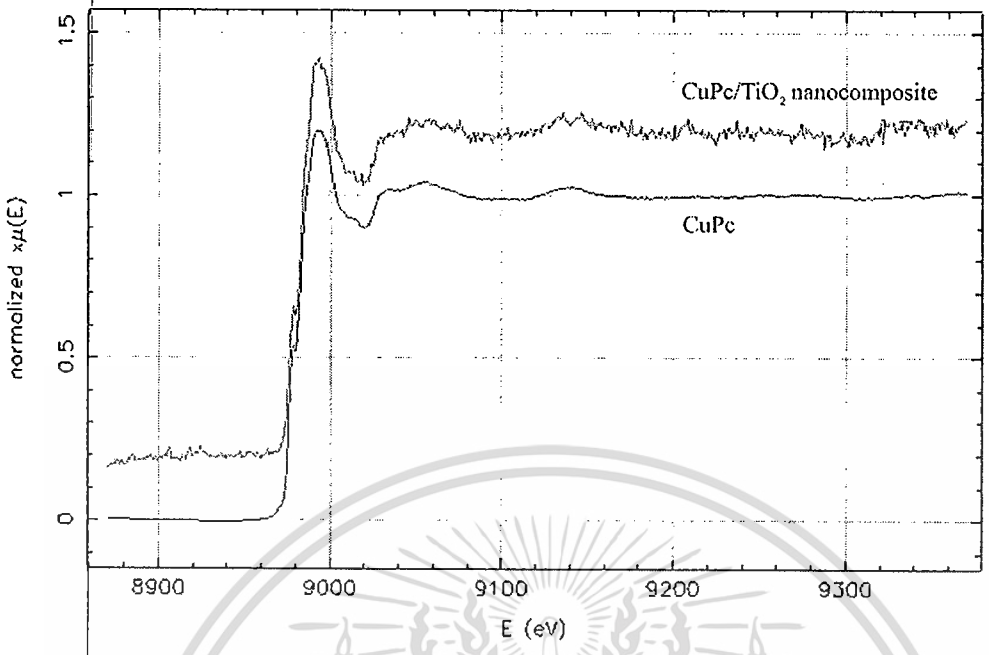

Figure 4.12 Experimental X-ray absorption Cu K edges for CuPc and TiO_2/CuPc nanocomposite.

4.1.2.5 Absorption Spectra

The absorption spectra of TiO_2 and TiO_2/CuPc nanocomposite with different loading amounts of CuPc are illustrated in Figure 4.13. The strong absorption of TiO_2 in a range of 200-400 nm is originated from typical band gap energy of TiO_2 (3.2 eV) [103]. The extended absorption of bare TiO_2 nanopowder in range of 400-700 nm may be due to scattering-induced absorption of longer wavelength in colloidal solution or low density of state in the conduction band of TiO_2 [10]. The enhancement of optical absorption in UV region and visible light was clearly observed in TiO_2/CuPc composite. Comparing to pure TiO_2, the absorption spectra of the composites exhibits an obvious red-shift to higher wavelength in visible region with stronger intensity as the CuPc loading content increases up to 1% thereafter decreases. In fact, CuPc has two distinct absorption bands in the range of 200-400 nm called B-band and 600-800 nm called Q-band [104]. The optical absorption enhancement of the composite in visible region are resulted from π-π^* excitation between bonding and antibonding molecular orbital of the Q band of phthalocyanine molecules [105-106].

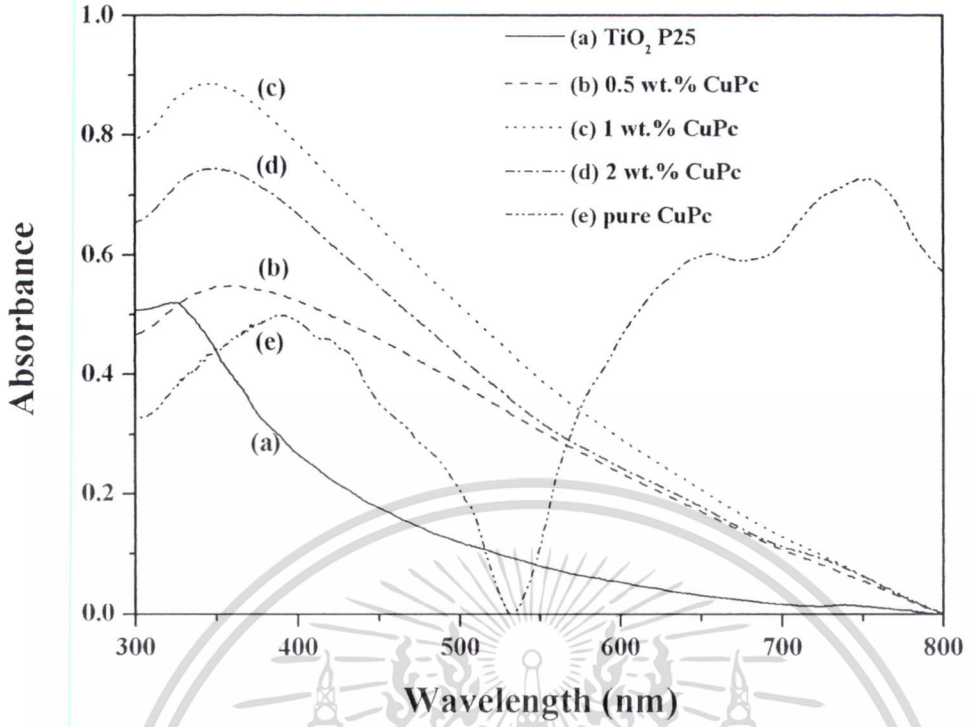

Figure 4.13 UV-Vis spectra of pure TiO_2 and various the amount of CuPc in TiO_2 treated, (a) TiO_2 P25, (b) 0.5, (c) 1 and (d) 2 wt.% CuPc loading in the composite.

4.2 Application of TiO_2/CuPc Hybrid Nanocomposite

4.2.1 Utilization of TiO_2/CuPc Hybrid Nanocomposite on Modified Working Electrode in DSSC

4.2.1.1 Morphology of TiO_2/CuPc Hybrid Nanocomposite Modified Working Electrode

From SEM image in Figure 4.14(a) – (e) shows the surface morphology of pure TiO_2 and TiO_2/CuPc nanocomposites layers with four different methods on FTO electrodes. Each SEM image indicates the uniform distribution and excellent coalition of the composites on the electrodes owing to suitable binding agent and sufficient nucleation energy from thermal treatment after annealing at 150 °C. Furthermore, the presence of nanopores in the composite layer is observed at the surface of modified working electrode. This feature advises that the absorption of dye molecules to metal oxide layer can increase significantly due to the assistance of the porosity on modified working electrode. Increasing amount of absorbed dyes can consequently enhance the

rapid injection of electrons to TiO_2/CuPc working electrode [107-108]. The average thickness of TiO_2/CuPc nanocomposites layer deposited on FTO electrode was evaluated to be approximately 10 μm.

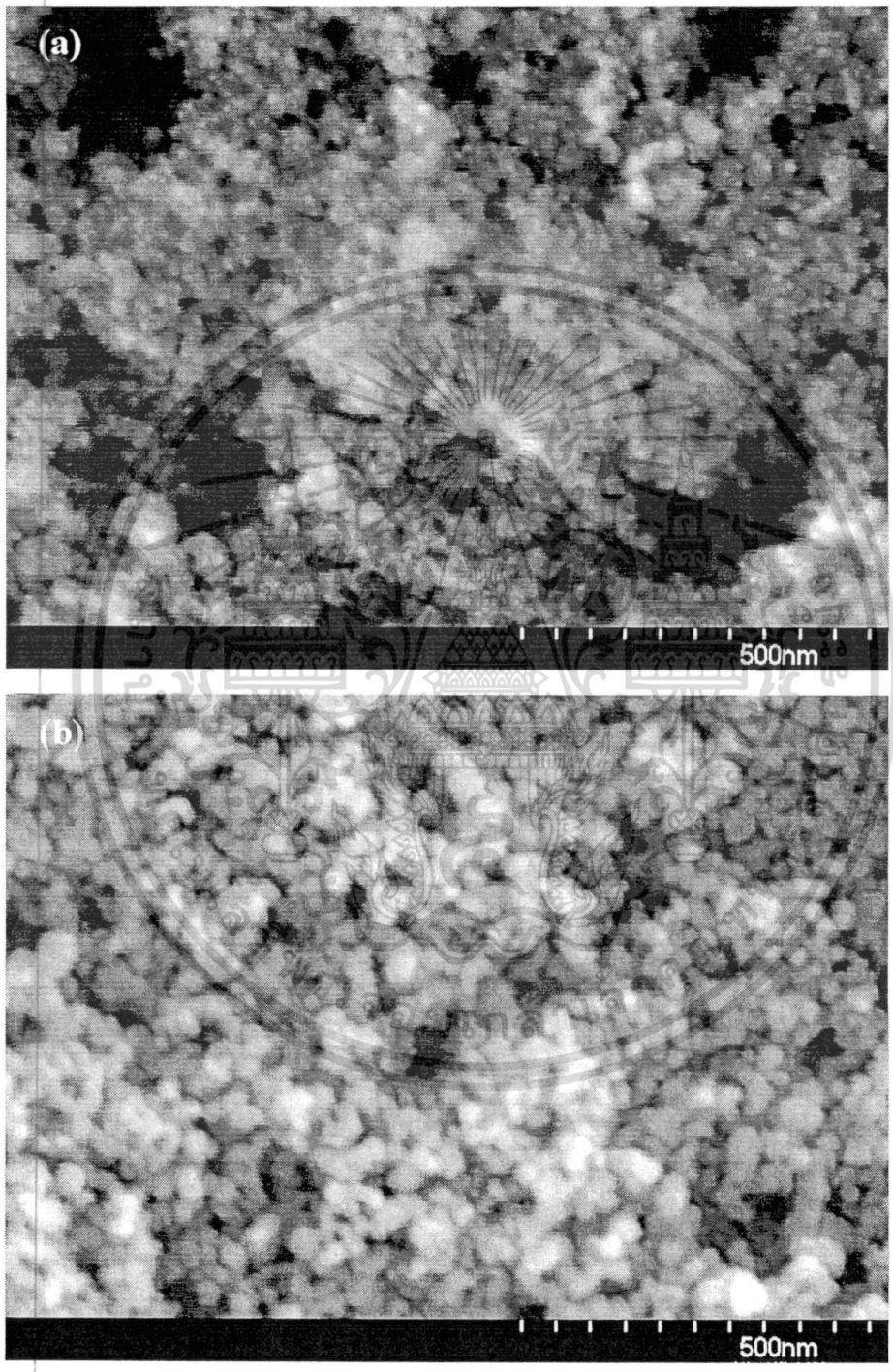

Figure 4.14 FE-SEM images of working electrode in devices (a) TiO_2 P25, (b) DCM1, (c) DCM2, (d) DCM3, (e) DCM4 and (f) the cross-section image of working electrode.

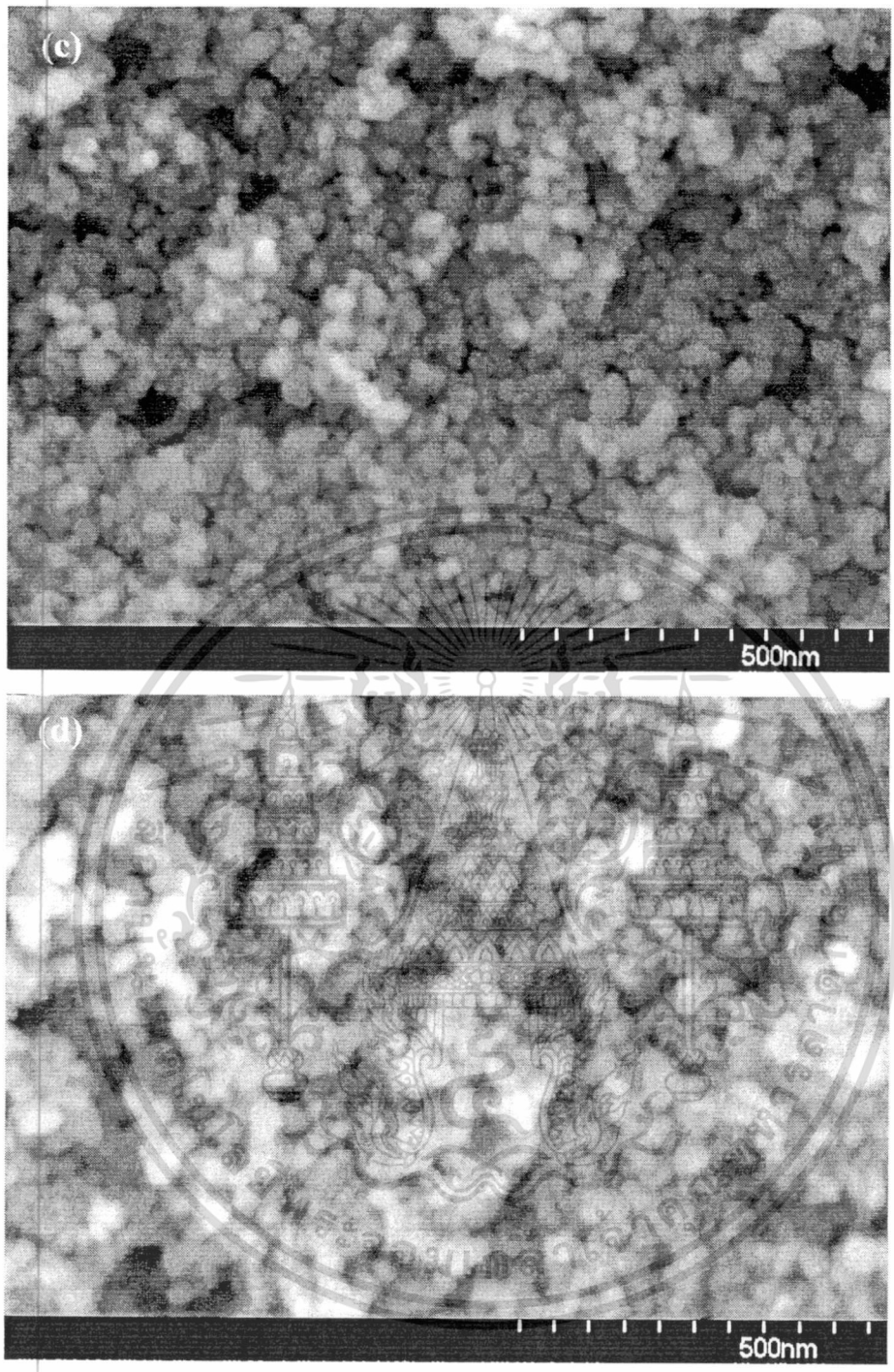

Figure 4.14 (cont.) FE-SEM images of working electrode in devices (a) TiO_2 P25, (b) DCM1, (c) DCM2, (d) DCM3, (e) DCM4 and (f) the cross-section image of working electrode.

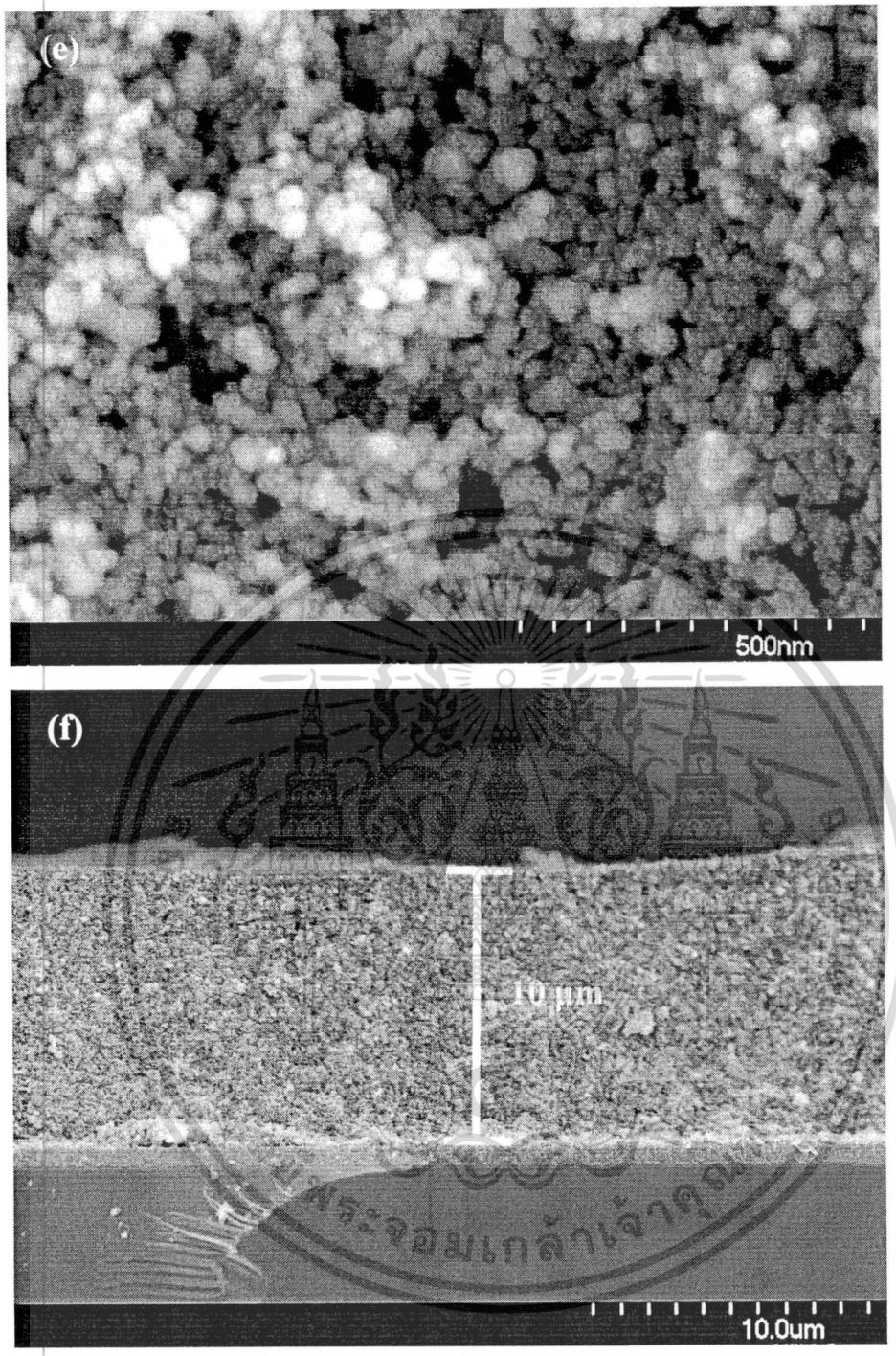

Figure 4.14 (cont.) FE-SEM images of working electrode in devices (a) TiO_2 P25, (b) DCM1, (c) DCM2, (d) DCM3, (e) DCM4 and (f) the cross-section image of working electrode.

4.2.1.2 Solar Cell Efficiency Measurement

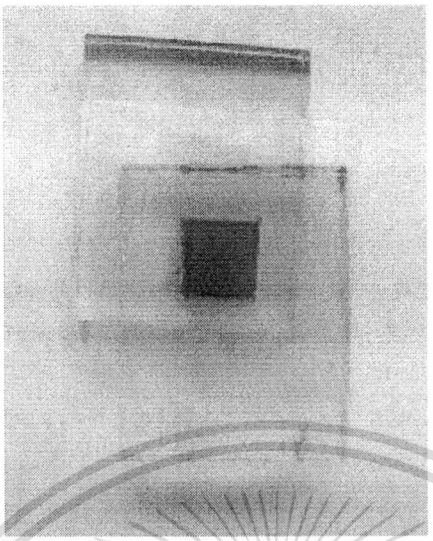

Figure 4.15 DSSC device with TiO_2/CuPc nanocomposite on modified working electrode using liquid electrolyte.

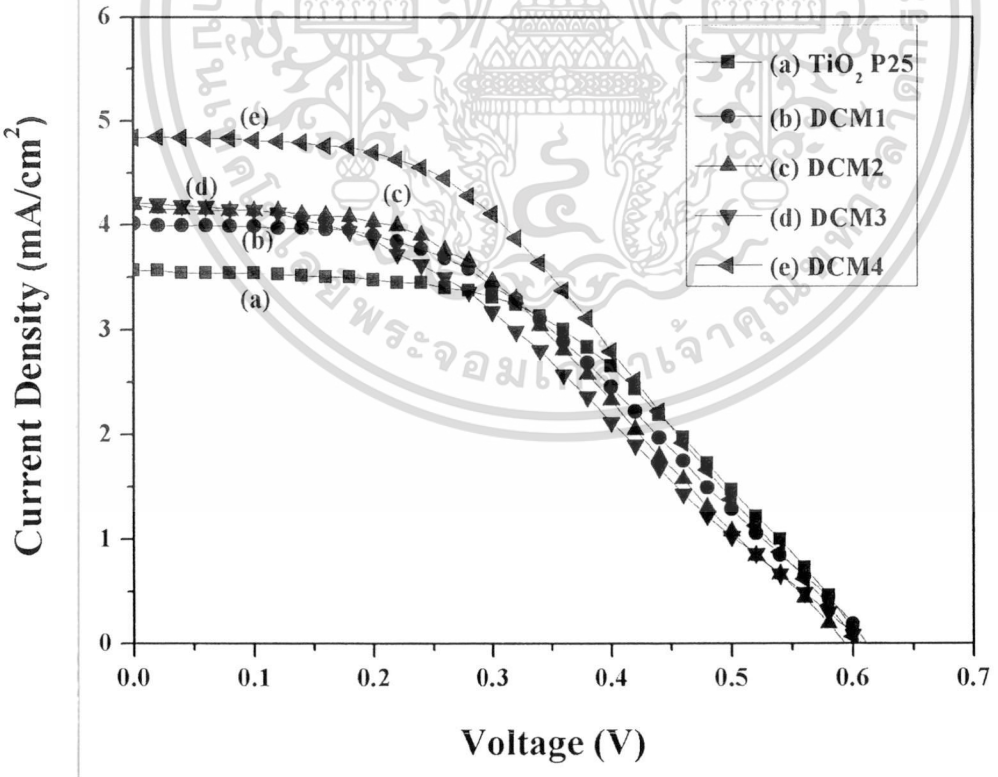

Figure 4.16 Photocurrent-voltage curves of DSSC device (a) TiO_2 P25, (b) DCM1, (c) DCM2, (d) DCM3 and (e) DCM4.

The assembly of DSSC device with TiO_2/CuPc nanocomposite on modified working electrode using liquid electrolyte is shown in Figure 4.15. Current density versus voltage (*J*-V) curves of DSSCs whose working electrode was modified by TiO_2/CuPc nanocomposites with 0.05 wt% CuPc content are illustrated in Figure 4.16. The device labeled as DCM4 displayed superiority in current density to the others. TiO_2/CuPc nanocomposites for DCM1 was prepared by mechanically stirring process that is able to increase the current density comparing to pure TiO_2 meanwhile homogenization and ball milling process employed to synthesize the nanocomposite in DCM2 and DCM3 enhance the dispersion and adherence of CuPc all over TiO_2 matrix. By utilizing these advantages of homogenization and ball milling for preparing the corresponding composite, the most desirable composite is achieved via CM4 method resulting in the highest performance efficiency of the DCM4 device. Two possible mechanisms are anticipated to take a responsibility on this enhancement of the device performance. First, with the presence of CuPc in the composite, the decrease of recombination of photoinjected electrons is expected to appear attributing to the more effective charge separation on the interface of TiO_2 and CuPc [109]. CuPc can also enhance the excited electron transfer and promote the rapid injection these electrons to TiO_2 layer resulting in the significant improvement of photocurrent of the device.

The second possible mechanism is the reduction of charge transfer resistances at the interface of the device. These resistances are correlated to the barrier height at the interface [110]. Referring to vacuum level, the electronic structure of the conduction band and valence bands of TiO_2 are 4.2 and 7.4 eV, respectively [111]. The lowest unoccupied molecular orbital (LUMO) and highest occupied molecular orbital (HOMO) levels of CuPc are at 3.5 and 5.2 eV, respectively [112]. The energy band diagram of the modified working electrode of the device is schematically drawn in Figure 4.17. With the existence of CuPc, the barrier height between TiO_2 and dye layer can be reduced and electron can move rapidly step-by-step to TiO_2. The faster the electron transport over the interface, the lower the charge resistance and, consequently a greater current density of the device can be attained.

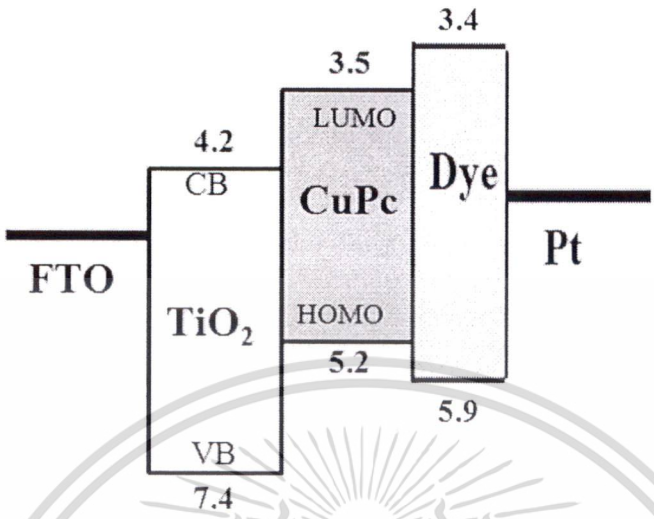

Figure 4.17 Schematic structure and energy band diagram for DSSC fabricated with TiO_2/CuPc hybrid nanocomposite.

Table 4.1 Photovoltaic parameters of DSSC devices DCM1, DCM2, DCM3, DCM4 at loading CuPc 0.05 wt.% comparing to reference device (TiO_2) using liquid electrolyte.

Sample	Open circuit voltage, V_{oc} (V)	Short Circuit current density, J_{sc} (mA/cm^2)	Fill Factor, FF	Energy conversion efficiency, η (%)
TiO_2	0.61	3.66	0.54	1.19
DCM1	0.58	4.02	0.46	1.07
DCM2	0.56	4.19	0.45	1.06
DCM3	0.57	4.20	0.41	1.03
DCM4	0.57	4.84	0.45	1.24

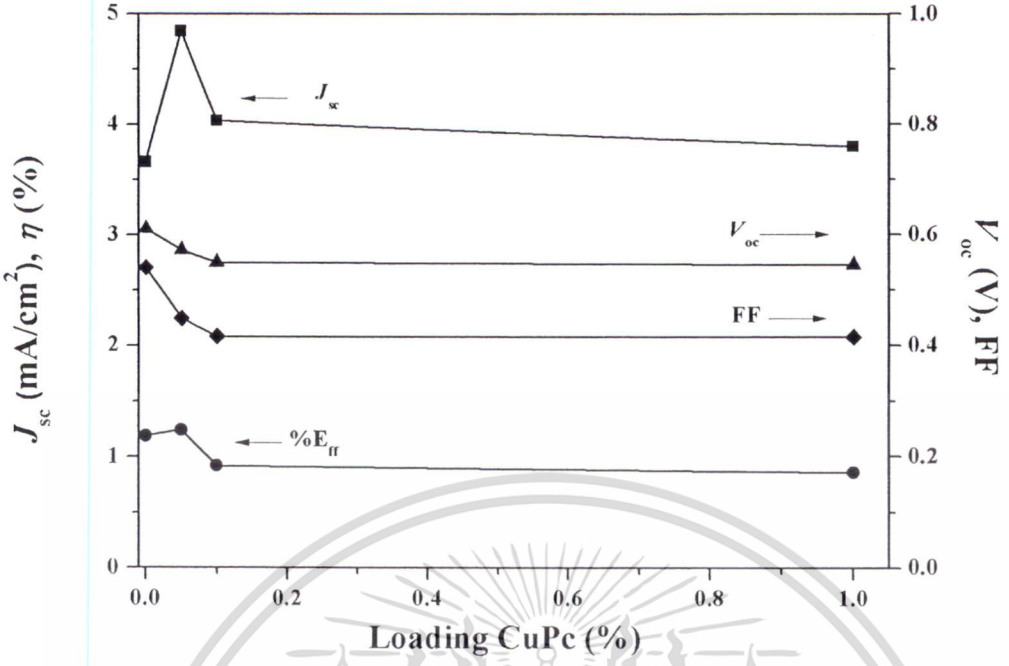

Figure 4.18 The photovoltaic parameters as a function of loading the amount of CuPc in the composite prepared by CM4.

The photovoltaic parameters of devices were summarized in Table 4.1. The maximum J_{sc} of 4.84 mA/cm^2 and η of 1.24% were obtained from the DCM4 whereas the current density of DCM1, DCM2 and DCM3 are 4.02, 4.19 and 4.20 mA/cm^2, respectively. The increase in current density of DCM4, comparing to pure TiO_2, is approximately 32%. In contrast, V_{oc} and FF values of all devices exhibit insignificant improvement. The effect of loading amount of CuPc on the device performance was also investigated. The results interpreted from the photovoltaic parameters as a function of CuPc amount were exhibited in Figure 4.18. The optimized ratio of CuPc in TiO_2 of 0.05% which give the maximum current density was obtained.

Figure 4.19 shows the relationship of the amount of absorbed dye and the amount of loading CuPc. The highest dye absorption of modified working electrode was received at loading 0.05 wt.% CuPc in TiO_2. The greater amount of dye molecules absorbed on TiO_2/CuPc modified working electrode may generate more free charge carriers resulting to the increase of short circuit current density and energy conversion efficiency. This result is coincidently agreeable to the results interpreted from the photovoltaic measurement. Further increase of loading CuPc in the

apparently decreases the photovoltaic parameters, especially in J_{sc}. This occurrence may attribute to the truth that the larger amount of CuPc molecules could reduce the dye absorption on TiO_2 and the interception of electron from the electrolyte.

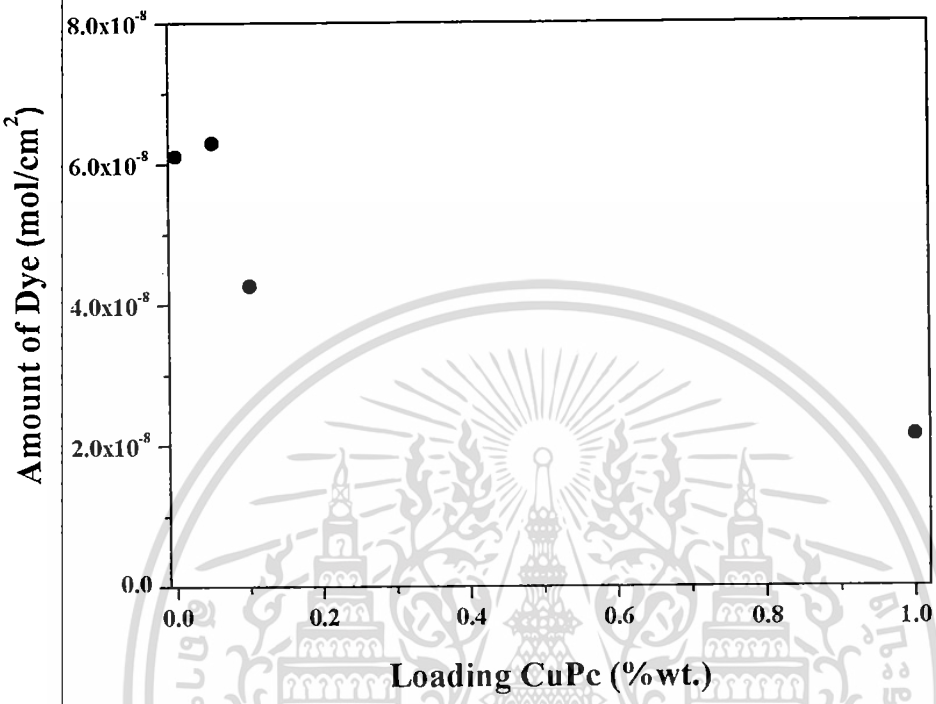

Figure 4.19 The amount of absorbed dyes on modified working electrode as a function of CuPc in the composite prepared by CM4.

In addition, one alternative for improving DSSC efficiency is the fabrication in quasi-DSSC with gel polymer electrolyte. Due to high ion conductivity and increased stability in thermal and mechanical properties, the photovoltaic parameters of DSSC were enhanced by using gel polymer electrolyte. The current density-voltage characteristics of quasi-DSSC are illustrated in Figure 4.20 and summarized in Table 4.2. The maximum energy conversion efficiency of 0.81% was obtained from the DCM4 whereas the energy conversion efficiency of DCM1, DCM2, DCM3 and TiO_2 are 0.68, 0.79, 0.79 and 0.61%, respectively. The improvement of V_{oc} and FF was achieved because of the elimination of dark current at the semiconductor electrolyte junction by *tert*-butylpyridine blocker at this interface [113]. Charge transfer in the device is enhanced by this mechanism. Meanwhile, the increase of J_{sc} in DSSC with TiO_2/CuPc working electrodes was obtained due to strong interaction of PEG polymer and TiO_2 nano-filler phase that enhanced ion conductivity in the electrolyte.

Table 4.2 Photovoltaic parameters of DSSC devices DCM1, DCM2, DCM3, DCM4 at loading CuPc 0.05 wt.% comparing to reference device (TiO_2) using gel polymer electrolyte.

Sample	Open circuit voltage, V_{oc} (V)	Short Circuit current density, J_{sc} (mA/cm^2)	Fill Factor, FF	Energy conversion efficiency, η (%)
TiO_2	0.63	4.02	0.24	0.61
DCM1	0.66	4.33	0.21	0.68
DCM2	0.66	4.67	0.26	0.79
DCM3	0.67	5.04	0.23	0.79
DCM4	0.66	4.91	0.25	0.81

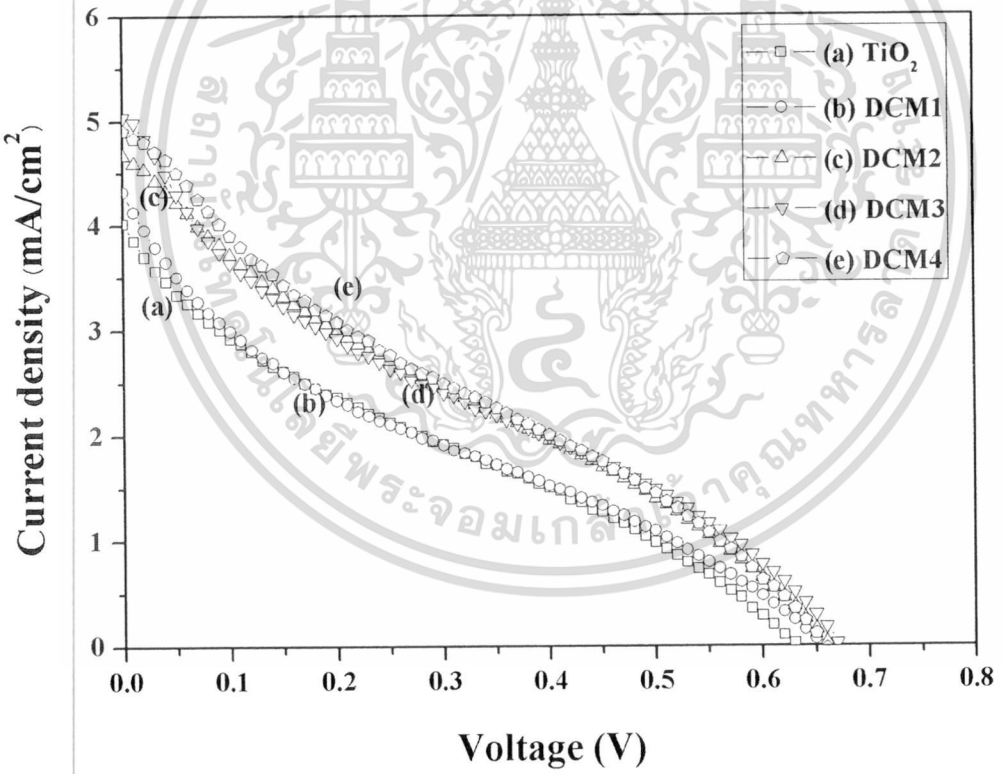

Figure 4.20 Photocurrent-voltage curves of DSSC device using gel electrolyte (a) TiO_2 P25, (b) DCM1, (c) DCM2, (d) DCM3 and (e) DCM4.

4.2.2 Application of TiO_2/CuPc Hybrid Nanocomposite in Dye Photocatalytic Degradation

4.2.2.1 The Photocatalytic Experiment

For proving the effective photocatalytic reaction of TiO_2/CuPc photocatalyst under UV irradiation, RhB degradation were carried out with the absence of photocatalyst and ball milled TiO_2 at various time as controlling condition in this section. RhB solution was dissolved in DI water appearing in bright pink solution. Figure 4.21 (a) and (b) show that RhB was rather stable phase at room temperature although UV illumination and the absence of light. The stable concentrations of pure RhB solution under light and dark conditions were observed as shown Figure 4.21 (c). These results suggest that the degradation of RhB is unable to initiate without the catalyst neither light nor dark conditions.

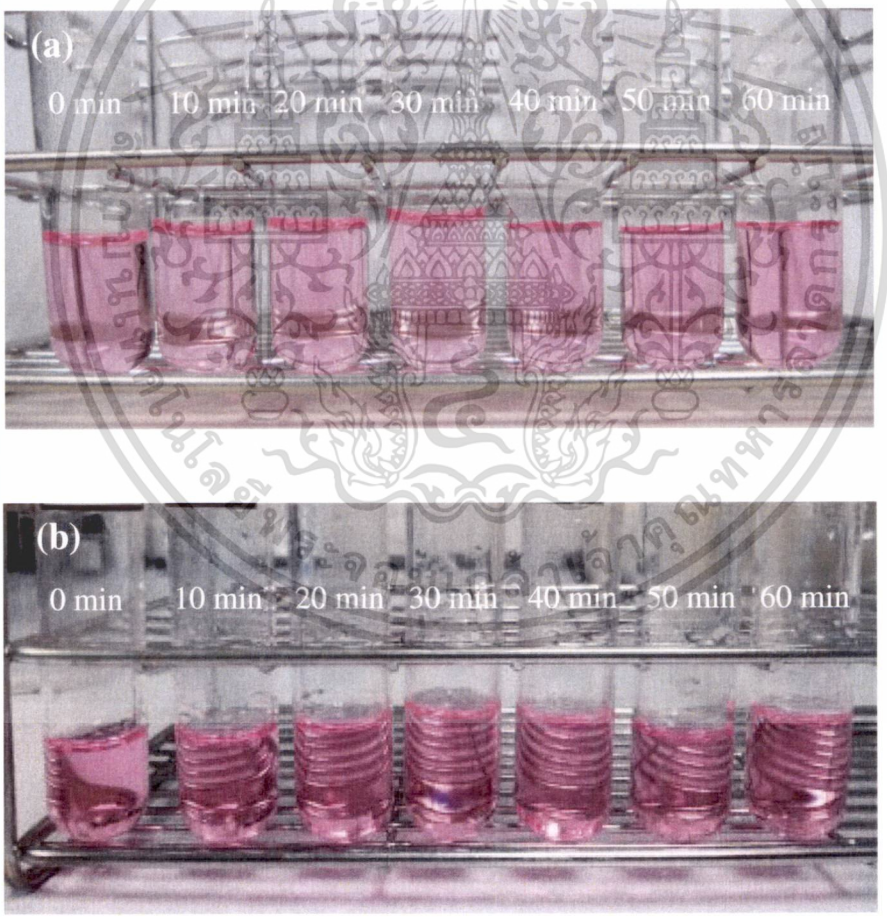

Figure 4.21 Photographs of pure RhB solution under (a) UV illumination and (b) dark condition and (c) the concentration of pure RhB solution under light and dark condition.

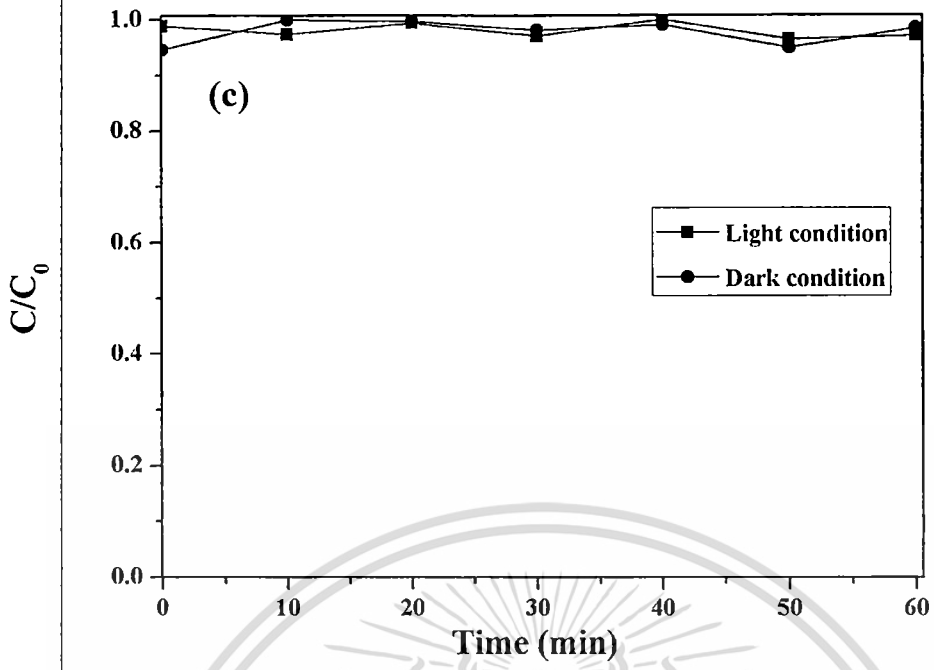

Figure 4.21 (cont.) Photographs of pure RhB solution under (a) UV illumination and (b) dark condition and (c) The concentration of pure RhB solution under light and dark condition.

In addition, other control RhB photodegradation experiment was also performed using ball-milled TiO_2 photocatalyst at various reaction time under dark and UV light conditions. For Figure 4.22(a), insignificant change in RhB concentration under the absence of UV light was monitored. This result indicates that dye degradation by TiO_2 catalyst was only performed under light illustration. Therefore, the decrease of dye concentration is attributed to the photocatalytic process shown as Figure 4.22(b). The effective RhB degradations were obtained by precursor TiO_2 and various milling time of TiO_2. The time period for the decolorization of RhB by ball-milled TiO_2 photocatalyst was faster than that of pure TiO_2 at the initial stage with reaction time less than 10 min. After that, their effeciencies ignorably changed with increasing milling time. In this case, it can be duduced that the increase of milling time insignificantly affect the photocatalytic degradation performance of pure TiO_2.

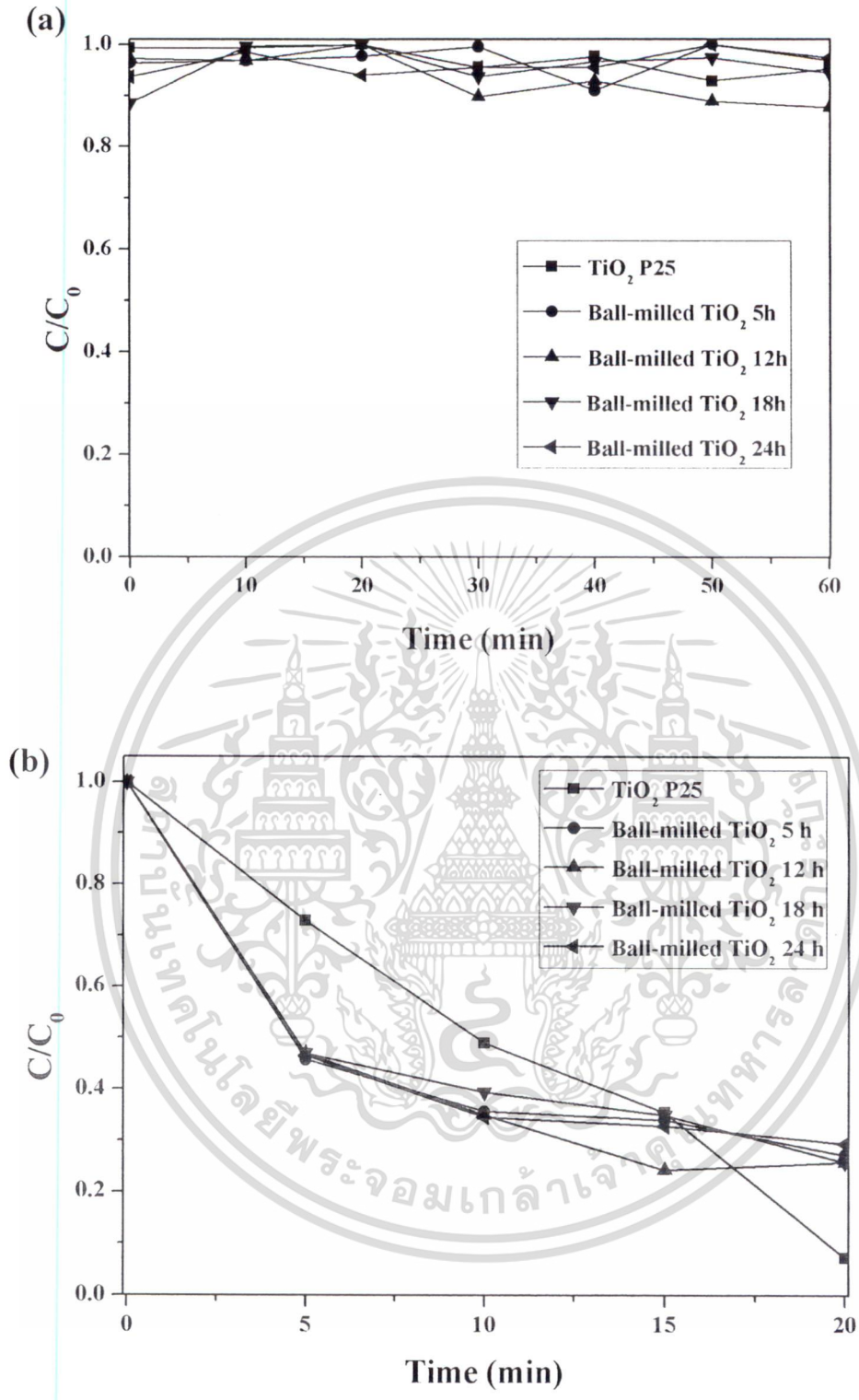

Figure 4.22 The normalized concentration of RhB versus reaction time in (a) dark and (b) UV light condition using TiO_2 P25 and ball milled TiO_2 P25 at 5, 12, 18 and 24 h.

4.2.2.2 Dye Degradation with TiO_2/CuPc Photocatalyst

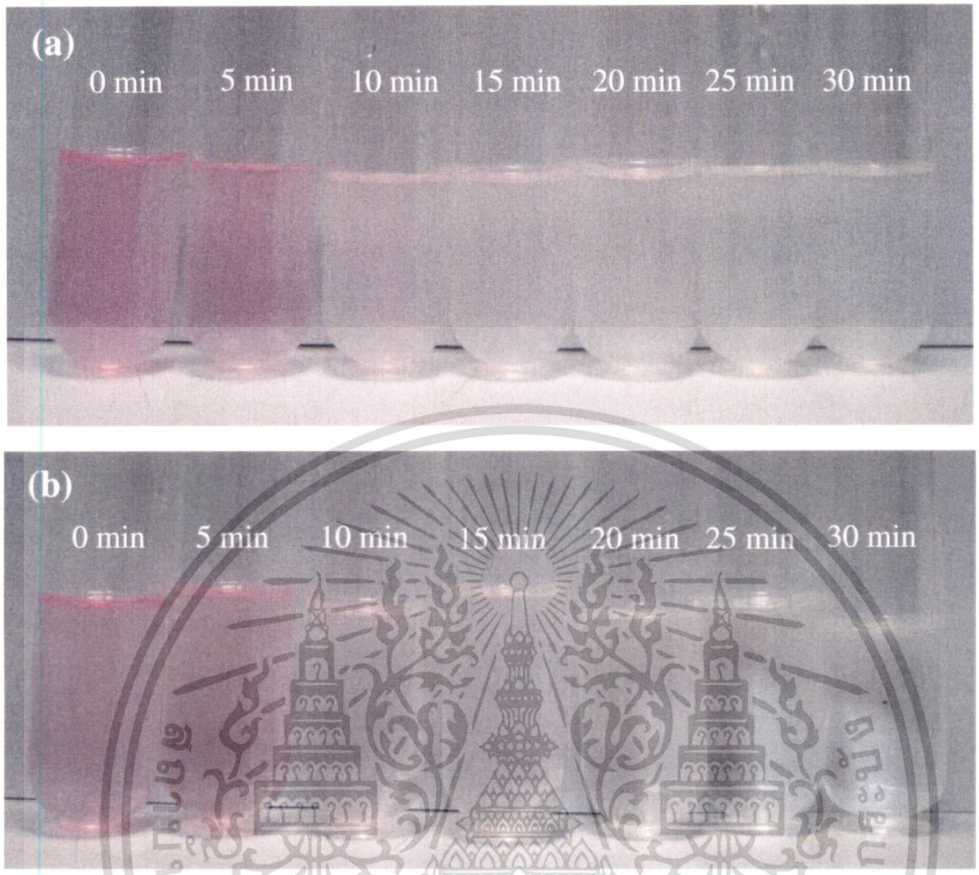

Figure 4.23 RhB solution photographs at various times using (a) pure TiO_2 and (b) 1 wt.% CuPc in TiO_2/CuPc nanocomposite.

The photocatalytic efficiency of pure TiO_2 and 1 wt.% TiO_2/CuPc nanocomposite was scrutinized by the photodegradation of aqueous RhB under UV illumination. Photographs of dye degradation at various irradiation times are shown in Figure 4.23(a) and (b), respectively. Decolorized RhB can be completed until 40 min by pure TiO_2 meanwhile the complete of reaction by TiO_2/CuPc nanocomposite can be achieved within 30 min. In order to confirm the dye degradation, the results in term of absorption spectra of RhB are illustrated in Figure 4.24(a) and (b), respectively. It is clearly observed that the photocatalytic activity of TiO_2/CuPc photocatalyst is more effective, accompanying the rapid decrease of the absorption spectrum after 10 min of reaction and complete degradation of RhB was attained within 25 min. The time period for the decolorization of RhB by TiO_2/CuPc

photocatalyst was approximately 10 min faster than that of pure TiO_2, implying that the photocatalytic activity was significantly enhanced by an assistance of CuPc loaded into TiO_2 photocatalyst.

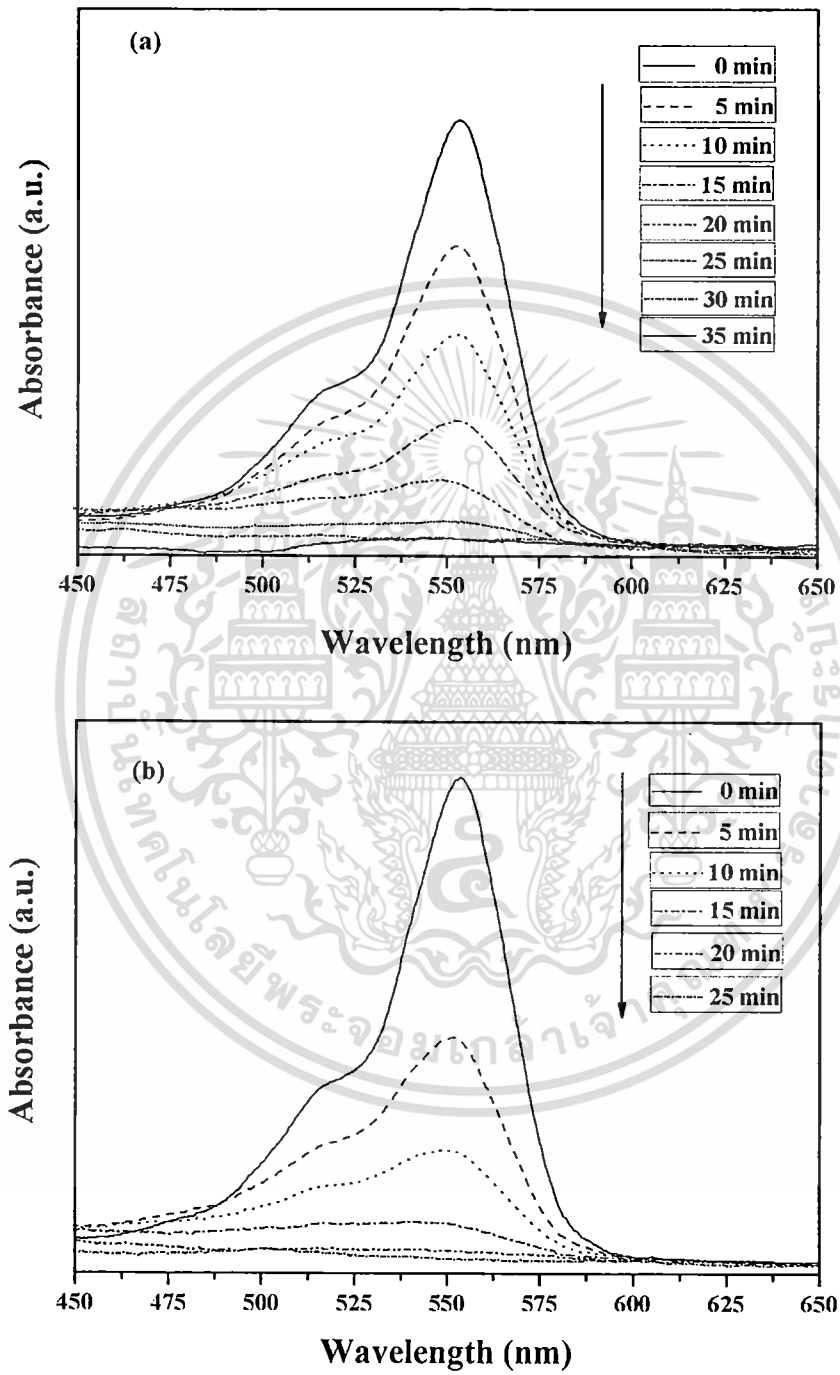

Figure 4.24 Absorption of RhB under UV light using (a) TiO_2 nanopowder (b) 1 wt.% CuPc in TiO_2/CuPc nanocomposite.

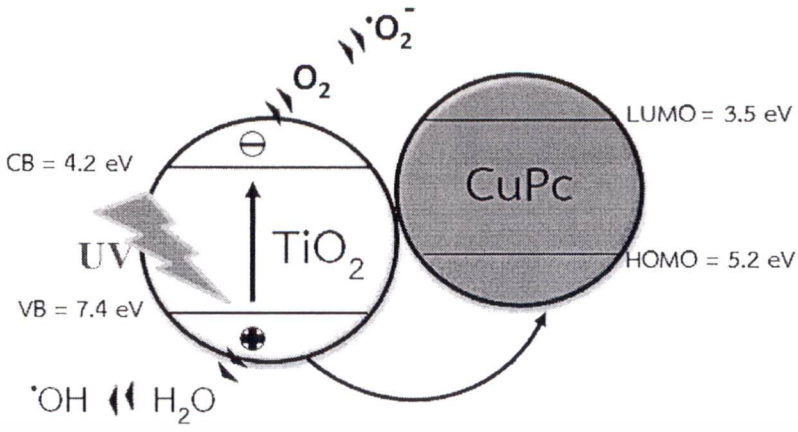

Figure 4.25 Possible processes involved in a photocatalytic process by TiO_2/CuPc nanocomposites.

In general, the hydroxyl and active oxygen groups from TiO_2 photocatalyst play an important role in photocatalytic reaction to decompose a structure of organic molecules. The continuous mechanism and the efficiency of photocatalytic reaction are enhanced by the increase amount of radical groups in the system. If the photogenerated electron - hole pairs are unoccupied by water molecule or oxygen in the air to produce the radical groups, the recombination of photogenerated electron-hole pair will occur in a few nanoseconds. The photocatalytic efficiency of pure TiO_2 is consequently diminished by this phenomenon. A key role of CuPc anticipated to the enhancement of photocatalytic performance of TiO_2 is suggested. The electronic structure of the conduction band and valence bands of TiO_2 are at –4.2 and –7.4 eV below vacuum level, respectively. Meanwhile, the lowest unoccupied molecular orbital (LUMO) and highest occupied molecular orbital (HOMO) levels of CuPc are at –3.5 and –5.2 eV below vacuum level, respectively, The HOMO level of CuPc is 2.2 eV higher than the valence band of TiO_2. When loading into TiO_2, CuPc may suitably perform as a hole capture, resulting to the effective transfer of hole form valence band of TiO_2 to HOMO of CuPc following Figure 4.25 and equation 4.1 [114]. This mechanism can potentially delay the recombination of photogenerated electron - hole pair, leading to the effective interface charge separation. Sequentially, unpaired electron of TiO_2 can react to oxygen group, leading to the continuity of higher photocatalytic reaction due to the decrease of e^- - hole pair recombination.

$$CuPc + TiO_2\left(e^- + h^+\right) \longrightarrow CuPc^+ + TiO_2\left(e^-\right) \quad (4.1)$$

In addition, the blue-shift in absorption peak of RhB during degradation process is investigated. The decrease of absorption intensity and the peak shift to high energy under UV illumination were caused by de-ethylation of RhB in a stepwise manner. The de-ethylation mechanism is occurred by the attacking of active oxygen species on N-ethyl group of RhB that cause the change of RhB structure [115]. The initial structure of RhB before the illumination is *N,N,N',N'*-tetraethylated rhodamine molecule at λ_{max} = 554 nm. After illumination, RhB structure is oxidized by oxygen species and changed to *N,N,N'*-triethylated rhodamine at 539 nm, *N,N'*-diethylated rhodamine at 522 nm and *N*-ethylated rhodamine at 510 nm [116].

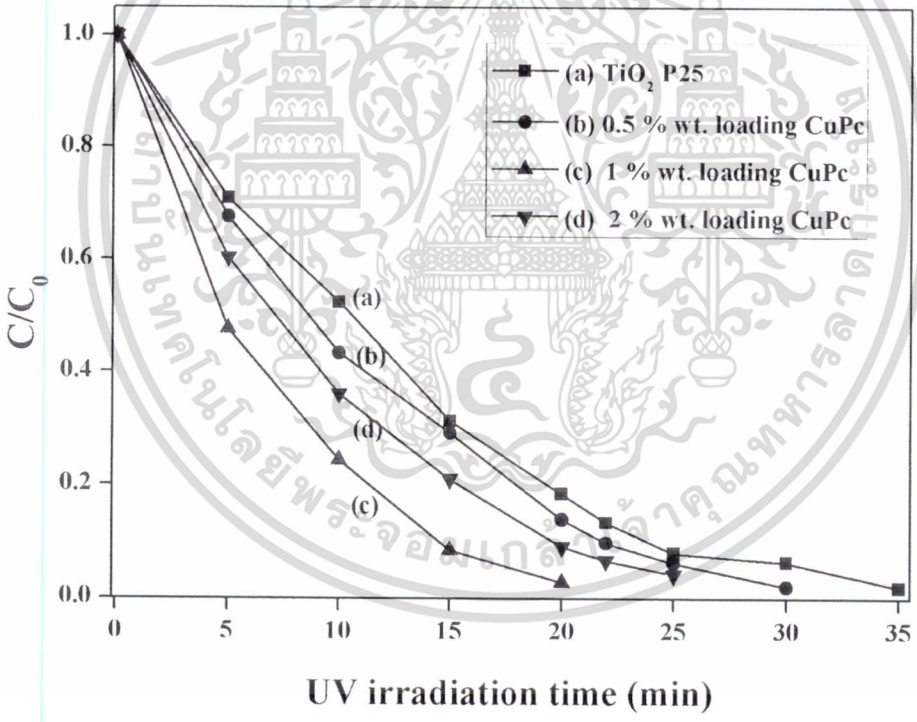

Figure 4.26 The normalized concentration of RhB versus reaction time under UV illumination using (a) TiO_2 P25 and (b) 0.5, (c) 1 and (d) 2 wt.% CuPc loading.

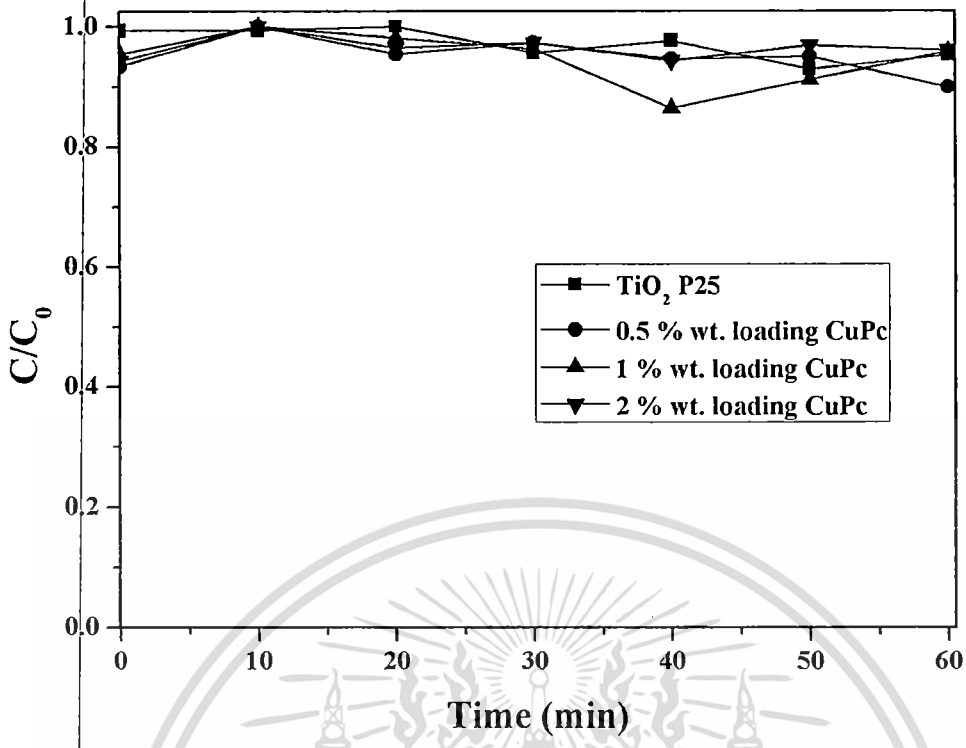

Figure 4.27 The normalized concentration of RhB versus reaction time in dark condition using TiO_2 P25 and 0.5, 1 and 2 wt.% CuPc loading.

The normalized RhB concentrations versus the illuminated time are shown in Figure 4.26. The complete decolorization of RhB by pure TiO_2 nanopowder was achieved after 35 min of reaction. Comparing to pure TiO_2, the degradations of RhB by TiO_2/CuPc nanocomposites obviously exhibit shorter reaction time and the composite with 1 wt%. CuPc loading performs much better activity than the others. At low loading amount of CuPc in the composite, the hole acceptor may be insufficient therefore the discontinued mechanism is occurred because of fast charge recombination. When loading amount rises to 1 %wt., an appropriate amount of CuPc can efficiently suppress the recombination of photo-generated charges and greater amount of functional groups responsible for the degradation reaction is sufficiently provided in the system. However, over CuPc loading (2%wt.) in nanocomposite may cause the aggregation and agglomeration of CuPc on TiO_2 surface that may act as a blocking layer of entrance light onto TiO_2 surface, resulting to the decrease of photogenerated charge in the system and the deterioration of photocatalytic reaction.

The controlled system in dark condition is illustrated in Figure 4.27. RhB concentrations remain unchanged, comparing to the initial concentration. This result

confirms that higher efficiency of TiO_2/CuPc photocatalyst can be effectively performed under UV illustration.

The reaction rates of photocatalytic degradation using different amount of CuPc at 0, 0.5, 1 and 2 %wt. in TiO_2 are shown in Figure 4.28. The greatest reaction rate of 0.15 min^{-1} was obtained by 1 %wt. TiO_2/CuPc nanocomposite. This reaction rate is approximately 87.5% greater than that of pure TiO_2. The increased reaction rate of TiO_2/CuPc photocatalyst reflects to the improved performance in photocatalytic degradation. Nevertheless, further increase of CuPc loading amount results to an insignificant increase of reaction rate. All results suggest that the existence of CuPc with certain loading amount can significantly ameliorate the photocatalytic performance of TiO_2.

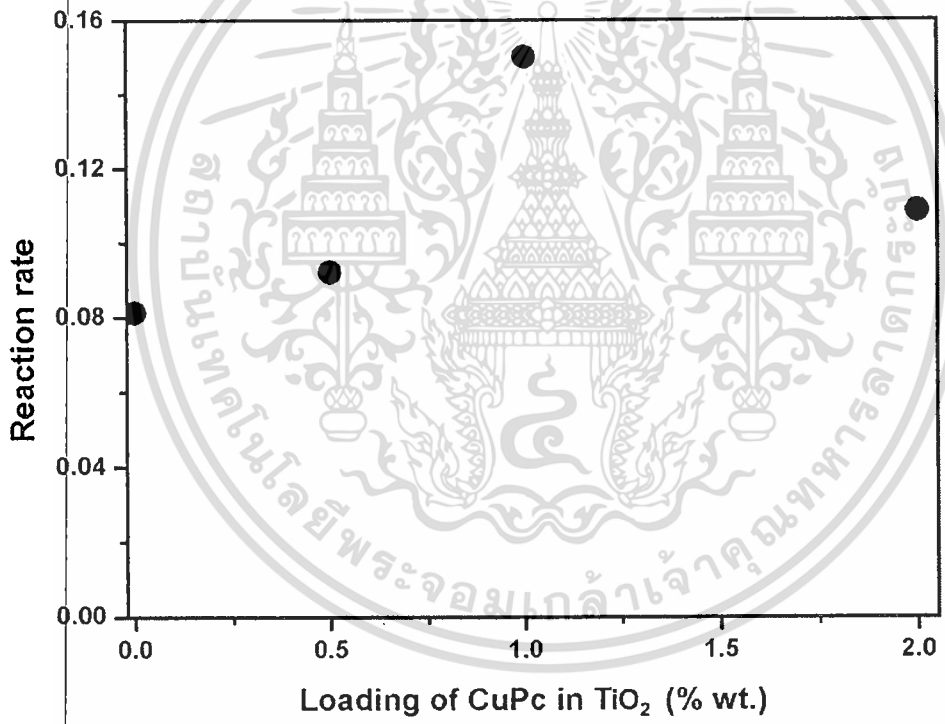

Figure 4.28 Reaction Rate of RhB photodegradation by different loading of CuPc in TiO_2.

CHAPTER 5
TiO_2/NiO INORGANIC/INORGANIC NANOCOMPOSITE

5.1 Characterizations of TiO_2/NiO Nanocomposite

5.1.1 Effect of Ball Milling Time in TiO_2/NiO Nanocomposite

The effect of ball-milling time on micro structure of TiO_2/NiO nanocomposite obtained by low energy ball milling process was investigated via SEM characterization. The morphologies of TiO_2/NiO nanocomposite prepared at various milling time from 5, 12 and 18 h are illustrated in Figure 5.1. SEM images reveal that the interconnected aggregates of TiO_2 matrix was clearly occurred by ball milling process with sol-gel assisted process. The morphologies of TiO_2/NiO nanocomposite are insignificantly changed with varied milling time but the corporation of TiO_2 and NiO can be enhanced by increase of milling time. Therefore Time milling condition of TiO_2/NiO nanocomposite was chosen as 18 h that is identical to milling condition of modified TiO_2/CuPc nanocomposite.

Figure 5.1 The morphologies of TiO_2/NiO nanocomposite prepared at various ball-milling times (a) 5h, (b) 12h and (c) 18h.

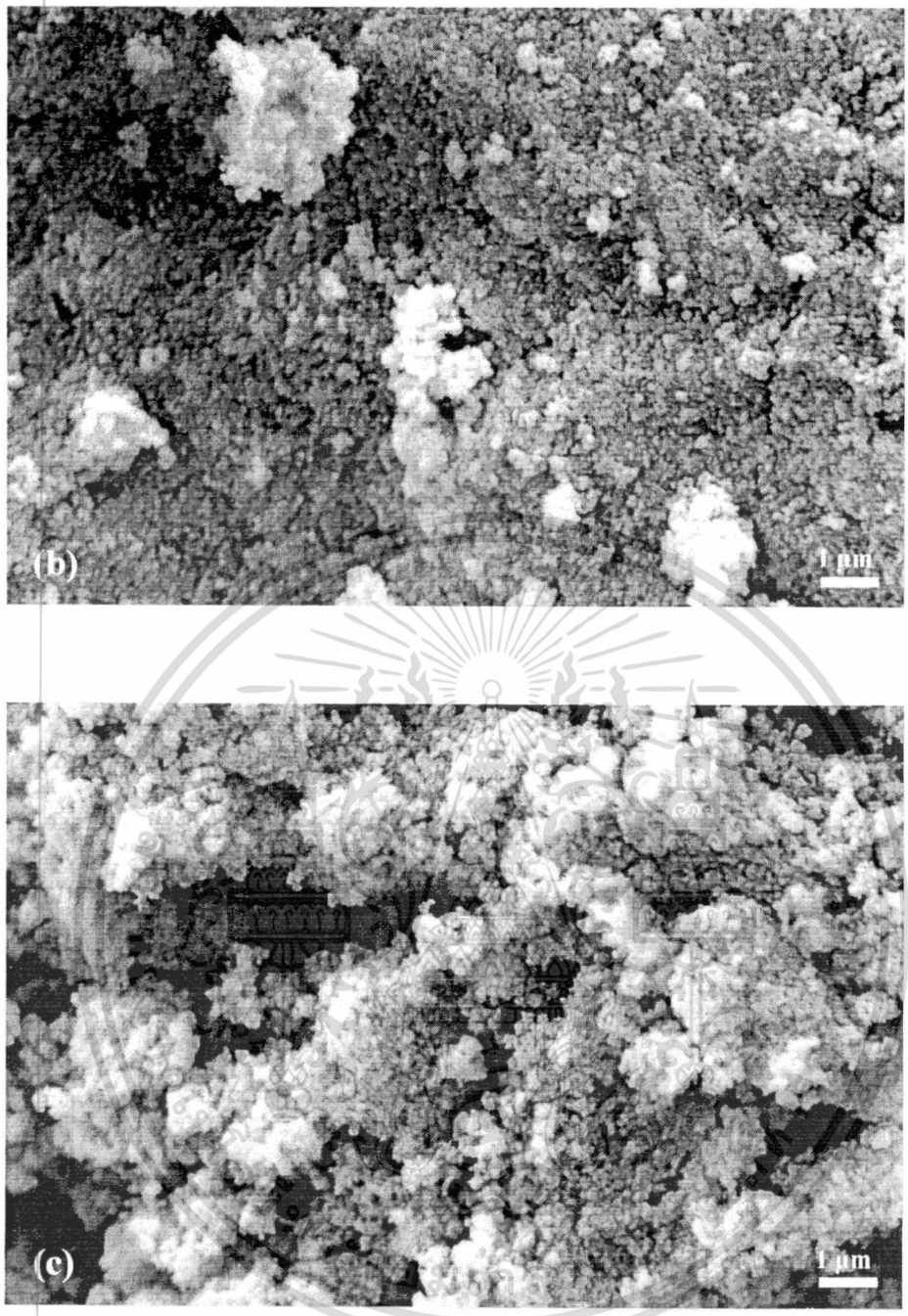

Figure 5.1 (cont.) The morphologies of TiO_2/NiO nanocomposite prepared at various ball-milling times (a) 5h, (b) 12h and (c) 18h.

5.1.2 Effect of Annealing Temperatures

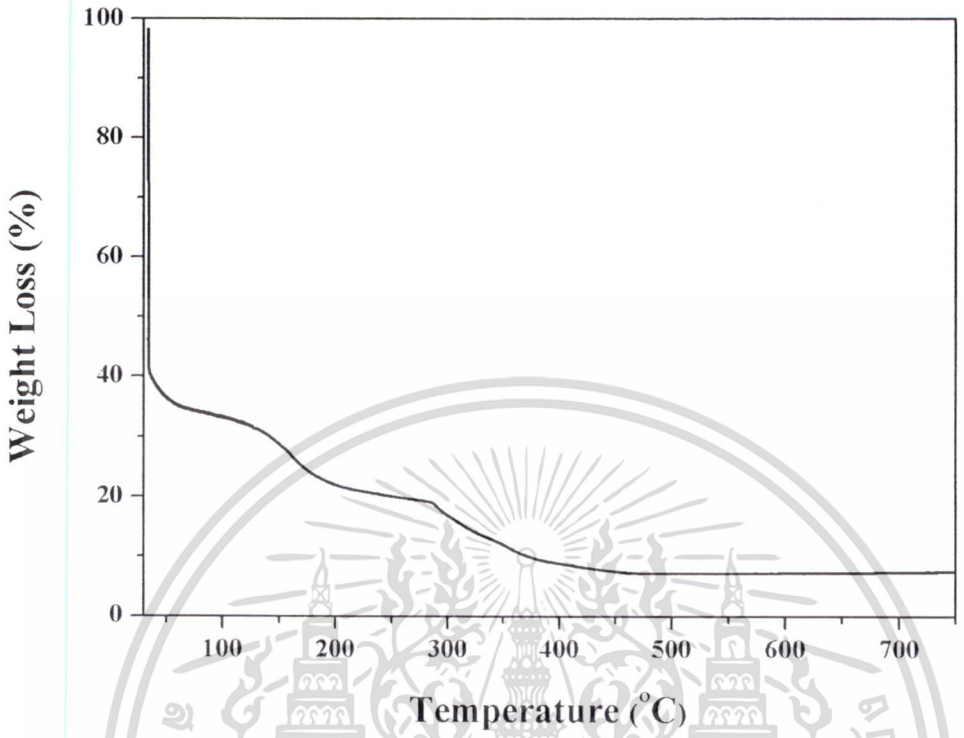

Figure 5.2 Weight loss versus temperature of nickel acetate precursor.

The appropriate annealing temperatures for TiO_2/NiO nanocomposites were determined by TGA analysis. The decomposition profile of nickel acetate tetrahydrate is shown in Figure 5.2. Weight loss in range of 50 to 150 °C typically corresponds to loss of water molecules. The last weight loss between 280 and 350 °C corresponds to the decomposition of organic compounds leading to the initial transformation of NiO. Therefore appropriate annealing temperature for the formation of NiO structure should be more than 350 °C.

The surface morphologies of TiO_2, ball-milled TiO_2/NiO nanocomposites at various annealing temperatures were monitored by SEM images. SEM images of TiO_2/NiO composites annealed at different temperature are illustrated in Figure 5.2 (a)-(c). These images indicate that the homogeneous dispersion of the composites was attained. As annealed temperature elevates, the crystallinity and size of TiO_2/NiO composite significantly improves resulted from the raising accumulation of TiO_2/NiO composites induced by increasing thermal energy.

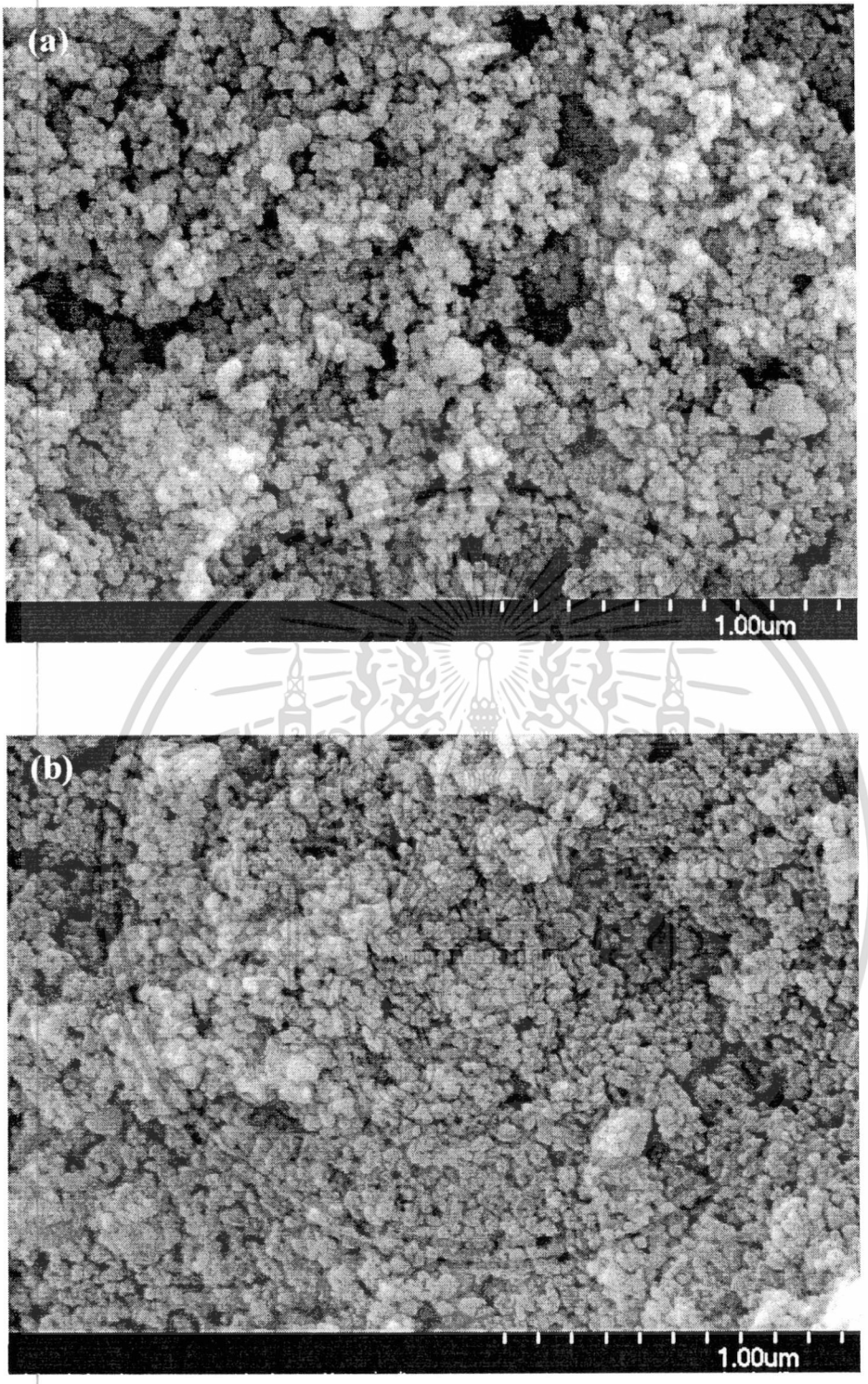

Figure 5.3 SEM images of TiO_2/NiO nanocomposite annealed at (a) 350 °C, (b) 450 °C and (c) 550 °C.

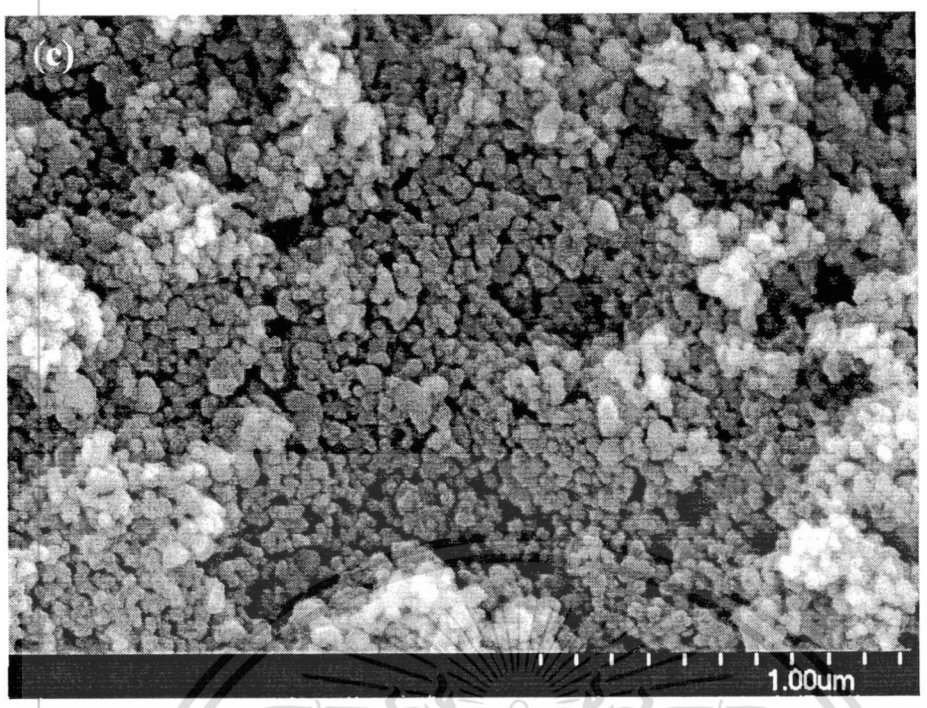

Figure 5.3 (cont.) SEM images of TiO_2/NiO nanocomposite annealed at (a) 350 °C, (b) 450 °C and (c) 550 °C.

The formation of NiO in TiO_2 nanocomposite is demonstrated by TEM image as shown in Figure 5.4. The surface of TiO_2 nanoparticle was thoroughly coated by thin NiO layer in light region with ~2 nm thick. This result confirmsthat NiO in the composite prepared by this technique was formed on TiO_2 surface, which is in good accordance with XRD results that show the indication of the presence of NiO peak.

The EDX spectrum and mapping of TiO_2/NiO nanocomposite at 2 %wt is illustrated in Figure 5.5. The peaks of Ti and Ni in EDX result confirms that TiO_2/NiO nanocomposite is composed of TiO_2 and NiO. Dots on mapping analysis show the major elements of Ti, O and Ni in the composite. This result affirms that the ratio of NiO is 2 %wt in the composite shown in Table 5.1.

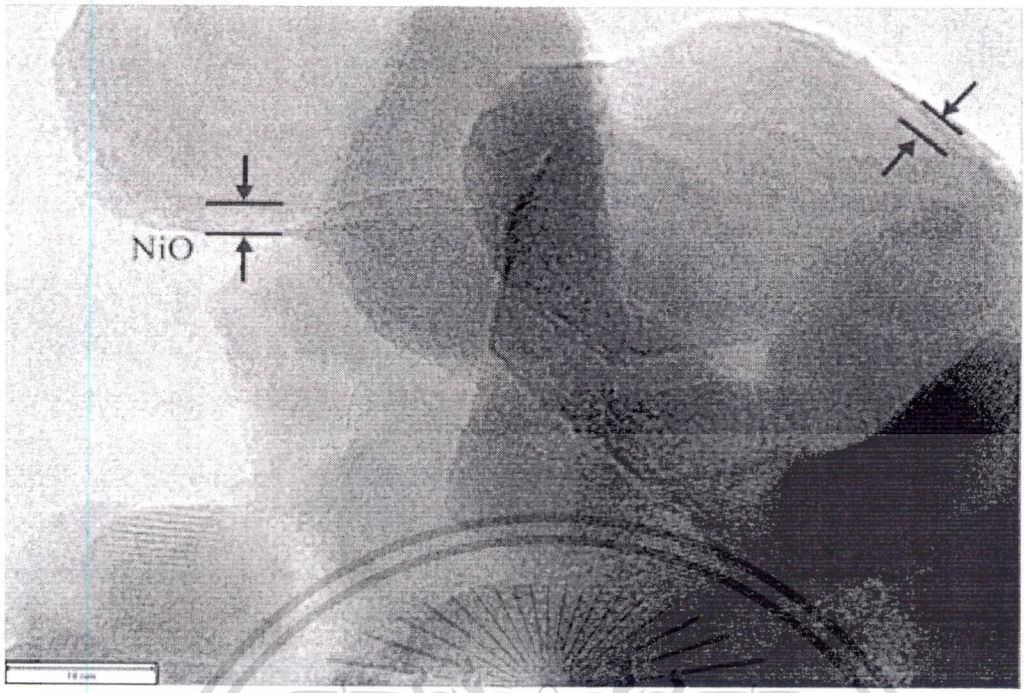

Figure 5.4 TEM image of TiO_2/NiO nanocomposite annealed at 550 °C.

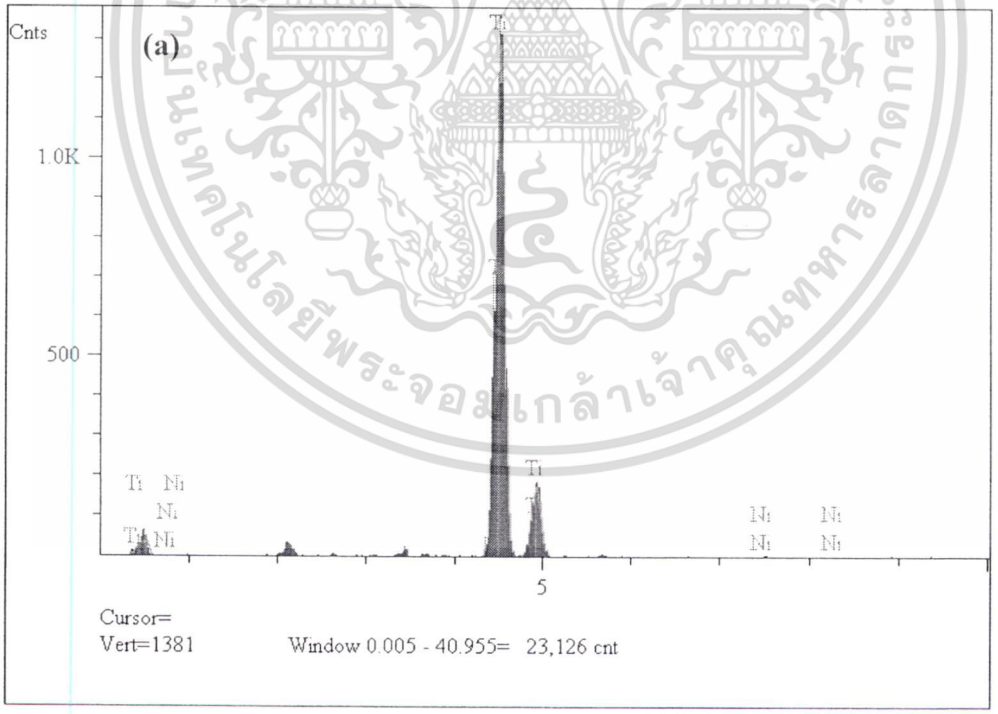

Figure 5.5 (a) The EDX spectrum and (b) mapping of 2 wt.% TiO_2/NiO nanocomposite annealed at 450 °C.

(b)

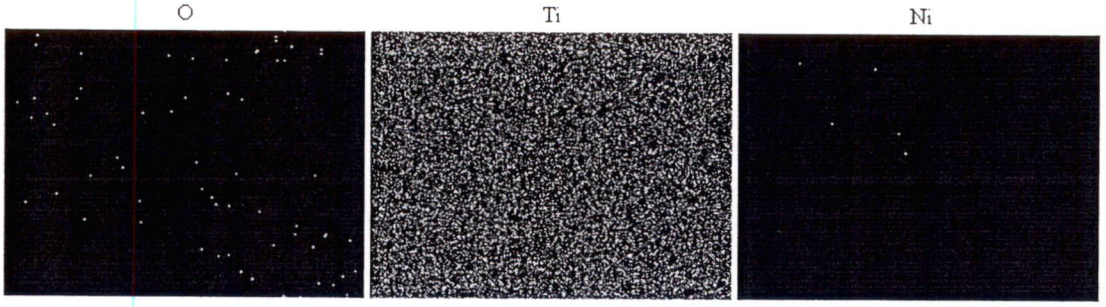

Figure 5.5 (cont.) (a) The EDX spectrum and (b) mapping of 2 wt.% TiO_2/NiO nanocomposite annealed at 450 °C.

Table 5.1 Mapping characterization of 2 wt.% TiO_2/NiO nanocomposite.

Element	Line	Intensity(c/s)	Weight (%wt.)
O	Kα	10.04	3.971
Ti	Kα	588.97	94.203
Ni	Kα	1.28	1.826
Total			100.000

5.1.3 XRD Characterization

The XRD patterns of pre-annealed and post-annealed TiO_2/NiO nanocomposites at 350 °C, 450 °C and 550 °C are illustrated in Figure 5.6. The XRD peaks situated at 2θ = 25.4°, 38.1°, 48.1°, 55.1° and 62.5°, correspond to (101), (004), (200), (211) and (204) planes of anatase phase of TiO_2 P-25, consecutively whereas rutile phase in (110), (101), (111), (211) and (220) plane is related to the peak at 2θ = 27.5°, 36.2°, 41.2°, 54.3° and 56.6°, respectively. The other three distinct diffraction peaks at 2θ = 37.2° and 62.8° are related to (111) and (220) orientation planes of cubic-NiO [117]. These three peaks were unobservable so far in XRD pattern of pre-annealed sample, indicating that the crystallization of NiO was not formed. After annealing, these characteristic peaks are clearly observed and their peak intensity exhibits the significant increase with increasing annealing temperature, implying the formation of crystalline of NiO on the TiO_2 matrix. Meanwhile, characteristic peaks

of TiO_2 also display noticeable stronger and narrower feature as the annealing temperature elevates. As temperature increases, the sufficient thermal energy is supplied to the system and the agglomeration of TiO_2 particles takes place resulting to the increase in crystallite size.

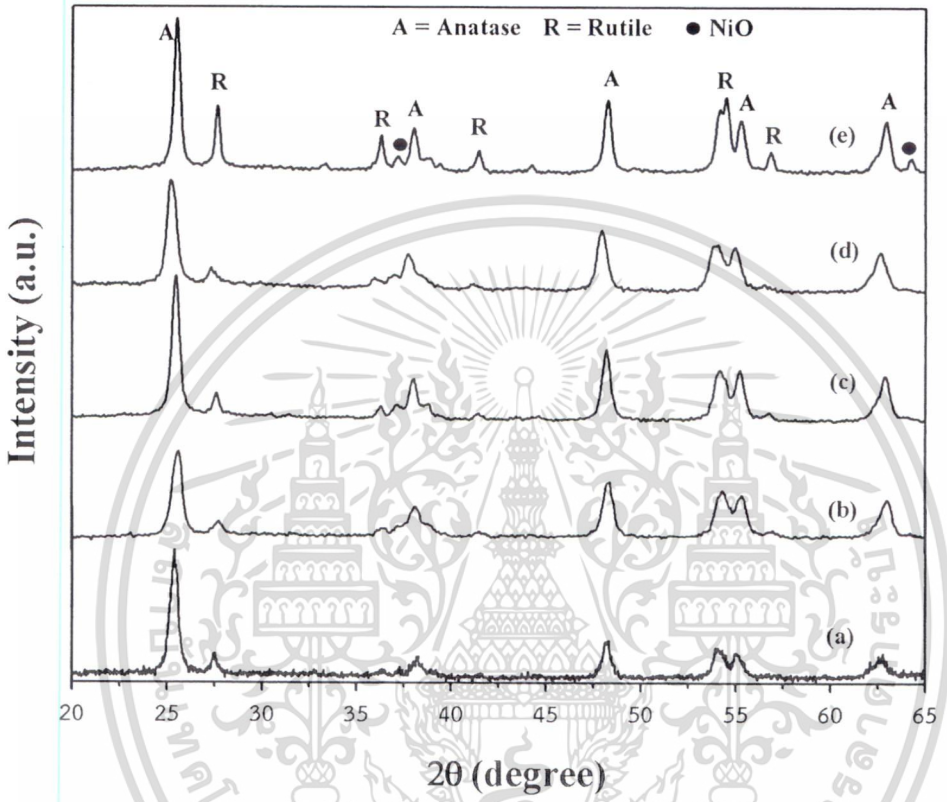

Figure 5.6 XRD pattern of (a) TiO_2 nanoparticles, (b) pre-annealed TiO_2/NiO nanocomposite, TiO_2/NiO nanocomposite annealed at (c) 350 °C, (d) 450 °C and (e) 550 °C.

5.1.4 Raman Characterization

Raman spectra of TiO_2 and TiO_2/NiO nanocomposite with different loading NiO at 450 °C are shown in Figure 5.7. For TiO_2 P25, Raman bands at 144, 197, 395, 515 and 683 cm^{-1} are indicated anatase phase which related to Raman-active mode with the symmetries of E_g, E_g, A_{1g}, B_{1g} and E_g, respectively. Whereas rutile phase in Raman band appears at 235 cm^{-1} are attributed to two-phonon scattering mode [118]. For TiO_2/NiO nanocomposites, Raman patterns are resembled to TiO_2 P25 pattern. This result suggests that loading NiO in the composite insignificantly effects in TiO_2

structure. However, the existence of NiO is confirmed by the detected Raman band in range of 1400-1500 cm^{-1} due to two-magnon (2M) scattering as shown in Figure 5.8 [119]. This peak can be readilydetected because of far location from the elastic scattering and the separation of phonon contributions [120]. In this experiment, NiO Raman peak can be detected at 2 %wt of loading NiO due to sufficient NiO content being detected in the composite.

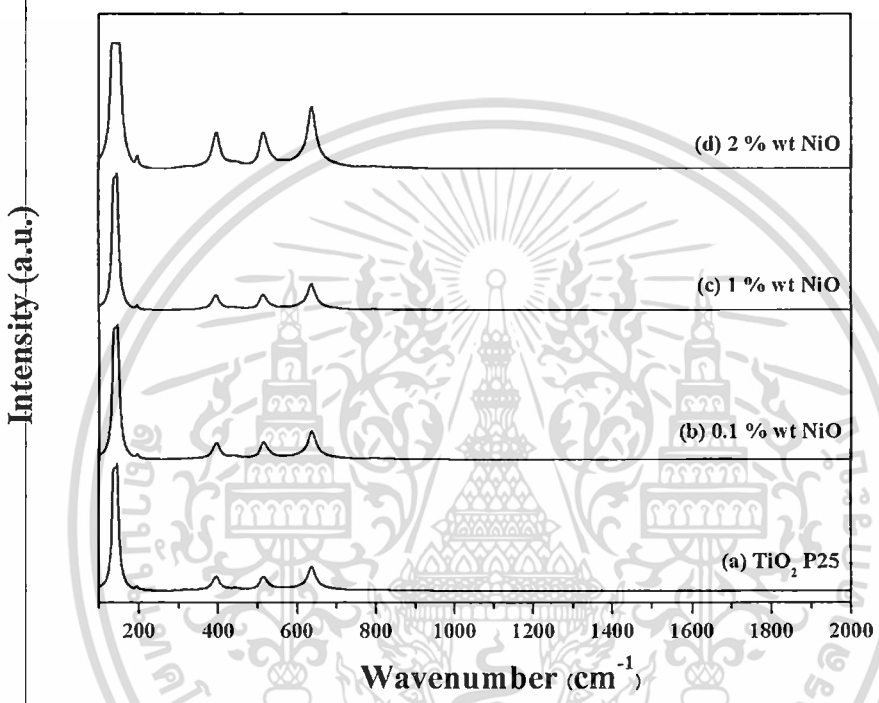

Figure 5.7 Raman spectra of (a) TiO_2 P25 and TiO_2/NiO nanocomposite with loading NiO of (b) 0.1, (c) 1 and (d) 2 wt.% and annealed at 450 °C.

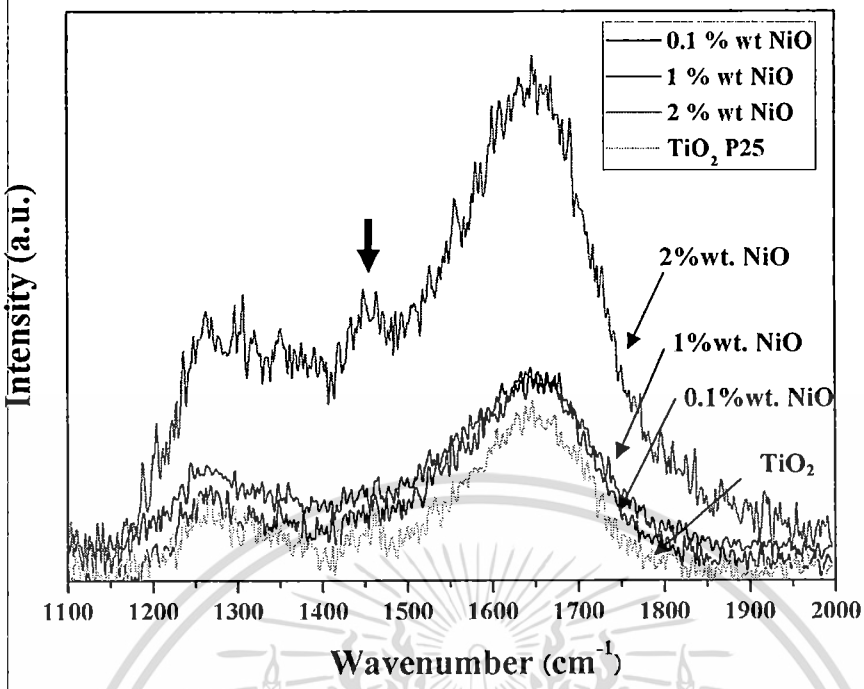

Figure 5.8 Raman band in range of 1100-2000 cm^{-1} of TiO_2 P25 and TiO_2/NiO nanocomposite with loading NiO of 0.1, 1 and 2 wt %.

5.1.5 XPS Results

XPS survey spectrum of TiO_2/NiO nanocomposite (2 wt. % NiO) is illustrated in Figure 5.9. The XPS pattern can informatively affirm the chemical bonding states of Ti 2*p*, O 1*s* and Ni 2*p* in the composite. The peaks at 458.7, 464.8 and 530.4 eV are attributable to binding energy of Ti $2p_{3/2}$, Ti $2p_{1/2}$ and O 1*s* determined as the characteristic of Ti^{4+} and O^{2-} as shown in Figure 5.10(a) and (b) [121]. This result confirms that TiO_2 P25 is still stable structure after loading NiO or even high temperature supplied to the system. Meanwhile, NiO was detected in the composite accompanying the peak at 856.1 eV as shown in Figure 5.10 (c). Because of low NiO loading ratio, small signal intensity of Ni was detected. Hence, it is difficult to determine exactly amount of NiO on the surface of TiO_2 matrix. However, the existing peak can highly indicateto the binding energy of Ni $2p_{3/2}$ corresponding to the occurrence of Ni^{2+} ion due tothe decomposition of nickel acetate tetrahydrate into NiO under annealing process at certain elevated temperature[122].

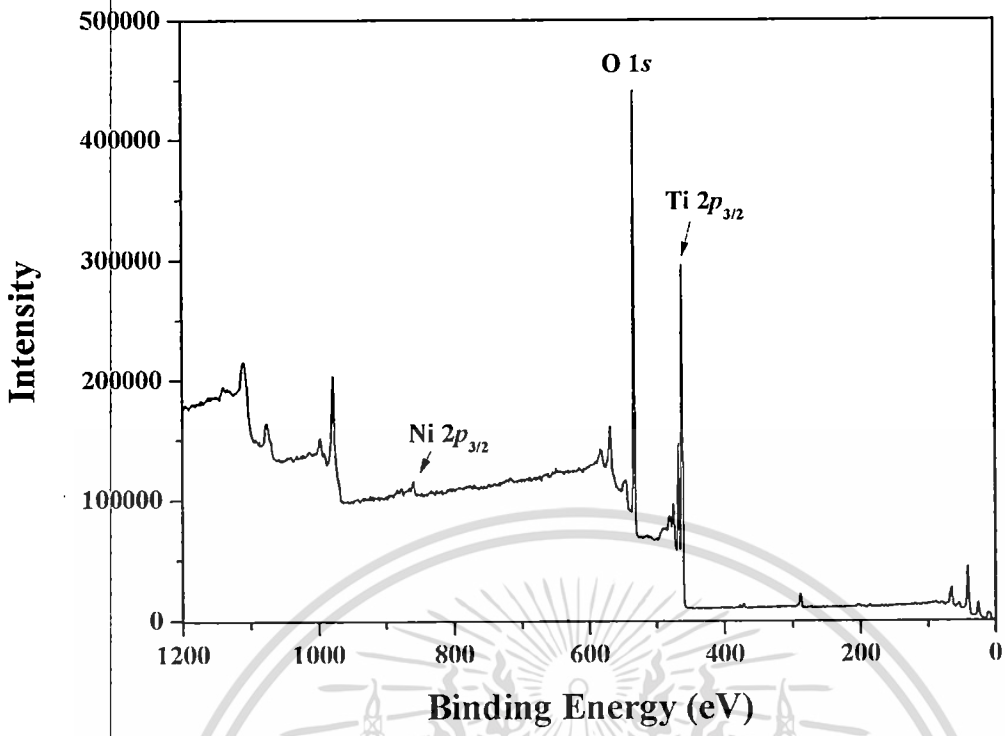

Figure 5.9 XPS survey spectrum of TiO_2/NiO nanocomposite (2 wt.% loading NiO).

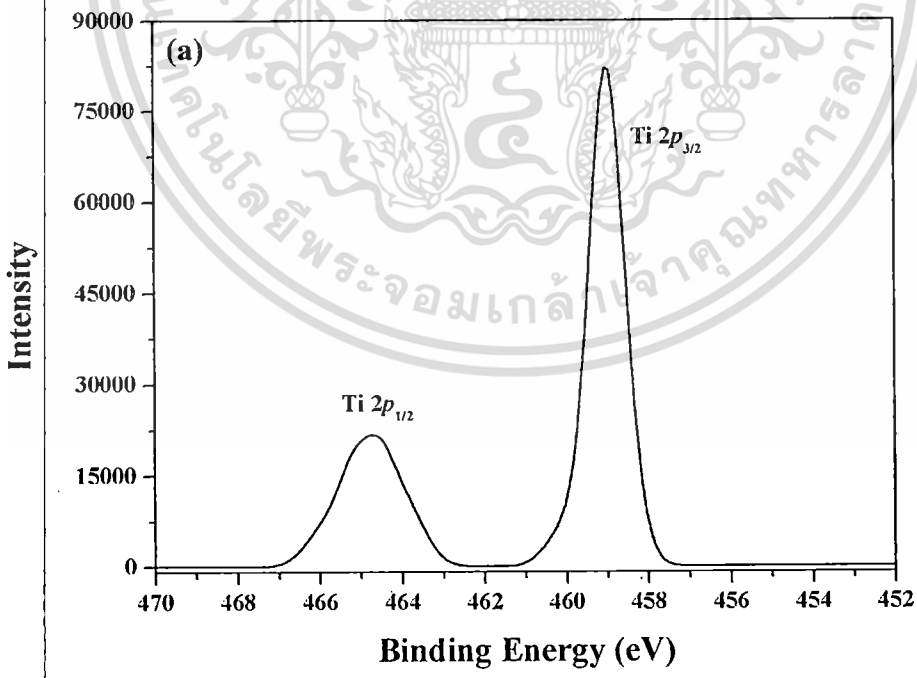

Figure 5.10 Higher resolution scanning XPS spectra of (a) Ti 2p, (b) O 1s and (c) Ni 2p in TiO_2/NiO nanocomposite (2 wt.% NiO loading).

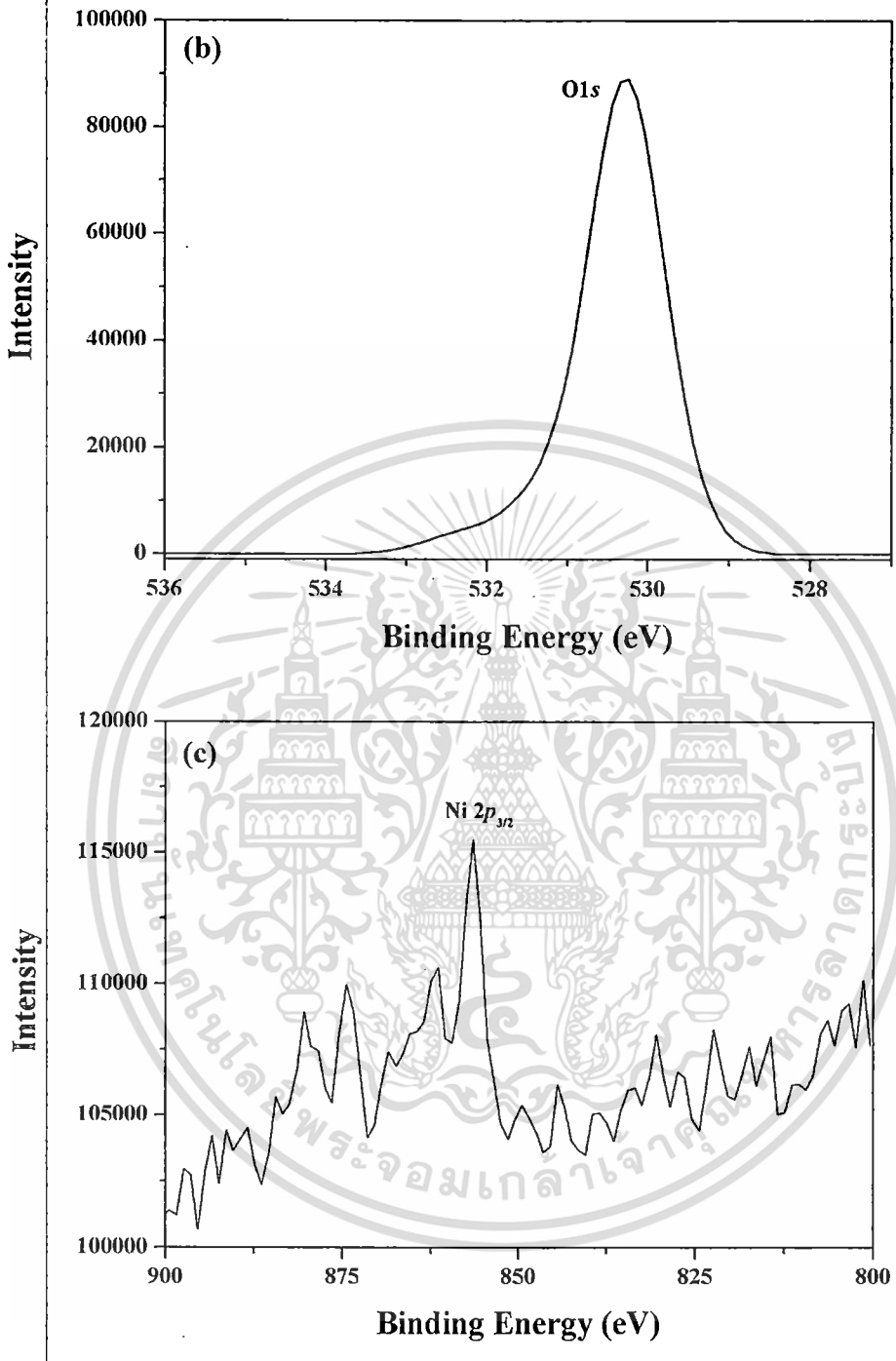

Figure 5.10 (cont.) Higher resolution scanning XPS spectra of (a) Ti 2p, (b) O 1s and (c) Ni 2p in TiO_2/NiO nanocomposite (2 wt.% NiO loading).

5.1.6 Absorption Spectra

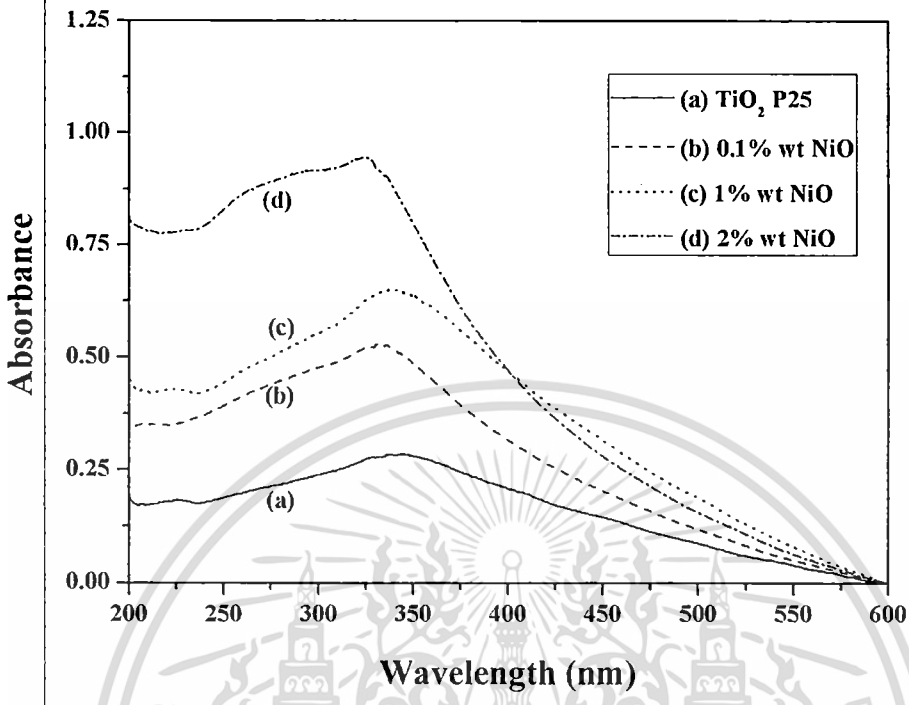

Figure 5.11 UV-vis absorption spectra of (a) TiO_2 P25 and NiO-loaded TiO_2 with loading at (b) 0.1, (c) 1 and 2 wt.% and annealed at 450 °C.

UV-vis absorption spectra of TiO_2 P25 and TiO_2/NiO nanocomposites with different NiO loading are shown in Figure 5.11. NiO-loaded TiO_2 absorbance in UV region is similar to pure TiO_2 and its absorption intensity is heightened by increasing loading amount of NiO. This enhancement maybe attributed to the intrinsic absorption of TiO_2 with some red shift originated from the size effect and the electronic excitation of the valence band O 2*p* electron to the conduction band Ti 3d level that is induced by NiO [123].

5.2 Application of TiO_2/NiO nanocomposite

5.2.1 The Utilization of TiO_2/NiO Nanocomposite on Modified Working Electrode in DSSC

The current density-voltage characteristics of modified TiO_2/NiO working electrode in DSSC using liquid electrolyte are illustrated in Figure 5.12 and summarized in Table 4.3. The maximum energy conversion efficiency was obtained from pure TiO_2 whereas the energy conversion efficiency of TiO_2/NiO at various temperatures in the device is lower than TiO_2. Therefore the improvement of DSSC with TiO_2/NiO working electrodes was further researched by gel polymer electrolyte substituted to conventional liquid electrolyte.

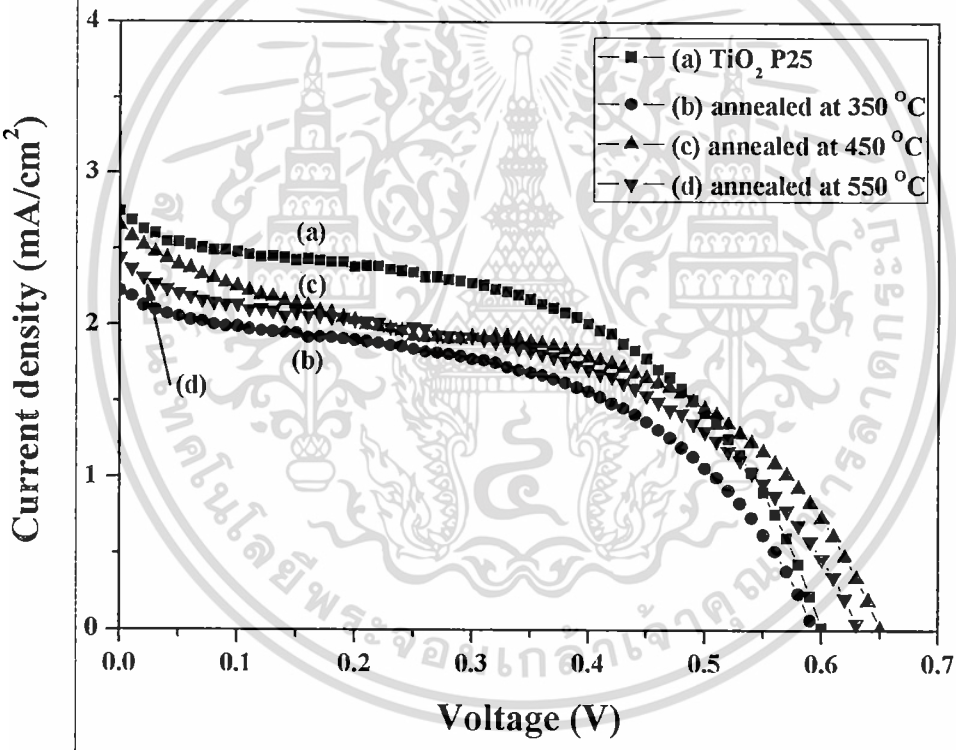

Figure 5.12 Photocurrent-voltage curves of DSSC device using liquid electrolyte on modified working electrode with (a) TiO_2 P25, TiO_2/NiO nanocomposites annealed at (b) 350, (c) 450 and (d) 550 °C.

Table 5.2 Photovoltaic parameters of DSSC devices A1, A2 and A3 at loading NiO 0.1 wt.% comparing to reference device (TiO_2) using liquid electrolyte.

Sample	Open circuit voltage, V_{oc} (V)	Short Circuit current density, J_{sc} (mA/cm^2)	Fill Factor, FF	Energy conversion efficiency, η(%)
TiO_2	0.69	2.75	0.49	0.82
A1	0.56	2.22	0.48	0.63
A2	0.66	2.65	0.44	0.79
A3	0.61	2.44	0.45	0.70

The assembly of DSSC device with TiO_2/NiO nanocomposite on modified working electrode using liquid electrolyte is shown in Figure 5.13. The characteristic current density vs. voltage (J-V) curves of the quasi-DSSCs with 0.1-wt.% of NiO in TiO_2/NiO nanocomposites annealed at various temperatures are shown in Figure 5.14. The modified working electrodes with TiO_2 P-25 and TiO_2/NiO nanocomposites annealed at 350 °C, 450 °C, and 550 °C were labeled as RD, D1, D2, and D3, respectively. D2 exhibits the most efficient performance, especially in terms of current density, compared to the others. The photovoltaic parameters of the devices are summarized in Table 5.3. The maximum J_{sc} of 7.21 mA/cm^2 with an η of 2.29% was obtained from D2, whereas the current densities of D1 and D3 were 6.51 and 7.10 mA/cm^2, respectively. The increasing current density of D2, compared to that of RD, is approximately 15%. In contrast, the V_{oc} and FF values of all the devices exhibited insignificant improvement

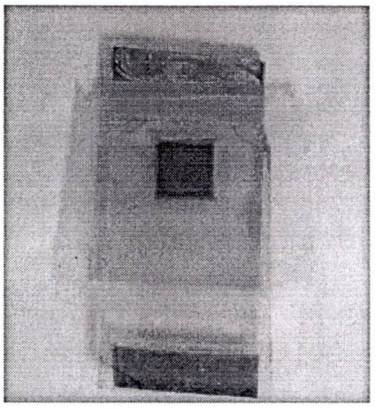

Figure 5.13 DSSC device with TiO_2/NiO nanocomposite on modified working electrode using gel electrolyte.

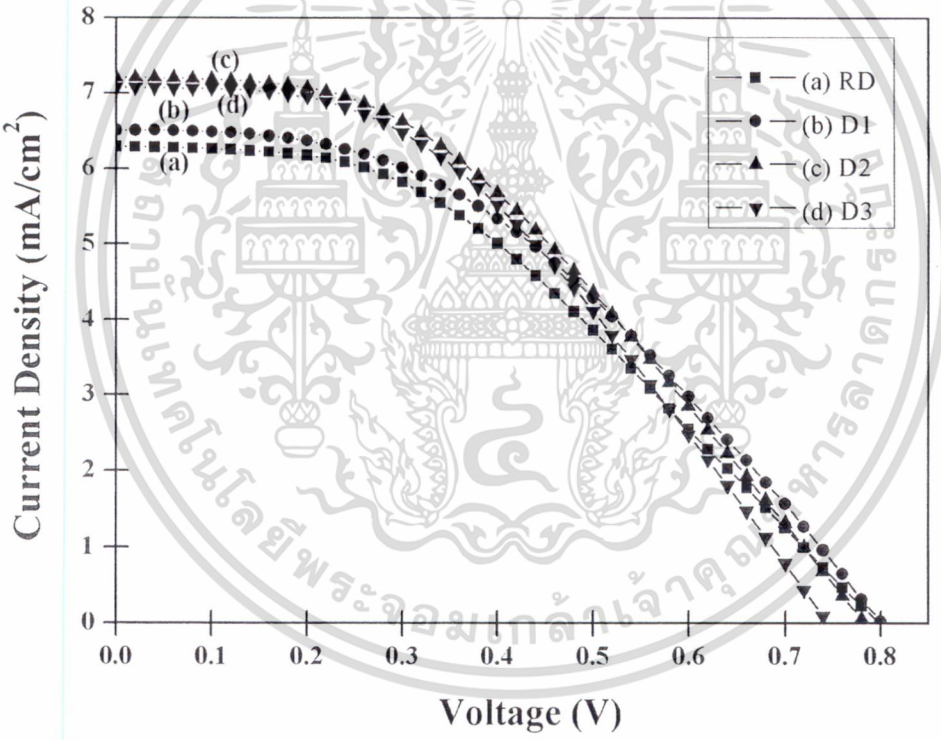

Figure 5.14 Photocurrent-voltage curves of quasi-DSSC with (a) TiO_2 P-25 and 0.1%wt TiO_2/NiO nanocomposite annealed at (b) 350 °C (D1), (c) 450 °C (D2) and (d) 550 °C (D3).

Table 5.3 Photovoltaic parameters of DSSC devices D1, D2 and D3 at 0.1 wt.% TiO_2/NiO nanocomposite annealed at different temperatures using gel electrolyte comparing to reference device (TiO_2).

Sample	Open circuit voltage, V_{oc} (V)	Short circuit current density, J_{sc} (mA/cm^2)	Fill factor (FF)	Energy conversion efficiency, η (%)
RD	0.80	6.29	0.40	2.02
D1	0.80	6.51	0.42	2.20
D2	0.78	7.21	0.41	2.29
D3	0.75	7.10	0.42	2.22

It can be deduced that the performance of the devices can be influenced by the presence of NiO in the composite, and by the annealing temperature of the as-prepared nanocomposites. The optimized conditions providing the best performance were obtained by the device prepared from the 0.1wt.% loading NiO annealed at 450°C. The possible mechanisms and key roles of NiO on the improvement of the device performance are proposed in 2 type; the action of NiO layer for electron barrier and forming of p-n junction for electron separation. With regard to the vacuum level, the conduction band (CB) and valence bands of TiO_2 were found to be 4.2 and 7.4 eV, respectively; those of NiO were 1.8 and 5.4 eV; and those of the dye were 3.4 and 5.9 eV, respectively [124-125]. Energy band diagram schematic of TiO_2/NiO nanocomposites and dye is shown in Figure 5.15. Due to the higher CB of NiO compared to both TiO_2 and the dye-excited state, the NiO shell layer can act as an electron-blocking layer that can retard the recombination of the injected electrons [126].

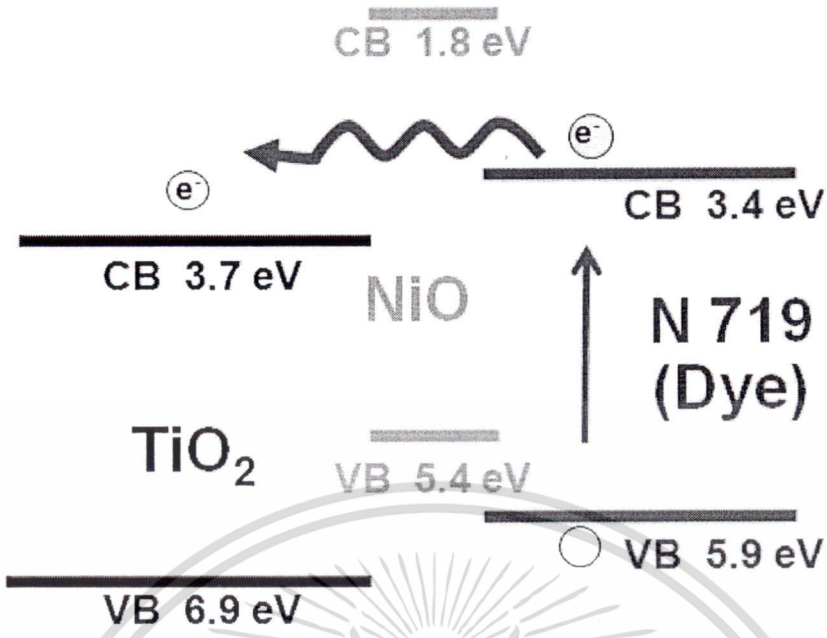

Figure 5.15 Schematic structure and energy band diagram for DSSC fabricated with TiO_2/NiO nanocomposite.

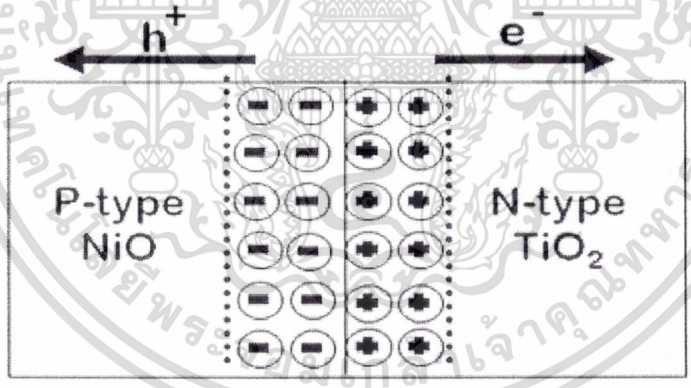

Figure 5.16 Schematic of p-n junction in TiO_2/NiO nanocomposite.

Meanwhile, p-type NiO can act as a hole collector. The possible formation of the p-n junction as illustrated in Figure 5.16 can be formed at NiO/TiO_2 interface, resulting in a potential gradient that can enhance the charge separation [127]. The efficiency of the device can therefore be enhanced by the blocking effect of the NiO layer associated with the possibility of p-n junction formation at the interface.

During illumination, the photoexcited electrons from the dye-excited state probably encounter difficulty in overcoming the potential barrier formed by NiO

[128]. These electrons, however, can penetrate the layer through the tunneling effect, which strongly depends on the width of the adjacent NiO barrier. According to the XRD and SEM results, the crystallite size of NiO increased when the composite was annealed at higher temperatures, resulting in the wideness of the potential barrier formed by NiO. When the NiO shell thickness exceeded the tunneling thickness (~2 nm), the electron injection into TiO_2 was blocked. Therefore, the broadened width of the NiO barrier causes a decrease in the tunneled electrons, reflecting lower device performance. At a low annealed temperature (350°C), the crystallinity of NiO still becomes weaker because the formation of NiO initially occurs from the precursor material at this temperature [129]. When the annealing temperature rises to 450°C, the system can obtain adequate energy, leading to the strong nucleation of the NiO-shell layer, and better crystallinity. Further heating from this temperature can further increase the NiO layer thickness, resulting in the deterioration not only of the photogenerated current through the NiO barrier but also of the device performance. Therefore, the optimized annealing temperature is essential for the formation of an appropriate NiO barrier in the composite, leading to the enhancement of the device efficiency.

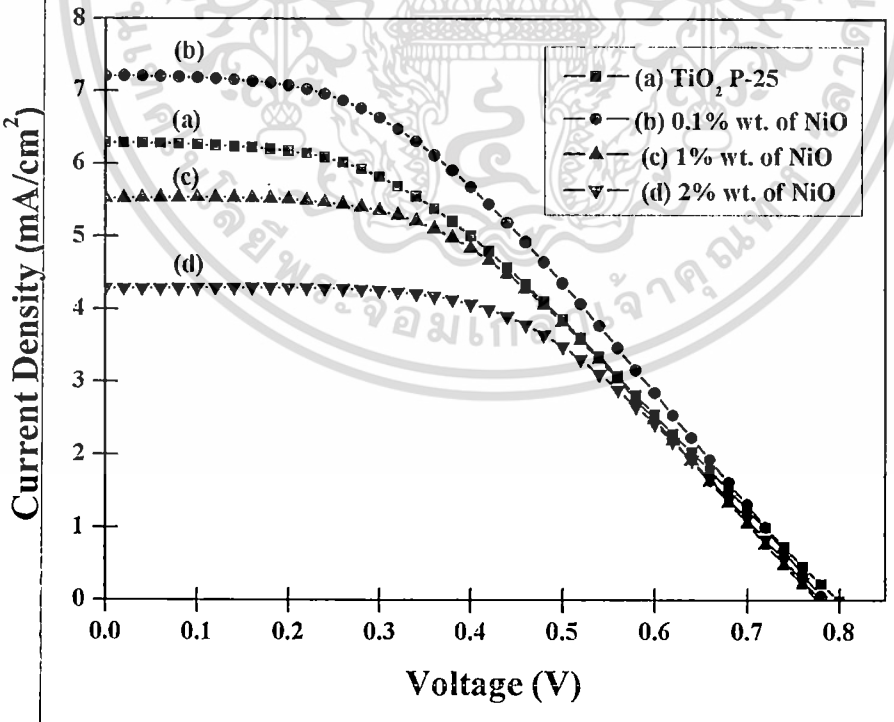

Figure 5.17 Photocurrent-voltage curves of quasi-DSSC with (a) TiO2 P-25 and (b) 0.1-, (c) 1-, and (d) 2-wt% TiO_2/NiO nanocomposite annealing at 450 °C.

The effect of the loading amount of NiO on the device performance was also investigated, as shown in Figure 5.17 and 5.18. The optimized ratio of 0.1-wt.% NiO in TiO_2 exhibited the maximum J_{sc} of 7.21 mA/cm^2. After reaching this value, the J_{sc} and η significantly decreased with an increasing loading amount of NiO in the composite, as shown in Figure 5.17. Possible mechanisms of this phenomenon are suggested herein. With the presence of a NiO blocking layer, the recombination of the injection electrons is suppressed, causing greater electron accumulation near the interface. The increasing charge population at the interface with increasing NiO loading amount will result in a rise in the quasi-Fermi level of TiO_2, and consequently to the higher V_{oc} of the device. The greater amount of NiO loaded into the composite may also lead to the agglomeration of NiO crystalline and the wideness of the NiO barrier, resulting in a lower transport rate of the tunneled electrons. NiO can also play a negative role beyond determining the tunneling distance if it becomes overabundant in the composites [130].

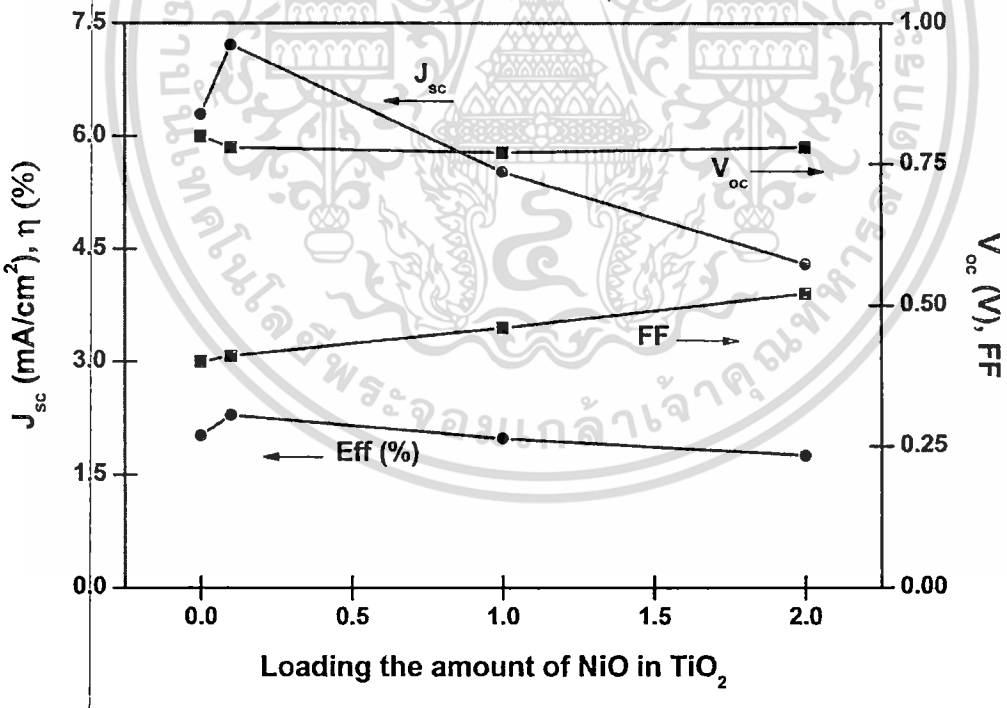

Figure 5.18 Photovoltaic parameters of quasi-DSSC fabricated with different loading of TiO_2/NiO nanocomposites annealed at 450 °C.

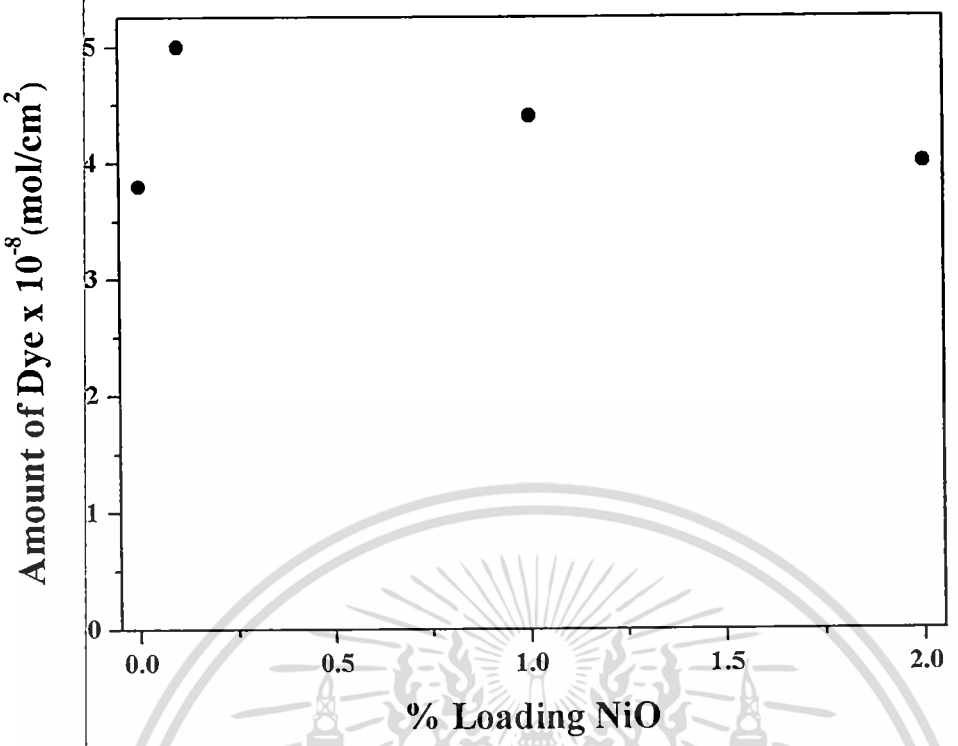

Figure 5.19 The photovoltaic parameters as a function of loading the amount of NiO in the composite.

Figure 5.19 shows the relationship of the amount of absorbed dye and the amount of loading NiO. The highest dye absorption of modified working electrode was received at loading 0.1 wt.% NiO in TiO_2. Amount of dye molecules may be extremely absorbed on TiO_2/NiO modified working electrode due to increasing surface area in the composite according to research of T.sreethawong and co-worker [131]. More free charge carriers are generated resulting to the increase of short circuit current density and energy conversion efficiency. This result is coincidently agreeable to the results interpreted from the photovoltaic measurement. Further increase of loading NiO in the composite apparently decreases the photovoltaic parameters, especially in J_{sc}. This occurrence may attribute to the truth that the larger layer of NiO could reduce surface area and dye absorption on TiO_2 and the interception of electron from the electrolyte.

CHAPTER 6
CONCLUSIONS

In summary, TiO_2 in form of organic-inorganic and inorganic-inorganic nanocomposites were successfully prepared by low-energy ball milling route as a main part of the processing, without any binders or high temperature heat treatment. Uniform dispersion, good formation and excellent adherence of loading materials (CuPc and NiO) in the composite were enhanced via assisted-ball milling process corresponding to SEM and TEM results.

For TiO_2/CuPc hybrid nanocomposite, the optimized condition to obtain good formation of the composite was received by ball milling assisted process and homogenization through method CM4 at milling time 18 h. SEM images reveal that ball milling process can evidently reduce CuPc size and assist the formation of well-dispersed composite. XRD results suggest that TiO_2 structures are not affected by CuPc loading in the composite meanwhile Raman and XANES results reveal the presence of CuPc in the composite and insignificant changing TiO_2 matrix structure. The optical absorption properties of TiO_2 is improved by the existence of CuPc due to strong absorption manner of CuPc in UV and visible region.

TiO_2/CuPc composites were utilized as modified working electrode material in DSSC and photocatalyst in dye degradation under UV illumination. For the application in DSSC, the device DCM4 at 0.05 wt.% CuPc loading in the composite granted the highest improvement in the current density and the greatest amount of absorbed dye molecules on TiO_2. The maximum J_{sc} and η of 4.84 mA/cm^2 and 1.24%, respectively were obtained at this condition. The enhancement of current density was occurred by TiO_2/CuPc modified working electrode due to the decrease of recombination of photo-injected electrons and reduction of charge transfer resistances at the interface of the device. These mechanisms can increase the rapid injection electrons to TiO_2 layer and play key roles on the enhancement of current density. However, increasing amount of CuPc in TiO_2 causes the deterioration of device performance since the dye absorption on TiO_2 and the interception of electron from the electrolyte could be obstructed by CuPc covered on TiO_2 surface. For TiO_2/CuPc photocatalyst utilization in RhB degardation, excellent efficiency of the photocatalyst can be activated under UV light condition. In absent of light, RhB concentration was

constant resulting from the suppression of catalyst performance. Specific loading content of 1 wt.% CuPc can efficiently heighten the catalytic performance of TiO_2 upto 87.5 %, greater than bare TiO_2 in the photodegradation of aqueous RhB. This feature could be explained by the major contribution of CuPc on the increase in charge separation of photogenerated electron-hole pair of TiO_2 and free functional radicals participated in degradation process.

For TiO_2/NiO nanocomposites, XRD results suggested that NiO crystalline structure existed in the TiO_2 matrix, and that better formation of the composite was achieved as the increase of annealing temperature. Good crystallinity and increasing size of the nanocomposite were revealed by the SEM images. The formation of a thin NiO layer on TiO_2 particles was confirmed by the EDX analysis and TEM image. TiO_2/NiO nanocomposites were applied as modified working electrode materials in quasi-DSSCs and good performance in gel electrolyte. The optimized conditions for the excellent DSSC performance with TiO_2/NiO modified working electrode were achieved by loading 0.1 wt% NiO onto TiO_2 at annealing at 450 °C especially in terms of the current density. NiO layer in the composite can serve as a blocking layer, at which electron injection recombination is suppressed, and may lead to the formation of a *p–n* junction at the interface. This present NiO shell layer is playing key roles with regard to the functionality of the fabricated nanocomposite in the device. A further increase in NiO loading amount, however, and in the annealing temperature, may result in the reduction of electron injection tunneling through the composite interface due to the excessive thickness of the NiO blocking layer.

REFERENCES

[1] K. Jiang, A. Zakutayev, J. Stowers, M. D. Anderson, J. Tate, D. H. Mcintyre, D. C. Johnson, and D. A. Keszler "Low-Temperature, Solution Processing of TiO_2 Thin Films and Fabrication of Multilayer Dielectric Optical Elements" **Solid State Sciences**, vol. 11, 2009. Pp. 1692-1699.

[2] J.Yu,H. Yu, B. Cheng, M. Zhou and X. Zhao "Enhanced Photocatalytic Activity of TiO_2 Powder (P25) by Hydrothermal Treatment." **Journal of Molecular Catalysis A:Chemical,** vol. 253, 2006. Pp. 112-118.

[3] B. Liu and E. S. Aydil "Growth of Oriented Single-Crystalline Rutile TiO_2 Nanorods on Transparent Conducting Substrates for Dye-Sensitized Solar Cells" **Journal of the American Chemical Society,** vol. 131, 2009. Pp. 3985-3990.

[4] M.Wei, Y. Konishi and H. Arakawa "Synthesis and Characterization of Nanosheet-Shaped Titanium Dioxide" **Journal of Materials Science**, vol. 42, 2007. Pp. 529-533.

[5] X. Zhang, J. Zhang, Y. Jia, P. Xiao and J. Tang "TiO_2 Nanotube Array Sensor for Detecting the SF_6 Decomposition Product SO_2" **Sensors,** vol. 12, 2012. Pp. 3302-3313.

[6] S. Songara, M.K. Patra, M. Manoth, L. Saini, V. Gupta, G.S. Gowd, S.R. Vadera and N. Kumar "Synthesis and Studies on Photochromic Properties of Vanadium doped TiO_2 Nanoparticles" **Journal of Photochemistry and Photobiology A: Chemistry**, vol. 209, 2010. Pp. 68-73.

[7] X. Su, J. Zhao, Y. Li, Y. Zhu, X. Ma, F. Sun and Z. Wang "Solution Synthesis of Cu_2O/TiO_2 Core-Shell Nanocomposites" **Colloids and Surface A: Physicochem. Eng. Aspects**, vol. 349, 2009. Pp. 151-155.

[8] T.V. Nguyen, H.C. Lee, M.A. Khan and O-B. Yang "Electrodeposition of TiO_2/SiO_2 Nanocompsoite for Dye-Sensitized Solar Cell" **Solar Energy**, vol. 81, 2007. Pp. 529-534.

[9] **"TiO_2-Titanium Dioxide."** [Online]. Available : http://alanassad.com/sabbath/Elements/Inorganic/TiO2-Titanium%20Dioxide.pdf.

[10] D. R.-Coronado, G. R.-Gattorno, M. E. E.-Pesqueira, C. Cab, R. de Coss and G. Oskam "Phase-Pure TiO_2 Nanoparticles: Anatase, Brookite and Rutile" **Nanotechnology**, vol. 19, 2008. Pp. 145605 (10pp).

[11] Pollution Control Department. "**Material Safety Data Sheet (MSDS). Titanium dioxide**" [Online]. Available : msds.pcd.go.th/searchName.asp?vID=1421. 2007.

[12] "Aluminum oxide, Titanium Dioxide P25 Two Highly Dispersed Metallic Oxide from Degussa Produced by the AEROSIL Process Degussa" **Technical Bulletin** vol. 56, 1982.

[13] D. Verma, R. Dash, K.S. Katti, D.L. Schulz and A.N. Caruso "Role of Coordinated Metal Ions on the Orientation of Phthalocyanine based Coatings" **Spectrochimica Acta Part A: Molecular and Biomolecular Spectroscopy**, vol. 70, 2008. Pp. 1180-1186.

[14] Monchawal Nartasilpa and Sirintra Khantham. 2006. "**Study of CuPc Organic Thin Film Growth by Electron Beam Evaporation.**" A Special Project for the Degree of Bachelor of Science, Department of Applied Physics, Faculty of Science, King Mongkut's Institute of Technology Ladkrabang.

[15] "COPPER PHTHALOCYANINE CAS N°: 147-14-8", UNEP PUBLICATIONS. Pp. 125-152.

[16] W. Mekprasart and W. Pecharapa. 2007. "**Optical Absorption Study on TiO_2-Nanostructure:Copper Phthalocyanines (CuPc) Composite.**" The Third National Conference on Optics and Applications (NCOA-3), Thailand.

[17] "**Nickel Chemistry.**" [Online]. Available : http://wwwchem.uwimona.edu.jm/courses/nickel.html.

[18] S. Thota and J. Kumar "Sol–gel Synthesis and Anomalous Magnetic Behavior of NiO Nanoparticles" **Journal of Physics and Chemistry of Solids**, vol. 68, 2007. Pp. 1951-1964.

[19] "**Nickle (II) Oxide.**" [Online]. Available : http://en.wikipedia.org/wiki/Nickel(II)_oxide.

[20] Y. Wang, J. Zhu, X. Yang, L. Lu and X. Wang "Preparation of NiO Nanoparticles and their Catalytic Activity in the Thermal Decomposition of Ammonium Perchlorate" **Thermochimica Acta**, vol. 437, 2005. Pp. 106-109.

[21] A. Qureshi, A. Mergen, and A. Altindal "Preparation and Characterization of Li and Ti Codoped NiO Nanocomposites for Gas Sensors Applications" **Sensors and Actuators B: Chemical,** vol.135, 2009. Pp. 537-540.

[22] C. G. Granqvist, P. C. Lansker, N. R. Mlyuka, G. A. Niklasson, and E. Avendaåo "Progress in Chromogenics: New Results for Electrochromic and Thermochromic Materials and Devices" **Solar Energy Materials and Solar Cells**, vol. 93, 2009. Pp. 2032-2039.

[23] U. M. Patil, R. R. Salunkhe, K. V. Gurav, and C. D. Lokhande "Chemically Deposited Nanocrystalline NiO Thin Films for Supercapacitor Application" **Applied Surface Science**, vol. 255, 2008. Pp. 2603-2607.

[24] M. Tadić, M. Panjan, D. Marković, I. Milošević and V. Spasojević "Unusual Magnetic Properties of NiO Nanoparticles Embedded in a Silica Matrix" **Journal of Alloys and Compounds,** vol. 509, 2011. Pp. 7134-7138.

[25] A.K. Kaw, 2006. **Mechanics of Composite Materials**, 2nd ED. New York, Taylor&Francis Group.

[26] P. H. C. Camargo, K. G. Satyanarayana and F. Wypych "Nanocomposites: Synthesis, Structure, Properties and New Application Opportunities" **Materials Research**, Vol. 12, 2009. Pp. 1-39.

[27] C. L. De Castro and B. S. Mitchell. 2002. "Nanoparticles from Mechanical Attrition." **Synthesis, Functionalization and Surface Treatment of Nanoparticles.** ISBN: 1-58883-009-8, American Scientific.

[28] C. Suryanarayana "Mechanical Alloying and Milling" **Progress in Materials Science**, vol. 46, 2001. Pp.1-184.

[29] Raphaël Janot and Daniel Guérard "Ball-milling in liquid media application to the preparation of anodic materials for lithium-ion batteries" **Progress in Materials Science.** vol. 50, 2005. Pp. 1-92.

[30] "**BALL MILLING.**" [Online]. Available : https://www.classle.net/book/ball-milling.

[31] Shruti Gour. 2010. "**Manufacturing Nano-Sized Powders using Salt- and Sugar-Assisted Milling.**" Master thesis of Science in Biomedical Engineering, Drexel University.

[32] "**Bottom-up approach.**" [Online]. Available : http://www.gitam.edu/eresource/nano/nanotechnology/bottamup%20app.htm.

[33] "**Sol-Gel methods.**" [Online]. Available : http://www.uio.no/studier/emner/matnat/kjemi/KJM5100/h06/undervisningsmateriale/10KJM5100_2006_sol_gel_d.pdf.

[34] Janne Halme. 2002. "**Dye-Sensitized Nanostructured and Organic Photovoltaic Cells: Technical Review and Preliminary Tests.**" Master thesis of Department of Engineering Physics and Mathematics, HELSINKI UNIVERSITY OF TECHNOLOGY.

[35] K. Kalyanasundaram and M. Grätzel. "Applications of functionalized transition metal complexes in photonic and optoelectronic devices." **Coordination Chemistry Reviews.** vol. 77, 1998. Pp. 347-414.

[36] M. Grätzel. "Dye-sensitized solar cells" **Journal of Photochemistry and Photobiology C: Photochemistry Reviews.** vol. 4, 2003. Pp. 145-153.

[37] M. Muneer, M. Saquib, M. Qamar and D. Bahnemann "Titanium-dioxide-mediated photocatalysis reaction of three selected pesticide derivatives" **Research on Chemical Intermediates**, vol. 30, 2004. Pp. 663-672.

[38] L. Hugo de, S. Benito and S. Miguel "**Photocatalytic Reaction Engineering**" [Online]. Available: http://www.springer.com/chemistry/book/978-0-387-23450-2. 2005.

[39] W. Baran, E. Adamek and A. Makowski "The influence of selected parameters on the photocatalytic degradation of azo-dyes in the presence of TiO_2 aqueous suspension" **Chemical Engineering Journal**, vol. 145, 2008. Pp. 242-248

[40] "**X-ray scattering techniques.**" [Online]. Available : http://en.wikipedia.org/wiki/X-ray_scattering_techniques.

[41] Dr. A. Ahmad, G. H. Awan and S. Aziz "Synthesis and applications of TiO_2 nanoparticles" Pakistan Engineering Congress, **70th Annual Session Proceedings**, Pp. 405-412.

[42] Dr. Sharon Mitchell and Prof. Javier Pérez-Ramírez "X-ray diffraction." **Surface Science and Methods in Catalysis.** 529-0611-00L, Advanced Catalysis Engineering, Institute for Chemical and Bioengineering, Switzerland.

[43] "**Scanning Electron Microscope.**" [Online]. Available : http://www.purdue.edu/rem/rs/sem.htm.

[44] "**Transmission Electron Microscope (TEM) and Scanning Transmission Electron Microscope (STEM).**" [Online]. Available : http://www.eaglabs.com/mc/scanning-transmission-electron-microscopy.html.

[45] "**XANES: Theory.**" [Online]. Available : http://chemwiki.ucdavis.edu/Wikitexts/UCD_Chem_205%3A_Larsen/Chem Wiki_Module_Topics/XANES%3A_Theory.

[46] "**X-ray Absorption Spectroscopy (XAS).**" [Online]. Available : http://www.chem.ucalgary.ca/research/groups/faridehj/xas.pdf.

[47] "**XANES spectroscopy.**" [Online]. Available : http://www.ung.si/~arcon/xas/xanes/xanes-theory.pdf.

[48] "**X-Ray Photoelectron Spectrometry.**" [Online]. Available : http://dmseg5.cwru.edu/Groups/Ernst/Courses/EMSE-515-F05/Pages/ transparencies/XPS-01-Intro.pdf.

[49] "**Photoelectron Spectrometry.**" [Online]. Available : http://www.chem.qmul.ac.uk/surfaces/scc/scat5_3.htm.

[50] "**Raman Spectroscopy Basics.**" [Online]. Available : http://content.piacton.com/Uploads/Princeton/Documents/Library/UpdatedLib rary/Raman_Spectroscopy_Basics.pdf.

[51] "**Thermogravimetric Analysis (TGA).**" [Online]. Available : http://www.perkinelmer.com/CMSResources/ Images/44-74556GDE_ TGAB eginnersGuide.pdf.

[52] "**UV-Visible Spectroscopy.**" [Online]. Available : http://www2.chemistry.msu.edu/faculty/reusch/VirtTxtJml/Spectrpy/UV-Vis/ uvspec.htm#uv1.

[53] "**Solar Cell I-V Measurement Systems.**" [Online]. Available : http://www.pvmeasurements.com/products/i-v-testing-system.

[54] Y. Lee, J. Chae and M. Kang. "Comparison of the Photovoltaic Efficiency on DSSC for nanometer sized TiO_2 using a conventional sol–gel and solvothermal methods." **Journal of Industrial and Engineering Chemistry**, vol. 16, 2010. Pp. 609-614.

[55] F. Han, V.S.R. Kambala, M. Srinivasan, D. Rajarthnam and R. Naidu. "Tailored Titanium Dioxide Photocatalysts for the Degradation of Organic Dyes in Wastewater Treatment: A Review." **Applied Catalysis A: General**, vol. 359, 2009. Pp. 25-40.

[56] M. Janus and A.W. Morawski. "New Method of Improving Photocatalytic Activity of Commercial Degussa P25 for Azo Dyes Decomposition" **Applied Catalysis B: Environmental**, vol. 75, 2007. Pp. 118-123.

[57] Y. Liu, C. Lu, M. Li, L. Zhang and B. Yang "High Refractive Iindex Organic–Inorganic Hybrid Coatings with TiO_2 Nanocrystals" **Colloids and Surfaces A: Physicochem. Eng. Aspects**, vol. 328, 2008. Pp. 67-72.

[58] M. Gratzel "Conversion of Sunlight to Electric Power by Nanocrystalline Dye-Sensitized Solar Cell" **Journal of Photochemistry and Photobiology A: Chemistry,** vol. 164, 2004. Pp. 3-14.

[59] C.Y. Huang, Y.C. Hsu, J.G. Chen, V. Suryanarayanan, K.M. Lee and K.C. Ho "The Effects of Hydrothermal Temperature and Thickness of TiO_2 Film on the Performance of a Dye-Sensitized Solar Cell" **Solar Energy Materials & Solar Cells,** vol. 90, 2006. Pp. 2391-2397.

[60] K.M. Lee, V. Suryanarayanan and K.C. Ho "Influences of Different TiO_2 Morphologies and Solvents on the Photovoltaic Performance of Dye-Sensitized Solar Cells" **Journal of Power Sources,** vol. 188, 2009. Pp. 635-641.

[61] V. Iliev, D. Tomova, L. Bilyarska, L. Prahov and L. Petrov "Phthalocyanine Modified TiO_2 or WO_3-Catalysts for Photooxidation of Sulfide and Thiosulfate Ions upon Irradiation with Visible Light" **Journal of Photochemistry and Photobiology A: Chemistry,** vol. 159, 2003. Pp. 281-287.

[62] L. Giribabu, Ch.V. Kumar, V.G. Reddy, P.Y. Reddy, Ch.S. Rao, S.-R. Jang, J.-H.Yum, Md.K. Nazeeruddin and M. Gratzel "Unsymmetrical Alkoxy Zinc Phthalocyamine for Sensitization of Nanocrystalline TiO_2 Film" **Solar Energy Materials and Solar Cells**, vol. 91, 2007. Pp. 1611-1617.

[63] K.-M. Lee, V. Suryanarayanan and K.-C. Ho "The Influence of Surface Morphology of TiO_2 Coating on the Performance of Dye-Sensitized Solar Cells" **Solar Energy Materials & Solar Cells,** vol. 90, 2006. Pp. 2398-2400.

[64] L. Andronic and A. Duta "The Influence of TiO_2 Powder and Film on the Photodegradation of Methyl Orange" **Materials Chemistry and Physics,** vol. 112, 2008. Pp. 1078-1082.

[65] J. Jitputti, S. Pavasupree, Y. Suzuki and S. Yoshikawa "Synthesis and Photocatalytic Activity for Water-Splitting Reaction of Nanocrystalline Mesoporous Titania Prepared by Hydrothermal Method" **Journal of Solid State Chemistry,** vol. 180, 2007. Pp. 1743-1749.

[66] E. Jardinier, G. Pandraud, M. H. Pham, P. J. French and P. M. Sarro "Atomic Layer Deposition of TiO_2 Photonic Crystal Waveguide Biosensors" APCTP–ASEAN Workshop on Advanced Materials Science and Nanotechnology (AMSN08), **Journal of Physics: Conference Series**, vol. 187, 2009. doi:10.1088/1742-6596/187/1/012043

[67] K. H.Ko, Y. C. Lee and Y. J. Jung "Enhanced Efficiency of Dye-Sensitized TiO_2 Solar Cells (DSSC) by Doping of Metal Ions" **Journal of Colloid and Interface Science**, vol. 283, 2005. Pp. 482-487.

[68] Y. Huo, J. Zhu, J. Li, G. Li, H. Li "An Active La/TiO_2 photocatalyst Prepared by Ultrasonication-Assisted Sol-Gel Method Followed by Trearment under Supercritical Conditions" **Journal of Molecular Catalysis A: Chemical**, vol. 278, 2007. Pp. 237-243.

[69] L.R. Hou, C.Z. Yuan and Y. Peng "Synthesis and Photocatalytic Property of SnO_2/TiO_2 Nanotubes Composites" **Journal of Hazardous Materials**, vol. 139, 2007. Pp. 310-315.

[70] Y.-H. Xu, D.-H. Liang, M.-L. Liu, D.-Z. Liu, "Preparation and Characterization of Cu_2O-TiO_2: Efficient Photocatalytic Degradation of Methylene Blue" **Materials Research Bulletin**, vol. 43, 2008. Pp. 3474-3482.

[71] Y. Xiaodan, W. Qingyin, J. Shicheng and G. Yihang "Nanoscale ZnS/TiO_2 Composites: Preparation, Characterization, and Visible-Light Photocatalytic Activity" **Materials Characterization**, vol. 57, 2006. Pp. 333-341.

[72] Jing, L.; Chang, J.L.; Yue, K.L.; and Rong, G.D. "Photogenerated Cathodic Protection of Flower-Like, Nanostructured, N-doped TiO_2 Film on Stainless Steel" **Surface & Coatings Technology**, vol. 205, Pp. 557-564.

[73] T. Ohno, M. Akiyoshi, T. Umebayashi, K. Asai, T. Mitsui and M. Matsumura "Preparation of S-doped TiO_2 Photocatalysts and their Photocatalytic Activities under Visible Light" **Applied Catalysis A: General**, vol. 265, 2004. Pp. 115-121.

[74] M. Wang and X. Wang "PPV/TiO_2 Hybrid Composites Prepared from PPV Precursor Reaction in Aqueous Media and their Application in Solar Cells" **Polymer**, vol. 49, 2008. Pp. 1587-1593.

[75] Y. Zhu and Y. Dan "Photocatalytic Activity of Poly(3-hexylthiophene)/Titanium Dioxide Composites for Degrading Methyl Orange" **Solar Energy Materials and Solar Cells**, vol. 94, 2010. Pp. 1658-1664.

[76] X. Lu, Q. Wang and D. Cui "Preparation and Photocatalytic Properties of g-C_3N_4/TiO_2 Hybrid Composite" **Journal of Materials Science & Technology**, vol. 26, 2010. Pp. 925-930.

[77] A. Nakajima, T. Koike, S. Yanagida, T. Isobe, Y. Kameshima and K. Okada "Preparation and Photocatalytic Activity of $[PW_xMo_{12-x}O_{40}]3^-$/TiO_2 Hybrid Film Composites" **Applied Catalysis A: General**, vol. 385, 2010. Pp. 130-135.

[78] W.-C. Oh, A.-R. Jung and W.-B. Ko "Preparation of Fullerene/TiO_2 Composite and its Photocatalytic Effect" **Journal of Industrial and Engineering Chemistry**, vol. 13, 2007. Pp. 1208-1214.

[79] L. Tian, L. Ye, K. Deng and L. Zan "TiO_2/Carbon Nanotube Hybrid Nanostructures: Solvothermal Synthesis and their Visible Light Photocatalytic Activity" **Journal of Solid State Chemistry**, vol. 184, 2011. Pp. 1465-1471.

[80] W.-C. Lin, C.-N. Chen, T.-T. Tseng, M.-H. Wei, J.H. Hsieh and W. J. Tseng "Micellar Layer-by-Layer Synthesis of TiO_2/Ag Hybrid Particles for Bactericidal and Photocatalytic Activities" **Journal of the European Ceramic Society**, vol. 30, 2010. Pp. 2849-2857.

[81] P. Borker and A.V. Salker "Synthesis, Characterization and Photocatlytic Studies of some Metal Phthalocyanines" **Indian Journal of Chemical Technology**, vol. 13, 2006. Pp. 341-346.

[82] A.E.H. Machado, M.D. Franc, V. Velani, G.A. Magnino, H.M.M. Velani, F.S. Freitas, P.S.Müller Jr., C. Sattler and M. Schmücker "Characterization and Evaluation of the Efficiency of TiO_2/Zinc Phthalocyanine Nanocomposites as Photocatalysts for Wastewater Treatment using Solar Irradiation" **International Journal of Photoenergy**, vol. 2008, doi:10.1155/2008/482373.

[83] V. Iliev, D. Tomova, L. Bilyarska, L. Prahov, L. Petrov, "Phthalocyanine modified TiO_2 or WO_3-Catalysts for Photooxidation of Sulfide and Thiosulfate Ions upon Irradiation with Visible Light" **Journal of Photochemistry and Photobiology A: Chemistry**, vol. 159, 2003. Pp. 281-287.

[84] J. Bandara, U.W. Pradeep, and R.G.S.J. Bandara "The role of n–p Junction Electrodes in Minimizing the Charge Recombination and Enhancement of Photocurrent and Photovoltage in Dye Sensitized Solar Cells" **Journal of Photochemistry and Photobiology A: Chemistry**, vol. 170, 2005. Pp. 273-278.

[85] J. Bandara, C.M. Divarathne and S.D. Nanayakkara "Fabrication of n–p Junction Electrodes Made of n-type SnO_2 and p-type NiO for Control of Charge Recombination in Dye Sensitized Solar Cells" **Solar Energy Materials & Solar Cells,** vol. 81, 2004. Pp. 429-437.

[86] C. Shifu, Y. Xiaoling and L. Wei "Preparation and Photocatalytic Activity Evaluation of Composite Photocatalyst Fe-TiO_2/TiO_2" **ECS Transactions,** vol. 21, 2009. Pp. 3-22.

[87] L. Xiong, J. Li and Y. Yu "Energy Storage in Bifunctional TiO_2 Composite Materials under UV and Visible Light" **Energies**, vol. 2, 2009. Pp. 1009-1013

[88] X. Li, R. Huang, Y. Hu, Y. Chen, W. Liu, R. Yuan and Z. Li "A Templated Method to Bi_2WO_6 Hollow Microspheres and their Conversion to Double-Shell Bi_2O_3/Bi_2WO_6 Hollow Microspheres with Improved Photocatalytic Performance" **Inorganic Chemistry**, vol. 51, 2012. Pp. 6245-6250.

[89] J. Tatami, H. Nakano, T.Wakihara and K. Komeya "Development of Advanced Ceramics by Powder Composite Process" **KONA Powder and Particle Journal**, vol. 28, 2010. Pp. 227-240.

[90] K.Balachandaran, R.Venckatesh and R. Sivaraj "Synthesis of Nano TiO_2-SiO_2 Composite Using Sol-Gel Method: Effect on Size, Surface Morphology and Thermal Stability" **International Journal of Engineering Science and Technology,** vol. 2, 2010. Pp. 3695-3700.

[91] T. Ishizaki,Y.Masuda, and N. Saito "Chemical Deposition and Corrosive Resistance of TiO_2/MgF_2 Composite Nanofilm on Magnesium Alloy AZ31" **Electrochemical and Solid-State Letters,** vol. 12, 2009. Pp. D68-D71.

[92] D.Su, J. Wang, Y. Tang, C. Liu, L. Liu and X. Han "Constructing WO_3/TiO_2 Composite Structure towards Sufficient Use of Solar Energy" **Supplementary Material (ESI) for Chemical Communications,** This journal is © The Royal Society of Chemistry 2011.

[93] V. Štengl, S. Bakardjieva, N. Murafa, V. Houškaová and K. Lang "Visible-Light Photocatalytic Activity of TiO_2/ZnS Nanocomposites Prepared by Homogenous Hydrolysis" **Microporous and Mesoporous Materials,** vol. 110, 2008. Pp. 370-378.

[94] J. A.-Gamboa, F.C. Gennari, P. A. Larochette, C. Neyertz, M. Ahlers and J.L. Pelegrina "Stability of Cu-Zn Phases under Low Energy Ball Milling" **Materials Science and Engineering A,** vol. 447, 2007. Pp. 324-331.

[95] Y. Jin, Y. Liu, Y. Wang and J. Ye "Synthesis of Ultrafine (Ti, W, Mo, V)(C, N)–Ni Composite Powders by Low-Energy Milling and Subsequent Carbothermal Reduction–Nitridation Reaction" **Journal of Alloys and Compounds,** vol. 486, 2009. Pp. L34–L36.

[96] R. Angers, M.R. Krishnadev, R. Tremblay, J.-F. Corriveau and D. Dube "Characterization of SiCp:2024 Aluminum Alloy Composites Prepared by Mechanical Processing in a Low Energy Ball Mill" **Materials Science and Engineering**, vol. A262, 1999. Pp. 9–15.

[97] K.Y. Zhao, C.J. Li, J.M. Tao, Dickon H.L. Ng and X.K. ZHU "The Synthesis, Microstructure, Hardness and Thermal Properties of Bulk Nanocrystalline Al Produced by in Situ Consolidation with Low-Energy Ball Milling" **Journal of Alloys and Compounds**, vol. 504, 2010. Pp. S306-S310.

[98] Z. Hussain and L. C. Kit "Properties and Spot Welding Behavior of Copper–Alumina Composites through Ball Milling and Mechanical Alloying" **Materials and Design,** vol. 29, 2008. Pp. 1311-1315.

[99] H.C. Weerasinghe, P.M. Sirimanne, G.P. Simon and Y.B. Cheng "Fabrication of Efficient Solar Cells on Plastic Substrates using Binder-Free Ball Milled Titania Slurries" **Journal of Photochemistry and Photobiology A: Chemistry**, vol. 206, 2009. Pp. 64-70.

[100] C.S. Chou, R.Y. Yang, M.H. Weng and C.H. Yeh "Preparation of TiO_2/Dye Composite Particles and their Applications in Dye-Sensitized Solar Cell" **Powder Technology,** vol. 187, 2008. Pp. 181-189.

[101] Z. Liu, X. Zhang, Y. Zhang and J. Jiang, "Theoretical Investigation of the Molecular, Electronic Structures and Vibrational Spectra of a Series of First Transition Metal Phthalocyanines" **Spectrochimica Acta Part A: Molecular and Biomolecular Spectroscopy**, vol. 67, 2007. Pp. 1232-1246.

[102] M. Szybowicz, T. Runka, M. Drozdowski, W. Bala, A. Grodzicki, P. Piszczek and A. Bratkowski "High Temperature Study of FT-IR and Raman Scattering Spectra of Vacuum Deposited CuPc Thin Films" **Journal of Molecular Structure,** vol. 704, 2004. Pp. 107-113.

[103] D. Wang, J. Zhang, Q. Luo, X. Li and Y. Duan "Characterization and Photocatalytic Activity of Poly(3-hexylthiophene)- Modified TiO_2 for Degradation of Methyl Orange under Visible Light" **Journal of Hazardous Materials**, vol. 169, 2009. Pp. 546-550.

[104] W. Liu, Y. Wang, L. Gui and Y. Tang "Preparation and Characterization of Novel Nanoscopic Titanium Dioxide Phthalocyanine Complex Films" **Langmuir,** vol. 15, 1999. Pp. 2130-2133.

[105] Y. Ohmori, E. Itoh and K. Miyari "Photovoltaic Properties of Phthalocyanine Based p–n Diode Evaporated onto Titanium Dioxide" **Thin Solid Films**, vol. 499, 2006. Pp. 369-373.

[106] G.D. Sharma, R. Kumar, S. K. Sharma and M.S. Roy "Charge Generation and Photovoltaic Properties of Hybrid Solar Cells Based on ZnO and Copper phthalocyanines (CuPc)" **Solar Energy Materials and Solar Cells**, vol. 90, 2006. Pp. 933-943.

[107] W. Jarernboon, S. Pimanpang, S. Maensiri, E. Swatsitang and V. Amornkitbamrung "Optimization of Titanium Dioxide Film Prepared by Electrophoretic Deposition for Dye-Sensitized Solar Cell Application" **Thin Solid Films**, vol. 517, 2009. Pp. 4663-4667.

[108] K.M. Lee, V. Suryanarayanan, J.H. Huang, K.R.J. Thomas, J.T. Lin and K.C. Ho "Enhancing the Performance of Dye-Sensitized Solar Cells Based on an Organicdye by Incorporating TiO_2 Nanotube in a TiO_2 Nanoparticle Film" **Electrochimica Acta**, vol. 54, 2009. Pp. 4123-4130.

[109] X. Zhao, Z. Li, Y. Chen, L. Shi and Y. Zhu "Enhancement of photocatalytic degradation of polyethylene plastic with CuPc modified TiO_2 photocatalyst under solar light irradiation" **Applied Surface Science,** vol. 254, 2008. Pp. 1825-1829.

[110] S.S. Kim, J.H. Yum and Y.E. Sung "Improved Performance of a Dye-Sensitized Solar Cell Using a TiO_2/ZnO/Eosin Y Electrode" **Solar Energy Materials and Solar Cells**, vol.79, 2003. Pp.495-505.

[111] M.N. Shan, S.S. Wang, Z.Q. Bian, J.P. Liu and Y.L. Zhao "Hybrid Inverted Organic Photovoltaic Cells Based on Nanoporous TiO_2 Films and Organic Small Molecules" **Solar Energy Materials and Solar Cells,** vol. 93, 2009. Pp. 1613-1617.

[112] S.H. Lee, D.H. Kim, J.H. Kim, T.H. shim and J.G. Park "Impact of Donor, Acceptor, and Blocking Layer Thickness on Power Conversion Efficiency for Small-Molecular Organic Solar Cells" **Synthetic Metals**, vol. 159, 2009. Pp. 1705-1709.

[113] J. Wu, Z. Lan, D. Wang, S. Hao, J. Lin, Y. Wei, S. Yin and T. Sato "Quasi-Solid State Dye-Sensitized Solar Cells-Based Gel Polymer Electrolytes with Poly (acrylamind)-Poly(ethylene glycol) Composite" **Journal of Photochemistry and Photobiology A: Chemistry,** vol. 181, 2006. Pp. 333-337.

[114] J. Shang, M. Chai and Y. Zhu "Photocatalytic Degradation of Polystyrene Plastic under Fluorescent Light" **Environmental Science & Technology**, vol. 37, 2003. Pp. 4494-4499.

[115] T. Xu, G. Liu and J. Zhao "Photoassisted Degradation of Dye Pollutants. V. Self-Photosensitization Oxidative Transformation of Rhodamine B under Visible Light Irradiation in Aqueous TiO_2 Dispersions" **Journal of Physical Chemistry B**, vol. 102, 1998. Pp. 5845-5851.

[116] H.M.S.-Suh, J.R. Choi, H.J. Hah, S.M. Koo and Y.C. Bae "Comparison of Ag Deposition Effects on the Photocatalytic Activity of Nanoparticulate TiO_2 under Visible and UV Light Irradiation" **Journal of Photochemistry and Photobiology A: Chemistry,** vol. 163, 2004. Pp. 37-44.

[117] S. Thota and J. Kumar "Sol–Gel Synthesis and Anomalous Magnetic Behavior of NiO Nanoparticles" **Journal of Physics and Chemistry of Solids,** vol. 68, 2007. Pp.1951-1964.

[118] H. Lu, J. Zhao, L. Li, L. Gong, J. Zheng, L. Zhang, Z. Wang, J. Zhang and Z. Zhu "Selective Oxidation of Sacrificial Ethanol over TiO_2-based Photocatalysts during Water Splitting" **Supplementary Material (ESI) for Energy and Environmental Science,** This journal is © The Royal Society of Chemistry 2011.

[119] N. Mironova-Ulmane, A. Kuzmin, I. Steins, J. Grabis, I. Sildos and M. Pärs "Raman Scattering in Nanosized Nickel Oxide NiO" **Journal of Physic: Conference Series,** vol. 93, 2007. D OI:10.1088/1742-6596/93/1/012039.

[120] N. Mironova-Ulmane, A. Kuzmin, I. Sildos and M. Pärs "Polarisation Dependent Raman Study of Single-Crystal Nickel Oxide" **Central European Journal of Physics,** vol. 9, 2011. Pp. 1096-1099.

[121] U. Diebold "TiO_2 by XPS" **Surface Science Spectra,** vol. 4, 1998. Pp. 227-231.

[122] L. Soriano, I. Preda, A. Gutiérrez and S. Palacín "Surface Effects in the Ni 2*p* X-Ray Photoemission Spectra of NiO" **Physical Review B,** vol. 75, 2007. Pp. 233417(1-4).

[123] L. Ren, Y.-P. Zeng and D. Jiang "The Improved Photocatalytic Properties of P-type NiO Loaded Porous TiO_2 Sheets Prepared via Freeze Tape-Casting" **Solid State Sciences,** vol. 12, 2010. Pp. 138–143.

[124] M. D. Irwin, D. B. Buchholz, A. W. Hains, R. P. H. Chang, and T. J. Marks "*p*-Type Semiconducting Nickel Oxide as an Efficiency-Enhancing Anode Interfacial Layer in Polymer Bulk-Heterojunction Solar Cells" **Proceedings of the National Academy of Science of the United States of America,** vol. 105, 2008. Pp. 2783-2787.

[125] B. Peng, G. Jungmann, C. Jger, D. Haarer, H.-W. Schmidt and M. Thelakkat "Systematic Investigation of the Role of Compact TiO_2 Layer in Solid State Dye-Sensitized TiO_2 Solar Cells" **Coordination Chemistry Reviews,** vol. 248, 2004. Pp. 1479-1489.

[126] V. Ganapathy, B. Karunagaran, and S.-W. Rhee "Improved Performance of Dye-Sensitized Solar Cells with TiO_2/Alumina Core–Shell Formation Using Atomic Layer Deposition" **Journal of Power Sources,** vol. 195, 2010. Pp. 5138-5143.

[127] Y.-M. Lee and C.-H. Lai "Preparation and Characterization of Solid n-TiO_2/ p-NiO Heterojunction Electrodes for All-Solid-State Dye-Sensitized Solar Cells" **Solid-State Electronics,** vol. 53, 2009. Pp. 1116-1125.

[128] J. Bandara, U. W. Pradeep and R. G. S. J. Bandara "The role of n–p Junction Electrodes in Minimizing the Charge Recombination and Enhancement of Photocurrent and Photovoltage in Dye Sensitized Solar Cells" **Journal of Photochemistry and Photobiology A: Chemistry**, vol. 170, 2005. Pp. 273-278.

[129] M.-W. Xu, S.-J. Bao and H.-L. Li "Synthesis and Characterization of Mesoporous Nickel Oxide for Electrochemical Capacitor" **Journal of Solid State Electrochemical,** vol. 11, 2007. Pp. 372-377.

[130] L. Li, R. Chen, G. Jing, G. Zhang, F. Wu and S. Chen "Improved Performance of TiO_2 Electrode Coated with NiO by Magnetron Sputtering for Dye-Sensitized Solar Cell" **Applied Surface science,** vol. 256, 2010. Pp. 4533-4537.

[131] T. Sreethawong, Y. Suzuki and S. Yoshikawa "Photocatalytic evolution of hydrogen over mesoporous TiO_2 supported NiO photocatalyst prepared by single-step sol-gel process with surfactant template" **International Journal of Hydrogen Energy,** vol. 30, 2005. Pp. 1053-1062.

APPENDIX A

The supplementary data on charge transfer in TiO_2/CuPc nanocompsoite by quantum chemical calculation

The interaction between TiO_2 and CuPc in form of nanocomposite, the mechanism of the electron injection process, has been initially studied by quantum chemical investigation. Density functional theory (DFT) was chosen as the method for quantum chemistry due to suitable system for nanocrystalline structure calculation. DFT and time-dependent (TD) DFT calculations were performed to investigate the geometric and electronic structure of anatase (101) plane of TiO_2 clusters [$(TiO_2)_8$], metal-free Pc (H_2Pc) and CuPc molecule. The electronic structures were investigated via B3LYP/LANL2DZ method via Gaussion 09 program. Charge transfer transition was occurred in HOMO-LUMO of TD mode shown as red and green area from this calculation.

1. The Investigation of H_2Pc and Ti_8O_{16}

1.1 Optimized Structure of H_2Pc and Ti_8O_{16}

Geometry-optimized structures of H_2Pc and Ti_8O_{16} obtained from X-ray structure were firstly calculated using B3LYP/LANL2DZ method. Two hydrogen atoms are surrounded with four macrocycle of aromatics and benzene rings composed of H_2Pc molecule shown as Appendix Figure A1(a). The referent model was used as the initial format and comparing to CuPc molecule. Simple TiO_2 model "Ti_8O_{16}" was obtained by a scissors operator from anatase TiO_2 cluster (Appendix Figure A1(b)). Complex structure of TiO_2 cluster was complicated for the initial calculation. Composite form of TiO_2 and metal-Pc was simulated as Appendix Figure A1(c). From XRD and Raman confirm that the structures of TiO_2 and CuPc are insignificantly changed after composite process relating to unbonding between composite. Therefore, the interaction between two materials performed in the physical adsorption.

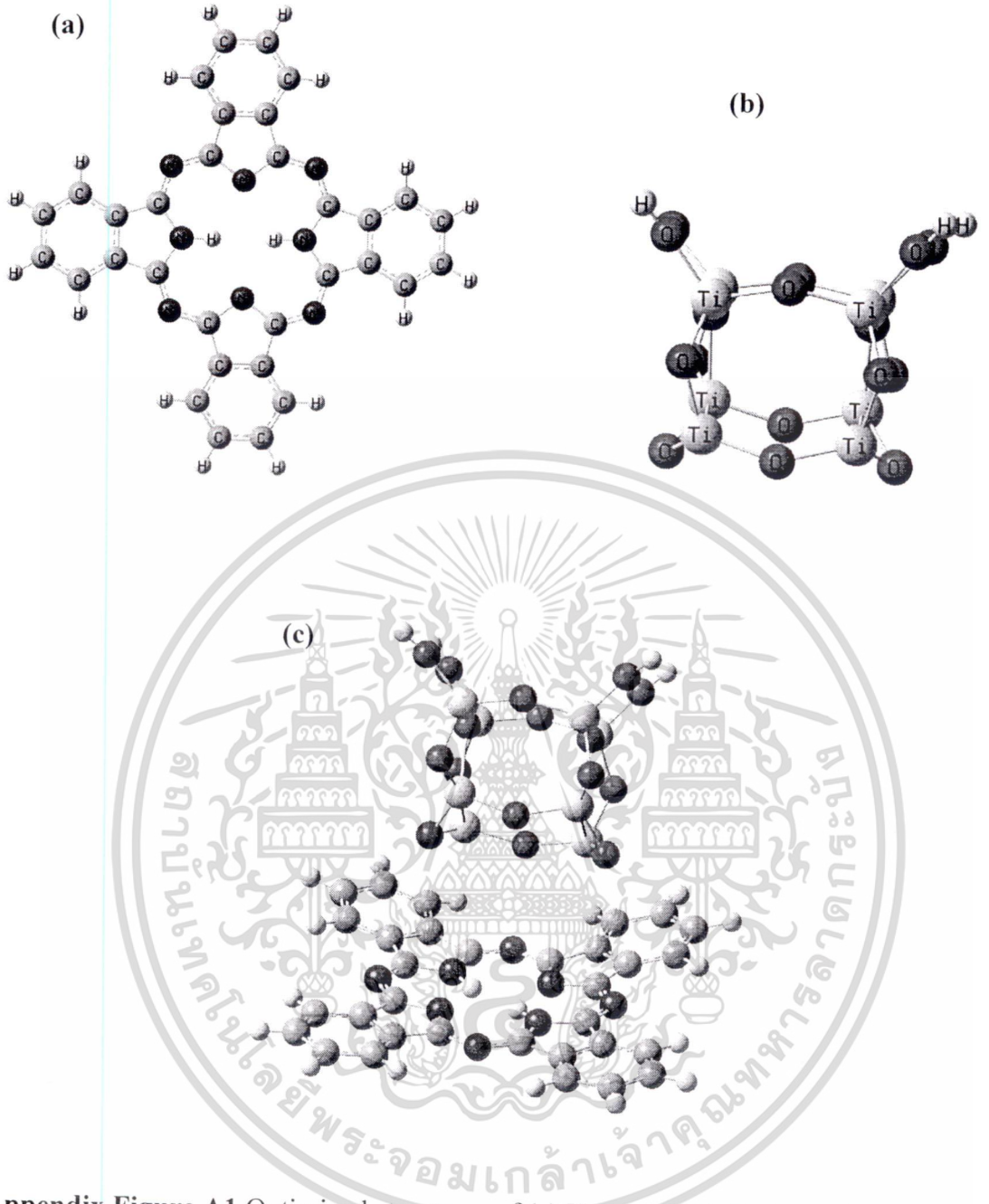

Appendix Figure A1 Optimized structures of (a) H_2Pc and (b) Ti_8O_{16} and (c) Ti_8O_{16}-H_2Pc system using B3LYP/LANL2DZ method.

1.2 Charge Transfer Transition in TD Mode of TiO_2/H_2Pc

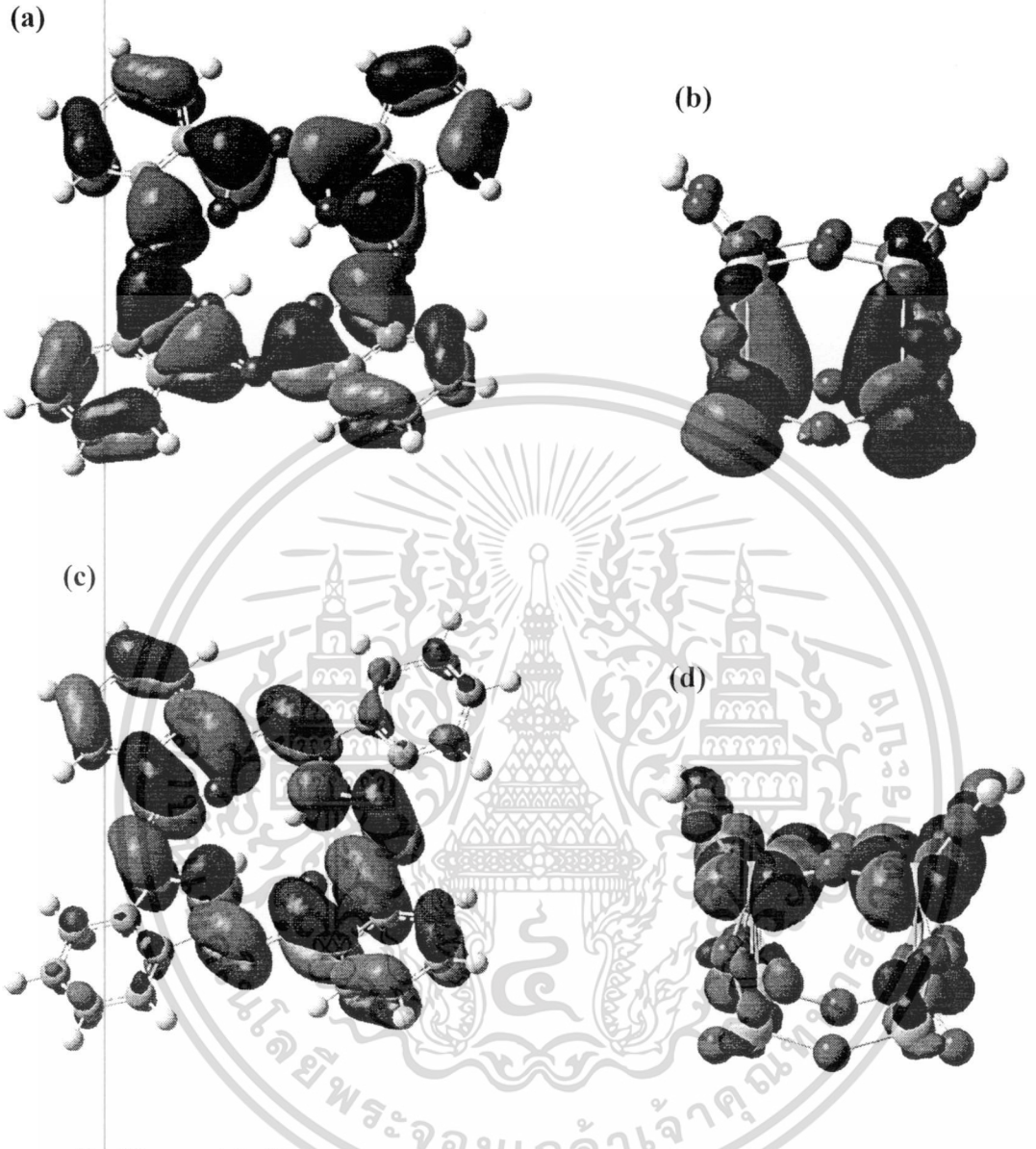

Appendix Figure A2 Charge transfer transition at HOMO level of (a) H_2Pc, (b) Ti_8O_{16} and LUMO level of (c) H_2Pc, (d) Ti_8O_{16}.

As seen in Appendix Figure A2 (a) and (c), charges in H_2Pc is thoroughly localized on macro rings at HOMO level. After stimulation, whole charges are transferred to the opposite ring in straight line at LUMO level. Whereas charge transfer transition of Ti_8O_{16} is moved from the bottom cycle position to uppermost chains illustrated in Appendix Figure A2 (b) and (d).

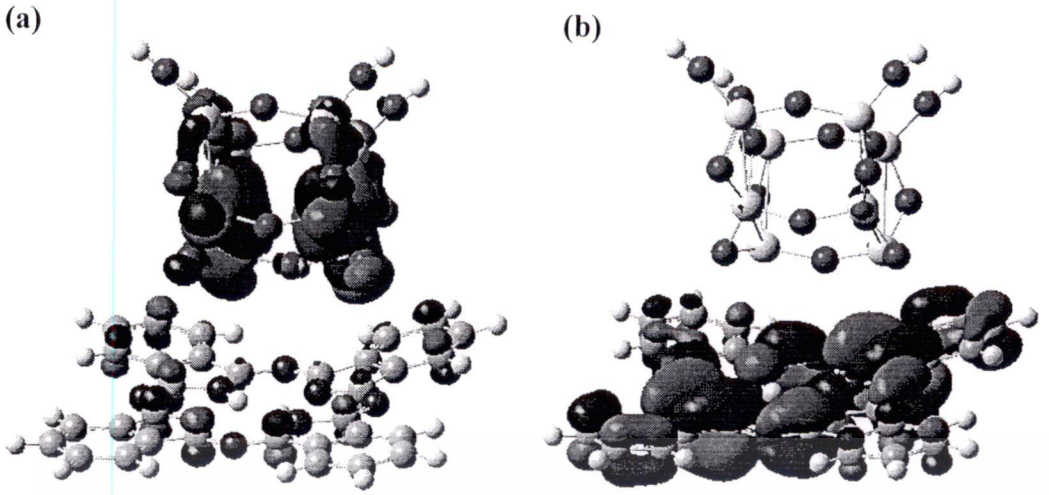

Appendix Figure A3 Charge transfer transition at (a) HOMO and (b) LUMO level of Ti_8O_{16}- H_2Pc system.

From Appendix Figure A3 indicates that charge transition is transferred from Ti_8O_{16} to CuPc at benzene and aromatic ring.

2. The Investigation of CuPc and Ti_8O_{16}

2.1 Optimized Structure of CuPc and Ti_8O_{16}

Appendix Figure A4 Optimized structures of (a) CuPc and (b) Ti_8O_{16} and (c) Ti_8O_{16}-CuPc system using B3LYP/LANL2DZ method.

Geometry-optimized structures of CuPc and Ti_8O_{16} obtained from X-ray structure were calculated using B3LYP/LANL2DZ method as same method with H_2Pc/Ti_8O_{16} as shown in Appendix Figure A4(a-b). Complex structure of TiO_2 cluster was complicated for the initial calculation. Composite form of TiO_2 and CuPc was

simlulated as Appendix Figure A4(c). From XRD and Raman confirm that the structures of TiO_2 and CuPc are insignificantly changed after composite process relating to unbonding between composite. Therefore, the interaction between two materials performed in the physical adsorption.

2.2 Charge Transfer Transition in TD Mode of TiO_2/CuPc

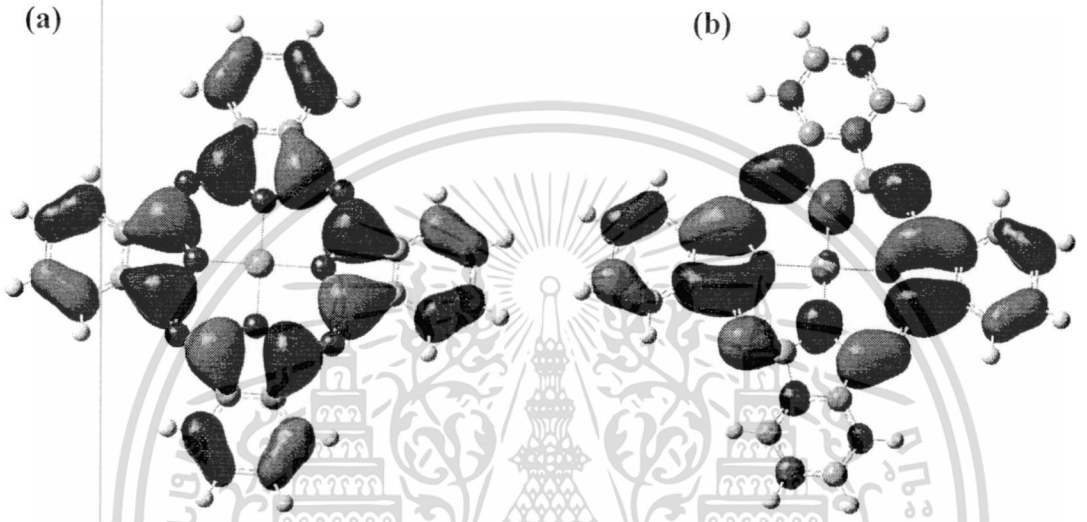

Appendix Figure A5 Charge transfer transition at (a) HOMO and (b) LUMO level of α-CuPc.

Appendix Figure A6 Charge transfer transition at (a) HOMO and (b) LUMO level of β-CuPc.

In this section, the structures of CuPc are 2 types; alfa (α) and beta (β) phase. As seen in Appendix Figure A5 and A6 (a) and (b), charges in CuPc is thoroughly localized on macro rings at HOMO level. After stimulation, whole charges are transferred to the opposite ring in straight line at LUMO level. This result is identical to stimulated H_2Pc at HOMO and LUMO level.

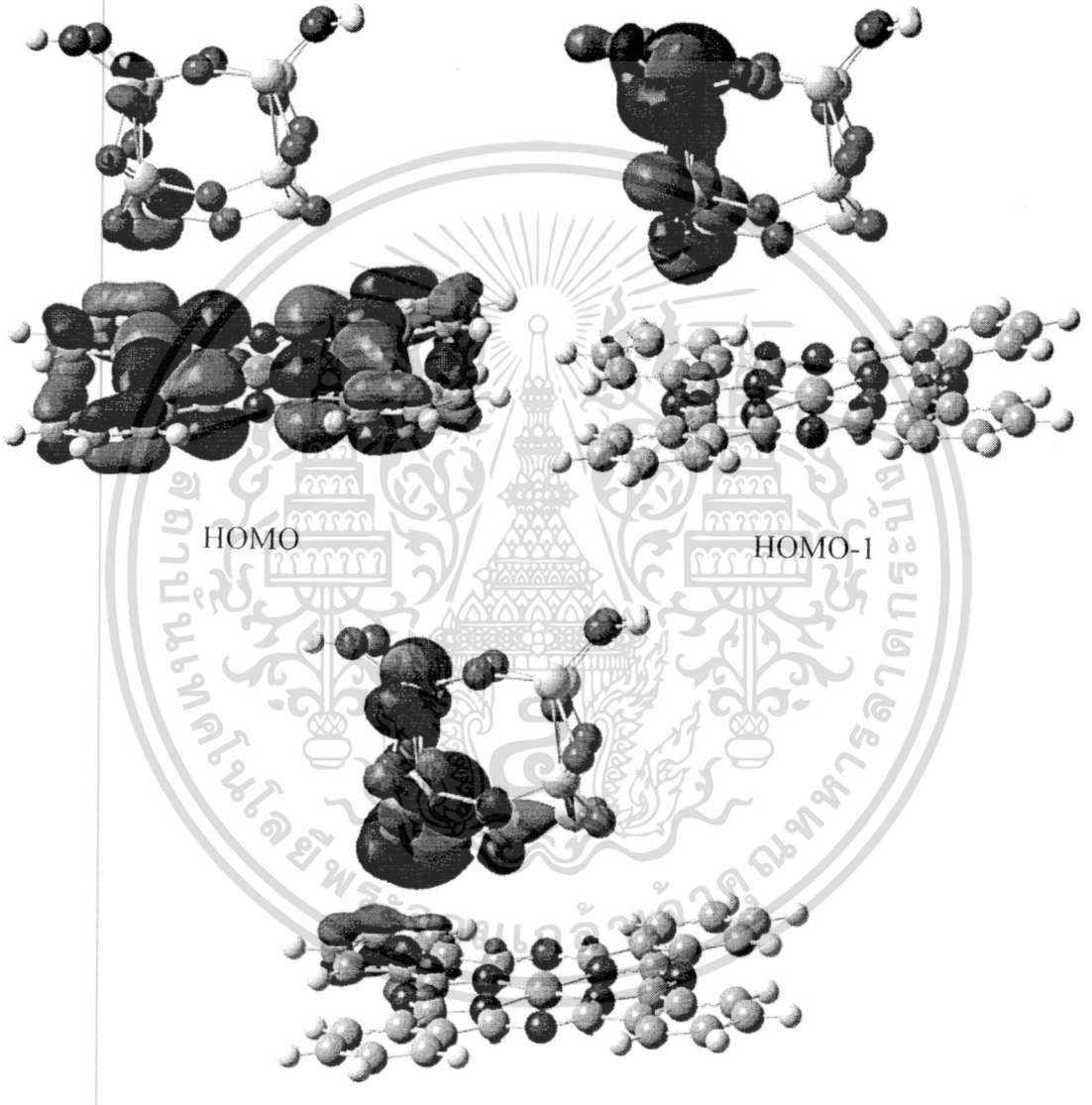

Appendix Figure A7 Charge transfer transition at HOMO level of Ti_8O_{16}-α-CuPc system.

LUMO LUMO+1

Appendix Figure A8 Charge transfer transition at LUMO level of Ti_8O_{16}- α-CuPc system.

HOMO HOMO-3

Appendix Figure A9 Charge transfer transition at HOMO level of Ti_8O_{16}- β-CuPc system.

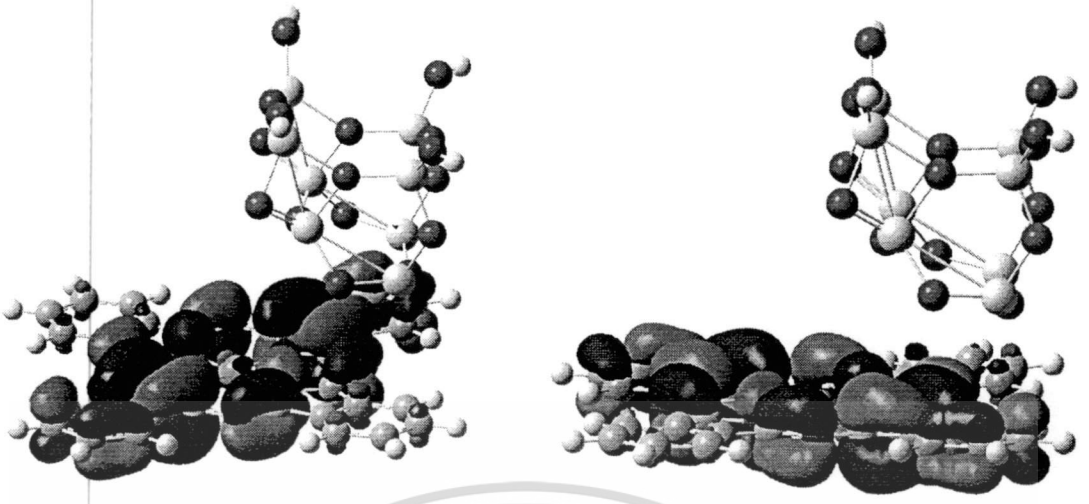

LUMO LUMO+1

Appendix Figure A10 Charge transfer transition at LUMO level of Ti_8O_{16}- β-CuPc system.

The structure of Ti_8O_{16}-α-CuPc system at HOMO level is shown in Appendix Figure A7. Mostly charges were located at Ti_8O_{16} and some charge was transferred to α-CuPc that is the presence of error. After stimulation to LUMO level in Appendix Figure A8, whole charges are transferred to CuPc at benzene and aromatic ring. The result of Ti_8O_{16}- β-CuPc system in Appendix Figure A9 and A10 was still identical to Ti_8O_{16}-α-CuPc system at HOMO and LUMO level. Some error in the simulation was occurred due to smaller Ti_8O_{16} comparing to CuPc. Therefore charge transfer was started from Ti_8O_{16} to CuPc that is opposed with the propose model in the experiment. However, this result requires further investigation and characterization for better clearification.

Appendix B
Nitrogen doped Titanium dioxide

TiO_2 Photocatalysts have been widely researched and obtained great attraction since the past decades due to high efficiency in photocatalytic activities. The utilizations of TiO_2 photocatalyst have been reported in various environmental applications. However, TiO_2 can be activated in UV illumination due to its wide band gap energy. Thus, only 3-5% of UV in solar spectrum is less absorbed by itself. This is the main drawback of TiO_2 photocatalyst that is hardly activated in visible light. High recombination rate of photoelectron-hole is also one of its hindrances that still retarded the photocatalytic mechanism. Many efforts have been made to conquer these problems by doping with non-metal in TiO_2 such as Carbon (C), Sulfur (S) and Nitrogen (N). Among the non-metal dopant, N is one of material that was acknowledged for enhancing the photoresponding range into visible light. Horst Kisch and co-workers reported that band gap energy of TiO_2 can be reduced from 3.18 to 2.20 eV by nitrogen incorporation [B1]. Jing Li and co-workers proved that the significant visible light response and strong increase of photocurrent under UV and visible range were obtained by N-doped TiO_2 [B2]. S. Bangkedphol and colleague reported on the improvement of photocatalytic degradation of tributyltin under natural light by using N-doped TiO_2 [B3].

The main objective in this part is to investigate the effect of the different content of N doping in commercial TiO_2 powder and baking time on its structure and response in visible range. The efficiency of N-doped TiO_2 photocatalysts were proved by the photocatalytic degradation of Rhodamine B (RhB) under visible illumination.

1. Experiment

N-doped TiO_2 was prepared by mechanical mixing through homogenization and magnetic stirring. Commercially available TiO_2 (Aeroxide® TiO_2 P25, Nippon Aerosil Co. Ltd.) was used as precursor-TiO_2 nanopowders. Ammonium hydrogen carbonate (NH_4HCO_3) was chosen as nitrogen source for doping in TiO_2. NH_4HCO_3 was dispersed in 100 ml of deionized water and stirred for 30 min at room temperature. The ratio of doping N in 6.0 g of TiO_2 P25 is designated at 10, 30 and 50 %wt. The suspension was mixed via homogenizer at 6000 rpm for 1h followed by

stirring at 120°C until the evaporation of DI water was obtained. After that the precursor was kept as 100°C for 24 h. Finally, the white powder of N-doped TiO_2 was obtained by baking at 100°C for 30, 60 and 120 min. These samples were assigned as NT_30m, NT_60m, and NT_120m. The structural properties of N-doped TiO_2 were characterized by X-ray diffraction (XRD).

The photocatalyst of N-doped TiO_2 was carried out by dye photodegradation of Rhodamine B (RhB) under visible light via halogen lamp (450 W). 50 mg of N-doped TiO_2 was dispersed in 3 mM RhB and stirred for 20 min in the dark to obtain absorption/desorption equilibrium between RhB and the catalyst surfaces. The solution was irradiated in visible light at room temperature until color of dye completely disappeared. RhB degradation was investigated by the decrease of its absorbance at maximum wavelength (λ_{max}) via Helios UV-Vis spectrometer. The kinetic rate was calculated following the expression of exponential equation by;

$$A = A_0 + ke^{(R_0 t)}, \tag{B1}$$

where A is absorbance at λ_{max},

k is constant,

R_0 is reaction rate and

t is illustration time

2. Results and Discussion

XRD patterns of raw TiO_2 P25 and 30%wt. N-doped TiO_2 baked at 100 °C for different baking time are illustrated in Appendix Figure B1. For TiO_2 P25, the anatase phase located at 2θ = 25.4°, 37.8°, 38.6°, 48.1° and 55.2° correspond to (101), (004), (112), (200) and (211) planes whereas the peak at 2θ = 27.5°, 36.2°, 39.3°, 41.3° and 54.4° relates to the rutile phase in (110), (101), (200), (111) and (211) planes, respectively. For N-doped TiO_2, the XRD patterns have identical peaks pattern to raw TiO_2 P25 patterns. As baking time increases, its phase is still retained without significant change. This result implies that doping N in TiO_2 does not change the basis crystalline of TiO_2 but it may be intermingle on TiO_2 surface. The crystalline size of N-doped TiO_2 which was calculated using Scherrer's equation is in the range

of 13 to 15 nm. The decrease of crystalline size of N-doped TiO_2 may be caused by the less movement of hydroxyl carbonate from precursor [B4].

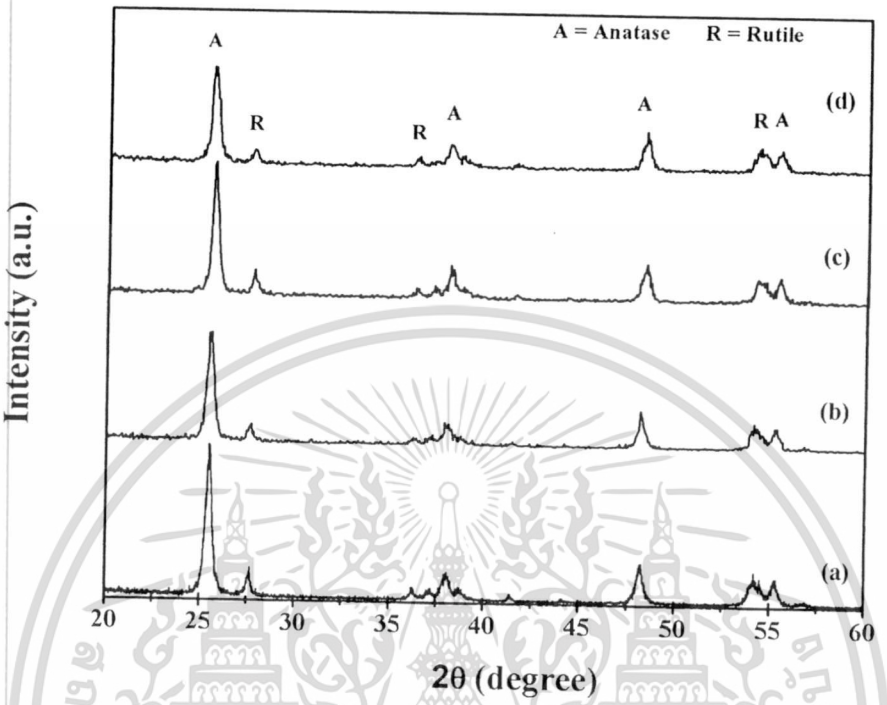

Appendix Figure B1 XRD patterns of (a) raw TiO_2 P25 and 30 %wt of N-doped TiO_2 at 100C with different baking time (b) 30, (c) 60 and (d) 120 min.

Appendix Table B1 Structural characteristics of TiO_2 P-25 and N-doped TiO_2 with different baking time.

Sample	β	*cos θ*	Crystalline size (nm)
TiO_2 P-25	0.43	0.22	14.56
NT_30m	0.45	0.22	13.83
NT_60m	0.43	0.22	14.70
NT_120m	0.46	0.22	13.45

Absorption spectra of TiO_2 P25 and N-doped TiO_2 at 100 °C with different baking time are illustrated in Appendix Figure B2. It can be seen that the enhancement in optical absorption was clearly seen in NT_60m photocatalyst. This result suggests that NH_4HCO_3 can be used as proper nitrogen source for doping in TiO_2 powder. The spectrum patterns of NT_30m and NT_120m were similar to TiO_2 P25 because of low nitrogen content when compared to pure TiO_2 [18]. It can be deduced that shift of absorption in visible range could be remarkably influenced by the presence of N in the powder and baking time. The amount of nitrogen content is also crucial factor that can further affect the absorption attribute as seen in Appendix Figure B3. The spectrum patterns of N-doped powders performed good absorption in UV region but visible region. For the sample with 10 %wt N doping, this small amount of N loading may produce insufficient nitrogen atoms for modification. On the other hand, the large doping nitrogen content (50%wt.) could not completely decompose precursor for combining in TiO_2 matrix. Therefore, it can be deduced that optimized conditions providing the best photoresponse performance in visible light from this experiment was obtained by 30 %wt. N-doped TiO_2 baked at 100°C for 60 min accompanying the excellent efficiency in photocatalytic degradation.

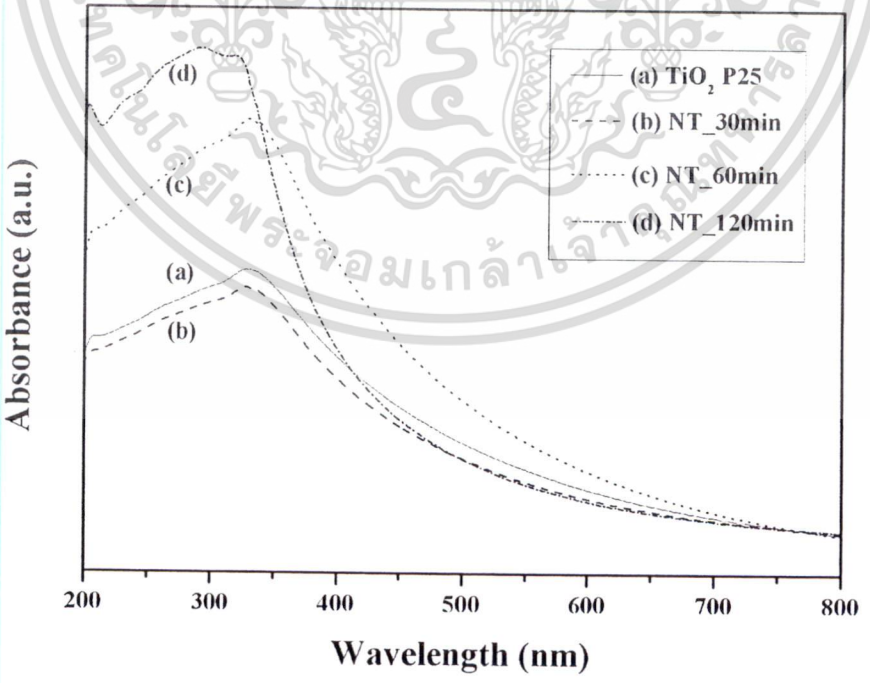

Appendix Figure B2 UV-Vis absorbance spectra of (a) TiO_2 P-25 and N-doped TiO_2 with different baking time at (b) 30, (c) 60 and (d) 120 min.

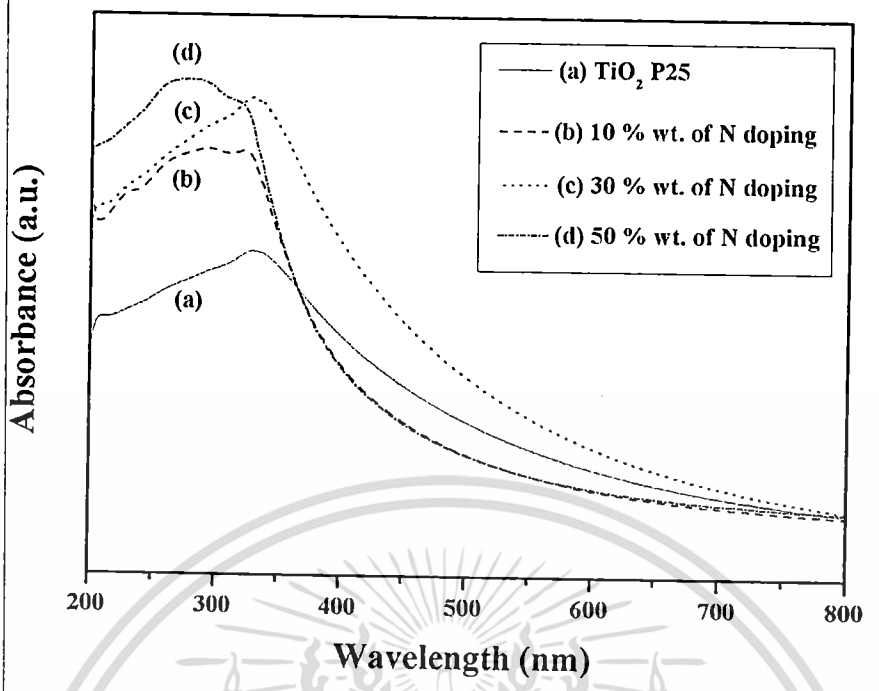

Appendix Figure B3 UV-Vis absorbance spectra of (a) TiO_2 P-25 and N-doped TiO_2 with different content of nitrogen doping at (b) 10, (c) 30 and (d) 50 %wt.

The photodegradation of RhB in aqueous solution under visible light for 1 hour was conducted in order to make the comparison of photocatalyst efficiency of TiO_2 itself and N-doped TiO_2 and the corresponding results are shown in Appendix Figure B4(a) and B4(b). Both N-doped TiO_2 and TiO_2 P25 can effectively degrade and decolorize RhB. The absorption spectrum of RhB degraded by N-doped TiO_2 photocatalyst exhibits that the decreased absorbance was initially higher than TiO_2 P25. The decolorization of dye was completely reached as the irradiation time up to 30 min for N-doped TiO_2 and 40 min for TiO_2 P25. The loss in absorption is associated to the destruction of dye chromogen. A noticeable shift of absorption spectra to higher energy was obiviously observed by N-doped TiO_2 photocatalyst. This phenomenon is related to the generation of N-de-ethylation that is the last product of RhB [B5].

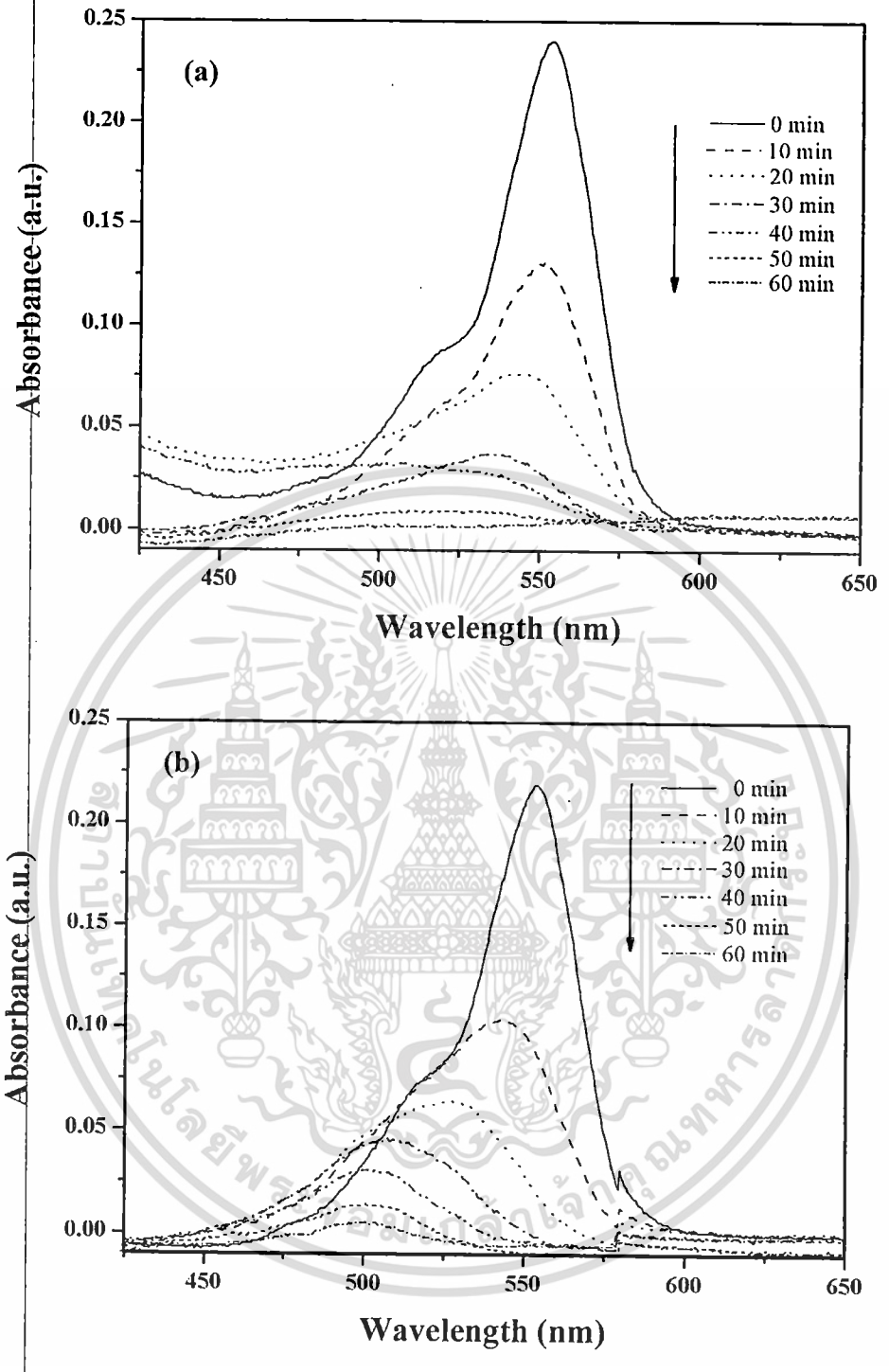

Appendix Figure B4 Absorption of RhB under visible light by using (a) TiO_2 P25 (b) 30 %wt. N-doped TiO_2.

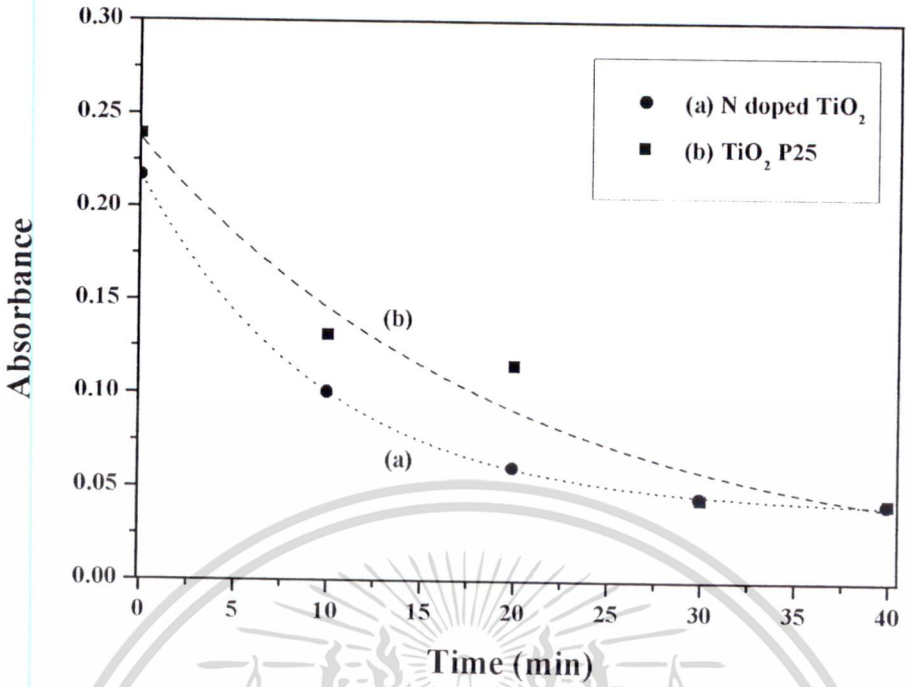

Appendix Figure B5 Absorbance versus decay time of RhB under visible light by using (a) TiO_2 P25 (b) 30 %wt. N-doped TiO_2

The change of RhB absorbance versus irradiation time of N-doped TiO_2 and TiO_2 P25 is shown in Fig. 5. The constant rate of RhB degradation with TiO_2 P25 is 0.051 min^{-1} whereas N-doped TiO_2 photocatalyst shows the constant rate of the activity of about 0.105 min^{-1}. These results imply that nitrogen additive doped in TiO_2 can significantly improve the photocatalytic degradation comparing to pure TiO_2 due to nitrogen-induced band gap energy contraction leading to the enhancement of optical absorption of photocatalyst under visible illumination [B6].

References of Appendix B

[B1] K. Horst, S. Shanmugasundaram, J. Marcin and M. Dariusz "A low-band gap, nitrogen-modified titania visible-light Photocatalyst" **Journal of Physical Chemistry C,** vol. 111, 2007. Pp. 11445-11449

[B2] L. Jing, J.L. Chang, K.L. Yue and G.D. Rong "Photogenerated cathodic protection of flower-like, nanostructured, N-doped TiO_2 film on stainless steel" **Surface and Coatings Technology**, vol. 205, 2010. Pp. 557–564

[B3] S. Bangkedphol, H.E. Keenan, C.M. Davidson, A. Sakultantimetha, W. Sirisaksoontorn and A.Songsasen "Enhancement of tributyltin degradation under natural light by N-doped TiO_2 photocatalyst" **Journal of Hazardous Material**, vol. 184, 2010. Pp. 533–537

[B4] W. Yujun, Z. Chunling, B. Siwei and L. Guangsheng "Preparation of ZnO nanoparticle using the direct precipitation method in a membrane dispersion micro-structured reactor" **Powder Technology**, vol. 202, 2010. Pp. 130-136

[B5] M. Ying and N.Y. Jian "Photodegradation of Rhodamin B catalyzed by TiO_2 thin film" **Journal of Photochemistry and Photobiology A: Chemistry,** vol. 116, 1998. Pp. 167-170

[B6] Y.M Ji, S.K. Chan, K.C. Han and O.K. Tae "Synthesis and Characterization of N-doped TiO_2/ZrO_2 visible light photocatalysts" **Advance Powder Technology**, vol. 22, 2011. Pp. 443-448

Appendix C

1. Data of BET Characterization of Ball Milled TiO_2 P25

1.1 Ball Milled TiO_2 at 5 h

Sample weight	0.1203	[g]
Standard volume	24.236	[cm^3]
Dead volume	15.89	[cm^3]
Equilibrium time	0	[sec]
Adsorptive	N2	
Apparatus temperature	0	[C]
Adsorption temperature	77	[K]

Starting point	6	
End point	16	
Slore	0.088481	
Intercept	0.0018487	
Correlation coefficient	0.9999	
$a_{s,BET}$	48.184	[$m^2\ g^{-1}$]
Total pore volume (p/p_0=0.351)	0.025061	[$cm^3\ g^{-1}$]
Average pore diameter	2.0805	[nm]

No	p/p_0	$p/V_a(p_0-p)$
1	0.0044158	0.00076212
2	0.030901	0.0040851
3	0.039808	0.0050243
4	0.048683	0.0059211
5	0.052546	0.0063101
6	0.073224	0.0083111
7	0.082385	0.0091716
8	0.1005	0.010807
9	0.1246	0.012986
10	0.15	0.015205
11	0.1757	0.017425
12	0.2014	0.019661
13	0.2266	0.021854
14	0.2521	0.024107
15	0.2779	0.026414
16	0.3029	0.028698
17	0.3512	0.033383

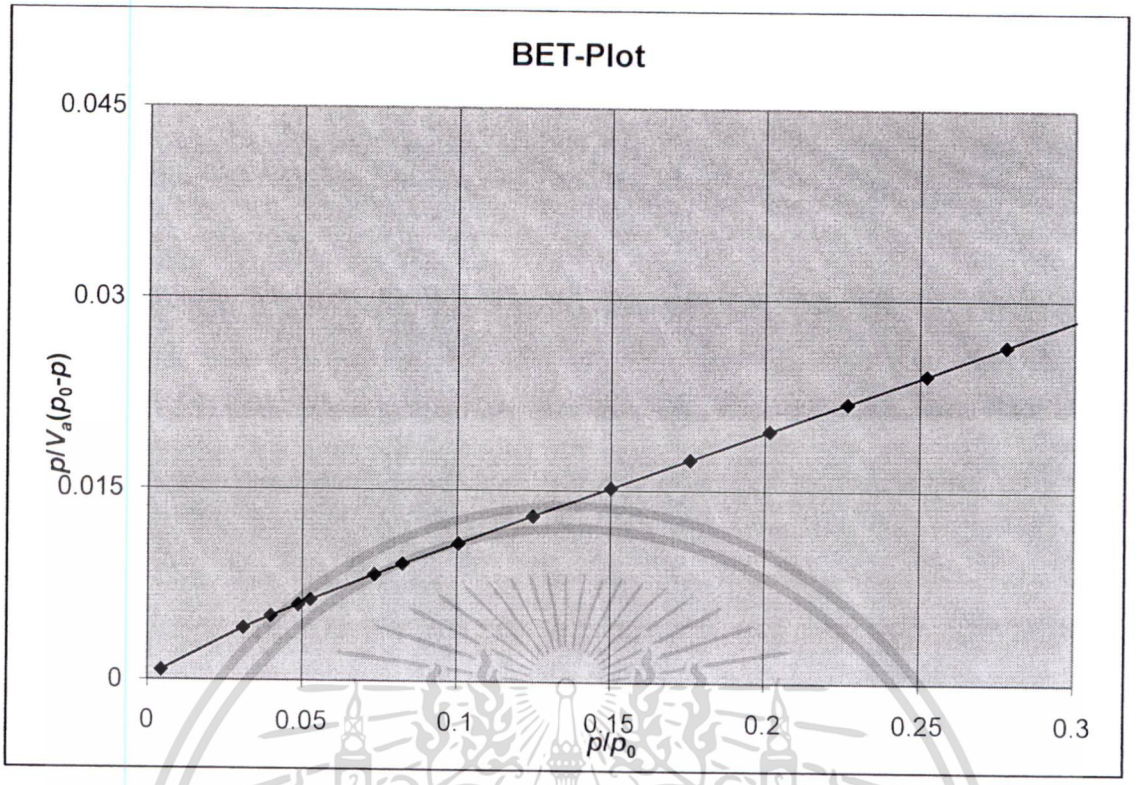

1.2 Ball Milled TiO_2 at 12 h

Sample weight	0.11	[g]
Standard volume	24.236	[cm^3]
Dead volume	26.829	[cm^3]
Equilibrium time	0	[sec]
Adsorptive	N2	
Apparatus temperature	0	[C]
Adsorption temperature	77	[K]

Starting point	3	
End point	12	
Slore	0.082571	
Intercept	0.0011277	
Correlation coefficient	1	
$a_{s,BET}$	52.002	[$m^2\ g^{-1}$]
Total pore volume (p/p_0=0.351)	0.027176	[$cm^3\ g^{-1}$]
Average pore diameter	2.0904	[nm]

No	p/p_0	$p/V_a(p_0-p)$
1	0.001429	0.00019739
2	0.042389	0.0044647
3	0.053884	0.0054937
4	0.074587	0.0073059
5	0.1005	0.0094842
6	0.1255	0.011544
7	0.1507	0.013577
8	0.1763	0.01569
9	0.2014	0.017719
10	0.2267	0.019793
11	0.2522	0.021927
12	0.2774	0.024082
13	0.3027	0.026328
14	0.3514	0.030821

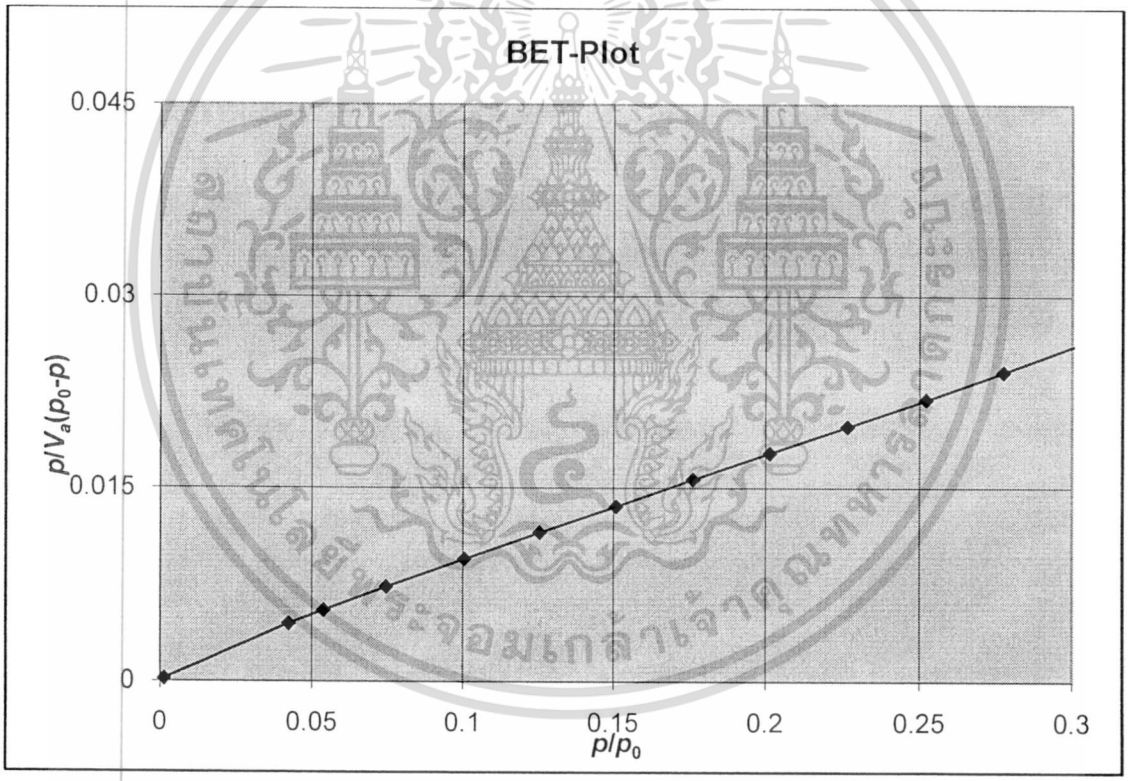

1.3 Ball Milled TiO_2 at 18 h

Sample weight	0.151	[g]
Standard volume	24.236	[cm^3]
Dead volume	22.237	[cm^3]
Equilibrium time	0	[sec]
Adsorptive	N2	
Apparatus temperature	0	[C]
Adsorption temperature	77	[K]

Starting point	6	
End point	16	
Slore	0.086118	
Intercept	0.0016409	
Correlation coefficient	0.9999	
$a_{s,BET}$	49.596	[$m^2\ g^{-1}$]
Total pore volume (p/p_0=0.351)	0.025862	[$cm^3\ g^{-1}$]
Average pore diameter	2.0858	[nm]

No	p/p_0	$p/V_a(p_0-p)$
1	0.00076613	-0.039174
2	0.0032685	0.00054511
3	0.028778	0.0036019
4	0.044804	0.0052342
5	0.049625	0.0057083
6	0.05115	0.0058505
7	0.073197	0.0079354
8	0.075523	0.0081424
9	0.09906	0.010256
10	0.1246	0.012491
11	0.1503	0.014683
12	0.1758	0.016832
13	0.2012	0.018941
14	0.2269	0.02115
15	0.252	0.023286
16	0.2776	0.025508
17	0.3031	0.027787
18	0.3512	0.032352

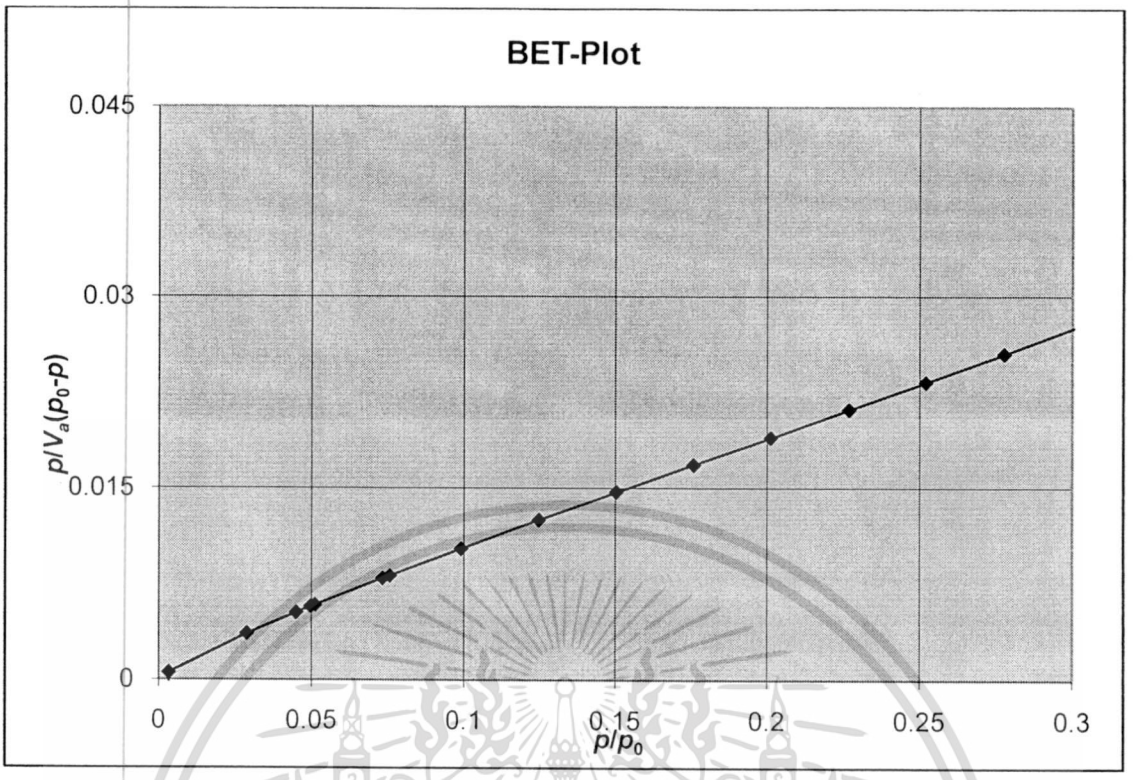

1.4 Ball Milled TiO_2 at 24 h

Sample weight	0.3321	[g]
Standard volume	24.236	[cm^3]
Dead volume	33.896	[cm^3]
Equilibrium time	0	[sec]
Adsorptive	N2	
Apparatus temperature	0	[C]
Adsorption temperature	77	[K]

Starting point	4	
End point	12	
Slore	0.079844	
Intercept	0.0014238	
Correlation coefficient	1	
$a_{s,BET}$	53.557	[$m^2\ g^{-1}$]
Total pore volume (p/p_0=0.348)	0.027729	[$cm^3\ g^{-1}$]
Average pore diameter	2.071	[nm]

No	p/p_0	$p/V_a(p_0-p)$
1	0.0086175	0.0010323
2	0.042321	0.0044871
3	0.054119	0.0055414
4	0.078135	0.0076084
5	0.1005	0.0094653
6	0.1297	0.011822
7	0.1496	0.01341
8	0.1745	0.015361
9	0.2002	0.017389
10	0.2255	0.019396
11	0.2509	0.021426
12	0.2765	0.023531
13	0.3019	0.025666
14	0.3482	0.029785

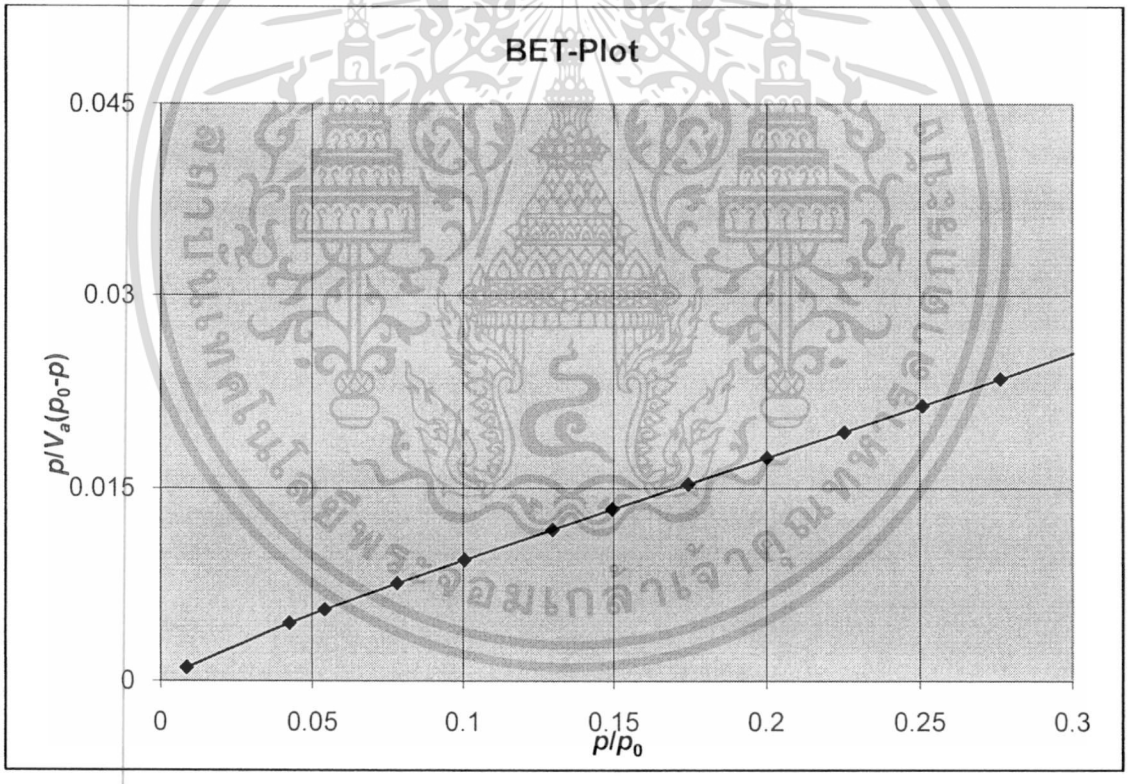

BIOGRAPHY

Miss Wanichaya Mekprasart

DATE OF BIRTH 13 April 1986, Bangkok

ADDRESS 150/193 Town Plus Petchkasame-Bangkae, Bangduan, Pasichalern, Bangkok, Thailand 10160

EDUCATION Bachelor of Science in Applied Physics-Science and Industrial Instrumentation, Faculty of Science from King Mongkut's Institute of technology Ladkrabang (KMITL), Bangkok, Thailand (2008).

PUBLICATION;

1. W. Mekprasart,W. Jarernboon and W. Pecharapa, "**TiO_2/CuPc hybrid nanocomposites prepared by low-energy ball milling for dye-sensitized solar cell application**", Materials Science and Engineering B, vol. 172, Pp. 231–236, 2010.
2. Wanichaya Mekprasart, Russameeruk Noonuruk, Wirat Jarernboon and Wisanu Pecharapa, "**Quasi-Solid-State Dye-Sensitized Solar Cells Based on TiO_2/NiO Core–Shell Nanocomposites**", Journal of Nanoscience and Nanotechnology, vol. 11, Pp. 6483–6489, 2011.
3. Wanichaya Mekprasart and Wisanu Pecharapa, "**Synthesis and characterization of nitrogen-doped TiO2 and its photocatalytic activity enhancement under visible light**", Energy Procedia, vol. 9, pp. 509 – 514, 2011.
4. W. Mekprasart, N. Vittayakorn, W. Pecharapa, "**Ball-milled CuPc/TiO2 hybrid nanocomposite and its photocatalytic degradation of aqueous Rhodamine B**", Materials Research Bulletin, Article in press, 2012.

CONFERENCE PRESENTATION;

1. W. Pecharapa and W. Mekprasart, **"Optical absorption study on TiO_2-Nanostructure:CuPc Composite"**, *The Third National Conference on Optics and Applications (NCOA-3),* 15th August 2008, Bangkok, Thailand.
2. W. Mekprasart and W. Pecharapa, **"Photocytalytic Degradation Study of Copper Phthalocyanines by TiO_2 Nanostructures"**, Commemorative International Conference on *Sustainable Development to Save the Earth 2008 (SDSE 2008)*, December 11-13, 2008, Bangkok, Thailand.
3. Wanichaya Mekprasart and Wisanu Pecharapa **"Preparation of TiO_2/CuPc composite for Photodegradation Applications"**, *International Science, Social Science, Engineering and Energy Conference (I-SEEC 2008)*, December 15-16, 2008, Nongkai, Thailand.
4. W. Mekprasart, W. Jarernboon and W. Pecharapa, **"Preparation of TiO_2/CuPc hybrid nanocomposite and their utilization as electrode materials of Dye-Sensitized Solar Cell"**, ***7th Eco-Energy and Materials Science and Engineering*** *Symposium (EMSES 2009),* November 19-22, 2009, Chiang Mai, Thailand.
5. W. Mekprasart and W. Pecharapa, **"Photodegradation of Dye Pollutant by Low-Dimensional Structure TiO_2/Metal Phthalocyanine Composites"**, *1st Nanotoday 2009 Conference*, August 2-5, 2009, Singapore.
6. W. Pecharapa and W. Mekprasart, **"Structural and Optical Properties of Functional Hybrid Composites Based on TiO_2 Nanostructures and Metal Phthalocyanine"**, *1st Nanotoday 2009 Conference*, August 2-5, 2009, Singapore.
7. Wanichaya Mekprasart, Russameeruk Noonuruk, Wirat Jareanboon and Wisanu Pecharapa, **"Quasi Solid-State Dye-Sensitized Solar Cells based on n-TiO_2/p-NiO Nanocomposites"**, *Joint Symposium of IEEE Nano Korea*, Aug17-20, 2010, South Korea.
8. W. Mekprasart and W. Pecharapa, **"Synthesis and characterization of Nitrogen-doped TiO_2 and its photocatalytic activity enhancement under visible light"**, ***9th Eco-Energy and Materials Science and Engineering*** *Symposium (EMSES 2011),* May 25-28, 2011, Chiang Rai, Thailand.

Materials Science and Engineering B 172 (2010) 231–236

Contents lists available at ScienceDirect

Materials Science and Engineering B

journal homepage: www.elsevier.com/locate/mseb

iO_2/CuPc hybrid nanocomposites prepared by low-energy ball milling for ye-sensitized solar cell application

J. Mekprasart[a,b,*], W. Jarernboon[a,b], W. Pecharapa[a,b]

ollege of KMITL Nanotechnology, King Mongkut's Institute of Technology Ladkrabang, Chalongkrung Rd., Ladkrabang, Bangkok 10520, Thailand
hEP Center, CHE, 328 Si Ayutthaya Rd., Bangkok 10400, Thailand

RTICLE INFO

icle history:
ceived 22 February 2010
ceived in revised form 25 April 2010
cepted 22 May 2010

ywords:
O_2
Pc
mposite
l milling

ABSTRACT

The hybrid nanocomposites of titanium dioxide nanoparticle (TNP) and copper phthalocyanine (CuPc) were successfully synthesized by low-energy ball milling as a main part of synthesis and processing via three different methods without additional heating. Structural properties of as-prepared composites were well characterized by X-ray diffraction, Raman spectroscopy, Field Emission-Scanning Electron Microscopy and Transmission Electron Microscopy. TNP/CuPc hybrid nanocomposites acting as photocatalyst were used as a modified working electrode materials in dye-sensitized solar cells. Among all prepared conditions, the composite with 0.05 wt.% CuPc prepared by homogenization and ball milling process exhibited the best performance with optimized solar energy conversion efficiency of 1.24% with fill factor of 0.45. The significant enhancement of current density of the device may be associated to the decrease of recombination of photo-injected electrons and reduction of charge transfer resistances at the interface caused by the presence of CuPc on TNP matrix.

Introduction

Among functional metal oxide semiconductors, TiO_2 is currently ne of the most widely used materials due to its distinguished operties including wide optical band gap (~3.2 eV), strong ultraolet absorptivity, non-toxicity, long-term chemical stability, good notocatalysis and high energy conversion efficiency [1–5]. Owing its excellent properties, TiO_2 is utilized in various applications nging from photocatalyst for organic pollutants degradation in ater treatment process [6–8], the filler in polymer matrix for nproving their optical function as photo-carrier collector [9], nd electron transport layer in optoelectronic device applications ich as the working electrode material in dye-sensitized solar cell)SSC) [10–12]. However, the rather high recombination of photonerated electron–hole pairs and the weak absorption in visible gion are its main drawbacks [13,14]. Therefore, various techques have been proposed in order to modify TiO_2 to overcome ese inferiorities. A number of research works have employed the lvantage of comparably large surface area of TiO_2 nanostructures ch as thin film structure, nanoparticle, nanorod, nanosheet and notube to improve its performance [15–18]. Recently, it was also ported that TiO_2 incorporated with appropriate semiconductors in form of composite material is one of the alternating methods for solving its disadvantages. Ko et al. reported that the increasing of open circuit voltage and short circuit current in DSSC was attained by doping aluminum and tungsten into TiO_2 [19]. Hou et al. gave the report on decreasing the recombination of electron–hole pairs in photoreactivity using SnO_2/TiO_2 nanotube composite [20]. Xiaodan et al. successfully enhanced visible light absorption of TiO_2 using ZnS/TiO_2 nanocomposite [21]. Wang and Wang reported that the photoelectric conversion in solar cell could be increased by PPV/TiO_2 hybrid nanocomposite [22].

The idea for improving the performance of TiO_2 in form of organic–inorganic hybrid nanocomposite is one of the effective techniques. Typically, the potential organic material for loading in the composite is metal phthalocyanine (MPc) because it is well known for excellent resistance of chemical degradation, strong absorption in blue-green region and good thermal stability [23,24]. MPc has been utilized as functional material in many applications such as diode, transistor, gas sensor and photovoltaic device [25–29]. Copper phthalocyanine (CuPc) is delegated for loading in TiO_2 hybrid nanocomposite in this experiment. It is believed that CuPc in the composite can retard the recombination of photo-generated electron–hole pair of TiO_2 and can increase the absorption capability in the visible region of the composite. Owing to this exceptional property, feasible usages of this hybrid composite were proposed for practical applications such as working electrode material in DSSC [30] and the photocatalyst in photocatalytic degradation of plastic [31] and organic pollutant [32]. Nevertheless, to our best knowledge, few research works

Corresponding author at: College of KMITL Nanotechnology, King Mongkut's titute of Technology Ladkrabang, Chalongkrung Rd., Ladkrabang, Bangkok 10520, ailand. Tel.: +66 865655376; fax: +66 3264733..
E-mail address: wani.mek@gmail.com (W. Mekprasart).

21-5107/$ – see front matter © 2010 Elsevier B.V. All rights reserved.
:10.1016/j.mseb.2010.05.022

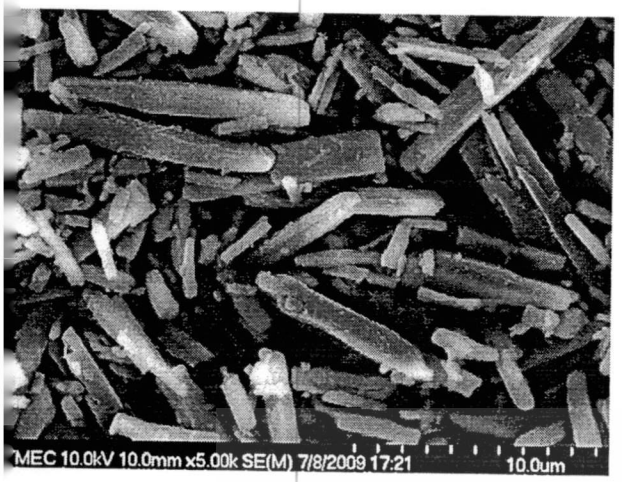

Fig. 1. FE-SEM image of physical structure of CuPc.

e dedicated on preparation of hybrid TiO_2/CuPc nanocompos-
by different methods including dry coating process [30] and
netic stirring process [32]. However, for practical usage, the
ssity of suitable method that can make the homogeneous
ersion between two materials is required. Among these pro-
es, ball milling has been chosen as a potential process for
le blending solid-state powder technique which could pro-
nanocrystalline powder [33]. High energy ball milling process
reduce particle size because of their high smashing between
materials–materials and material–internal wall of the vial.
temperature and the accumulation of defects in powder were
uced by this method therefore low-energy ball milling pro-
is a kind of methods for composite synthesis. The advantages
w-energy ball milling process are reported that it is sim-
nd cost-effective process. Nanocrystalline powder is not only
uced in this process, but also the attrition in equipment is
ced because of its negligible heating by impact [34]. In this
, we report on the synthesis of hybrid TiO_2/CuPc nanocom-
te based on ball milling process at low temperature following
e different preparation methods. We believed that the pro-
with ball milling could be enhanced CuPc dispersion in TiO_2
ix and the homogeneity in hybrid composite. Their funda-
tal physical properties were thoroughly investigated by X-ray
action, Raman spectroscopy, Field Emission-Scanning Elec-
Microscopy (FE-SEM) and Transmission Electron Microscopy
I). These functional composites were applied as modifying
ting electrode materials in DSSC.

xperimental

Preparation of TNP/CuPc hybrid composites

O_2 nanoparticles (TNP), Degussa P-25 (Germany) with aver-
particle size of 20 nm were chosen as the host matrix. CuPc
$H_{16}CuN_8$) with dye content of 97%, supplied by Aldrich was
nated as guest material. The physical structure of CuPc pow-
naturally acicular shape with approximately 10 μm in size as
n in Fig. 1. Ball milling process is essential to minimize size
nhance the dissolution itself [34]. The particle size of CuPc
educed after milling process.
w-energy ball milling process was operated by conventional
ontal ball milling process. For ball-milled conditions, several
nia balls with diameter 1.47 and 5.36 mm were contained
e cylindrical plastic vial of height 7.7 cm and inner diameter
n. Ethanol was used as disperser for blending two materials.
illing process continuously operated for 18 h on the cylindri-
cal roller at 100 rpm (10.47 rad s^{-1}). For homogenization process, Heidolph® Silent Crusher M homogenizer was used for dispersing the composite homogeneously with high speed blade operated at room temperature. The dispersed rotator was immersed in 2/3 depth of solution.

The synthesis of TNP/CuPc hybrid composites was carried out by three different methods as follows:

Method 1 (CM1): Firstly, CuPc and ethanol were loaded for ball milling process operated at room temperature with speed of 100 rpm for 18 h with a ball-to-powder weight ratio of 10:1. After that, CuPc solution was stirred at 120 °C until ethanol completely evaporated and kept at 100 °C for 24 h. Ball-milled CuPc was obtained and introduced into TNP dispersed in 100 ml ethanol solution. The suspension was homogenized at 7000 rpm for 30 min and stirred at 120 °C until ethanol completely evaporated. As-prepared solid precipitate of TNP/CuPc composite was dried at 100 °C for 24 h. The composite in method 1 was recognized as CM1.

Method 2 (CM2): CuPc and ethanol were loaded for ball milling process operated at room temperature with speed of 100 rpm for 18 h with a ball-to-powder weight ratio of 10:1. After that, CuPc solution was stirred at 120 °C until ethanol completely evaporated and kept at 100 °C for 24 h. Ball-milled CuPc was then supplied to TNP dispersed in ethanol solution before loading for ball milling process conducted at room temperature with speed of 100 rpm for 18 h with a ball-to-powder weight ratio 30:1. After that, the suspension was stirred at 120 °C until ethanol completely evaporated. As-prepared solid precipitate of TNP/CuPc was dried at 100 °C for 24 h. The composite in method 2 was recognized as CM2.

Method 3 (CM3): CuPc was mixed with TNP dispersed in 100 ml ethanol solution by homogenizer at room temperature with speed of 7000 rpm for 30 min. The suspension was stirred at 120 °C until solid precipitate was obtained. After that, the solid precipitate was milled at room temperature with speed of 100 rpm. After that the suspension was stirred at 120 °C until ethanol completely evaporated. Finally, as-prepared solid precipitate of TNP/CuPc was dried at 100 °C for 24 h. The composite in method 3 was recognized as CM3.

The ratio of loading CuPc in 5 g of TNP for all methods was fixed at 0.05, 0.1 and 1 wt.% For comparison to three methods, CuPc was mixed with TNP in 100 ml ethanol solution using homogenizer at room temperature with speed of 7000 rpm for 30 min and was recognized as reference composite.

2.2. TNP/CuPc composite-based working electrode preparation

The preparation of TNP/CuPc working electrode started from blending 1 g of each hybrid composite with 2 ml deionized water and fluorosilicic acid binder. After that the mixture was ground in a white mortar for 5 min. The blue CuPc/TNP colloid was deposited on fluorine-doped tin oxide (FTO, 15 Ω/□) conductive substrate by doctor blade technique. These working electrodes were dried at 150 °C for 1 h in ambient air, followed by immersing in concentration 3×10^{-4} mol of N719 dye solution [*cis*-bis(isothiocyanato)bis(2,2′-bipyridyl-4,4′-dicarboxylato)-ruthenium (II)bis-tetrabutylammonium] at room temperature for 24 h in the dark. Finally, TNP/CuPc working electrodes in each method were obtained.

2.3. Fabrication DSSC with TNP/CuPc working electrode

DSSC was designed in the sandwich structure with TNP/CuPc working electrode and platinum film coated on FTO counter electrode. The para polymer film was inserted between both electrodes to prevent short circuit of the device. Liquid electrolyte consisting of 0.1 M I_2, 0.5 M LiI, and 0.5 M ethylene carbonate in 10 ml

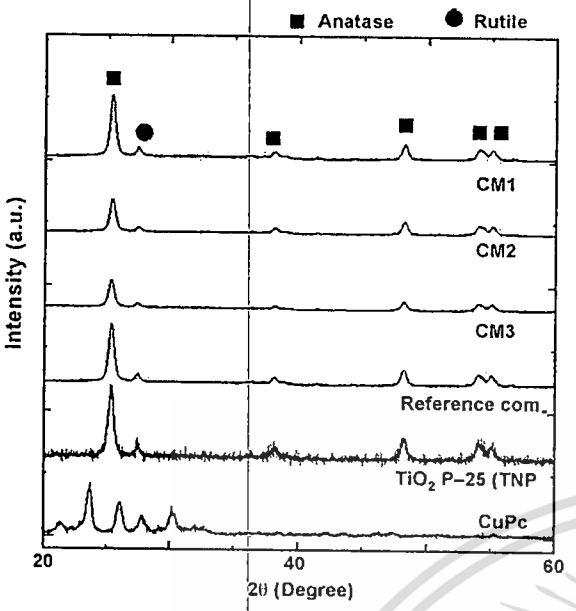

g. 2. XRD patterns of CuPc, TNP and TNP/CuPc hybrid composites prepared by M1, CM2, CM3 and reference composite.

opylene carbonate was finally filled in the device. The active area as-prepared DSSC was about 0.25 cm^2. Modified working electodes with hybrid composites using CM1, CM2 and CM3 method ere labeled as DCM1, DCM2 and DCM3, respectively. The referice composite was used in the application of working electrode aterials for the comparison of DSSC efficiency by three methods volved with ball milling process. The corresponding device was beled as reference device.

4. Characterization of hybrid TNP/CuPc composite and DSSC ficiency measurement with TNP/CuPc working electrode

1 wt.% of CuPc loaded in TNP matrix was chosen for XRD, SEM d Raman measurement. The structural properties of TNP/CuPc mposites were characterized by X-ray diffraction (XRD, BRUKER 3 Discover) and Raman spectroscopy (RENISHAW, Raman microope enclosure RE02, the excitation by laser with 785-nm line). ne surface morphology of hybrid composites and film thickness ere monitored by Field Emission-Scanning Electron Microscope E-SEM, Hitachi S-4700). Transmission Electron Microscopy (TEM) as performed using Phillips TECHAI 20. Photocurrent–voltage and e efficiency of DSSC with TNP/CuPc composites was measured nder the AM 1.5 irradiation (1000 W m^{-2}).

Results and discussion

1. Characteristics of TNP/CuPc composite and working electrode

The XRD patterns of CuPc, TNP and TNP/CuPc composites prered by three different methods are illustrated in Fig. 2. For TNP, e XRD peaks situated at $2\theta = 25.4°$, 38.1°, 48.1°, 54.2° and 54.4°, rrespond to (101), (004), (200), (105) and (211) planes of natase phase, consecutively whereas rutile phase in (110) plane is lated to the peak at $2\theta = 27.5°$. The crystalline size of the particle calculated by Scherrer equation from the major peak of anatase ase (101) in XRD pattern that shows approximately 18 nm [35]. e XRD patterns of CuPc in the range of 20–30° which are correonded to beta phase of CuPc (β-CuPc) [36] are clearly observed. eanwhile, XRD characteristics of all TNP/CuPc hybrid composites ve identical patterns to TNP patterns without noticeable peaks CuPc because of slight amount of CuPc in TNP host matrix. This

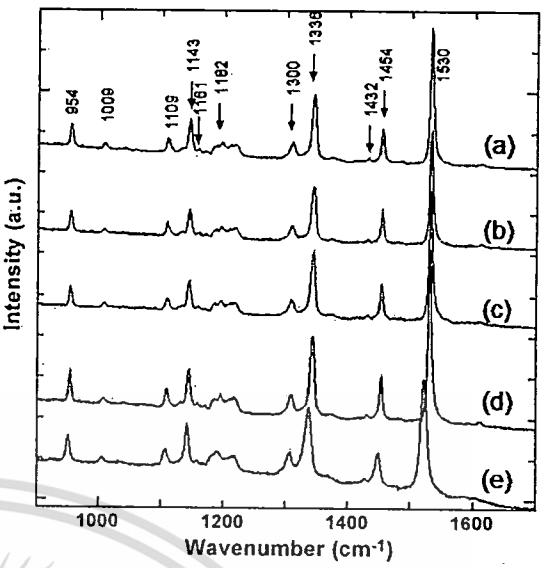

Fig. 3. Raman patterns of TNP, CuPc and hybrid TNP/CuPc composite prepared by CM1, CM2, CM3 and reference composite.

result implies that loading CuPc in TNP does not change the basis crystalline of TNP but it exists on the surface of TNP [30,32].

The Raman spectra of CuPc and TNP/CuPc hybrid composites are illustrated in Fig. 3. The wave numbers of Raman mode of CuPc and corresponding symmetries of vibration are listed in Table 1. The symmetry of A_{1g} and B_{2g} modes are noted as in-plane vibrations. The strongest peak of CuPc at 1530 cm^{-1} corresponds to C–N_m–C bonds as well as pyrrole rings expanding coupled with C–H in-plane bending vibrations [37]. Comparing to CuPc spectra, the Raman peaks of TNP/CuPc composites was slightly moved to high frequency. This noticeable shift may be initiated from anharmonic scattering effect from TNP closely adhered to CuPc particle [38].

The morphology of TNP, ball-milled CuPc and TNP/CuPc composites monitored from SEM images are illustrated in Fig. 4. It is obviously noticed from Fig. 4(a) that TNP particles is good crystalline and dispersion with particle size about 20–30 nm. The crystallite sizes observed by TEM are in good agreement with the results calculated by XRD pattern. Fig. 4(b) reveals that the minimized structures and magnificent dispersion of CuPc powder can be received by ball milling process. SEM images of TNP/CuPc composites prepared by three different methods at 1 wt.% of CuPc are shown in Fig. 4(c)–(e). TEM image of the composite prepared by method CM3 was carried out and shown in Fig. 4(f). This image indicates that the homogeneous dispersion and the spreading deposition of CuPc powder on TNP particles was attained after ball milling process and the small particles of TNP were covered with the expanding sheet (CuPc). These results suggest that, dur-

Table 1
Band assignment of Raman shifts of CuPc.

Raman wavenumber (cm^{-1})	Symmetry of vibration
954	B_{2g}
1009	A_{1g}
1109	A_{1g}
1143	A_{1g}
1161	B_{1g}
1182	B_{2g}
1300	B_{1g}
1336	A_{1g}
1432	B_{1g}
1454	B_{2g}
1530	B_{2g}

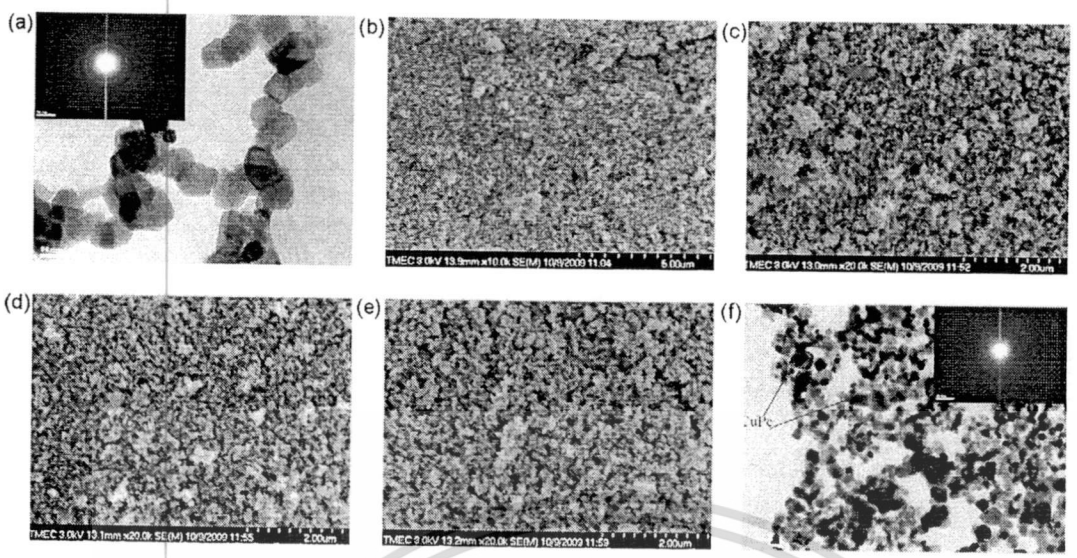

(a) TEM of TNP powder (inset: TNP diffraction), FE-SEM of (b) ball-milled CuPc powder, (c–e) CM1, CM2 and CM3 with 1 wt.% of CuPc and (f) TEM of the composite red by CM3 (insert: TNP/CuPc composite diffraction).

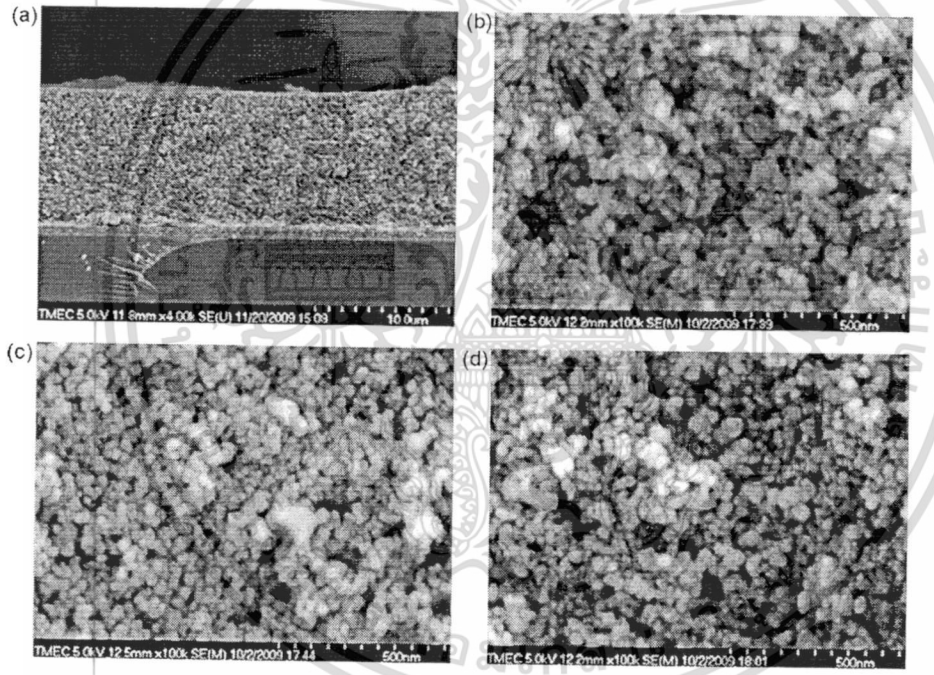

Fig. 5. FE-SEM of working electrode (a) the cross-section image (4k×) in device DCM1, (b) DCM1, (c) DCM2 and (d) DCM3.

all milling process, CuPc powder and TNP obtain sufficient no-mechanical energy for attaching them together to form a defined composite [39].

om SEM image in Fig. 5(a), the average thickness of TNP/CuPc d composite layer deposited on FTO electrode was evalu- o be approximately 10 μm. Fig. 5(b)–(d) shows the surface hology of hybrid TNP/CuPc composite layers on FTO elec- s. Each SEM image indicates the uniform distribution and ent coalition of the composites on the electrodes owing to le binding agent and sufficient nucleation energy from ther- eatment after annealing at 150 °C. Furthermore, the presence nopores in the composite layer is observed at the surface of ied working electrode. This feature advises that the absorp- f dye molecules to metal oxide layer can increase significantly the assistance of the porosity on modified working electrode. sing amount of absorbed dyes can consequently enhance the injection of electrons to TNP/CuPc working electrode [40,41].

3.2. Solar cell efficiency

Current density versus voltage (J–V) curves of DSSCs whose working electrode was modified by TNP/CuPc composites with 0.05 wt.% CuPc content are illustrated in Fig. 6. The device labeled as DCM3 displayed superiority in current density to the others. TNP/CuPc composite for DCM1 was prepared by homogenization process that is able to increase the dispersion of CuPc all over TNP matrix meanwhile ball milling process employed to synthesize the composite in DCM2 could enhance the adherence of CuPc on TNP surface. By utilizing these advantages of two processes for preparing the corresponding composite, the most desirable composite is achieved via CM3 method resulting in the highest performance efficiency of the DCM3 device. Two possible mechanisms are anticipated to take a responsibility on this enhancement of the device performance. First, with the presence of CuPc in the composite, the decrease of recombination of photo-injected electrons is expected

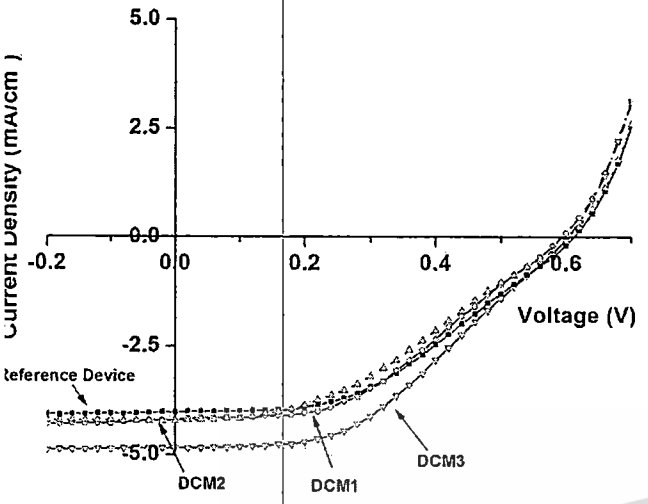

. 6. Photocurrent–voltage curves of DSSC device DCM1 (○), DCM2 (△), DCM3 (□) l reference device (■).

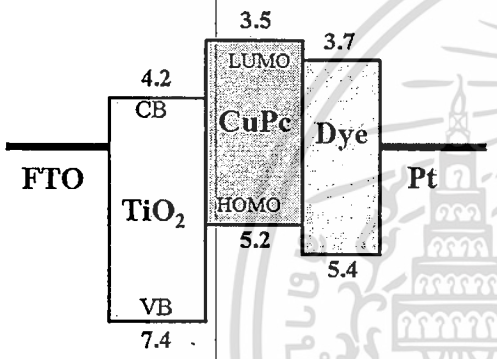

. 7. Schematic structure and energy band diagram for DSSC fabricated with ²/CuPc hybrid composite.

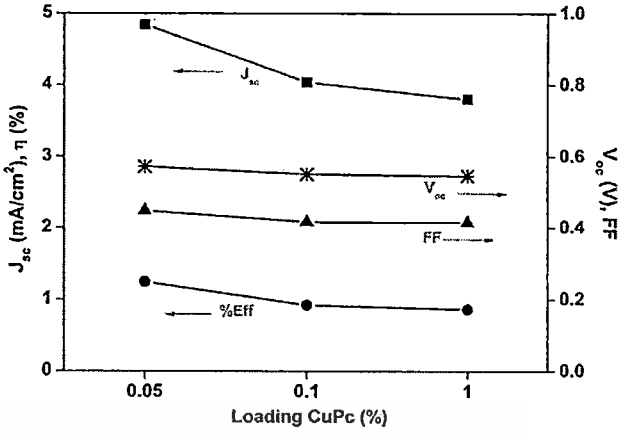

Fig. 8. The photovoltaic parameters as a function of loading the amount of CuPc in the composite prepared by CM3.

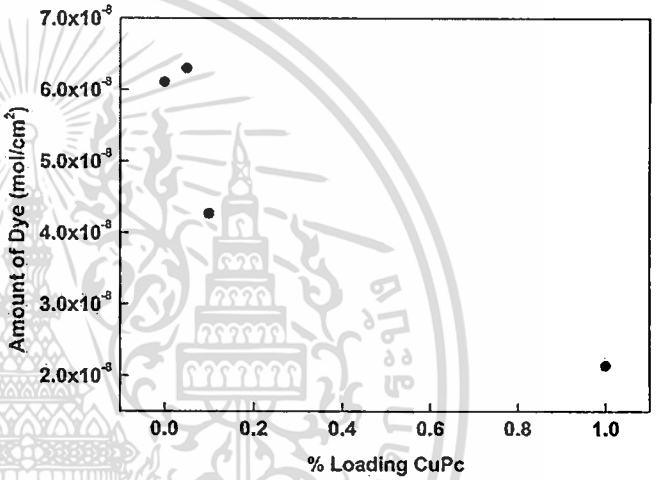

Fig. 9. The amount of absorbed dyes on modified working electrode as a function of CuPc in the composite prepared by CM3.

appear attributing to the more effective charge separation on the erface of TiO_2 and CuPc [31]. CuPc can also enhance the excited ctron transfer and promote the rapid injection these electrons TNP layer resulting in the significant improvement of photocur- nt of the device. The second possible mechanism is the reduction charge transfer resistances at the interface of the device. These istances are correlated to the barrier height at the interface [42]. ferring to vacuum level, the electronic structure of the conduc- n band and valence bands of TiO_2 are 4.2 and 7.4 eV, respectively 3]. The lowest unoccupied molecular orbital (LUMO) and highest upied molecular orbital (HOMO) levels of CuPc are at 3.5 and eV, respectively [44]. The energy band diagram of the modified rking electrode of the device is schematically drawn in Fig. 7. th the existence of CuPc, the barrier height between TiO_2 and dye er can be reduced and electron can move rapidly step-by-step to O_2. The faster the electron transport over the interface, the lower charge resistance and, consequently a greater current density of device can be attained. The photovoltaic parameters of devices re summarized in Table 2. The maximum J_{sc} of 4.84 mA/cm² and f 1.24% were obtained from the DCM3 whereas the current density of DCM1 and DCM2 are 4.20 and 4.19 mA/cm², respectively. The increase in current density of DCM3, comparing to the others, is approximately 15%. In contrast, V_{oc} and FF values of all devices exhibit insignificant improvement.

The effect of loading amount of CuPc on the device performance was also investigated. The results interpreted from the photovoltaic parameters as a function of CuPc amount were exhibited in Fig. 8. The optimized ratio of CuPc in TNP of 0.05% which gives the maximum current density was obtained. Fig. 9 shows the relationship of the amount of absorbed dye and the amount of loading CuPc. The highest dye absorption of modified working electrode was received at loading 0.05 wt.% CuPc in TNP. The greater amount of dye molecules absorbed on TNP/CuPc modified working electrode may generate more free charge carriers resulting to the increase of short circuit current density and energy conversion efficiency [40]. This result is coincidently agreeable to the results interpreted from the photovoltaic measurement. Further increase of loading CuPc in

le 2
tovoltaic parameters of DSSC devices DCM1, DCM2, DCM3 and reference device at loading CuPc 0.05 wt.%.

ample	Open circuit voltage, V_{oc} (V)	Short circuit current density, J_{sc} (mA/cm²)	Fill factor (FF)	Energy conversion efficency, η (%)
CM1	0.56	4.19	0.45	1.06
CM2	0.57	4.20	0.41	1.03
CM3	0.57	4.84	0.45	1.24
eference device	0.58	4.02	0.46	1.07

omposite apparently decreases the photovoltaic parameters, cially in J_{sc}. This occurrence may attribute to the truth that the r amount of CuPc molecules could reduce the dye absorption NP and the interception of electron from the electrolyte.

onclusion

summary, TNP/CuPc hybrid composites were successfully ared by low-energy ball milling route as a main part of the pro-ng, without any binders or high temperature heat treatment. and Raman results suggest that TNP structures are not affected ading CuPc in the composite. The optimized condition to obtain ood formation of this hybrid composite was received by ball ng process and homogenization through method CM3. The images indicate the uniform dispersion and excellent adher- of CuPc on TNP matrix. TNP/CuPc composites were applied odified working electrode material in DSSC. The device per-ance using current–voltage measurement was conducted and orresponding results exhibited that the device DCM3 granted ighest improvement in the current density. The decrease of nbination of photo-injected electrons and reduction of charge fer resistances at the interface of the device resulting rapid tion of these electrons to TNP layer are two possible mech-ns playing key roles on the enhancement of current density. optimum loading CuPc that allows the greatest amount of dye cules to be absorbed by TNP is 0.05 wt.%. Further increasing unt of CuPc in TNP causes the deterioration of device perfor-ce since the dye absorption on TNP and the interception of ron from the electrolyte could be obstructed by CuPc covered NP.

owledgements

is work has partially been supported by the National Nan-nology Center (NANOTEC), NSTDA, Ministry of Science and nology, Thailand, through its program of Center of Excellence ork. Authors would like to thank Thai Microelectronic (TMEC) E-SEM measurement, Central Institute of Forensic Science) for XRD measurement and NANOTEC for solar cell measure-t.

rences

Jitputti, S. Pavasupree, Y. Suzuki, S. Yoshikawa, J. Solid State Chem. 180 (2007) 743–1749.
. Wang, J. Zhang, Q. Luo, X. Li, Y. Duan, J. An, J. Hazard. Mater. 169 (2009) 46–550.
. Dong, Y. Ma, Y. Wang, Y. Tian, G. Ye, X. Jia, G. Cao, Mater. Lett. 63 (2009) 598–1600.
. O'Regan, M. Grätzel, Nature 353 (1991) 737–740.
[5] A.R. Malagutti, H.A.J.L. Mourão, J.R. Garbin, C. Ribeiro, Appl. Catal. B: Environ. 90 (2009) 205–212.
[6] F. Han, V.S.R. Kambala, M. Srinivasan, D. Rajarthnam, R. Naidu, Appl. Catal. A: Gen. 359 (2009) 25–40.
[7] M. Janus, A.W. Morawski, Appl. Catal. B: Environ. 75 (2007) 118–123.
[8] C. Yogi, K. Kojima, N. Wada, H. Tokumoto, T. Takai, T. Mizoguchi, H. Tamiaki, Thin Solid Films 516 (2008) 5881–5884.
[9] Y. Liu, C. Lü, M. Li, L. Zhang, B. Yang, Colloids Surf. A 328 (2008) 67–72.
[10] M. Grätzel, J. Photochem. Photobiol. A 164 (1–3) (2004) 3–14.
[11] C.Y. Huang, Y.C. Hsu, J.G. Chen, V. Suryanarayanan, K.M. Lee, K.C. Ho, Sol. Energy Mater. Sol. Cells 90 (2006) 2391–2397.
[12] K.M. Lee, V. Suryanarayanan, K.C. Ho, J. Power Sources 188 (2009) 635–641.
[13] V. Iliev, D. Tomova, L. Bilyarska, L. Prahov, L. Petrov, J. Photochem. Photobiol. A 159 (2003) 281–287.
[14] L. Giribabu, Ch.V. Kumar, V.G. Reddy, P.Y. Reddy, Ch.S. Rao, S.-R. Jang, J.-H. Yum, Md.K. Nazeeruddin, M. Grätzel, Sol. Energy Mater. Sol. Cells 91 (2007) 1611–1617.
[15] Y. Ma, J.N. Yao, J. Photochem. Photobiol. A 116 (1998) 167–170.
[16] S. Ngamsinlapasathian, S. Sakulkhaemaruethai, S. Pavasupree, A. Kitiyanan, T. Sreethawong, Y. Suzuki, S. Yoshikawa, J. Photochem. Photobiol. A 164 (2004) 145–151.
[17] X.H. Xia, Y. Liang, Z. Wang, J. Fan, Y.S. Luo, Z.J. Jia, Mater. Res. Bull. 43 (2008) 2187–2195.
[18] J.S. Chen, X.W. Lou, Electrochem. Commun. 11 (2009) 2332–2335.
[19] K.H. Ko, Y.C. Lee, Y.J. Jung, J. Colloid Interface Sci. 283 (2005) 482–487.
[20] L.R. Hou, C.Z. Yuan, Y. Peng, J. Hazard. Mater. B 139 (2007) 310–315.
[21] Y. Xiaodan, W. Qingyin, J. Shicheng, G. Yihang, Mater. Charact. 57 (2006) 333–341.
[22] M. Wang, X. Wang, Polymer 49 (2008) 1587–1593.
[23] D. Verma, R. Dash, K.S. Katti, D.L. Schulz, A.N. Caruso, Spectrochim. Acta Part A 70 (2008) 1180–1186.
[24] X. Tian, Z. Xu, F. Zhang, S. Zhao, G. Yuan, J. Li, Q. Sun, Y. Wang, Curr. Appl. Phys. 10 (2009) 129–132.
[25] F. Yakuphanoglu, Sol. Energy Mater. Sol. Cells 91 (2007) 1182–1186.
[26] C.M. Joseph, C.S. Menon, Mater. Lett. 52 (2002) 220–222.
[27] G. Chaidogiannos, F. Petraki, N. Glezos, S. Kennou, S. Nešpúrek, Mater. Sci. Eng., B: Solid 152 (2008) 105–108.
[28] F. Siviero, N. Coppedè, A.M. Taurino, T. Toccoil, P. Siciliano, S. Iannotta, Sens. Actuators, B: Chem. 130 (2008) 405–410.
[29] P. Balraju, M. Kumar, M.S. Roy, G.D. Sharma, Synth. Met. 159 (2009) 1325–1331.
[30] C.S. Chou, R.Y. Yang, M.H. Weng, C.H. Yeh, Powder Technol. 187 (2008) 181–189.
[31] X. Zhao, Z. Li, Y. Chen, L. Shi, Y. Zhu, Appl. Surf. Sci. 254 (2008) 1825–1829.
[32] K.C. Li, L. Yu, G. Ping, Z. Fan, Y.H. Bing, L.X. Yu, Chem. Res. Chin. Univ. 23 (2007) 154–158.
[33] R. Janot, D. Guérard, Prog. Mater. Sci. 50 (2005) 1–92.
[34] Y. Jin, Y. Liu, Y. Wang, J. Ye, J. Alloys Compd. 486 (2009) L34–L36.
[35] S.A. Amin, M. Pazouki, A. Hosseinnia, Powder Technol. 196 (2009) 241–245.
[36] K.S. Jung, J.H. Kwon, S.M. Son, J.S. Shin, G.D. Lee, S.S. Park, Synth. Met. 14 (2004) 259–264.
[37] Z. Liu, X. Zhang, Y. Zhang, J. Jiang, Spectrochim. Acta Part A 67 (2007) 1232–1246.
[38] M. Szybowicz, T. Runka, M. Drozdowski, W. Bala, A. Grodzicki, P. Piszczek, A. Bratkowski, J. Mol. Struct. 704 (2004) 107–113.
[39] H.C. Weerasinghe, P.M. Sirimanne, G.P. Simon, Y.B. Cheng, J. Photochem. Photobiol., A 206 (2009) 64–70.
[40] W. Jarernboon, S. Pimanpang, S. Maensiri, E. Swatsitang, V. Amornkitbamrung, Thin Solid Films 517 (2009) 4663–4667.
[41] K.M. Lee, V. Suryanarayanan, J.H. Huang, K.R.J. Thomas, J.T. Lin, K.C. Ho, Electrochim. Acta 54 (2009) 4123–4130.
[42] S.S. Kim, J.H. Yum, Y.E. Sung, Sol. Energy Mater. Sol. Cells 79 (2003) 495–505.
[43] M.N. Shan, S.S. Wang, Z.Q. Bian, J.P. Liu, Y.L. Zhao, Sol. Energy Mater. Sol. Cells 93 (2009) 1613–1617.
[44] S.H. Lee, D.H. Kim, J.H. Kim, T.H. shim, J.G. Park, Synth. Met. 159 (2009) 1705–1709.

Journal of
Nanoscience and Nanotechnology
Vol. 11, 6483–6489, 2011

Quasi-Solid-State Dye-Sensitized Solar Cells Based on TiO_2/NiO Core–Shell Nanocomposites

Wanichaya Mekprasart*, Russameeruk Noonuruk, Wirat Jarernboon, and Wisanu Pecharapa

College of KMITL Nanotechnology, King Mongkut's Institute of Technology Ladkrabang, Bangkok 10520, Thailand, and Thailand Center of Excellence in Physics (ThEP Center), CHE, 328 SiAyutthaya Rd., Bangkok 10400, Thailand

The core–shell nanocomposites of titanium dioxide (TiO_2) and nickel oxide (NiO) used as modified photoelectrode materials in a quasi-solid-state dye-sensitized solar cell (quasi-DSSC) were synthesized using TiO_2 P-25 and a nickel acetate precursor, via ball milling. The as-obtained intermediate products were annealed at 350, 450, and 550 °C. The structural properties of the NiO/TiO_2 nanocomposites were well characterized via X-ray diffraction, field emission scanning electron microscopy, and transmission electron microscopy. The results imply that NiO-shell-coated TiO_2 nanoparticles can be obtained with the assistance of sufficient thermal energy in the system. The crystallite size of the composite increased as the annealing temperature increased. Among all the prepared conditions, the composite with 0.1 wt% NiO exhibited the best performance, with an optimized solar-energy conversion efficiency of 2.29% and with a short-circuit current density of 7.21 mA/cm^2. The significant enhancement of the device's current density may be associated with the charge recombination suppression by the NiO shell, which acted as a potential barrier in the composite. The decrease in the recombination of the photo-injected electrons, and the increase in the number of electrons tunneling through the NiO layer at the interface, may have resulted from the presence of a NiO layer on the TiO_2 nanoparticles.

Keywords: NiO, TiO_2, Core–Shell Nanocomposite, Ball Milling.

RESEARCH ARTICLE

INTRODUCTION

e pioneer of the dye-sensitized solar cell (DSSC) based a nanocrystalline film of TiO_2 was first reported O'Regan and Grätzel in 1991.[1] In the last decade, SC has received increasing attention because of its nsiderable advantages of low-cost fabrication and high ergy conversion efficiency (~11%).[2,3] The evaporation liquid electrolytes at a high temperature, however, l the permeation of water and oxygen molecules into the electrolytes, are its crucial drawbacks.[4] To overne these problems, the solid-sate dye-sensitized solar l (SSDSSC) and the quasi-solid-state dye-sensitized ar cell have been proposed. A number of reports ently focused on pioneer works to improve the perfornce of these devices through the use of various techues. Chen et al. successfully improved the durability the quasi-solid-state DSSC at high temperatures by ng a novel composite electrolyte based on 1-propylnethylimidazolium iodide and polyaniline-load carbon black.[5] Akhtar et al. reported on the preparation of a novel carbon nanotube-polyethylene oxide composite electrolyte, which was used as a substitute electrolyte in DSSC. It was found that the device associated with this electrolyte performed enhanced interfacial contact between the electrodes and the electrolytes, thus reflecting an improvement in the device performance.[6] Katsaros et al. reported that the high efficiency of all solid-state DSSCs was observed by using polyethylene oxide (PEO), titanium oxide, and LiI-I_2 composite polymer/inorganic electrolytes.[7]

Meanwhile, the improvement of the DSSC efficiency can be achieved by modifying the TiO_2 working electrode layer through the use of compatible materials.[8–10] The core–shell nanocomposite of the TiO_2 structure is one of the potential structures that can enhance the physical and chemical properties of DSSC. This core–shell structure was recently applied to optoelectronic devices, catalysts, and the modified working electrodes in DSSCs. Fu et al. reported that an increase in magnetic performance and electron absorbance was observed when the TiO_2 surface was enwrapped with the $BaFe_{12}O_{19}$ magnetic material.[11] He et al. developed a novel biomaterial composed of

uthor to whom correspondence should be addressed.

Fe_3O_4:TiO_2 core–shell nanoparticles for a higher HeLa cell killing efficiency in photocatalytic activity by generating much more oxidative free radicals than pure TiO_2.[12] Ganapathy et al. reported that the TiO_2/alumina core–shell acting as a modified working electrode can enhance the dye absorption and decrease the carrier recombination of DSSCs.[13] The core–shell structure technique was recently synthesized with the incipient wetness impregnation method, ball milling process, and solution synthesis, which have been reported in various researches.[14–16] In addition, the *p–n* heterojunction structure is effectively utilized in quasi-solid-state DSSCs to enhance the device performance. A previous work provided evidence that a modified working electrode in the form of a *p–n* junction layer can suppress the leakage of trapped electrons to the electrolyte interface.[17] NiO is a natural *p*-type semiconductor material with a relatively wide bandgap (3.6–4.0 eV) and excellent chemical and electrical stability. Various uses of NiO have been cited, including as an electrochemical supercapacitor, a gas sensor, an electrochromic display device, and a fuel cell electrode.[18–21] Meanwhile, TiO_2 is the most commonly used material for the working electrodes in DSSCs due to its high energy conversion efficiency compared to other metal oxide semiconductors.[22,23] It has been found that when loading *p*-type NiO onto *n*-type TiO_2, a *p–n* junction can be formed at the NiO/TiO_2 interface, resulting in improved device performance due to the minimization of charge recombination and the enhancement of the charge transferat the interface. A number of techniques of loading NiO onto a TiO_2 matrix were recently reported, including dry mixing, the sol–gel process, and chemical deposition,[24–26] but how to improve the homogenous dispersion of NiO onto TiO_2 in the form of a composite is still being explored. Low-energy ball milling is a potential technique for synthesizing the desired composites, because of its simple preparation, cost-effective process, and lesser defect accumulation compared to high-energy ball milling.[27]

In this work, the synthesis of a NiO/TiO_2 core–shell nanocomposite by coating a nickel acetate precursor via ball milling onto TiO_2 nanoparticles, and then annealing at an intermediate temperature, is reported. This process can provide homogeneity and good dispersion of a NiO shell onto a TiO_2 core matrix, leading to a well-defined composite of the two materials. The fundamental physical properties of the composite were thoroughly investigated via X-ray diffraction (XRD), field emission scanning electron microscopy (FESEM), and transmission electron microscopy (TEM). This functional composite was applied as a modified working electrode material in quasi-DSSCs. The performance of the device with the modified electrodes was measured and compared with that of the conventional device.

2. EXPERIMENTAL DETAILS

2.1. Preparation of the NiO/TiO_2 Core–Shell Nanocomposite

Degussa P-25 TiO_2 nanoparticles with an average particle size of 20 nm were purchased from Germany. Nickel(II)-acetate tetrahydrate (98%) purchased from Aldrich was chosen as the NiO precursor. The conventional ball-milling process for the synthesis of a NiO/TiO_2 core–shell nanocomposite was carried out with horizontal rolling. To create the ball-milled condition, several zirconia balls with 1.47 and 5.36 mm diameters were placed in a cylindrical plastic vial with a height of 7.7 cm and an inner diameter of 4.5 cm. Ball milling was continuously carried out for 18 h on a cylindrical roller, at 100 rpm (10.47 rad s^{-1}), with a ball-to-powder weight ratio of 30:1.

Nickel acetate tetrahydrate was dissolved in 10 ml ethanol solution and 1 ml DEA and was stirred at 100 °C for 2 h. Afterwards, the gel solution was supplied to TiO_2 dispersed in ethanol solution via ball milling for 18 h. The suspension was stirred at 100 °C until the ethanol had completely evaporated. The as-prepared solid precipitate of NiO/TiO_2 was dried at 100 °C for 24 h. The ratios of NiO loading onto 3 g TiO_2 were fixed at 0.1, 1, and 2 wt%. Finally, the composites with varied amounts of NiO in TiO_2 were heated in air at 350, 450, and 550 °C for 2 h, respectively.

2.2. NiO/TiO_2 Core–Shell-Nanocomposite-Based Working Electrode Preparation

The preparation of the NiO/TiO_2 working electrode started with the deposition of a compact layer[28] on a fluorine-doped tin oxide (FTO, 15 Ω/□) conductive substrate. 0.2 g of each loading amount of NiO in the TiO_2 matrix was blended with a few drops of acetic acid, deionized water, and Triton-X binder, after which the mixture was ground in a white mortar for 30 min and was deposited on the top part of the dense layer via the doctor blade technique. The working electrodes were then dried at 100 °C for 1 h in ambient air, followed by annealing at 450 °C for 1 h, resulting in a compact NiO/TiO_2 layer. The electrodes were then immersed in a 3×10^{-4}-mol N719 dye solution [Cis-bis(isothiocyanato)bis(2,2′-bipyridyl-4,4′dicarboxylato)-ruthenium(II)bis-tetrabutylammonium] at room temperature for 24 h, in the dark. Finally, NiO/TiO_2 working electrodes in each ratio were obtained.

2.3. Fabrication of DSSC with a NiO/TiO_2 Core–Shell-Nanocomposite-Based Working Electrode

A DSSC was designed with a sandwich structure, with a NiO/TiO_2 working electrode and a platinum film coated onto the FTO counterelectrode. The parapolymer film was

nserted between the two electrodes to prevent device ·ort-circuiting. The composite gel electrolyte consisting f 3 ml of 6 g polyethylene glycol (PEG-6000) dispersed n 10 ml acetonitrile with 0.05 M I_2, 0.5 M KI, 0.2 M butyl pyridine, and 0.2 g TiO_2 P-25 was finally made to ll the device.[29] The active area of the as-prepared DSSC as about 0.25 cm^2.

4. Characterization of the NiO/TiO_2 Nanocomposite, and DSSC Efficiency Measurement with a NiO/TiO_2 Working Electrode

he structural properties of the NiO/TiO_2 core–shell nocomposite were characterized via XRD (BRUKER 8 Discover) and TEM (JEOL JEM-2010). The surface orphology of the composite was monitored via FESEM (itachi S-4700). The photocurrent-voltage characteris-s and efficiency of the quasi-DSSC with NiO/TiO_2 nocomposites were measured under AM1.5 irradiation 000 $W \cdot m^{-2}$).

RESULTS AND DISCUSSION

1. Characteristics of the NiO/TiO_2 Nanocomposite and Working Electrode

e XRD patterns of the pre- and post-annealed NiO/TiO_2 nocomposites at 350, 450, and 550 °C are shown in ;ure 1. The XRD peaks that appeared at $2\theta = 25.4$, 38.1, .1, 54.2, and 54.4°, correspond to the (101), (004), (200),)5), and (211) planes of the anatase phase of TiO_2 P-25, pectively, whereas the rutile phase in the (110) plane related to the peak that appeared at $2\theta = 27.5°$. The

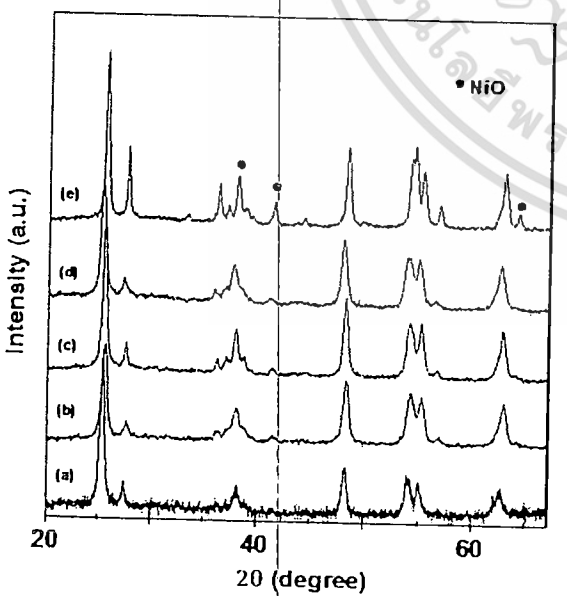

1. XRD patterns of (a) TiO_2 P-25, (b) the pre-annealed NiO/TiO_2 composite, and the NiO/TiO_2 nanocomposites annealed at (c) °C, (d) 450 °C, and (e) 550 °C.

other three distinct diffraction peaks at $2\theta = 37.4$, 43.4, and 63.1° correspond to the (111), (200), and (220) orientation planes of cubic-NiO.[30] These three peaks were not observed in the XRD pattern of the pre-annealed sample, indicating that the crystallization of NiO was not formed. After annealing, however, these characteristic peaks were clearly observed, and their peak intensity exhibited a significant increase with increasing annealing temperature, implying the formation of a crystalline of NiO on the TiO_2 matrix. Meanwhile, the characteristic peaks of TiO_2 also displayed noticeably stronger and narrower features with increasing annealing temperature. With an increase in temperature, sufficient thermal energy was supplied to the system, and the TiO_2 particles agglomerated, resulting in an increase in crystallite size.[31]

The surface morphologies of the working electrodes of TiO_2, the NiO/TiO_2 nanocomposites ball-milled at various annealing temperatures, monitored from the SEM images, are shown in Figure 2. It can be clearly seen in Figure 2(a) that the TiO_2 particles well dispersed in cluster form throughout the film surface. SEM images of the NiO/TiO_2 composites annealed at different temperature are shown in Figures 2(b)–(d). These images indicate that the homogeneous dispersion of the composites was attained. As the annealing temperature rose, the crystallinity and size of the NiO/TiO_2 composite film significantly improved due to the stronger accumulation of NiO/TiO_2 composites induced by the higher thermal energy. The results disclosed by the SEM images are in good agreement with the interpreted XRD results. The EDX spectrum and mapping of the NiO/TiO_2 nanocomposite at 2 wt% are shown in Figure 3. The peaks of Ti and Ni in the EDX result confirm that the NiO/TiO_2 nanocomposite was composed of TiO_2 and NiO. The dots on the map show the major elements of Ti, O, and Ni in the composite. This result affirms that the ratio of NiO in the composite is 2 wt%.

The formation of a core–shell structure of the NiO/TiO_2 nanocomposite is demonstrated by the TEM image shown in Figure 4. The surface of the TiO_2 nanoparticle was thoroughly coated with a ~2-nm-thick NiO layer in the light region. This result indicates that the NiO/TiO_2 nanocomposite prepared using the technique described above assumed a core–shell structure.

3.2. Solar-Cell Efficiency

The characteristic current density versus voltage (J–V) curves of the quasi-DSSCs with 0.1-wt% NiO/TiO_2 nanocomposites annealed at various temperatures are shown in Figure 5. The modified working electrodes with TiO_2 P-25 and NiO/TiO_2 core–shell nanocomposites annealed at 350, 450, and 550 °C were labeled as RD, D1, D2, and D3, respectively. D2 exhibits the most efficient performance, especially in terms of current density, compared to the others. The photovoltaic parameters of the

RESEARCH ARTICLE

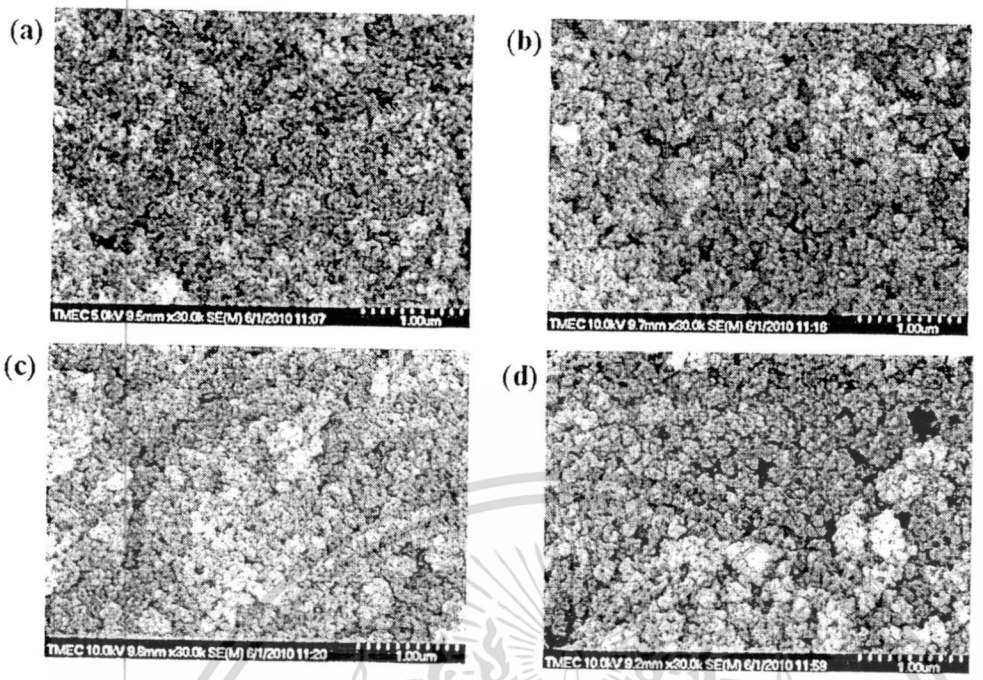

ig. 2. SEM images of the (a) TiO_2 P-25 and NiO/TiO_2 nanocomposites annealed at (b) 350 °C, (c) 450 °C, and (d) 550 °C.

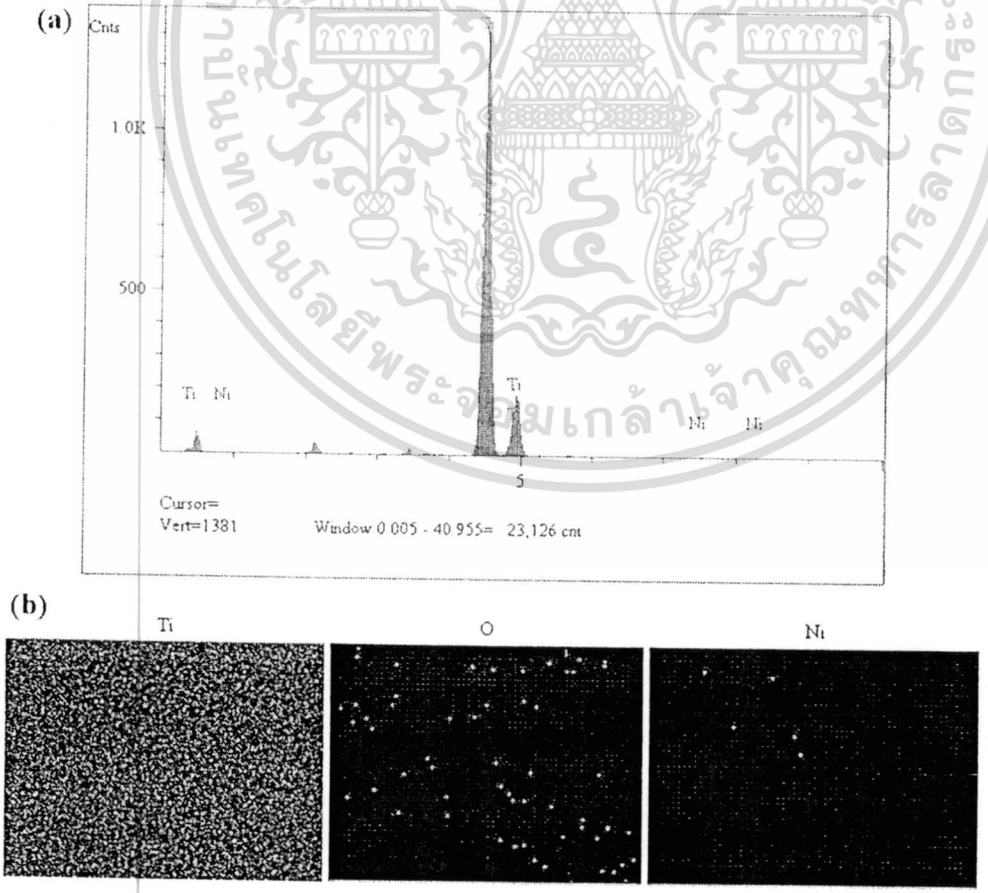

g. 3. EDX spectrum and mapping of the 2-wt% NiO/TiO_2 nanocomposite annealed at 450 °C.

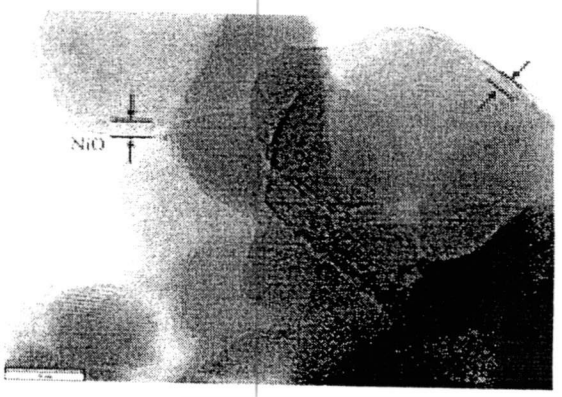

ig. 4. TEM image of the NiO/TiO_2 core–shell nanocomposite nnealed at 550 °C.

evices are summarized in Table II. The maximum J_{sc} of .21 mA/cm^2 with an η of 2.29% was obtained from D2, hereas the current densities of D1 and D3 were 6.51 and .10 mA/cm^2, respectively. The increasing current density f D2, compared to that of RD, is approximately 15%. In ontrast, the V_{oc} and FF values of all the devices exhibited significant improvement.

It can be deduced that the performance of the devices an be influenced by the presence of NiO in the compos- e, and by the annealing temperature of the as-prepared anocomposites. The optimized conditions providing the est performance were obtained by the device prepared om the 0.1-wt% NiO/TiO_2 nanocomposite annealed at 50 °C. The possible mechanisms and key roles of NiO nd of the annealing temperature on the improvement of ie device performance are proposed. With regard to the acuum level, the conduction band (CB) and valence bands f TiO_2 were found to be 4.2 and 7.4 eV, respectively; iose of NiO were 1.8 and 5.4 eV; and those of the dye ere 3.4 and 5.9 eV, respectively.[32–34] Due to the higher B of NiO compared to both TiO_2 or the dye-excited ate, the NiO shell layer can act as an electron-blocking

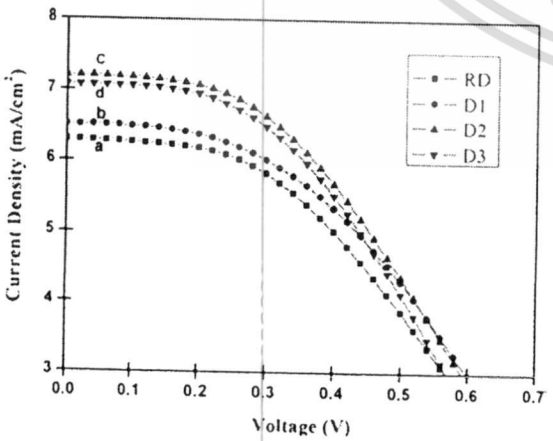

g. 5. Photocurrent-voltage curves of quasi-DSSC with the (a) TiO_2 25 and 0.1-wt% NiO/TiO_2 nanocomposites annealed at (b) 350 °C 1), (c) 450 °C (D2), and (d) 550 °C (D3).

Table I. Mapping characterization of the 2-wt% NiO/TiO_2 composite.

Element	Line	Intensity (c/s)	Weight (wt%)
O	Kα	10.04	3.971
Ti	Kα	588.97	94.203
Ni	Kα	1.28	1.826
Total			100.000

layer that can retard the recombination of the injected electrons.[13] Meanwhile, p-type NiO can act as a hole collector. The formation of the p–n junction can occur at the NiO/TiO_2 interface, resulting in a potential gradient that can enhance the charge separation.[35] The efficiency of the device can therefore be enhanced by the blocking effect of the NiO layer associated with the possibility of p–n junction formation at the core–shell interface.

During illumination, the photoexcited electrons from the dye-excited state probably encounter difficulty in overcoming the potential barrier formed by NiO.[36] These electrons, however, can penetrate the layer through the tunneling effect, which strongly depends on the width of the adjacent NiO barrier. According to the XRD and SEM results, the crystallite size of NiO increased when the composite was annealed at higher temperatures, resulting in the wideness of the potential barrier formed by NiO. When the NiO shell thickness exceeded the tunneling thickness (~2 nm), the electron injection into TiO_2 was blocked. Therefore, the broadened width of the NiO barrier causes a decrease in the tunneled electrons, reflecting lower device performance. At a low annealed temperature (350 °C), the crystallinity of NiO still becomes weaker because the formation of NiO initially occurs from the precursor material at this temperature.[37] When the annealing temperature rises to 450 °C, the system can obtain adequate energy, leading to the strong nucleation of the NiO-shell layer, and better crystallinity. Further heating from this temperature can further increase the NiO layer thickness, resulting in the deterioration not only of the photogenerated current through the NiO barrier but also of the device performance. Therefore, the optimized annealing temperature is essential for the formation of an appropriate NiO barrier in the composite, leading to the enhancement of the device efficiency.

Table II. Photovoltaic parameters of DSSC fabricated 0.1%wt NiO/TiO_2 composite annealed at different temperature.

Sample	Open circuit voltate, V_{oc} (V)	Short circuit current density, J_{sc} (mA/cm^2)	Fill factor (FF)	Energy conversion efficienty, η (%)
RD	0.80	6.29	0.40	2.02
D1	0.80	6.51	0.42	2.20
D2	0.78	7.21	0.41	2.29
D3	0.75	7.10	0.42	2.22

RESEARCH ARTICLE

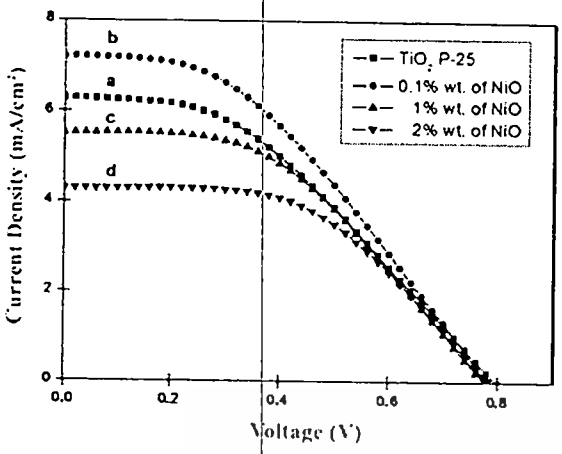

g. 6. Photocurrent-voltage curves of quasi-DSSC with (a) TiO_2 P-25 d (b) 0.1-, (c) 1-, and (d) 2-wt% NiO/TiO_2 composite annealing at 0 °C.

The effect of the loading amount of NiO on the device erformance was also investigated, as shown in Figure 6. he optimized ratio of 0.1-wt% NiO in TiO_2 exhibited the aximum J_{sc} of 7.21 mA/cm^2. After reaching this value, e J_{sc} and □ significantly decreased with an increasing ading amount of NiO in the composite, as shown in gure 6. Possible mechanisms of this phenomenon are ggested herein. With the presence of an NiO blocking layer, the recombination of the injection electrons suppressed, causing greater electron accumulation near e interface. The increasing charge population at the terface with increasing NiO loading amount will result a rise in the quasi-Fermi level of TiO_2, and consequently to the higher V_{oc} of the device, as shown in gure 6.[13] The greater amount of NiO loaded into the mposite may also lead to the agglomeration of NiO ystalline and the wideness of the NiO barrier, resulting in a lower transport rate of the tunneled electrons. iO can also play a negative role beyond determining e tunneling distance if it becomes overabundant in the mposites.[38]

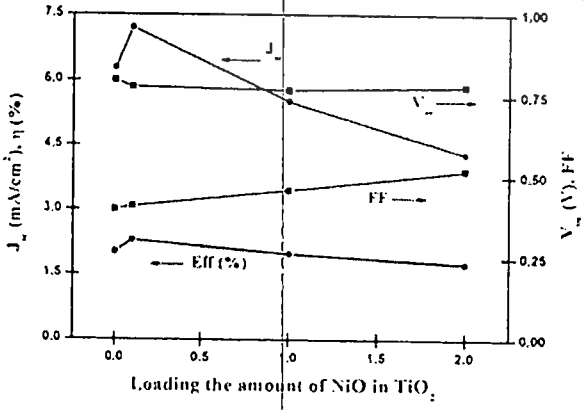

g. 7. Photovoltaic parameters of quasi-DSSC fabricated with different dings of NiO/TiO_2 nanocomposites annealed at 450 °C.

4. CONCLUSION

NiO/TiO_2 core–shell nanocomposites were successfully prepared via low-energy ball milling without using any binder. The XRD results suggested that a NiO structure existed in the TiO_2 matrix, and that better formation of NiO/TiO_2 nanocomposites was achieved as the annealing temperature was increased. The good crystallinity and the increasing size of the nanocomposite were revealed by the SEM images. The formation of a NiO-shell layer on the TiO_2 particles was confirmed by the EDX analysis and the TEM image that was obtained. The NiO/TiO_2 core–shell nanocomposites were applied as modified working electrode materials in quasi-DSSCs. The device performance was evaluated, and the results showed that device D2 had the highest efficiency, especially in terms of the current density. The optimized conditions that paved the way for the excellent performance of a nanocomposite were achieved by loading 0.1 wt% NiO onto TiO_2 and then annealing at 450 °C. The NiO shell in the core–shell composite can serve as a blocking layer, at which electron injection recombination is suppressed, and may lead to the formation of a *p–n* junction at the core–shell interface. This present NiO shell layer is playing key roles with regard to the functionality of the fabricated nanocomposite in the device. A further increase in the NiO loading amount, however, and in the annealing temperature, may result in the reduction of electron injection tunneling through the composite interface due to the excessive thickness of the NiO blocking layer.

Acknowledgment: This work was partially supported by National Nanotechnology Center (NANOTEC), NSTDA, Ministry of Science and Technology, Thailand, through its "Center of Excellence Network" program. The authors would like to thank Thai Microelectronic (TMEC) and NANOTEC for the FESEM and solar-cell measurements they conducted for this work, respectively.

References and Notes

1. B. O'Regan and M. Grätzel, *Nature* 353, 737 (1991).
2. M. Grätzel, *J. Photoch. Photobio. A* 164, 3 (2004).
3. K. H. Ko, Y. C. Lee, and Y. J. Jung, *J. Hazard Mater. B* 139, 310 (2007).
4. J. Wu, Z. Lan, D. Wang, S. Hao, J. Lin, Y. Wei, S. Yin, and T. Sato, *J. Photoch. Photobio. A* 181, 333 (2006).
5. P.-Y. Chen, C.-P Lee, R. Vittal, and K.-C. Ho, *J. Power Sources* 195, 3933 (2010).
6. M. S. Akhtar, J.-G. Park, H.-C. Lee, S.-K. Lee, and O.-B. Yang, *Electrochim. Acta* 55, 2418 (2010).
7. G. Katsaros, T. Stergiopoulos, I. M. Arabatzis, K. G. Papadokostaki, and P. Falaras, *J. Photoch. Photobio. A* 149, 191 (2002).
8. W. Mekprasart, W. Jarernboo, and W. Pecharapa, *Mat. Sci. Eng. B* 172, 231 (2010).
9. K. H. Ko, Y. C. Lee, and Y. J. Jung, *J. Colloid Interface Sci.* 283, 482 (2005).
10. M. Wang and X. Wang, *Polymer* 49, 1587 (2008).

1. W. Fu, H. Yang, M. Li, L. Chang, Q. Yu, J. Xu, and G. Zou, *Matter. Lett.* 60, 2723 (**2006**).
2. Q. He, Z. Zhang, J. Xiong, Y. Xiong, and H. Xiao, *Opt. Mater.* 31, 380 (**2008**).
3. V. Ganapathy, B. Karunagaran, and S.-W. Rhee, *J. Power Sources* 195, 5138 (**2010**).
4. X.-L. Yang, W.-L. Dai, C. Guo, H. Chen, Y. Cao, H. Li, H. He, and K. Fan, *J. Catal* 234, 438 (**2005**).
5. W. K. Chang, K. K. Rao, H. C. Kuo, J. F. Cai, and M. S. Wong, *Appl. Catal. A-Gen.* 321, 1 (**2007**).
6. X. Su, J. Zhao, Y. Li, Y. Zhu, X. Ma, F. Sun, and Z. Wang, *Collid Surface* 349, 151 (**2009**).
7. J. Bandara, C. M. Divarathne, and S. D. Nanayakkara, *Sol. Energ. Mat. Sol. C* 81, 429 (**2004**).
8. U. M. Patil, R. R. Salunkhe, K. V. Gurav, and C. D. Lokhande, *Appl. Surf. Sci.* 255, 2603 (**2008**).
9. A. Qureshi, A. Mergen, and A. Altindal, *Sensor Actuat. B-Chem.* 135, 537 (**2009**).
10. C. G. Granqvist, P. C. Lansåker, N. R. Mlyuka, G. A. Niklasson, and E. Avendaåo, *Sol. Energ. Mat. Sol. C* 93, 2032 (**2009**).
11. Y. Yin, W. Zhu, C. Xia, and G. Meng, *J. Power Sources* 132, 36 (**2004**).
12. W. Jarernboon, S. Pimanpang, S. Maensiri, E. Swatsitang, and V. Amornkitbamrung, *Thin Solid Films* 517, 4663 (**2009**).
13. S. Ngamsinlapasathian, S. Sakulkhaemaruethai, S. Pavasupree, A. Kitiyanan, T. Sreethawong, Y. Suzuki, and S. Yoshikawa, *J. Photoch. Photobio. A* 164, 145 (**2004**).
24. C.-S. Chou, Y.-J. Lin, R.-Y. Yang, and K.-H. Liu, *Adv. Powder Technol.* Article in press (**2010**).
25. J. Bandara and H. Weerasinghe, *Sol. Energ. Mat. Sol. C* 85, 385 (**2005**).
26. L. Ren, Y.-P. Zeng, and D. Jiang, *Solid State Sci.* 12, 138 (**2010**).
27. Y. Jin, Y. Liu, Y. Wang, and J. Ye, *J. Alloy Compd.* 486, L34 (**2009**).
28. H. Yu, S. Zhang, H. Zhao, G. Will, and P. Liu, *Electrochim. Acta* 54, 1319 (**2009**).
29. M. S. Akhtar, J.-M. Chun, and O-B. Yang, *Electrochem. Commun.* 9, 2833 (**2007**).
30. S. Thota and J. Kumar, *J. Phys. Chem. Solids* 68, 1951 (**2007**).
31. C.-Y. Huang, Y.-C. Hsu, J.-G. Chen, V. Suryanarayanan, K.-M. Lee, and K.-C. Ho, *Sol. Energ. Mat. Sol. C* 90, 2391 (**2006**).
32. M. N. Shan, S. S. Wang, Z. Q. Bian, J. P. Liu, and Y. L. Zhao, *Sol. Energ. Mat. Sol. C* 93, 1613 (**2009**).
33. M. D. Irwin, D. B. Buchholz, A. W. Hains, R. P. H. Chang, and T. J. Marks, *PANS* 105, 2783 (**2008**).
34. B. Peng, G. Jungmann, C. Jäger, D. Haarer, H.-W. Schmidt, and M. Thelakkat, *Coordin. Chem. Rev.* 248, 1479 (**2004**).
35. Y.-M. Lee and C.-H. Lai, *Solid State Electron.* 53, 1116 (**2009**).
36. J. Bandara, U. W. Pradeep, and R. G. S. J. Bandara, *J. Photoch. Photobio. A* 170, 273 (**2005**).
37. M.-W. Xu, S.-J. Bao, and H.-L. Li, *J. Solid State Electr.* 11, 372 (**2007**).
38. L. Li, R. Chen, G. Jing, G. Zhang, F. Wu, and S. Chen, *Appl. Surf. Sci.* 256, 4533 (**2010**).

Received: 7 July 2010. Accepted: 30 January 2011.

RESEARCH ARTICLE

Available online at www.sciencedirect.com

SciVerse ScienceDirect

Energy Procedia 9 (2011) 509 – 514

Energy Procedia

9th Eco-Energy and Materials Science and Engineering Symposium

Synthesis and characterization of nitrogen-doped TiO_2 and its photocatalytic activity enhancement under visible light

Wanichaya Mekprasart [a,b]* and Wisanu Pecharapa [a,b]

[a]*College of Nanotechnology, King Mongkut's Institute of Technology Ladkrabang, Bangkok 10520, Thailand*
[b]*ThEP Center, CHE, 328 SiAyutthaya Rd., Bangkok 10400, Thailand*

Abstract

Nitrogen-doped TiO_2 nanopowders were synthesized by homogenization and conventional mechanically stirred technique in DI water media. Different amount of nitrogen was loaded in TiO_2 matrix. As-obtained intermediate products were annealed at 100°C for 30, 60 and 120 min. The structural properties of samples were characterized by X-ray diffraction. The absorption spectrum of N-doped TiO_2 photocatalyst was analyzed via UV-Vis spectrophotometry. When doping TiO_2 with nitrogen, its absorption spectrum is shifted to visible region resulting in the enhancement of photocatalyst properties in dye photodegradation. The photocatalytic activity of TiO_2 and N-doped TiO_2 was investigated by the degradation of Rhodamine B dye under visible light.

Keywords: N-doped TiO_2; photocatalyst; photodegradation; visible light.

1. INTRODUCTION

Photocatalysts have been widely researched and obtained great attraction since the past decades. Titanium dioxide (TiO_2) is one of functional metal oxide semiconductor that performs high efficiency in photocatalytic activities because of non-toxicity, excellent energy conversion efficiency and long-term chemical stability [1]-[3]. Several studies have been reported on the usage of TiO_2 photocatalyst in various environmental applications such as photodegradation of organic and inorganic pollutants, decolorization of dyes, water purification and hydrogen production from water-splitting reaction [4]-[8].

* Corresponding author. Tel.: +66-23298000; fax: +66-23298256.
E-mail address: wani.mek@gmail.com.

1876-6102 © 2011 Published by Elsevier Ltd. Selection and/or peer-review under responsibility of CEO of Sustainable Energy System, Rajamangala University of Technology Thanyaburi (RMUTT).
doi:10.1016/j.egypro.2011.09.058

However, TiO_2 can be activated in UV illumination due to its wide band gap energy. Thus, only 3-5% of UV in solar spectrum is less absorbed by itself. This is the main drawback of TiO_2 photocatalyst that is hardly activated in visible light. High recombination rate of photoelectron-hole is also one of its hindrances that still retarded the photocatalytic mechanism. Many efforts have been made to conquer these problems by doping with non-metal in TiO_2 such as Carbon (C), Sulfur (S) and Nitrogen (N) [9]-[11]. Among the non-metal dopant, N is one of material that was acknowledged for enhancing the photoresponding range into visible light. Horst Kisch and co-workers reported that band gap energy of TiO_2 can be reduced from 3.18 to 2.20 eV by nitrogen incorporation [12]. Jing Li and co-workers proved that the significant visible light response and strong increase of photocurrent under UV and visible range were obtained by N-doped TiO_2 [13]. S. Bangkedphol and colleague reported on the improvement of photocatalytic degradation of tributyltin under natural light by using N-doped TiO_2 [14].

The main objective of this work is to investigate the effect of the different content of N doping in commercial TiO_2 powder and baking time on its structure and response in visible range. The efficiency of N-doped TiO_2 photocatalysts were proved by the photocatalytic degradation of Rhodamine B (RhB) under visible illumination.

2. EXPERIMENT

N-doped TiO_2 was prepared by mechanical mixing through homogenization and magnetic stirring. Commercially available TiO_2 (Aeroxide® TiO_2 P25, Nippon Aerosil Co. Ltd.) was used as precursor-TiO_2 nanopowders. Ammonium hydrogen carbonate (NH_4HCO_3) was chosen as nitrogen source for doping in TiO_2. NH_4HCO_3 was dispersed in 100 ml of deionized water and stirred for 30 min at room temperature. The ratio of doping N in 6.0 g of TiO_2 P25 is designated at 10, 30 and 50 %wt. The suspension was mixed via homogenizer at 6000 rpm for 1h followed by stirring at 120°C until the evaporation of DI water was obtained. After that the precursor was kept as 100°C for 24 h. Finally, the white powder of N-doped TiO_2 was obtained by baking at 100°C for 30, 60 and 120 min. These samples were assigned as NT_30m, NT_60m, and NT_120m. The structural properties of N-doped TiO_2 were characterized by X-ray diffraction (XRD, Panalytical x'Pert Pro MPD).

The photocatalyst of N-doped TiO_2 was carried out by dye photodegradation of Rhodamine B (RhB) under visible light via halogen lamp (450 W). 50 g of N-doped TiO_2 was dispersed in 3 mM RhB and stirred for 20 min in the dark to obtain absorption/desorption equilibrium between RhB and the catalyst surfaces. The solution was irradiated in visible light at room temperature until color of dye completely disappeared. RhB degradation was investigated by the decrease of its absorbance at maximum wavelength (λ_{max}) via Helios UV-Vis spectrometer. The kinetic rate was calculated following the expression [15] by

$$ln\,(C/C_0) = kt \qquad (1)$$

where k is the rate constant, C_0 and C are the concentration of RhB at initial and after illumination for time; t.

3. RESULTS AND DISCUSSION

The XRD patterns of raw TiO_2 P25 and 30%wt. N-doped TiO_2 baked at 100 °C for different baking time are illustrated in Fig. 1. For TiO_2 P25, the anatase phase located at 2θ = 25.4°, 37.8°, 38.6°, 48.1° and 55.2° correspond to (101), (004), (112), (200) and (211) planes whereas the peak at 2θ = 27.5°, 36.2°, 39.3°, 41.3° and 54.4° relates to the rutile phase in (110), (101), (200), (111) and (211) planes, respectively. For N-doped TiO_2, the XRD patterns have identical peaks pattern to raw TiO_2 P25 patterns.

As baking time increases, its phase is still retained without significant change. This result implies that doping N in TiO_2 does not change the basis crystalline of TiO_2 but it may be intermingle on TiO_2 surface. The crystalline size of N-doped TiO_2 which was calculated using Scherrer equation is in the range of 13 to 15 nm [16]. The decrease of crystalline size of N-doped TiO_2 may be caused by the less movement of hydroxyl carbonate from precursor [17].

Absorption spectra of TiO_2 P25 and N-doped TiO_2 at 100 °C with different baking time are illustrated in Fig. 2. It can be seen that the enhancement in optical absorption was clearly seen in NT_60m photocatalyst. This result suggests that NH_4HCO_3 can be used as proper nitrogen source for doping in TiO_2 powder. The spectrum patterns of NT_30m and NT_120m were similar to TiO_2 P25 because of low nitrogen content when compared to pure TiO_2 [18]. It can be deduced that shift of absorption in visible range could be remarkably influenced by the presence of N in the powder and baking time. The amount of nitrogen content is also crucial factor that can further affect the absorption attribute as seen in Fig. 3. The spectrum patterns of N-doped powders performed good absorption in UV region but visible region. For the sample with 10 %wt N doping, this small amount of N loading may produce insufficient nitrogen atoms for modification. On the other hand, the large doping nitrogen content (50%wt.) could not completely decompose precursor for combining in TiO_2 matrix. Therefore, it can be deduced that optimized conditions providing the best photoresponse performance in visible light from this experiment was obtained by 30 %wt. N-doped TiO_2 baked at 100°C for 60 min accompanying the excellent efficiency in photocatalytic degradation.

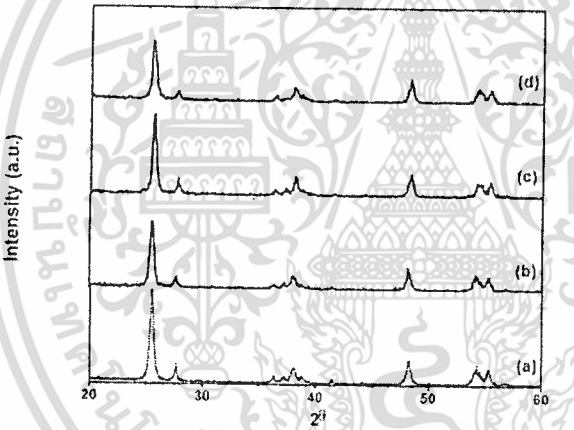

Fig. 1. XRD patterns of (a) raw TiO_2 P25 and 30 %wt of N-doped TiO_2 at 100C with different baking time (b) 30, (c) 60 and (d) 120 min.

Table 1. Structural characteristics of TiO_2 P-25 and N-doped TiO_2 with different baking time.

Sample	β	*cos θ*	Crystalline size (nm)
TiO2 P-25	0.43	0.22	14.56
NT_30m	0.45	0.22	13.83
NT_60m	0.43	0.22	14.70
NT_120m	0.46	0.22	13.45

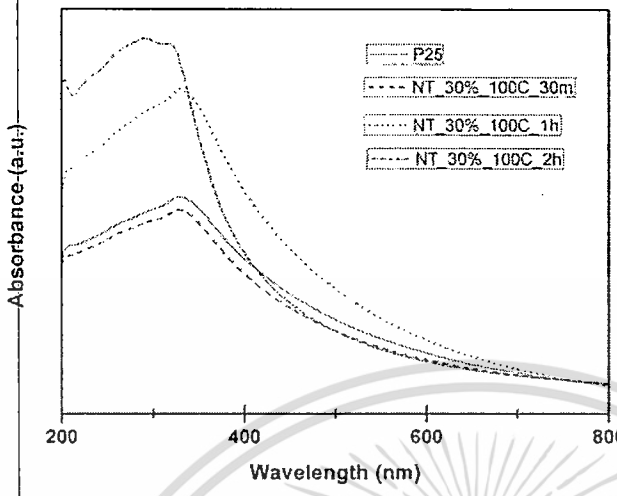

Fig. 2. UV-Vis absorbance spectra of TiO_2 P-25 and N-doped TiO_2 with different baking time

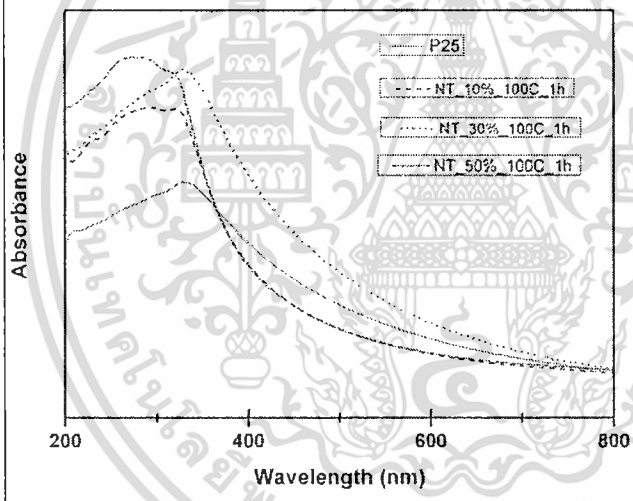

Fig. 3. UV-Vis absorbance spectra of TiO_2 P-25 and N-doped TiO_2 with different doping N.

The photodegradation of RhB in aqueous solution under visible light for 1 hour was conducted in order to make the comparison of photocatalyst efficiency of TiO_2 itself and N-doped TiO_2 and the corresponding results are shown in Fig. 4(a) and 4(b). Both N-doped TiO_2 and TiO_2 P25 can effectively degrade and decolorize RhB. The absorption spectrum of RhB degraded by N-doped TiO_2 photocatalyst exhibits that the decreased absorbance was initially higher than TiO_2 P25. The decolorization of dye was completely reached as the irradiation time up to 30 min for N-doped TiO_2 and 40 min for TiO_2 P25. The loss in absorption is associated to the destruction of dye chromogen. A noticeable shift of absorption spectra to higher energy was obiviously observed by N-doped TiO_2 photocatalyst. This phenomenon is related to the generation of N-de-ethylation that is the last product of RhB [19].

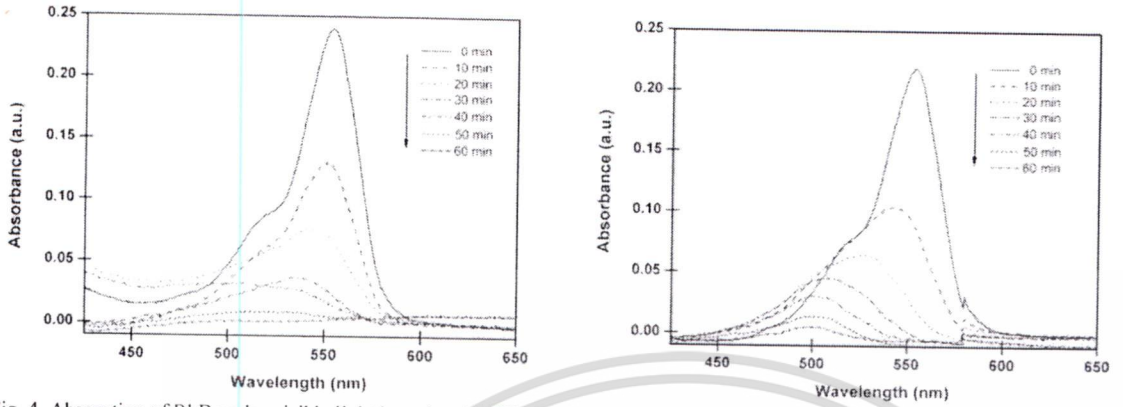

Fig. 4. Absorption of RhB under visible light by using (a) TiO_2 P25 (b) 30 %wt. N-doped TiO_2.

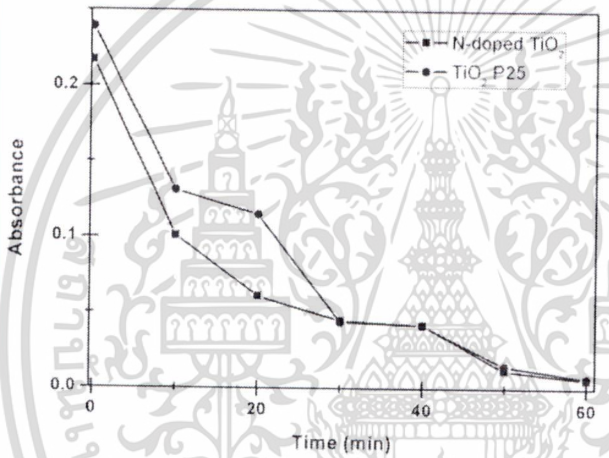

Fig. 5. Absorbance versus decay time of RhB under visible light by using (a) TiO_2 P25 (b) 30 %wt. N-doped TiO_2

The change of RhB absorbance versus irradiation time of N-doped TiO_2 and TiO_2 P25 is shown in Fig. 5. The constant rate of RhB degradation with TiO_2 P25 is 0.051 min^{-1} whereas N-doped TiO_2 photocatalyst shows the constant rate of the activity of about 0.105 min^{-1}. These results imply that nitrogen additive doped in TiO_2 can significantly improve the photocatalytic degradation comparing to pure TiO_2 due to nitrogen-induced band gap energy contraction leading to the enhancement of optical absorption of photocatalyst under visible illumination [20].

4. CONCLUSION

In summary, doping nitrogen in TiO_2 were successfully carried out by homogenization and magnetic stirring without any binders or high temperature heat treatment. XRD pattern suggests that TiO_2 P25 is not changed its structure by either N doping or varied baking time. The optimized condition for the best photoresponse of TiO_2 in visible light is obtained by doping TiO_2 with nitrogen in the ratio 30 %wt. and baked at 100°C for 60 min. The photocatalytic degradation of RhB solution by N-doped TiO_2

photocatalysts was experimentally investigated via its absorption spectra. TiO_2 itself shows less degradation rate than N-doped TiO_2 when the irradiation time is upto 60 min. These results imply that doping nitrogen in TiO_2 can improve the photocatalytic activity due to narrowed band gap energy that relates to the enhancement of photocatalytic degradation under visible light.

Acknowledgements

This work has partially been supported by the National Nanotechnology Center (NANOTEC), NSTDA, Ministry of Science and Technology, Thailand, through its program of Center of Excellence Network. The author would like to thank Rajamangala University of Technology Thanyaburi for XRD measurement.

References

[1] Hansheng L, Yaping Z, Shiying W, Wu Q, Changhao L. Study on nanomagnets supported TiO_2 photocatalysts prepared by a sol–gel process in reverse microemulsion combining with solvent-thermal technique. *J Hazard Mater* 2009;**169**:1045–1053.
[2] Xiaobo C, Schriver M, Suen T, Samuel S.M. Fabrication of 10 nm diameter TiO_2 nanotube arrays by titanium anodization. *Thin Solid Film* 2007;**515**:8511-8514.
[3] Khataee A.R, Kasiri M.B. Photocatalytic degradation of orgnaic dyes in the presence of nanostructured titanium dioxide: Influence of the chemical struture of dyes. *J Mol Catal A-Chem* 2010;**328**:8-26.
[4] Kositzi M, Poulios I, Malato S, Caceres J, Campos A. Solar photocatalytic treatment of synthetic municipal wastewater. *Water Res* 2004;**38**:1147-1154.
[5] Habibi M.H, Tangestaninejad S, Yadollahi B. Photocatalytic mineralisation of mercaptans as environmental pollutants in aquatic system using TiO_2 suspension. *Appl Catal B-Environ* 2009;**33**:57-63.
[6] Han F, Kambala V.S.R, Srinivasan M, Rajarathnam D, Naidu R. Tailored titanium dioixde photocatalysts for the degradation of organic dyes in wastewater treatment: A review. *Appl Catal A-Gen* 2009;**359**:25-40.
[7] Zhang L, Kanki T, Sano N, Toyoda A. Development of TiO_2 photocatalyst reaction for water purification. *Sep Purif Technol* 2003;**31**:105-110.
[8] Jitputti J, Pavasupree S, Suzuki Y, Yoshikawa S. Synthesis and photocatalytic activity for water-splitting reaction of nanocrystalline mesoporous titania prepared by hydrothermal method. *J Solid State Chem* 2007;**180**:1743–1749.
[9] Haiyan L, Dejun W, Haimei F, Ping W, Tengfei J, Tengfeng X. Synthesis of highly efficient C-doped TiO_2 photocatalyst and its photo-generated charge-transfer properties. *J Colloid Interf Sci* 2011;**354**:175–180.
[10] Znad H, Kawase Y. Synthesis and characterization of S-doped Degussa P25 with application in decolorization of Orange II dye as a model substrate. *J Mol Catal A-Chem* 2009;**314**:55–62.
[11] Senthilnathan J, Philip L. Photocatalytic degradation of lindane under UV and visible light using N-doped TiO_2. *Chem Eng J* 2010;**161**:83-92.
[12] Horst K, Shanmugasundaram S, Marcin J, Dariusz M. A Low-Band Gap, Nitrogen-Modified Titania Visible-Light Photocatalyst. *J Phys Chem C* 2007;**111**:11445-11449.
[13] Jing L, Chang J.L, Yue K.L, Rong G.D. Photogenerated cathodic protection of flower-like, nanostructured, N-doped TiO_2 film on stainless steel. *Surf Coat Tech* 2010;**205**:557–564.
[14] Bangkedphol S, Keenan H.E, Davidson C.M, Sakultantimetha A, Sirisaksoontorn W, Songsasen A. Enhancement of tributyltin degradation under natural light by N-doped TiO_2 photocatalyst. *J Hazard Mater* 2010;**184**:533–537.
[15] Jingjing X, Yanhui A, Mindong C, Degang F. Photoelectrochemical property and photocatalytic activity of N-doped TiO_2 nanotube arrays. App Surf Sci 2010;**256**:4397-4401.
[16] Yuexiang L, Yuan J, Shaoqin P, Fengyi J. Nitrogen-doped TiO_2 modified with NH_4F for efficient photocatalytic degradation of formaldehyde under blue light-emitting diodes. *J Hazard Mater* 2010;**182**:90-96.
[17] Yujun W, Chunling Z, Siwei B Guangsheng L. Preparation of ZnO nanoparticle using the direct precipitation method in a membrane dispersion micro-structured reactor. *Powder Technol* 2010;**202**:130-136.
[18] Fang D, Weirong Z, Zhongbiao W, Sen G. Band structure and visible light photocatalytic activity of multi-type nitrogen doped TiO_2 nanoparticles prepared by thermal decomposition. *J Hazard Mater* 2009;**162**:763–770.
[19] Ying M, Jian N.Y. Photodegradation of Rhodamin B catalyzed by TiO_2 thin film. *J Photoch Photobio A* 1998;**116**:167-170.
[20] Ji Y.M, Chan S.K, Han K.C, Tae O.K. Synthesis and Characterization of N-doped TiO2/ZrO2 visible light photocatalysts. *Adv Powder Technol* 2011;22:443-448.

Materials Research Bulletin xxx (2012) xxx–xxx

Contents lists available at SciVerse ScienceDirect

Materials Research Bulletin

journal homepage: www.elsevier.com/locate/matresbu

Ball-milled CuPc/TiO_2 hybrid nanocomposite and its photocatalytic degradation of aqueous Rhodamine B

W. Mekprasart [a,c,*], N. Vittayakorn [b,c,d], W. Pecharapa [a,c]

[a] Nanocomposite Material Research Laboratory, College of Nanotechnology, King Mongkut's Institute of Technology Ladkrabang, Bangkok 10520, Thailand
[b] Electroceramic Research Laboratory, College of Nanotechnology, King Mongkut's Institute of Technology Ladkrabang, Bangkok 10520, Thailand
[c] ThEP Center, CHE, 328 Si Ayutthaya Rd., Bangkok 10400, Thailand
[d] Department of Chemistry, Faculty of Science, King Mongkut's Institute of Technology Ladkrabang, Bangkok 10520, Thailand

ARTICLE INFO

Article history:
Received 31 December 2011
Received in revised form 10 July 2012
Accepted 11 August 2012
Available online xxx

Keywords:
A. Composites
D. Catalytic properties
D. Optical properties

ABSTRACT

Hybrid composites of titanium dioxide and copper phthalocyanine were synthesized by ball-milling assisted process in combination with mechanically stirring method. Structural properties of as-synthesized composites were characterized by X-ray diffraction (XRD), X-ray absorption fine structure (XANES) and scanning electron microscope (SEM). The optical absorbance of as-prepared composites and their photocatalytic activities were investigated by UV–vis spectroscopy. XRD and XANES results confirm that CuPc/TiO_2 nanocomposite is still in the same structure of TiO_2 and CuPc. SEM result reveals that the decreasing particle size of ball-milled CuPc has good dispersion on the surface of TiO_2. Absorptivity in UV region of the composites is heightened and shifted to visible light due to strong absorbance in blue-green spectrum of CuPc. The photocatalytic degradation of Rhodamine B dye solution using as-synthesized composites was investigated under ultraviolet irradiation. The optimized condition for RhB photodegradation was obtained for 1 wt.% CuPc/TiO_2 nanocomposite with efficiency of 87.5% and reaction rate of 0.15 min^{-1}. The significant improvement in photocatalytic activity of the hybrid composite may be associated to the enhancement of optical absorption and the inhibition of electron–hole recombination caused by the presence of CuPc in TiO_2 matrix.

1. Introduction

Semiconductor based photocatalysts have recently received considerable attentions in various environmental applications. Among functional metal oxide semiconductors, TiO_2 is acknowledged as an effective photocatalyst due to its distinguished properties including non-toxicity, excellent energy conversion efficiency, long-term chemical stability and high photosensitivity [1–4]. TiO_2 photocatalyst has extensively applied to energy and environment applications such as hydrogen generation [5], photodegradation of organic and inorganic pollutant in waste water [6,7], air purification [8], bacteria elimination [9] and dye degradation [10]. Meanwhile, TiO_2 nanostructures such as nanoparticle, nanorod, nanosheet, nanotube and nanofiber have been recognized as novel functional materials due to their drastically increasing specific surface area that is the key issue for enhancing the photocatalytic reaction [11–15]. However, photocatalytic performance of TiO_2 is naturally limited by high recombination rate of electron–hole pair and low absorption in visible region [16–19]. Various methods have been proposed to overwhelm these drawbacks. Recent research works have reported on the successes of improvement its catalytic performance of TiO_2 by incorporated with compatible metal ion, metal oxide and non-metal to form the well-defined composites. Huo et al. reported that the efficiency of photocatalytic activity of TiO_2 could be improved by doping lanthanum (La) into TiO_2, which might hinder the photoelectron–hole recombination and also facilitate the adsorption for reactant molecules and photons [20]. Xu et al. synthesized Cu_2O–TiO_2 photocatalyst with efficient photocatalytic degradation due to the existence of Cu_2O on the surface of TiO_2 that can effectively trap electrons of TiO_2, thereby avoiding electron–hole recombination [21]. Ohno et al. reported that strong absorption in visible light and high activities in photocatalytic degradation could be obtained by doping sulphur in TiO_2 matrix [22].

Another effective approach for improving the photocatalytic performance of TiO_2 is based on organic-inorganic hybrid composite that use appropriate organic materials to incorporate into TiO_2 matrix. Lu et al. reported that significant increase in optical absorptivity in visible region and improvement of TiO_2 photocatalytic activity were achieved by g-C_3N_4/TiO_2 hybrid

* Corresponding author at: Nanocomposite Material Research Laboratory, College of Nanotechnology, King Mongkut's Institute of Technology Ladkrabang, Bangkok 10520, Thailand. Tel.: +66 2329800x3147; fax: +66 3298265.
E-mail address: wani.mek@gmail.com (W. Mekprasart).

0025-5408/$ – see front matter © 2012 Elsevier Ltd. All rights reserved.
http://dx.doi.org/10.1016/j.materresbull.2012.08.024

composite because of the existence of N–Ti–O and N–Ti–N bonding in the composite [23]. Zhu et al. were able to synthesize P3HT on TiO_2 surface to enhance its photoresponse in visible range, leading to an effective photocatalytic reaction [24]. Oh et al. reported that improving quantum efficiency and charge transfer of photocatalyst in organic degradation were obtained by synergistic effect between TiO_2 matrix and fullerene [25]. Based on the work conducted by Zhang and Pan, the increases of dye absorption, electron–hole separation and visible light activation of TiO_2 could be obtained by presence of graphene in TiO_2 matrix [26]. Metallophthalocyanine (MPc) is a kind of organic semiconductor that possesses strong absorption in blue-green region, excellent resistance in chemical degradation and good photosensitivity [27,28]. Because of these exceptional properties, MPc has been practicable in many applications such as organic-based diode [29], OLED [30], gas sensor [31] and photovoltaic device [32]. Meanwhile the research of pollutant photodegradation disclosed that MPc photocatalyst exhibited good performance in this process. Borker and Salker reported that MPc is typically good photocatalyst under solar light in photocatalytic activity for complete degradation of Naphthol Blue Black [33]. The hybrid composite of MPc and TiO_2 nanostructure has been intensively investigated, in particular, the improvement of UV and visible light absorption, the modification of charge transfer and the decrease of charge recombination in TiO_2 [34,35]. Machado et al. reported that the enhancement of absorption spectra in UV–visible range and a good photocatalytic reaction of wastewater were well accomplished by TiO_2/ZnPc composite [36]. Iliev et al. gave the report on the improvement of sulfide and thiosulfate ion photoxidation under visible light using Phthalocyanine modified TiO_2 or WO_3-catalysts [37].

The main objectives of this work are to synthesize functional hybrid composite of CuPc organic dye and TiO_2 by ball-milling and facile mechanical mixing method and to investigate the effect of the loading of ball-milled CuPc on the physical properties and photocatalytic activity of TiO_2. The photocatalytic degradation of Rhodamine B (RhB) for CuPc/TiO_2 photocatalysts was conducted under UV illumination. CuPc plays a significant role as an hole acceptor from TiO_2, resulting to the decrease of recombination of electron–hole pair and the increase of the photocatalytic reaction rate.

2. Experiment

TiO_2 nanopowder purchased from Aldrich with average particle size about 50–100 nm was used as host material. 97% dye content of CuPc supplied by Aldrich was designated as guest material. As-obtained CuPc average size is in micron size therefore ball milling process is necessary for minimizing its size [38]. Firstly, CuPc and ethanol were loaded for ball-milling for 18 h with a ball-to-powder weight ratio of 10:1. After that, CuPc precursor was stirred at 120 °C until ethanol completely evaporated and was kept at 100 °C for 24 h. Secondly, 1 g of TiO_2 nanopowder was dispersed in 30 ml ethanol solution through ultrasonic vibration for 10 min. The different amounts of ball-milled CuPc powder of 0.5, 1 and 2 wt.% were loaded in TiO_2 suspension by ultrasonic vibration for 10 min. The suspension was heated at 100 °C by mechanically stirring process until the ethanol was completely evaporated. As-prepared solid precipitates of CuPc/TiO_2 composites were dried at 90 °C for 15 h until final blue composites were obtained. The structural properties of CuPc/TiO_2 nanocomposites were characterized using X-ray diffractometer (XRD, Panalytical x'Pert Pro MPD). The morphologies of composites were monitored by scanning electron microscope (SEM, JSM-6510). X-ray absorption measurement for Cu K edges has been carried out employing synchrotron radiation at the Siam Light Research Institute (SLRI), Thailand. Cu K edge (8979 eV) measurement was carried out using a Ge (2 2 0) crystal monochromator with a table step of 1 eV. The photocatalytic activity was conducted on the dye degradation of Rhodamine B (RhB) under UV illumination (450 W). 20 mg of CuPc/TiO_2 nanocomposites were dispersed in 5.9×10^{-6} mol/l of RhB and stirred for 15 min in the dark to obtain absorption/desorption equilibrium between RhB and the catalyst surfaces. The solution was irradiated by UV light at room temperature until color of dye completely disappeared. RhB degradation was investigated by mean of the decrease of its absorbance at maximum wavelength (λ_{max}) via UV–vis spectrometer. The kinetic rate was calculated by following equation [39];

$$\ln\left(\frac{C}{C_0}\right) = -kt \quad (1)$$

where k is the rate constant, C_0 and C are the concentrations of RhB at initial and after illumination time; t.

3. Results and discussion

XRD patterns of TiO_2, CuPc and CuPc/TiO_2 hybrid composite are shown in Fig. 1. In case of TiO_2 nanopowder, the diffraction peaks positioned at $2\theta = 25.4°$, 38.1°, 48.1° and 55.1° are assigned to (1 0 1), (0 0 4), (2 0 0) and (2 1 1) planes of anatase phase, respectively (ICDD 21-1272). Another noticeable peaks situated at $2\theta = 27.5°$, 36.2°, 41.3°, 44.1°, 54.3° and 56.6° are attributable to (1 1 0), (1 0 1), (1 1 1), (2 1 0), (2 1 1) and (2 2 0) orientation plane of rutile phase, respectively (ICDD 21-1276). This basic crystalline of anatase phase indicates tetragonal point group $I4_1/amd$ with lattice parameter $a = 4.71$ Å and $c = 9.41$ Å meanwhile the structure of rutile phase identifies primitive tetragonal point group $P4_2/mnm$ *amd* with lattice parameter a and $c = 4.97$ Å. The XRD patterns of CuPc in the range of 19–30° corresponding to beta phase of CuPc (β-CuPc) are clearly observed (ICDD 11-0893). For CuPc/TiO_2 nanocomposite, XRD patterns are identical to TiO_2 patterns indicating that CuPc additive insignificantly affects the basic crystal structure of TiO_2, accompanying the absence of XRD patterns of CuPc due to small loading amount into TiO_2 host matrix. This similar feature is supported by previous published work reported by Chou et al. [40].

The morphologies and structures of TiO_2, CuPc, ball-milled CuPc and CuPc/TiO_2 composite monitored by SEM and TEM images are shown in Fig. 2. As seen in Fig. 2(a), TiO_2 particles were

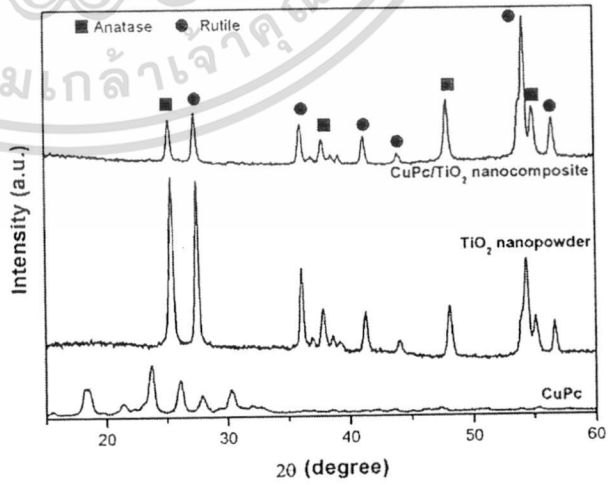

Fig. 1. XRD pattern of CuPc, TiO_2 nanopowder and CuPc/TiO_2 nanocomposite.

Please cite this article in press as: W. Mekprasart, et al., Mater. Res. Bull. (2012), http://dx.doi.org/10.1016/j.materresbull.2012.08.024

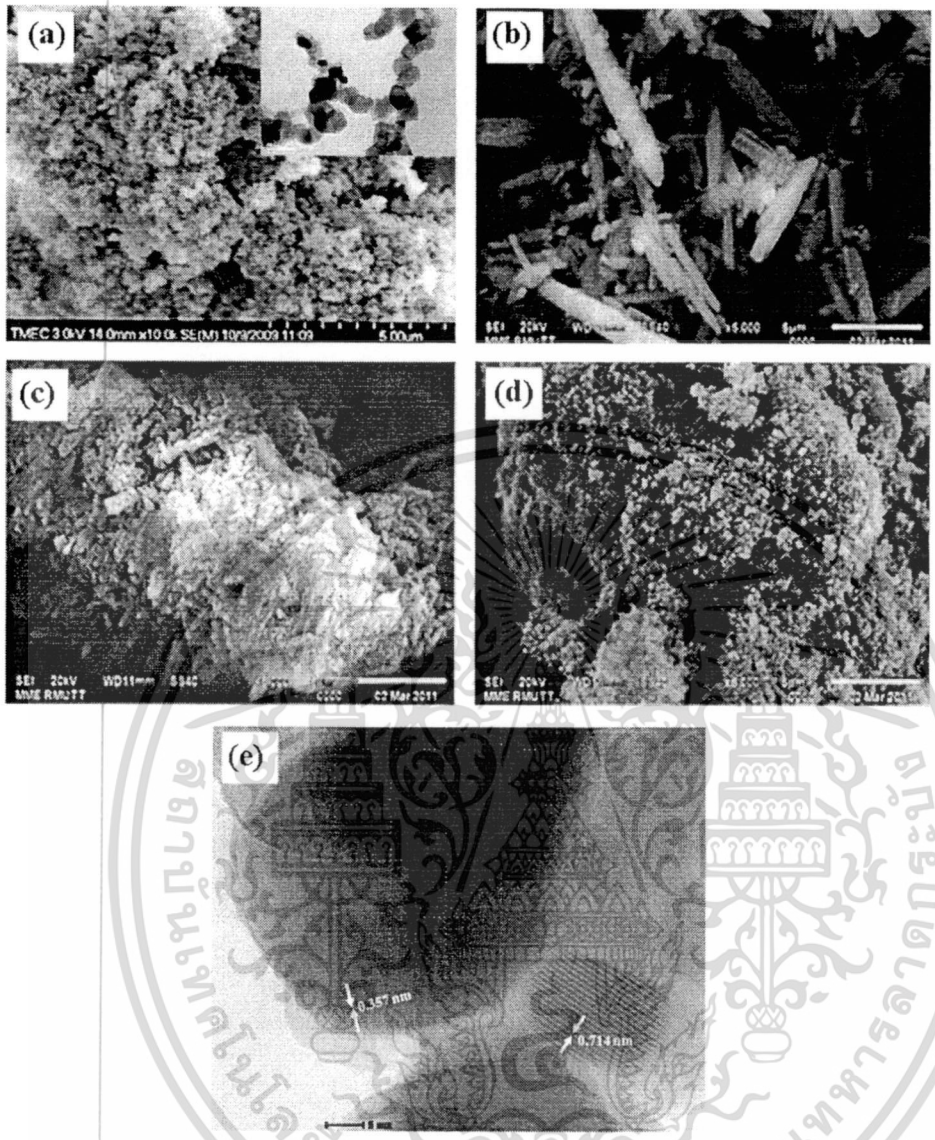

Fig. 2. SEM micrograph of (a) TiO_2 nanopowder, (b) CuPc, (c) ball-milled CuPc, (d) 1 wt.% CuPc/TiO_2 nanocomposite and (e) TEM image of CuPc/TiO_2 nanocomposite.

agglomerated in the cluster form with micron range. The average size of spherical TiO_2 nanoparticle enclosed by TEM image as the inset of Fig. 2(a) is approximately 20–30 nm. CuPc structure is naturally spiked shape with average length of 5–10 μm as shown in Fig. 2(b). The large size of CuPc is consequently difficult to be homogenously combined with TiO_2 to form well-defined composite therefore ball milling process is required as preliminary process to minimize its size. From the SEM image in Fig. 2(c), after milling process at room temperature, the spiked structure of CuPc was minimized and transformed to fine powder. Fig. 2(d) reveals that ball-milled CuPc powder can be intermingled and dispersed on the surface of TiO_2 particles via the assistance of mechanical stirring process, resulting to good dispersion of CuPc on TiO_2 host matrix and homogeneous composite between these two materials. The selected area electron diffraction (SAED) pattern of CuPc/TiO_2 nanocomposite is illustrated in Fig. 2(e). TEM image clearly exhibits TiO_2 fringe with *d*-spacing of 0.35 nm relating to anatase phase at (1 0 1) plane and CuPc fringe with the interplanar spacing

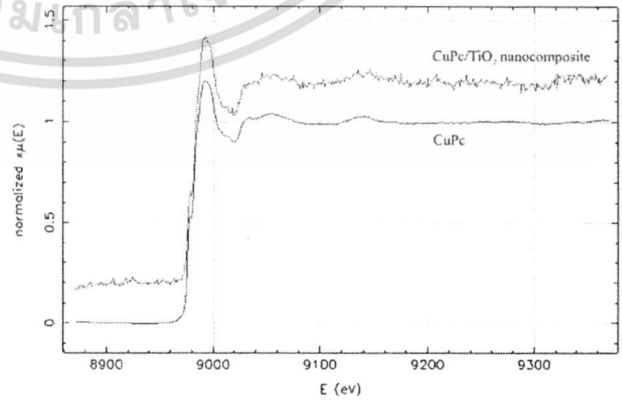

Fig. 3. Experimental X-ray absorption Cu K edges for CuPc and CuPc/TiO_2 nanocomposite.

Please cite this article in press as: W. Mekprasart, et al., Mater. Res. Bull. (2012), http://dx.doi.org/10.1016/j.materresbull.2012.08.024

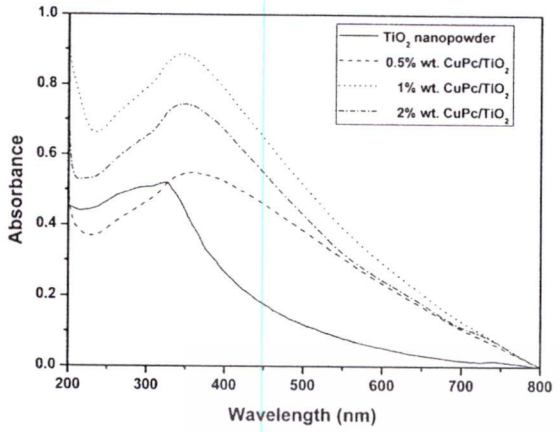

Fig. 4. UV–vis spectra of pure TiO_2 and various the amount of CuPc in TiO_2 treated. (a) TiO_2 nanopowder, (b) 0.5, (c) 1 and (d) 2 wt.% CuPc/TiO_2 nanocomposite.

of 0.71 nm assigning to $(\bar{2}\,0\,2)$ plane of β-phase. The Cu K edge X-ray absorption spectra of CuPc, CuPc/TiO_2 nanocomposites are shown in Fig. 3. A prominent absorption peak can be observed on the absorption edge at 8979 eV. When CuPc was loaded into TiO_2, XANES spectrum of the composite was similar to that of CuPc. This result suggests that local structure of CuPc loaded in TiO_2 matrix scarcely changes. This implication is in good accordance with the results revealed by XRD. Moreover, CuPc/TiO_2 nanocomposite may compatibly form in physical sorption without new bonding between two materials. However, the ripple of extended absorption regime in CuPc/TiO_2 composite can be observed, which may be attributed to the vibration between the molecules of Cu and neighbor atom by the disturbance of TiO_2.

The absorption spectra of TiO_2 and CuPc/TiO_2 nanocomposite with different loading amounts of CuPc are illustrated in Fig. 4. The strong absorption of TiO_2 in a range of 200–400 nm is originated from typical band gap energy of TiO_2 (3.2 eV) [41]. The extended absorption of bare TiO_2 nanopowder in range of 400–700 nm may be due to scattering-induced absorption of longer wavelength in colloidal solution or low density of state in the conduction band of TiO_2 [42]. The enhancement of optical absorption in UV region and visible light was clearly observed in CuPc/TiO_2 composite. Comparing to pure TiO_2, the absorption spectra of the composites exhibits an obvious red-shift to higher wavelength in visible region with stronger intensity as the CuPc loading content increases up to 1% thereafter decreases. In fact, CuPc has two distinct absorption bands in the range of 200–400 nm called B-band and 600–800 nm called Q-band [43]. The optical absorption enhancement of the composite in visible region are resulted from π–π^* excitation between bonding and antibonding molecular orbital of the Q band of phthalocyanine molecules [44,45].

The photocatalytic efficiencies of pure TiO_2 and 1 wt.% CuPc/TiO_2 nanocomposite were scrutinized by the photodegradation of aqueous RhB under UV illumination and corresponding results in term of absorption spectra are illustrated in Fig. 5(a) and (b), respectively. The photocatalytic activity of CuPc/TiO_2 photocatalyst is more effective, accompanying the rapid decrease of the absorption spectrum after 10 min of reaction and complete degradation of RhB within 25 min. The time period for the decolorization of RhB by CuPc/TiO_2 photocatalyst was approximately 10 min faster than that of pure TiO_2, implying that the photocatalytic activity was significantly enhanced by an assistance of CuPc loaded into TiO_2 photocatalyst. Under UV illumination, TiO_2 can effectively generate the electron–hole pair in conduction band (CB) and valence band (VB). The photogenerated hole of $TiO_2(h_{VB}^+)$ can be captured by water molecule and hydroxyl ion to produce hydroxyl radical ($OH^\bullet$). Meanwhile, oxygen molecule can be trapped by the photogenerated electron of $TiO_2(e_{CB}^-)$, resulting to active oxygen species ($O_2^{\bullet-}$). Photocatalytic mechanisms of TiO_2 under UV irradiation can be described by following equations [46];

$$TiO_2 \xrightarrow{h\nu} TiO_2(e_{CB}^- + h_{VB}^+) \quad (2)$$

$$TiO_2(h_{VB}^+) + H_2O \rightarrow TiO_2 + H^+ + OH^\bullet \quad (3)$$

$$TiO_2(h_{VB}^+) + OH^- \rightarrow TiO_2 + OH^\bullet \quad (4)$$

$$TiO_2(e_{CB}^-) + O_2 \rightarrow TiO_2 + O_2^{\bullet-} \quad (5)$$

The hydroxyl and active oxygen groups from TiO_2 photocatalyst play an important role in photocatalytic reaction to decompose a structure of organic molecules. The continuous mechanism and the efficiency of photocatalytic reaction are enhanced by the increase amount of radical groups in the system. If the photogenerated electron–hole pairs are unoccupied by water molecule or oxygen in the air to produce the radical groups, the recombination of photogenerated electron–hole pair will occur in a few nanoseconds. The photocatalytic efficiency of pure TiO_2 is consequently diminished by this phenomenon. A key role of CuPc anticipated to the enhancement of photocatalytic performance of TiO_2 is suggested. The electronic structure of the conduction band and valence bands of TiO_2 are at −4.2 and −7.4 eV below vacuum level, respectively [47]. Meanwhile, the lowest unoccupied molecular orbital (LUMO) and highest occupied molecular orbital (HOMO) levels of CuPc are at −3.5 and −5.2 eV below vacuum level, respectively [48]. The HOMO level of CuPc is 2.2 eV higher than the valence band of TiO_2. When loading into TiO_2, CuPc may

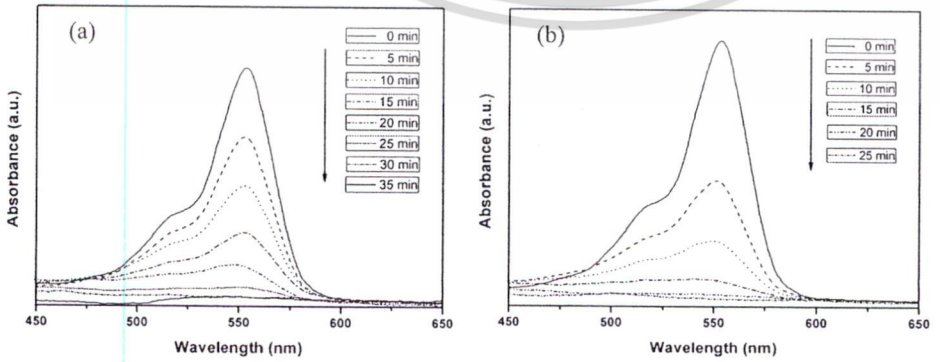

Fig. 5. Absorption of RhB under UV light using (a) TiO_2 nanopowder and (b) 1 wt.% CuPc/TiO_2 nanocomposite.

Please cite this article in press as: W. Mekprasart, et al., Mater. Res. Bull. (2012), http://dx.doi.org/10.1016/j.materresbull.2012.08.024

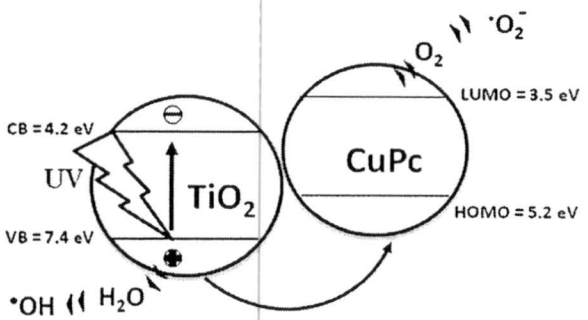

Fig. 6. Main processes involved in a photocatalytic process by CuPc/TiO_2 nanocomposites.

suitably perform as a hole capture, resulting to the effective transfer of hole form valence band of TiO_2 to HOMO of CuPc following Fig. 6 and Eq. (6) [49]. This mechanism can potentially delay the recombination of photogenerated electron–hole pair, leading to the effective interface charge separation. Sequentially, unpaired electron of TiO_2 can react to oxygen group, leading to the continuity of higher photocatalytic reaction due to the decrease of e^-–hole pair recombination.

$$CuPc + TiO_2\,(e^- + h^+) \rightarrow CuPc^- + TiO_2\,(e^-) \quad (6)$$

In addition, the blue-shift in absorption peak of RhB during degradation process is investigated. The decrease of absorption intensity and the peak shift to high energy under UV illumination were caused by de-ethylation of RhB in a stepwise manner. The de-ethylation mechanism is occurred by the attacking of active oxygen species on N-ethyl group of RhB that cause the change of RhB structure [50]. The initial structure of RhB before the illumination is *N,N,N′,N′*-tetraethylated rhodamine molecule at λ_{max} = 554 nm. After illumination, RhB structure is oxidized by oxygen species and changed to *N,N,N′*-triethylated rhodamine at 539 nm, *N,N′*-diethylated rhodamine at 522 nm and *N*-ethylated rhodamine at 510 nm [51]. The normalized RhB concentrations versus the illuminated time are shown in Fig. 7. The complete decolorization of RhB by pure TiO_2 nanopowder was achieved after 35 min of reaction. Comparing to pure TiO_2, the degradations of RhB by CuPc/TiO_2 nanocomposites obviously exhibit shorter

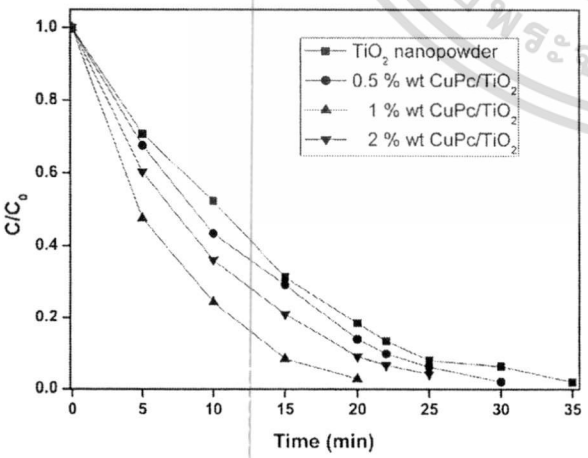

Fig. 7. Absorbance of RhB versus reaction time under UV illumination using TiO_2 nanopowder and 0.5, 1 and 2 wt.% CuPc/TiO_2 nanocomposite.

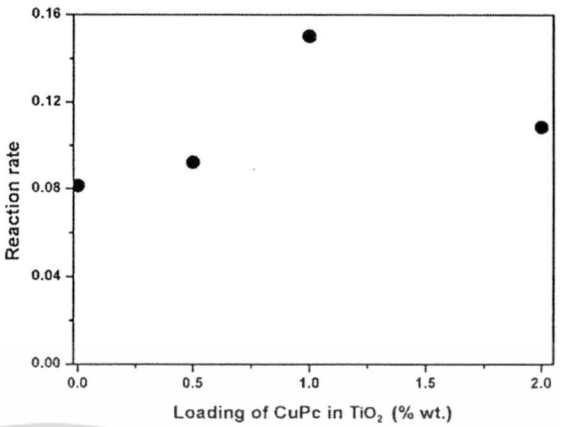

Fig. 8. Reaction rate of RhB photodegradation by different loading of CuPc in TiO_2.

reaction time and the composite with 1 wt.% CuPc loading performs much better activity than the others. At low loading amount of CuPc in the composite, the hole acceptor may be insufficient therefore the discontinued mechanism is occurred because of fast charge recombination. When loading amount rises to 1 wt.%, an appropriate amount of CuPc can efficiently suppress the recombination of photo-generated charges and greater amount of functional groups responsible for the degradation reaction is sufficiently provided in the system. However, over loading CuPc (2 wt.%) in nanocomposite may cause the aggregation and agglomeration of CuPc on TiO_2 surface that may act as a blocking layer of entrance light onto TiO_2 surface, resulting to the decrease of photogenerated charge in the system and the deterioration of photocatalytic reaction.

The reaction rates of photocatalytic degradation using different amount of CuPc at 0, 0.5, 1 and 2 wt.% in TiO_2 are shown in Fig. 8. The greatest reaction rate of 0.15 min^{-1}. was obtained by 1 wt.% CuPc/TiO_2 nanocomposite. This reaction rate is approximately 87,5% greater than that of pure TiO_2. The increased reaction rate of CuPc/TiO_2 photocatalyst reflects to the improved performance in photocatalytic degradation. Nevertheless, further increase of CuPc loading amount results to an insignificant increase of reaction rate. All results suggest that the existence of CuPc with certain loading amount can significantly ameliorate the photocatalytic performance of TiO_2.

4. Conclusion

The composites of TiO_2 nanopowder and CuPc were synthesized by ball milling and mechanically stirring process without any binder. Accompanying XRD and XAFS results, it was suggested that loaded CuPc has inconsiderable influence on basic crystal structure of TiO_2 matrix. SEM images reveal that ball milling process can evidently reduce CuPc size and assist the formation of well-dispersed composite. Meanwhile, the optical absorption properties of TiO_2 is improved with the existence of CuPc due to strong absorption manner of CuPc in UV and visible region. The photodegradation of aqueous RhB using this as-synthesized composite was carried out and the corresponding results notified that specific loading content of CuPc can efficiently heighten the catalytic performance of TiO_2 upto 87.5%, greater than bare TiO_2. This feature could be explained by the major contribution of CuPc on the increase in charge separation of photogenerated electron–hole pair of TiO_2 and free functional radicals participated in degradation process.

Please cite this article in press as: W. Mekprasart, et al., Mater. Res. Bull. (2012), http://dx.doi.org/10.1016/j.materresbull.2012.08.024

Acknowledgments

This work has partially been supported by the National Nanotechnology Center (NANOTEC), NSTDA, Ministry of Science and Technology, Thailand, through its program of Center of Excellence Network. The author would like to thank Rajamangala University of Technology Thanyaburi for SEM and XRD measurement.

References

[1] F.D. Mai, C.S. Lu, C.W. Wu, C.H. Huang, J.Y. Chen, C.C. Chen, Sep. Purif. Technol. 62 (2008) 423–436.
[2] S. Pavasupree, Y. Suzuki, S. Yoshikawa, R. Kawahata, J. Solid State Chem. 178 (2005) 3110–3116.
[3] Q. Zhang, L. Gao, J. Eur. Ceram. Soc. 26 (2006) 1535–1545.
[4] J. Li, W. Ma, C. Chen, J. Zhao, H. Zhu, X. Gao, J. Mol. Catal. A: Chem. 261 (2007) 131–138.
[5] R. Sasikala, V. Sudarsan, C. Sudakar, R. Naik, L. Panicker, S.R. Bharadwaj, Hydrogen Energy 34 (2009) 6105–6113.
[6] F. Han, V.S.R. Kambala, M. Srinivasan, D. Rajarathnam, R. Naidu, Appl. Catal. A: Gen. 359 (2009) 25–40.
[7] P.A.S.S. Marques, M.F. Rosa, F. Mendesl, M. Collares Pereiral, J. Blanco, S. Malato, Desalination 108 (1996) 213–220.
[8] P. Pichat, Appl. Catal. B: Environ. 99 (2010) 428–434.
[9] O. Seven, B. Dindar, S. Aydemir, D. Metin, M.A. Ozinel, S. Icli, J. Photochem. Photobiol. 165 (2004) 103–107.
[10] X. Qin, L. Jing, G. Tian, Y. Qu, Y. Feng, J. Hazard. Mater. 172 (2009) 1168–1174.
[11] P. Supphasrirongjaroen, P. Praserthdam, J. Panpranot, D. Na-Ranong, O. Mekasuwandumrong, Chem. Eng. J. 138 (2008) 622–627.
[12] X.H. Xia, Y. Liang, Z. Wang, J. Fan, Y.S. Luo, Z.J. Ji, Mater. Res. Bull. 43 (2008) 2187–2195.
[13] Q. Xiang, K. Lv, J. Yu, Appl. Catal. B: Environ. 96 (2010) 557–564.
[14] J. Zhang, B. Zhou, Q. Zheng, J. Li, J. Bai, Y. Liu, W. Cai, Water Res. 43 (2009) 1986–1992.
[15] S.J. Doh, C. Kim, S.G. Lee, S.J. Lee, H. Kim, J. Hazard. Mater. 154 (2008) 118–127.
[16] C.J. Chen, C.H. Liao, K.C. Hsu, Y.T. Wu, J.C.S. Wu, Catal. Commun. 12 (2011) 1307–1310.
[17] L. Samiolo, M. Valigi, D. Gazzoli, R. Amadelli, Electrochim. Acta 55 (2010) 7788–7795.
[18] G. Liu, X. Zhang, Y. Xu, X. Niu, L. Zheng, X. Ding, Chemosphere 59 (2005) 1367–1371.
[19] C. Wen, Y.J. Zhu, T. Kanbara, H.Z. Zhu, C.F. Xiao, Desalination 249 (2009) 621–625.
[20] Y. Huo, J. Zhu, J. Li, G. Li, H. Li, J. Mol. Catal. A: Chem. 278 (2007) 237–243.
[21] Y.-H. Xu, D.-H. Liang, M.-L. Liu, D.-Z. Liu, Mater. Res. Bull. 43 (2008) 3474–3482.
[22] T. Ohno, M. Akiyoshi, T. Umebayashi, K. Asai, T. Mitsui, M. Matsumura, Appl. Catal. A: Gen. 265 (2004) 115–121.
[23] X. Lu, Q. Wang, D. Cui, J. Mater. Sci. Technol. 26 (2010) 925–930.
[24] Y. Zhu, Y. Dan, Sol. Energy Mater. Sol. Cells 94 (2010) 1658–1664.
[25] W.-C. Oh, A.-R. Jung, W.-B. Ko, J. Ind. Eng. Chem. 13 (2007) 1208–1214.
[26] Y. Zhang, C. Pan, J. Mater. Sci. 46 (2011) 2622–2626.
[27] W. Jiang, X. Wang, Y. Chang, S. Yu, C. Ma, K. Ye, C. Cheng, G. Du, J. Cryst. Growth 290 (2006) 544–547.
[28] J.X. Tang, C.S. Lee, S.T. Lee, Appl. Surf. Sci. 252 (2006) 3948–3952.
[29] G. Chintakula, S. Rajaputra, V.P. Singh, Sol. Energy Mater. Sol. Cells 94 (2010) 34–39.
[30] J.H. Lee, C.C. Liao, P.J. Hu, Y. Chang, Synth. Met. 144 (2004) 279–283.
[31] F. Siviero, N. Coppedè, A.M. Taurino, T. Toccoli, P. Siciliano, S. Iannott, Sens. Actuators B 130 (2008) 405–410.
[32] V.P. Singh, B. Parsarathy, R.S. Singh, A. Aguilera, J. Anthony, M. Payne, Sol. Energy Mater. Sol. Cells 90 (2006) 798–812.
[33] P. Borker, A.V. Salker, Synthesis, Indian J. Chem. Technol. 13 (2006) 341–346.
[34] S. Yu, S. Ahmadi, P. Palmgren, F. Hennies, M. Zuleta, M. Göthelid, J. Phys. Chem. C 113 (2009) 13765–13771.
[35] S. Jäger, Thin Solid Films 286 (1996) 154–158.
[36] A.E.H. Machado, M.D. Franc, V. Velani, G.A. Magnino, H.M.M. Velani, F.S. Freitas, P.S. Müller Jr., C. Sattler, M. Schmücker, Hindawi Publishing Corporation, Int. J. Photoenergy, 2008, Article ID 482373, http://dx.doi.org/10.1155/2008/482373.
[37] V. Iliev, D. Tomova, L. Bilyarska, L. Prahov, L. Petrov, J. Photochem. Photobiol. A 159 (2003) 281–287.
[38] R. Angers, M.R. Krishnadev, R. Tremblay, J.-F. Corriveau, D. Dubé, Mater. Sci. Eng. A 262 (1999) 9–15.
[39] X.M. Song, J.M. Wu, M. Yan, Mater. Chem. Phys. 112 (2008) 510–515.
[40] C.S. Chou, R.Y. Yang, M.H. Weng, C.H. Yeh, Powder Technol. 187 (2008) 181–189.
[41] D. Wang, J. Zhang, Q. Luo, X. Li, Y. Duan, J. An, J. Hazard. Mater. 169 (2009) 546–550.
[42] D.R. Coronado, G.R. Gattorno, M.E.E. Pesqueira, C. Cab, R.d. Coss, G. Oskam, Nanotechnology 19 (145605) (2008) 10.
[43] W. Liu, Y. Wang, L. Gui, Y. Tang, Langmuir 15 (1999) 2130–2133.
[44] Y. Ohmori, E. Itoh, K. Miyari, Thin Solid Films 499 (2006) 369–373.
[45] G.D. Sharma, R. Kumar, S.K. Sharma, M.S. Roy, Sol. Energy Mater. Sol. Cells 90 (2006) 933–943.
[46] M.N. Chong, B. Jin, C.W.K. Chow, C. Saint, Water Res. 44 (2010) 2997–3027.
[47] G. Liu, W. Jaegermann, J. He, V. Sundström, L. Sun, J. Phys. Chem. B 106 (2002) 5814–5819.
[48] S.H. Lee, D.H. Kim, J.H. Kim, T.H. shim, J.G. Park, Synth. Met. 159 (2009) 1705–1709.
[49] J. Shang, M. Chai, Y. Zhu, Environ. Sci. Technol. 37 (2003) 4494–4499.
[50] T. Xu, G. Liu, J. Zhao, J. Phys. Chem. B 102 (1998) 5845–5851.
[51] H.M.S. Suh, J.R. Choi, H.J. Hah, S.M. Koo, Y.C. Bae, J. Photochem. Photobiol. A 163 (2004) 37–44.

Please cite this article in press as: W. Mekprasart, et al., Mater. Res. Bull. (2012), http://dx.doi.org/10.1016/j.materresbull.2012.08.024